12-2000

Development of Realistic Simulations of the Interactions Between Stars and the Interstellar Medium in Disk Galaxies

Thomas M. Zeltwanger

DEVELOPMENT OF REALISTIC SIMULATIONS OF THE INTERACTIONS BETWEEN STARS AND THE INTERSTELLAR MEDIUM IN DISK GALAXIES

BY

Thomas M. Zeltwanger

Diplom-Physiker (Univ.)

Ludwig-Maximilians-Universitat München, 1994

A THESIS

Submitted in Partial Fulfillment of the

Requirements for the Degree of

Doctor of Philosophy

(in Physics)

The Graduate School

The University of Maine

December, 2000

Advisory Committee:

Neil F. Comins, Professor of Physics, Advisor
David J. Batuski, Associate Professor of Physics
James L. Fastook, Professor of Computer Science
Peter H. Kleban, Professor of Physics
James P. McClymer, Associate Professor of Physics

External Reader: Richard V. E. Lovelace, Cornell University

DEVELOPMENT OF REALISTIC SIMULATIONS OF THE INTERACTIONS BETWEEN STARS AND THE INTERSTELLAR MEDIUM IN DISK GALAXIES

By Thomas M. Zeltwanger

Thesis Advisor: Dr. Neil F. Comins

An Abstract of the Thesis Presented
in Partial Fulfillment of the Requirements for the
Degree of Doctor of Philosophy
(in Physics)
December, 2000

We have developed GALAXY, a two dimensional, self-consistent N-body plus hydrodynamic computer program to model and study the behavior of disk galaxies like our Milky Way. Our goal is to better understand how such galaxies maintain their spiral structure for billions of years.

The program utilizes two independent gravitating N-body components. One simulates the collisionless star particles in the galaxy, and the other simulates colliding clouds. A gravitating hydrodynamic code simulates the interstellar medium. Additionally, a static spherical halo and a central black hole interact gravitationally with the other components of the model galaxy. All components interact with each other through various evolution processes and gravity, and they exchange mass, energy, and momentum.

For this dissertation I have primarily studied these interactions between the galaxy's individual components. These interactions include cloud formation from gas by Jeans instability, star formation through cloud collisions, star formation due to the snow-plow effect, gas infall from the halo, and supernovae. Each process is controlled by one or several parameters. These parameters are specified at the start of a simulation, along with other parameters which define the initial setup of the model galaxy. The influences of these evolutionary processes, and of different initial conditions of the model galaxy, were probed through series of simulations, during which all parameters were systematically varied. The simulations showed that the stellar evolution processes of the program have the ability to trigger the formation of spiral features in galaxies.

Through simulations involving galaxies with counter-rotating components we confirmed analytically derived predictions about such galaxies, like the formation of a leading one-armed spiral, the weakening of this spiral as Toomre's Q of the system exceeds 1.8, and the strengthening of this spiral as the fraction of counter-rotating components increases.

In another series of simulations we explored the properties and the origin of lopsided galaxies as a result of the high speed passage of a companion galaxy. We found that the disk's center of mass spiraled inward, creating observed or observable phenomena, including one-armed spirals, clumps of particles, and the possible suppression of a central bar.

ACKNOWLEDGEMENTS

I would like to thank foremost my thesis advisor, Professor Neil F. Comins, for his guidance, encouragement, and patience throughout this project. Thank you also to the other members of my advisory committee for their numerous useful comments and suggestions: David J. Batuski, James L. Fastook, Peter H. Kleban, and James P. McClymer. Special thanks to Richard V. E. Lovelace for the fruitful collaboration on two publications, and for agreeing to serve as the external reader of this dissertation.

I also want to express my gratitude towards the Department of Physics and Astronomy at the University of Maine for giving me the opportunity to do this project. Thank you to all faculty, staff, and graduate students in the department for all the help I received whenever I needed it. A special thank you goes to Pat Byard. I could not have done it without all those M&M's! Not to mention the moral support.

Special thanks go also to my wife Hanna, my son Robert, and my family in Germany. Without their continued support this work would not have been possible.

Thank you to Sun Microsystems and Electronic Data Systems for their generous donations of several Sun SPARCstations and HP workstations to our department.

This thesis was also greatly supported by a Graduate Teaching Assistantship and a University Graduate Research Assistantship from the University of Maine.

TABLE OF CONTENTS

ACKNOWLEDGEMENTS ii

LIST OF TABLES vii

LIST OF FIGURES viii

1 INTRODUCTION 1

2 THE GALAXY CODE 7

2.1 Initial Mass Distributions 11

2.1.1 A Black Hole in the Galaxy Center 11

2.1.2 Isothermal Sphere 13

2.1.3 Exponential Disk and Halo 15

2.2 Starting with an Isothermal Gas 17

2.3 Modified Cloud Formation 19

2.4 Simulating Counter-rotating Components 22

2.5 Displacing the Galactic Disk 23

2.6 Smoothing the Hydro Component 24

2.7 Porting the Code to Linux 25

2.8 Tools and Data Analysis 26

2.8.1 Toomre's Q 27

2.8.2 Center of Mass Motion 32

2.8.3 Gas Temperature 33

2.8.4 Making Movies 33

2.8.5 Data Output after every Integration Cycle 38

2.8.6 Fourier Analysis 39

2.8.7 Resonances 40

3 SIMULATIONS WITHOUT STELLAR EVOLUTION 42

3.1 The Base Run 43

3.2 Simulations with Counter-rotating Components 46

3.2.1 12.5% Counter-rotating Stars 46

3.2.2 25% Counter-rotating Stars 49

3.2.3 37.5% Counter-rotating Stars 51

3.2.4 50% Counter-rotating Stars 54

3.2.5 Summary of Runs with Counter-rotating Components 57

3.3 High Speed Interactions between two Galaxies 60

3.4 Simulations of Lopsided Galaxies 67

3.4.1 Small Offset, Low Angular Momentum 69

3.4.2 Small Offset, High Angular Momentum 72

3.4.3 Large Offset, Low Angular Momentum 73

3.4.4 Large Offset, High Angular Momentum 75

3.4.5 Summary of Runs with Lopsided Galaxies 77

4 SIMULATIONS WITH STELLAR EVOLUTION 78

4.1 Input Parameters of the GALAXY Code 79

4.1.1 Evolution Parameters 80

4.1.1.1 Gas Infall 80

4.1.1.2 Star Formation through Cloud Collisions 81

4.1.1.3 Cloud Formation by Jeans Collapse 83

4.1.1.4 Star Formation through Snowplow 83

4.1.1.5 Supernovae 84

4.1.2 Non-Evolution Parameters 85

4.2 Number of Star Particles 86

4.3 Mass Fractions 89

4.4 Toomre's Q for Stars 98

4.5 Number of Clouds 98

4.6 Toomre's Q for Clouds 99

4.7 Initial Internal Energy of the Gas 102

4.8 Isoergic Gas vs. Isothermal Gas 106

4.9 Modified Cloud Formation 116

4.10 Star and Cloud Formation Rates 119

4.10.1 Cloud Formation Rate 120

4.10.2 Star Formation Rate (i): From Cloud Collisions 124

4.10.3 Star Formation Rate (ii): From Snowplow 127

4.11 Energy Deposit to the ISM 129

4.12 Infall Rate 133

4.13 The Effects of Stellar Evolution 134

5 CONCLUSIONS AND OUTLOOK 141

5.1 Summary and Conclusions 141

5.2 Suggested future Work 144

REFERENCES 149

Appendix A UNIT CONVERSION 154

Appendix B OVERVIEW OF THE SIMULATIONS 155

Appendix C DATA ANALYSIS 163

BIOGRAPHY OF THE AUTHOR 207

LIST OF TABLES

3.1 Summary of runs with counter-rotating components 58

3.2 Summary of runs with an intruder 63

3.3 Summary of runs with lopsided galaxies 77

4.1 Runs differing by their mass fractions (with stellar evolution) 89

4.2 Runs differing by their mass fractions (no stellar evolution) 95

A.1 Unit conversions 154

B.l Explanation of parameters 155

B.2 Runs 14 through 20 156

B.3 Runs 21 through 27..... 157

B.4 Runs 28 through 33. 158

B.5 Runs 34 through 39 159

B.6 Runs 40through 45 160

B.7 Runs 46 through 51 161

B.8 Runs 52 through 56. 162

LIST OF FIGURES

2.1 Galaxy potentials for several mass distributions 15

2.2 Cloud formation - old and new 22

2.3 Toomre's Q - old and new 31

2.4 New Toomre's Q - few vs. many annuli 31

2.5 Gas temperature 34

2.6 Gas density 34

2.7 A snapshot of an MPEG movie 37

3.1 Base run - star mass distribution 44

3.2 Base run - Fourier amplitudes 45

3.3 12.5% counter-rotating stars - star mass distribution 47

3.4 12.5% counter-rotating stars - Fourier amplitudes 48

3.5 25% counter-rotating stars - star mass distribution 50

3.6 25% counter-rotating stars - Fourier amplitudes 51

3.7 37.5% counter-rotating stars - star mass distribution 53

3.8 37.5% counter-rotating stars - Fourier amplitudes 54

3.9 50% counter-rotating stars - star mass distribution 56

3.10 50% counter-rotating stars - Fourier amplitudes 57

3.11 Toomre's Q for the runs with counter-rotating components 59

3.12 Specific angular momentum 60

3.13 Photo of Karachentsev 64 62

3.14 Relative center of mass motion for a cold halo 64

3.15 Relative center of mass motion for a hot halo 64

3.16 Star mass distribution for the hot gas halo 65

3.17 Gas mass distribution for the hot gas halo 66

3.18 Small offset - Fourier amplitudes 71

3.19 Small offset - star mass distribution 71

3.20 Large offset - Fourier amplitudes 74

3.21 Large offset - star mass distribution 74

3.22 Center of mass motion of the stars, small offset 76

3.23 Center of mass motion of the stars, large offset 76

4.1 Star mass distribution of run # 14 87

4.2 Star mass distribution of run # 20 87

4.3 Rotation curve of run # 14 90

4.4 Rotation curve of run # 20 90

4.5 Star mass distribution of run # 27 92

4.6 Star mass distribution of run # 28 92

4.7 Star mass distribution of run # 39 97

4.8 Star mass distribution of run # 42 97

4.9 Star mass distribution of run # 14 101

4.10 Star mass distribution of run # 23 101

4.11 Temperature map for three different ceg values 105

4.12 Star mass distribution of run # 16 105

4.13 Star mass distribution of run # 22 105

4.14 Star mass distribution of run # 33 108

4.15 Clouds, gas, and temperature of run # 33 108

4.16 Star mass distribution of run # 37 109

4.17 Star mass distribution of run # 35 109

4.18 Star mass distribution of run # 36 109

4.19 Star mass distribution of run # 47 111

4.20 Star mass distribution of run # 48 111

4.21 Star mass distribution of run # 40 113

4.22 Star mass distribution of run # 41 113

4.23 Star mass distribution of run # 38 115

4.24 Star mass distribution of run # 49 115

4.25 Cloud mass distribution of runs # 31, # 32, and # 33 118

4.26 Star mass distribution of runs # 31, # 32, and # 33 118

4.27 Cloud mass distribution of run # 25 121

4.28 Star mass distribution of run # 21 126

4.29 Cloud mass distribution of run # 50 126

4.30 Cloud mass distribution of run # 51 128

4.31 Star mass distribution of run # 51 128

4.32 Star mass distribution of run # 50 135

4.33 Star mass distribution of run # 53 135

4.34 Star mass distribution of run # 44 139

4.35 Star mass distribution of run # 45 139

C.1 Data Analysis of run # 14 164

C.2 Data Analysis of run # 15 165

C.3 Data Analysis of run # 16 166

C.4 Data Analysis of run # 17 167

C.5 Data Analysis of run # 18 168

C.6 Data Analysis of run # 19 169

C.7 Data Analysis of run # 20 170

C.8 Data Analysis of run # 21 171

C.9 Data Analysis of run # 22 172

C.10 Data Analysis of run # 23 173

C.11 Data Analysis of run # 24 174

C.12 Data Analysis of run # 25 175

C.13 Data Analysis of run # 26 176

C.14 Data Analysis of run # 27 177

C.15 Data Analysis of run # 28 178

C.16 Data Analysis of run # 29 179

C.17 Data Analysis of run # 30 180

C.18 Data Analysis of run # 31 181

C.19 Data Analysis of run # 32 182

C.20 Data Analysis of run # 33 183

C.21 Data Analysis of run # 34 184

C.22 Data Analysis of run # 35 185

C.23 Data Analysis of run # 36 186

C.24 Data Analysis of run # 37 187

C.25 Data Analysis of run # 38 188

C.26 Data Analysis of run # 39 189

C.27 Data Analysis of run # 40 190

C.28 Data Analysis of run # 41 191

C.29 Data Analysis of run # 42 192

C.30 Data Analysis of run # 43 193

C.31 Data Analysis of run # 44 194

C.32 Data Analysis of run # 45 195

C.33 Data Analysis of run # 46 196

C.34 Data Analysis of run # 47 197

C.35 Data Analysis of run # 48 198

C.36 Data Analysis of run # 49 199

C.37 Data Analysis of run # 50 200

C.38 Data Analysis of run # 51 201

C.39 Data Analysis of run # 52 202

C.40 Data Analysis of run # 53 203

C.41 Data Analysis of run # 54 204

C.42 Data Analysis of run # 55 205

C.43 Data Analysis of run # 56 206

1 INTRODUCTION

Simulations of disk galaxies to study their spiral structures have been done for more than half a century. Michael Schroeder (1989) and Peter Shorey (1996) have given an overview of the simulations performed from the 1940s through 1995, and they established with their contributions to galaxy simulations the foundations on which this thesis is based.

Schroeder (1989) developed a two dimensional combined N-body and hydrodynamic computer code to model disk galaxies. An N-body portion of the code simulates the collisionless star particles and the hydrodynamics part of the code is used to model the dynamics and evolution of the Interstellar Medium (henceforth "ISM"). Additionally, a static halo is included in the code as a stabilizing element. Observational evidence confirms the existence of such halos (Faber and Gallagher, 1979; Bosma, 1999; Bosma, 1981; Persic and Salucci, 1990; Rubin et al., 1985), and their contribution to the total mass of a galaxy may be 84% (Persic and Salucci, 1990) or higher. Based on rotation curves of spiral galaxies, halo mass fractions as high as 95% are not unlikely (Batuski, 2000). The exact nature of halos is still subject to observational investigation. Suggestions include brown dwarfs (McCarthy et al., 1985), white dwarfs (Gates and Gyuk, 1999), MACHOs (Koopmans and de Bruyn, 2000; Green, 2000), and WIMPs (Jungman et al., 1996). MACHOs are "MAssive Compact Halo Objects", for example primordial black holes. WIMPs ("Weakly Interacting Massive Particles")

are conjectured to be fundamental particles (like the electron) but with no electric charge and no interaction with light or other electromagnetic radiation.

The hypothesis that two-body collisional relaxation in two-dimensional simulations is not negligible (White, 1988) was tested and confirmed by Schroeder. He found that collisions are a major cause of heating in axisymmetric, stable disk simulations (Schroeder, 1989). His experiments revealed that perturbations of such stable disks by weak logarithmic spiral potentials or by collisions with other (point mass) galaxies produces two-armed spirals which are kinematic waves rather than density waves. Furthermore, Schroeder found that the effect of the addition of an ISM is minimal and reduces the required stabilizing halo by only a few percent. Finally, he determined that the stellar birth rate and its cooling effects on the disk are quickly reduced, unless mass is constantly taken from the halo and added to the ISM.

Shorey continued and extended Schroeder's work (Shorey, 1996). Most noteworthy, he included colliding cloud particles in the code. For the calculation of the gravitational potential, these cloud particles are treated as point masses, just like the star particles. But they have also a "virtual radius" assigned to them, which depends on their mass. A spherical shape for the clouds is assumed. If two clouds get closer to each other than the sum of their radii, they collide. Earlier simulations demonstrated that strong spiral structure in a cloudy medium can exist many times longer than in the stellar component, due to energy dissipation during inelastic collisions (Carlberg and

Freedman, 1985; Shorey, 1990). Since stars often form from clouds (Elmegreen et al., 1995), the integration of these colliding cloud-particles into the code was a major step towards a more realistic model of dynamic, evolving, spiral galaxies.

Shorey also studied the effects of numerical artifacts in the hydrodynamics code and minimized them. He created response curves for each stellar evolution process and, based on those, he determined a set of input parameters which resulted in a near-steady-state system. Shorey explored the sensitivity of this near-steady-state system to variations in the input parameter space and the grid resolution, and he confirmed Schroeder's result that relaxation effects are present. His simulations demonstrated that strong spiral structures in a cloudy ISM can exist many times longer than in the stellar component, and provide a favorable environment for the birth of new stars through cloud collisions.

Several groups and individuals have contributed ground breaking work in computational research of spiral galaxies in the recent years since Shorey's overview (1996). Englmaier and Shlosman (2000) performed 2D numerical simulations of gas response to the background gravitational potential of a barred stellar disk to study the mechanism for the formation, maintenance, and the detailed shape of nuclear spirals. Korchagin and Theis (1999) used 2D nonlinear simulations to study the generation and nonlinear evolution of spiral structure in a star-forming multi-component gravitating disk. They show that the spiral structure growing on a non-stationary multi-phase

background reaches its saturation in a manner similar to the one-component disks. Athanassoula and Bureau (1999) found a reliable indicator for the presence of a bar in an edge-on spiral galaxy if a nuclear spiral is formed, using edge-on 2D hydrodynamical simulations of the gas flow in a barred galaxy potential. Fux (1999a; 1999b) modeled the gas dynamics in galactic disks with an initially axisymmetric SPH ("Smooth Particle Hydrodynamics") component in a completely self-consistent and symmetry-free 3D N-body simulation. The density center of the stellar bar wanders around the center of mass and the resulting gas flow is asymmetric and non-stationary.

Computer simulations of disk galaxies continue to be a valuable complement to observational and theoretical research in this field. Due to the continuing development of more powerful computers and the utilization of sophisticated and effective computer algorithms, simulations of disk galaxies become ever more realistic as the star particle numbers of the simulated galaxies approach those of their real counterparts ($\approx 2 \times 10^{11}$). Shalit (1995) for example showed that the lifetime of spiral structures in disk galaxies increases when more star particles are utilized. However, past results have also demonstrated that pure N-body simulations alone may not be sufficient to explain the long-lived spiral structures that are observed in spiral galaxies like our Milky Way, and that stellar evolution processes may play an important role. The improved modeling of the already implemented stellar evolution processes along with more realistic simulations of the interactions of the stars and the halo with the ISM in disk galaxies have therefore been the major purpose of this thesis.

Another goal has been to use the code to model specific galactic systems to explain some of their observed features, and to test existing theories about galactic dynamics. In particular, galaxies with counter-rotating components, and the origin and nature of lopsided galaxies have been the target of these studies. The simulations with counter-rotating components have been motivated by observations of such galactic systems, like NGC 3593 (Bertola et al., 1998), NGC 4138 (Jore et al., 1996; Thakar et al., 1997), NGC 4550 (Rubin et al., 1992; Rix et al., 1992), NGC 7217 (Merrifield and Kuijken, 1994), and NGC 7331 (Prada et al., 1996). The fraction of counter-rotating stars in these systems has been observed to be as high as 50%. This series of simulations served also the purpose of testing a theory of the two-stream instability found in flat counter-rotating galaxies (Lovelace et al., 1997).

Motivation to study lopsided galaxies also comes from observational evidence. Stellar distributions (Lauer et al., 1993; Lauer et al., 1996; Rix and Zaritsky, 1995; Davidge et al., 1997; Zaritsky and Rix, 1997; Conselice, 1997) as well as hydrogen distributions (Baldwin et al., 1980; Richter and Sancisi, 1994) of a significant fraction of spiral galaxies (30% to 50%) have been reported to be lopsided. Among possible scenarios that could cause such lopsidedness is the gravitational interaction between two galaxies. To verify the possible creation of lopsidedness through such interactions we sent a companion galaxy in a high-speed (positive energy) orbit around the model galaxy and observed the center-of-mass motion of the stellar disk (which is an indicator for lopsidedness).

The simulations for this thesis have been run on a variety of hardware/software combinations: Sun 3/60 and Sun SPARCstation 2 computers running SunOS 4.1.1, Sun SPARCstation 10 and Sun SPARCstation 20 machines under Solaris 2.5.1 and Linux, a Hewlett Packard Series 735 computer with the HP-UX 9.07 and the HP-UX 10.20 operating system, PCs running Linux, and finally on an SGI computer with the IRIX operating system. Great effort has been undertaken to write the code in standard ANSI Fortran, to ensure that it a) runs on virtually any computer with a Fortran compiler and b) produces the same qualitative result for the same set of input parameters, no matter which machine the code is run on.

In the next chapter I describe the GALAXY code in general, and the modifications and extensions that have been made as part of this thesis in particular. Additionally, a number of tools and helper programs that were developed to assist in analyzing and visualizing the vast amounts of data produced by the GALAXY simulations are also described in Chapter 2. Chapter 3 presents the results of simulations with stellar evolution switched off. These include simulations with counter-rotating star particles in a disk galaxy, and simulations which investigate the origin and nature of lopsided galaxies. In Chapter 4 I show the results of GALAXY simulations with stellar evolution switched on, and how variations in the parameter space that governs the stellar evolution process in the code affect the outcome of those simulations. And in Chapter 5 I present and discuss my conclusions.

2 THE GALAXY CODE

GALAXY is a two dimensional, self-consistent N-body plus hydrodynamic computer program to model and study the behavior of disk galaxies like our Milky Way. The program utilizes two independent gravitating N-body components. One simulates the collisionless star particles in the galaxy, and the other simulates colliding clouds. "*N*-body" means that the particles are modeled as point masses with no other properties than gravitational attraction and mass. A gravitating hydrodynamic portion of the code simulates the interstellar medium. Additionally, the gravitational potentials due to a static spherical halo and a central black hole are included. All components interact with each other through various evolution processes and gravity, and they exchange mass, energy, and momentum. These evolutionary processes include cloud formation from gas by Jeans instability, star formation through cloud collisions, star formation due to the snowplow effect, gas infall from the halo, and supernovae.

The simulations are done using a Cartesian grid, which is typically 256 x 256 cells in size. The star particles are modeled as point masses, and each star particle represents actually a whole cluster of stars. For a simulation with 10^5 star particles, the number of stars in each cluster is about 2 x 10^6. This is based on the assumption that a typical spiral galaxy contains about 2 x 10" stars (Binney and Tremaine, 1987). The cloud particles are modeled as point masses, too, but each cloud also has a "virtual" radius associated with it, which depends on the cloud's mass (the clouds are assumed

to have spherical shape). If two clouds approach each other to a distance less or equal to the sum of their radii, they collide. As a result, the colliding clouds may merge into one big cloud, bounce off each other (mass transfer from the smaller cloud to the bigger cloud is possible), or break into several fragments (mass breaks off from both colliding clouds and forms a third cloud). In every case, mass and momentum are conserved, and new stars may form at the collision interface.

The initial state of the model galaxy is determined by a set of input parameters, which are set at the start of a simulation. In this parameter input file, one can select the initial radial distribution of the mass, and the mass fractions assigned to the various components (stars, clouds, gas, and halo). The gas can be chosen to be either isothermal (initial uniform temperature), or isoergic (initial uniform energy density).

Additionally, the softening factor sf and the grid utilization gu can be specified in this parameter input file. “Softening” is a commonly used method in N-body simulations to avoid that the gravitational force F between two close star particles gets too large. F is inversely proportional to the square of the distance d between two particles: $F \propto d^{-2}$. With a softening factor sf, F is modified as follows: $F \propto (sf^2 - d^2)^{-1}$. That way, particles are always kept at an artificial distance greater or equal than sf^2, preventing the gravitational force F between them from becoming too large. The “grid utilization” gu specifies what fraction of the simulation grid is initially occupied by the model galaxy. For a 256 x 256 grid, gu = 1.0 corresponds to an initial galaxy

radius of 128 grid cells, and the usually used value of gu = 0.75 sets this radius to only 96 grid cells. That way, the model galaxy has some room to expand or deform without instantly reaching the edge of the simulation grid.

Other input parameters control the initial position of the stellar disk on the simulation grid, the fractions of counter-rotating components (for stars, clouds, and gas), and the numbers of star and cloud particles. The initial value of Toomre's Q (to be defined in Section 2.8.1) for both types of particles is also set in the parameter input file. Furthermore, the mass, the initial position, and the initial velocity of an optional intruder galaxy can be specified.

Finally, a group of input parameters controls all evolutionary processes. These evolution parameters are discussed in Chapter 4. For a more comprehensive description of the GALAXY code please refer to the PhD theses of Michael Schroeder (1989) and Peter Shorey (1996), and to the "GALAXY User Manual" (Zeltwanger, 2000). The following sections describe the modifications that have been made to the code and the extensions that have been added:

- In addition to the already existing mass distributions that can be selected for the model galaxy, two more have been implemented: an exponential mass distribution and an isothermal sphere model (for the halo only). Additionally, the gravitational potential due to a massive black hole at the galaxy center can be included.

- The initial state of the gas component can now be selected as isothermal.
- The cloud formation routine was modified to remedy the heavy cloud formation activity typically seen in the galaxy center under the old model.
- Fractions of the galaxy mass can be sent into counter-rotating motion at the beginning of the simulations.
- The galactic disk can be shifted as a whole to create an artificial offset between the centers of mass of the halo and of the stars.
- The hydro part of the code uses a new smoothing algorithm.
- The code now runs under Linux.

Any individual run of the GALAXY program creates a large amount of data output. Depending on which variables one is interested in for a particular run, and how frequently a data output is required, the amount of data created by a single run can easily exceed one gigabyte. The necessity to analyze and visualize this vast amount of data in a time efficient manner made the development of automated tools a topic for this thesis. New tools for data analysis had to be developed in addition to the already existing ones, and some of those already existing have been modified to accommodate additional requirements. The last section of this chapter describes those new and improved tools, and shows examples of their use.

2.1 Initial Mass Distributions

Unless otherwise noted, all simulations performed for this thesis have used an initial mass distribution that models an SC disk as described by Sellwood and Carlberg (Sellwood and Carlberg, 1984) and by Shorey (Shorey, 1996). This initial mass distribution is axisymmetric, and the resulting initial mass density, Σ_{Sc}, therefore depends only on the distance r from the galactic center:

$$\Sigma_{Sc}(r) = \Sigma_{0,Sc}\left(1+\frac{20r}{a}\right)^{-0.75}\left(1+\frac{r}{5a}\right)^{-2} \tag{2.1}$$

$\Sigma_{0,Sc}$ is the disk mass scale, a is the disk length scale, and for an SC disk $r_{tr} = 7a$, where r_{tr} is the truncation radius.

To study the response of some simulations to variations of the initial mass distribution, several new initial mass loads have been implemented into the code. These will be described in the following sections.

2.1.1 A Black Hole in the Galaxy Center

A growing body of evidence suggests that most galaxies – including disk galaxies – contain a super-massive black hole at their center (Elmegreen, 1998; Hozumi and Hernquist, 1999; Merritt, 2000; Fukuda et al., 1999; Richstone et al., 1998; Richstone,

1998; Ferrarese et al., 1998; Binney and Tremaine, 1987; Sridhar and Touma, 1999). These super-massive black holes may have already formed in the galaxy center, or they have been carried there through dynamical friction. Even if a black hole of $m = 10^7\ M_\odot$ or more forms far out in the galaxy, dynamical friction will carry it into the galaxy's center in less than a Hubble time (Richstone, 1998). To be able to simulate such galaxies, the possible addition of a black hole was implemented into the GALAXY code. To have a black hole as part of the model galaxy, one of the regular star particles is given a mass consistent with current knowledge (Binney and Tremaine, 1987; Salucci et al., 2000) about black hole masses ($10^3\ M_\odot$ to $2 \times 10^{10}\ M_\odot$), and is placed at rest at the center of the galaxy. Other than gravitationally, the black hole does not interact with its environment. Specifically, the black hole does not consume any nearby matter, its mass remains constant. Due to its high mass (equivalent to $4.2 \times 10^8\ M_\odot$) and placement at rest at the bottom of the well of the galactic potential, its position throughout a simulation remains virtually unchanged: during none of the simulations performed with a central black hole did it leave the central grid cell.

Figure 2.1 on page 15 compares several galactic potentials, including one with a central black hole. Galaxies with a potential due to an isothermal sphere combined with a central black hole show a higher stability against bar formation than an SC disk (Zeltwanger et al., 2000).

2.1.2 Isothermal Sphere

Rotation curves of many spiral galaxies are flat or slowly increasing out to the radius of the optical disk (Faber and Gallagher, 1979; Rubin et al., 1980; Rubin et al., 1982; Rubin et al., 1985), suggesting that spiral galaxies like our Milky Way possess massive dark halos that extend to larger radii than the optical disks (Freeman, 1970). If the dark halo is approximated as spherical, then a rotation curve with constant velocity v_c implies the following dark halo mass density p(r):

$$\rho(r) = \frac{v_c^2}{4\pi G r^2} \tag{2.2}$$

This is the density distribution for an isothermal sphere at large radii (Binney and Tremaine, 1987). In an isothermal sphere of stars, every part of the sphere has stars moving at the same average velocity as every other part (Elmegreen, 1998). For small radii, the halo density must fall below the value given by equation (2.2), because the rotation curves remain flat even when the disk mass contributes a substantial fraction of the rotation speed. A more appropriate form of the halo density – and the form used in the GALAXY code – is therefore

$$\rho(r) = \frac{\rho_0}{1 + \left(\frac{r}{r_c}\right)^2} \tag{2.3}$$

r_c is the core radius at which the projected density of the isothermal sphere falls to roughly one half of its central value. The value of r_c can be specified in the parameter input file. ρ_0 is determined as follows: the total mass of the halo, M_{halo}, is equal to the halo mass fraction, f_{halo}, times the total mass of the galaxy, M_{galaxy}:

$$M_{halo} = f_{halo} \cdot M_{galaxy} \tag{2.4}$$

where f_{halo} is specified in the parameter input file as a number between 0 and 1. With the constraint that the integration of equation (2.3) from r = 0 to the cutoff radius $r = r_{tr}$ must result in the total halo mass M_{halo}, the GALAXY program can compute the correct value of ρ_0.

The isothermal sphere halo mass distribution was implemented in the code to test the disk's response to an initial offset from the halo's center of mass under the influence of various halo potentials (Zeltwanger et al., 2000). Most noticeably, a galaxy with an isothermal sphere halo is more bar-unstable than one with an SC halo mass distribution.

Figure 2.1 compares several galactic potentials, including isothermal sphere potentials with and without a central black hole.

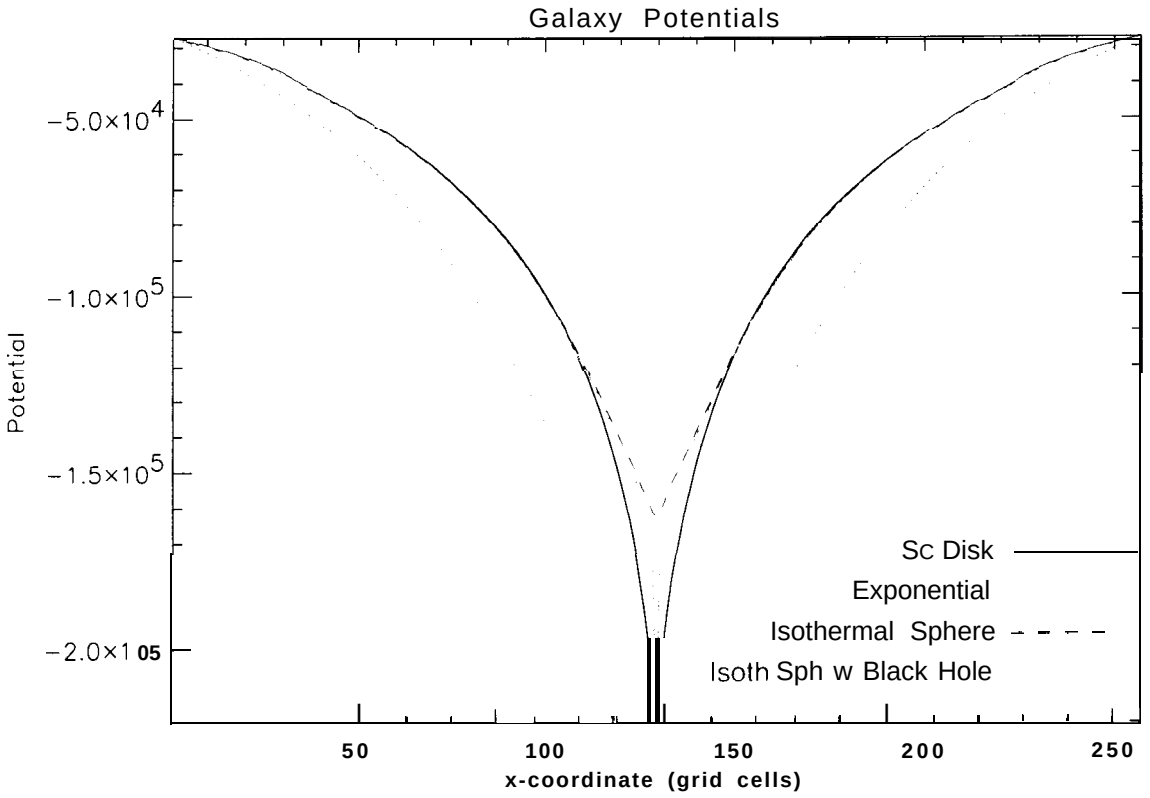

Figure 2.1: Galaxy potentials for several mass distributions. Most simulations in this thesis utilize the SC disk. The other mass distributions have been used to assess the influence of the halo shape in the runs with lopsided galaxies.

2.1.3 Exponential Disk and Halo

Observations of galaxies of a form similar to the Milky Way suggest that the radial mass density profile of the disk is an exponential function of the radius r:

$$\Sigma_{exp}\ (r) = \Sigma_{0,exp}\ \exp\left(-\frac{r}{r_d}\right) \tag{2.5}$$

(Binney and Tremaine, 1987). The disk scale length r_d has been determined to be 3.5 ± 0.5 kpc for the Milky Way (de Vaucouleurs and Pence, 1978). For most simulations in this thesis an SC disk as described by equation (2.1) has been used as the initial mass distribution. Therefore, the constants $\Sigma_{0,exp}$ and r_d have been chosen so that the mass density distribution of the exponential model at the galaxy center (at r = 0) and at the truncation radius (at r = r_{tr}) are equal to the mass density distribution of an SC disk at those two radii:

$$\begin{aligned} \Sigma_{exp}(0) &= \Sigma_{Sc}(0) \\ \Sigma_{exp}(r_{tr}) &= \Sigma_{Sc}(r_{tr}) \end{aligned} \tag{2.6}$$

With the constraints dictated by equations (2.6), $\Sigma_{0,exp}$ and r_d can be determined from equations (2.5) and (2.1):

$$\begin{aligned} \Sigma_{0,exp} &= \Sigma_{0,Sc} \\ r_d &= -\left[\frac{1}{r_{tr}} \log\left(\left(1+\frac{20r_{tr}}{a}\right)^{-0.75}\left(1+\frac{r_{tr}}{5a}\right)^{-2}\right)\right]^{-1} \end{aligned} \tag{2.7}$$

The potential due to this exponential mass distribution is also shown in Figure 2.1.

2.2 Starting with an Isothermal Gas

Previous simulations with the GALAXY code assigned the gas component a uniform internal energy across the disk (Schroeder, 1989; Shorey, 1996). The value of this internal energy can be set in the input parameter file. An alternate approach for setting the initial conditions of the gas was implemented into the code by specifying an initial temperature of the gas (an isothermal gas) rather than the initial internal energy (an isoergic gas). One can now choose in the parameter input file whether the gas should initially be isoergic or isothermal. If isothermal is selected, then the temperature of this isothermal gas (in Kelvin) can also be set in the parameter input file. In general, the energy density of the gas per unit volume, e(r), is given by

$$e(r) = \frac{1}{2}\rho(r)(v(r))^2 + \frac{P(r)}{\gamma - 1} \tag{2.8}$$

(Schroeder, 1989) where ρ is the mass density per unit volume of the gas, v is its velocity, P is its pressure, and γ is the ratio of the heat capacities, $\gamma = c_p/c_v$. The initial setup is axisymmetric, therefore there is only an r dependence of e, ρ, v, and P.

The first part of the right side in equation (2.8) is the *kinetic* energy density of the gas, the second part defines its *internal* energy density, U/V. From the latter, the

temperature of the gas can be determined, assuming that the gas obeys the ideal gas equation, which is the case in the GALAXY program.

$$T = \mathcal{F}\,\frac{U}{M} \tag{2.9}$$

U is the internal energy and M is the gas mass in the cell for which the temperature is computed, respectively. The 3 symbolizes a factor of physical quantities which has conveniently been set to unity in the code, to save computational time. Specifically:

$$\mathcal{F} = \frac{(\gamma - 1)\, m_p}{k_B} \equiv 1 \tag{2.10}$$

γ is the ratio of heat capacities, $\gamma = c_p/c_v$. m_p is the mass of one gas particle, and k_b is the Boltzmann constant. With equations (2.8) and (2.9) the stage is set for an initially isothermal gas by specifying a start temperature T_0, reversing equations (2.8) and (2.9) and then calculating the resulting energy density from there. This is necessary because the GALAXY program uses the energy density of the gas for evaluation of the hydrodynamic equations.

2.3 Modified Cloud Formation

As part of the evolution processes in the GALAXY code, localized portions of the ISM may undergo Jeans collapse to form cloud particles. Cloud particles may then collide with each other and trigger the formation of new stars at the collision interface. In regions of higher cloud density, there is, therefore, a higher probability of clouds colliding with each other, and these regions should thus be hosts to massive star formation. This is observed to occur in the simulations. In fact, previous versions of the cloud formation by a Jeans collapse routine produced a high cloud population in the galaxy core, which in turn increased the possibility of cloud collisions and churned out massive numbers of new stars in the disk center. The star formation in the outer regions of the galaxy, by contrast, was almost negligible, producing mostly featureless (little or no spiral arm formation) and thus unrealistic galaxy models.

To avoid the heavy cloud formation in the galaxy center, and to sustain a substantial cloud population in the outer galactic regions, we need to understand how the GALAXY code decides where and when to form a new cloud. For a given gas density ρ and temperature T, a volume of gas will collapse if its total mass exceeds the critical Jeans Mass, M_J, which is defined as (Binney and Tremaine, 1987):

$$M_J = \frac{1}{6}\pi\rho\left(\frac{\pi v_s^2}{G\rho}\right)^{\frac{3}{2}} \tag{2.11}$$

G is the gravitational constant, and v_s is the speed of sound. For an ideal gas, v_s is given by (Kuchling, 1988):

$$v_s = \sqrt{\gamma R T} \tag{2.12}$$

where R is the specific gas constant of the collapsing gas (with units of J kg-' K^{-1}), and γ has previously been defined as the ratio of heat capacities, $\gamma = c_p/c_v$.

The probability $\mathcal{P}$ for formation of a cloud through Jeans collapse is then (Shorey, 1996)

$$\mathcal{P} = \mathcal{P}_{cfr}\sqrt{\frac{\rho}{T^3}} \tag{2.13}$$

$\mathcal{P}_{cfrc}$ is a user defined input parameter which controls the cloud formation rate. A random number s is then compared to $\mathcal{P}$, and a new cloud is created if $\mathcal{P}$ > s. Clouds have been observed to have masses ranging from $10^{2.7}$ $M_\odot$ to $10^{5.7}$ $M_\odot$ (Chieze and Lazareff, 1980; Cowie, 1980; Casoli and Combes, 1982), and the mass of the newly formed cloud is randomly selected from within this range. The new cloud's velocity is set to the velocity of the gas in the grid cell in which the cloud formation happens. This process may happen several times during one time step for any given grid cell, provided that the cell sustains favorable conditions for a Jeans collapse.

These conditions are re-evaluated after a new cloud has formed, to determine whether to form yet another cloud, or to discontinue the process in that grid cell for the present time step. The gas mass that is not converted into a cloud, remains in the ISM. The total mass of the system is conserved that way.

The modification to equation (2.13) introduced for this thesis adds another factor, which modifies the original cloud formation probability depending on location. Specifically, the modified cloud formation probability, P', is calculated from

$$\mathcal{P}' = \frac{\mathcal{P}}{(40 - r)^2} \tag{2.14}$$

where r is the distance from the galaxy center, measured in units of grid cell length (see Appendix A for unit conversion). Equation (2.14) is only applied for locations with $r \leq 39$. Thus, for $r > 39$, $\mathrm{P}' = \mathcal{P}$, and for $r \leq 39$ the probability for cloud formation drops with a square law. The cutoff radius $r = 39$ has been chosen because this was approximately the radius of the immensely dense cloud core before modifying equation (2.13). Figure 2.2 compares the cloud density at $t = 14.229$ revolutions of two otherwise identical simulations for the old and the new cloud formation routine.

It should be noted that this modified model for the cloud formation by Jeans collapse is purely empirical and only used because it favors the formation of "more realistic" galaxies, as we shall see in Chapter 4. Other than that there is no obvious justification for preferring the new routine over the old one.

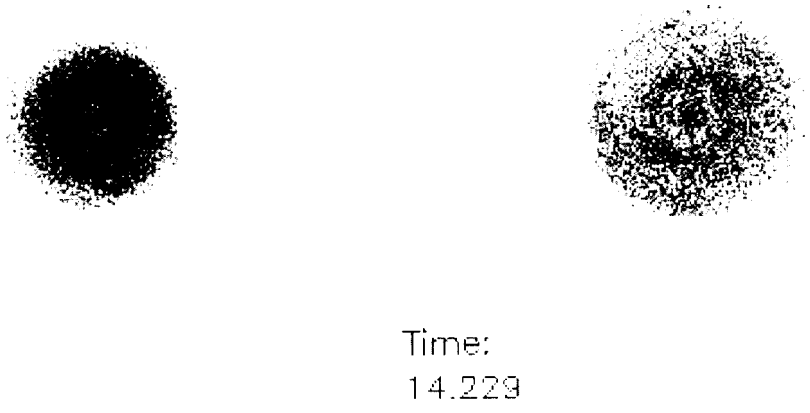

Figure 2.2: Cloud formation – old and new. The old cloud formation routine typically produced a very dense cloud population at the galaxy center (left panel). The new routine drives cloud formation away from the galactic center, leaving it less densely populated than originally (right panel). The two simulations are otherwise identical.

2.4 Simulating Counter-rotating Components

To be able to run simulations involving counter-rotating components, three new input parameters were introduced to the code. Those determine the fractions of counter-rotating star particles, clouds, and hydro cells, respectively. The value of these parameters can range from zero (everything rotates counterclockwise) to one (everything rotates clockwise), and they can be set independently from each other.

The fraction of counter-rotating stars, $f_{counter}$, and the total number of stars in the simulation, n_{total}, can be specified in the parameter input file. From these, the number of counter-rotating star particles, $n_{counter}$, is determined:

$$n_{counter} = f_{counter} \cdot n_{total} \tag{2.15}$$

The velocity vector of $n_{counter}$ randomly selected stars is then reversed following the initial load of the star mass distribution.

For clouds, the counter-rotating particles are initialized in the same way as star particles.

The counter-rotating gas portion is determined in a similar way, except that for the gas there are no particles for which the velocity vector could be reversed. Instead, for every cell on the simulation grid, the momentum of the gas in that cell is loaded according to the selected initial disk type. To get the desired counter-rotating gas portion, the momentum vector of a number of randomly selected grid cells, that corresponds to the fraction of counter-rotating gas, is reversed.

2.5 Displacing the Galactic Disk

To be able to do a series of simulations involving lopsided galaxies it was necessary to add a feature to the code that would displace the initial stellar disk's center of mass from the halo center of mass by a specified amount. Four new parameters in the input file accomplished this: *scoofx*, *scoofy*, *scnofx*, and *scnofy*. These set the initial offsets of the star particles in the x and y directions for the co-rotating *(scoofx* and *scoofy)* and the counter-rotating components *(scnofx* and *scnofy).*

The simulations with lopsided galaxies performed for this thesis are described in Chapter 3. Being able to specify a different initial offset for the co-rotating and the counter-rotating components, for example, makes it possible to simulate the interaction (close encounter, collision, or merger) of stellar disks with opposite angular momentum.

To determine which stars are initially co-rotating and which are initially counter-rotating, each star particle's angular momentum is determined prior to setting its offset. Stars with a positive angular momentum are called co-rotating, and a negative angular momentum identifies counter-rotating stars.

2.6 Smoothing the Hydro Component

Occasionally, the code would overestimate changes in the conserved variables, resulting in negative pressure, energy, or mass density in a cell. Previous attempts to "fix" this unphysical behavior included multiplying negative values by -1, replacing the negative values with a small, positive constant, and replacing them with a small fraction of their last nonzero value (Schroeder, 1989; Shorey, 1996).

While these schemes helped to remedy the problem somewhat, the central pressure in the hydro part would still rise quickly beyond reasonable bounds ($> 10^9$) and consequently increase the temperature accordingly. Reasonable central gas pressures are of the order 10^6 to 10^7 (in computer units. See Appendix A for unit conversions).

The implementation of a more successful smoothing algorithm was desirable. It was found in "Numerical Recipes in Fortran" (Press et al., 1994), from which a modified version of the "Bilinear Interpolation" method was adapted. Essentially, this method smoothes out discontinuities in a cell by averaging the values of the eight surrounding cells and assigning the result to the cell in question. Careful consideration needs to be given to those surrounding cells, to assure that they themselves do not also have negative values.

If one is willing to trade faster execution for higher accuracy, then the next best smoothing schemes would be "Bicubic Interpolation" and the "Bicubic Spline" method. These make use not only of the function value at the grid points, but also of its partial derivatives. For now, the implemented bilinear method seems to be sufficient, though, to smooth out the hydro component of the code, reducing the central pressure by some three orders of magnitude and keeping the central temperature within reasonable limits. In fact, in all runs with an initial isothermal gas of 10 K, the central temperature would never rise above 15 K. These runs are discussed in Chapter 4.

2.7 Porting the Code to Linux

At an early point during this thesis project, the fastest computer at my disposal was a Pentium class PC running the Linux operating system. To run the GALAXY code on this machine it was necessary to modify the subroutine which generates

random numbers for the Monte Carlo procedure that loads the initial star positions and velocities. The original implementation of the random number generator was machine specific in the sense that it produced sufficiently random numbers for the computers on which the code was first developed (SUN 3/60 workstations). But on the Linux machine it exhibited a periodicity in the series of produced random numbers that caused different stars to be placed at the exact same location with the exact same velocity vector.

To get rid of this problem a new random generating procedure replaced the original one. The new one is taken out of "Numerical Recipes in Fortran" (Press et al., 1994) and has a periodicity of $\approx 2.3 \times 10^{18}$. With a typical spiral galaxy containing "only" of the order 2×10^{11} stars, and with our largest simulations currently utilizing not more than 10^6 star particles, this new random number generator should be adequate for all future projects with the GALAXY code.

2.8 **Tools and Data Analysis**

This section is dedicated to the description of how the vast amount of data produced by the GALAXY code has been processed and visualized following the completion of a simulation.

Most tools for plotting and analyzing the data output produced by the GALAXY program have been developed earlier (Shorey, 1996) and were used "as is", or ported to

IDL (“Interactive Data Language”, a commercial computing environment by Research Systems, Inc. for the interactive analysis and visualization of data) with little or no modifications. Other plotting routines were originally written for a specific hardware/software combination (Shorey, 1996), which has not been available any more. Therefore, and to ensure a consistent “look and feel” for all included graphics, some plotting routines needed either more fundamental modifications, had to be rewritten entirely, or had to be coded from scratch (in IDL). Examples of these are discussed in the following sections.

2.8.1 Toomre’s Q

Toomre’s Q, a parameter introduced by Alar Toomre (Toomre, 1964), describes a local stability criterion for disk galaxies, and is defined as follows:

$$Q(r) = \frac{\kappa(r)\,\sigma(r)}{3.36\ G\ \Sigma(r)} \tag{2.16}$$

where K(T) is the radial epicyclic frequency, a(r) is the radial velocity dispersion, G is the gravitational constant, and $\Sigma(r)$ is the mass density of the stars. It can be shown (Binney and Tremaine, 1987) that any small circular area of a thin stellar disk is stable against radial perturbations if Q > 1. From equation (2.16) it can also be seen that Q is proportional to the radial velocity dispersion a(r). Q serves,

therefore, as a thermometer for galactic disks. A stellar disk with Q > 1 is stable against axisymmetric perturbations and such a disk is often called “warm”. For Q < 1 (“cool” disk), small circular areas of a thin stellar disk are unstable against radial perturbations. Such local instabilities in a disk can be the seeds for global instabilities, like central bars or spiral structures. Thus, to maintain prolonged spiral structures, we want to keep the disk cool. Q is, however, not an absolute measure for a disk’s tendency to grow instabilities. Once a localized portion of the disk becomes unstable, the instability can self-propagate and affect other parts of the disk, or the entire disk, even if the local Q value in those regions would suggest stability against perturbations. The evolution of Q can nonetheless provide valuable insight into a disk’s dynamics and it is widely used in disk analysis.

Equation (2.16) can be used to define a Q for stars or to define a Q for clouds. For clouds, $\kappa(r)$, a(r), and $\Sigma(r)$ refer to the clouds’ radial epicyclic frequency, radial velocity dispersion, and mass density, respectively. Throughout this dissertation, “Q” will generally refer to the stars’ Q. If the clouds’ Q is meant, then it will be noted so explicitly. For gaseous disks, a relationship similar to equation (2.16) exists, where $\sigma(r)$ is replaced with the sound speed v_s, and 3.36 is replaced with π:

$$Q(r) = \frac{\kappa(r)\ v_s}{\pi \mathbf{G}\ \Sigma(r)} \tag{2.17}$$

In previous calculations of Q, the Q(r)were averaged over all radii to obtain a mean Q for the entire disk (Schroeder, 1989; Shorey, 1996). This method proved to do injustice to the true characteristics of the disk, because the outer annuli of the disk, generally populated by only a small number of stars with often high radial velocities, boosted the average Q artificially and led to the false impression of a very hot disk.

To obtain a more realistic picture of this dynamic property of the disk, Q was henceforth calculated by averaging only over a number of annuli, centered around the half mass radius r_h, and thus omitting the outer (hot) annuli of the disk. This new calculation of Q is done after the completion of a GALAXY simulation with the help of an IDL routine which operates on the files containing the Q values of the individual annuli. The number of annuli to be taken into account can be specified in this IDL routine. To calculate the half mass radius, r_h, first the total stellar mass M_i in each annulus r_i is determined:

$$M_i = \sum_j m(j) \tag{2.18}$$

The summation is done over all j stars whose distance r is between r_i and r_{i+1}, $r_i \leq$ r < r_{i+1}. The m(j) are the masses of those stars. The total mass of the stellar disk, M_{total}, is obtained through summation over all M_i:

$$M_{total} = \sum_{i=1}^{r_{tr}} M_i \tag{2.19}$$

r_{tr} is the truncation radius of the disk. Because the star distribution at $t = 0$ was used for this determination of the half mass radius, no stars are located beyond a radius of $r > r_{tr}$. Finally, the half mass radius r_h is found by summing over the annuli, starting from the inner most, until the sum exceeds roughly one half of the total disk mass, M_{total}:

$$\sum_{i=1}^{r_h} M_i \lesssim \frac{1}{2} M_{total} \tag{2.20}$$

Figure 2.3 compares the old and new treatment of Q for the same set of data. Consequently, the inner-most annuli are also ignored for this calculation, if the number of annuli taken into account is less than $2 \cdot r_h$. Tests showed though that this is not a problem: For a typical SC galaxy with a truncation radius of $r_{tr} = 96$, the initial half mass radius is computed to be located at $r_h = 39$. Calculating the average Q from annuli 1 through 78 ($78 = 2 \cdot r_h$) compared to using, say, annuli 34 through 44 only, makes little, if any, difference. Figure 2.4 compares two such calculations for Q. One uses only 10 annuli for the calculation, the other one takes into account all annuli from the inner-most one at $r = 1$ to $r = 2 \cdot r_h$. Except for minor fluctuations the result is the same. This indicates that usually the "troublesome" annuli are indeed

only the outer-most ones. Because this part of the data analysis is not very time consuming, it is generally recommended to include all annuli from r = 1 to r = 2 . r_h, to make sure to catch any possible surprises that the inner annuli might hold.

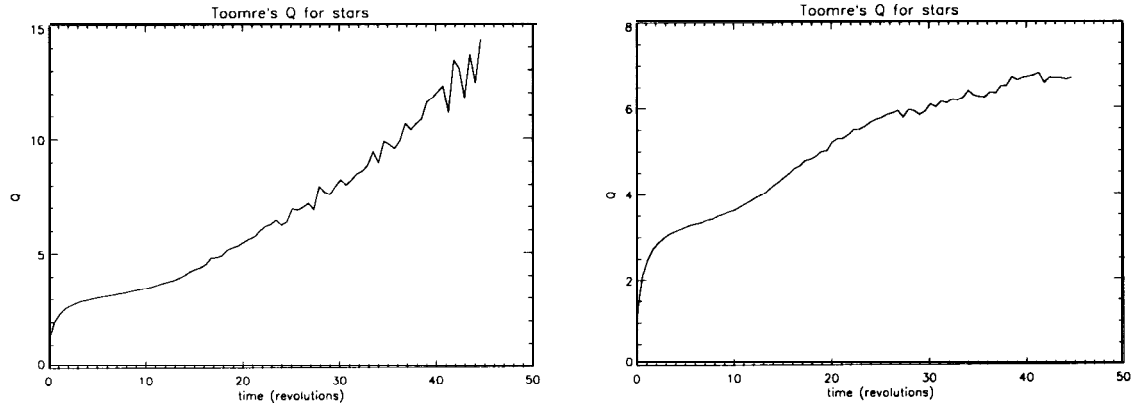

Figure 2.3: Toomre's Q − old and new. Q is shown here for the same set of data. The old method (left) produces higher values and also a more "erratic" behavior for the average Q than the new method (right).

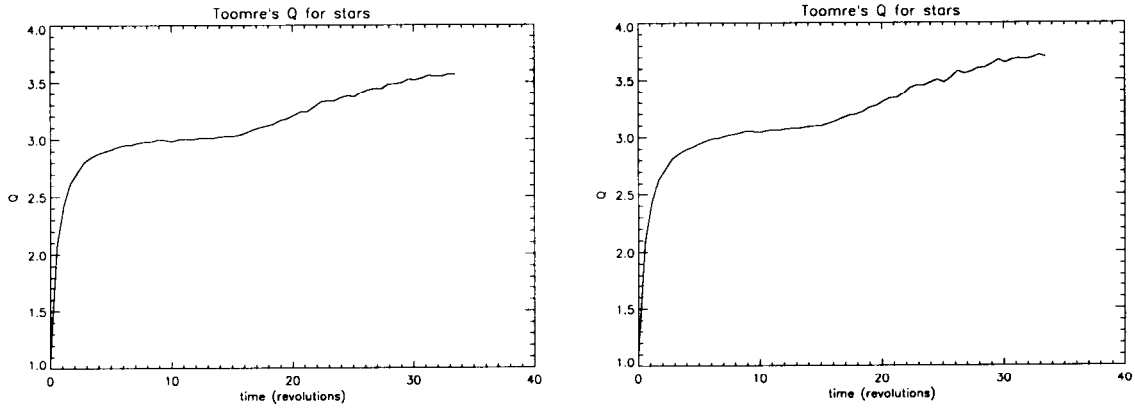

Figure 2.4: New Toomre's Q − few vs. many annuli. Q is shown here for the same set of data, calculated with the new method. The left plot uses only the annuli 34 through 44 for the calculation (r_h = 39). The right plot uses the annuli 1 through 78 (78 = 2 · r_h).

2.8.2 Center of Mass Motion

We studied lopsided galaxies and their possible cause through the rapid passage of a companion galaxy (Zeltwanger et al., 2000). For this project we ran a series of simulations with an intruder galaxy, and another series of simulations in which the centers of mass of the halo and of the stars do not coincide initially. These series are described in more detail in Sections 3.3 and 3.4, respectively.

The intruder runs were done to study whether such a close encounter scenario was capable of separating the center of mass of the stars from the halo's center of mass. In some of these runs the halo was kept fixed ("static"). In other runs a "dynamic" halo was simulated, either through a hydrodynamic component (the gas), or through another N-body component (the clouds), which were given a mass fraction appropriate for a typical disk galaxy's halo (75%). To determine how much the centers of mass of the halo and of the stellar disk would be separated in these simulations, it was necessary to independently observe the motions of the centers of mass of the stars, of the clouds, and of the gas. Furthermore, the relative motions of these centers of mass with respect to each other needed to be determined. The motions of the centers of mass of the various components could then be compared. Figures 3.14 and 3.15 on page 64, and Figures 3.22 and 3.23 on page 76, show examples of these motions. For a more thorough description of the results of these particular simulations please refer to Sections 3.3 and 3.4.

2.8.3 Gas Temperature

Prior to implementing the new smoothing algorithm for the hydro component, as described in Section 2.6, the increase in central gas pressure came hand in hand with an unrealistic increase of the gas temperature in the affected disk regions. To monitor this behavior more thoroughly, and to also test the new smoothing algorithm, the gas temperature was color coded or gray-scaled, and plotted explicitly in Kelvin. Figure 2.5 shows an example of the temperature distribution of a simulation at three different time steps. For comparison, and to demonstrate that regions of high gas density generally correspond to regions of high temperature, Figure 2.6 shows the gas density of the same simulation at the same three time steps. Note that there are regions in Figure 2.5 which have a temperature of 2 K and below. This is because the GALAXY program does not take the 2.7 K microwave background radiation into account, which keeps the gas in real galaxies at or above 2.7 K. Future versions of GALAXY will take this into consideration.

2.8.4 Making Movies

The creation of movies as a form of visualizing some of the vast amounts of data created by the GALAXY program provided the opportunity to observe the dynamical evolution of an entire simulation in a time-compressed manner without compromising spatial resolution or time resolution. To investigate the dynamical evolution of most of

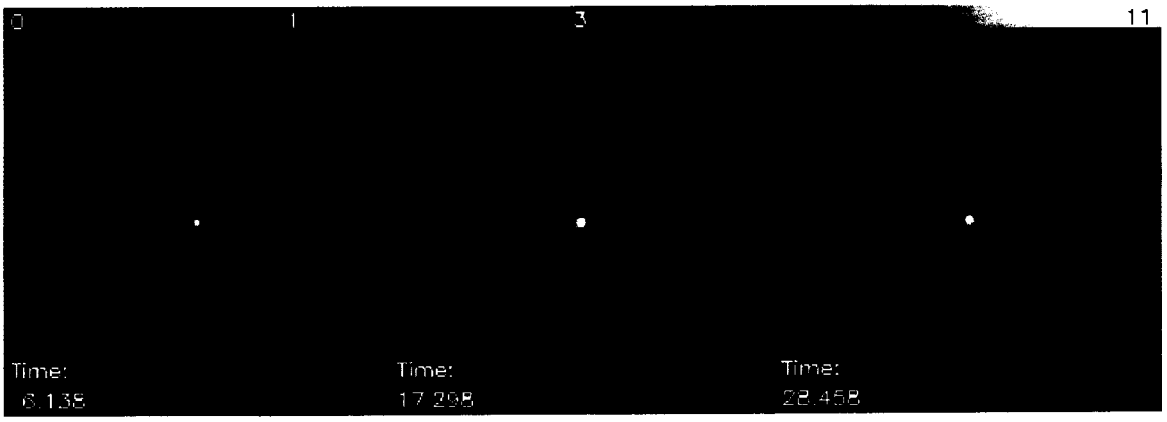

Figure 2.5: Gas temperature. Shown is the temperature distribution of a simulation at three different time steps. Lighter regions indicate higher temperature, and darker regions have low temperature. The temperature scale on the top of the figure is labeled in Kelvin.

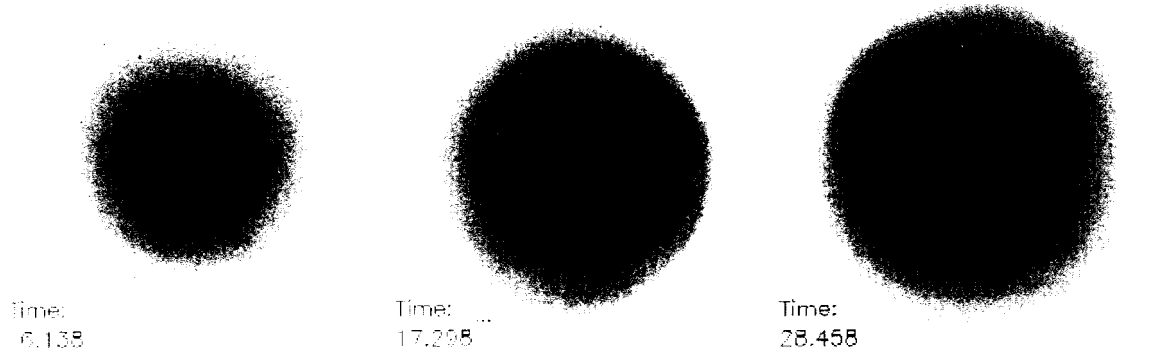

Figure 2.6: Gas density. Shown is the gas mass density distribution of the same simulation as in Figure 2.5. Darker regions indicate higher gas density, and lighter regions have low density.

the parameters of interest (like Toomre's Q, or Fourier amplitudes) it is not necessary to plot these parameters after each and every integration cycle. Instead, for most purposes it is sufficient to create a data dump for plotting after only every one quarter of a revolution of the model galaxy, i. e. after approximately every 70 integration cycles for a typical simulation run (this number varies, though, depending on the kind of galaxy being simulated).

To create a smooth and flicker-free movie a much higher resolution in time is necessary. Most movies created for this thesis use frames that are only two to four integration cycles apart, and they can have up to 1000 frames. This high resolution revealed some features and fine details which occur during a simulation that otherwise might have gone unnoticed. Several movies showing star density and the location of newly formed stars demonstrated that new stars form predominantly in the regions of higher cloud density, i. e. in the spiral arms, where it should occur.

The format chosen for the movies is MPEG. This format can be played across all computer platforms, and allows for easy inclusion in a web page, to share the outcome of the simulations with the scientific and non-scientific community. In fact, due to the visual beauty of some of those movies they provide the unique opportunity to make parts of my thesis results accessible and comprehensible to non-scientists. Figure 2.7 shows an example of what a snapshot of an MPEG movie might look like. The grayscale colors represent star densities. The higher the star density in

a certain volume of space, the darker the corresponding gray shade. The scale for this is logarithmic rather than linear, to enhance variations in the underlying star distribution. This is to take into account the fact that spiral arms are generally the nurseries of galaxies, in which young and bright stars make the spiral arms appear brighter than the pure star number densities would suggest. Such logarithmic scaling has been used for all plots in this dissertation involving the distribution of stars, clouds, or gas, as well as for the temperature maps.

The creation of a movie can be separated into four individual steps:

1. Run and complete a simulation of the GALAXY program to create the data to be featured in the movie.

2. Create the individual frames that make up the movie. For this step, a script was developed to be used in conjunction with IDL. This IDL script uses each data dump, analyzes it and produces a gray-scale representation of it. Each data dump is converted from a pure text format to a *.GIF file (“Graphics Interchange Format”, a compressed file format to store images). These first two steps are by far the two most time-consuming ones.

3. The *.GIF files need to be converted to *.YUV files (YUV is another image file format, suitable for making an MPEG movie). A UNIX shell script was developed for this purpose.

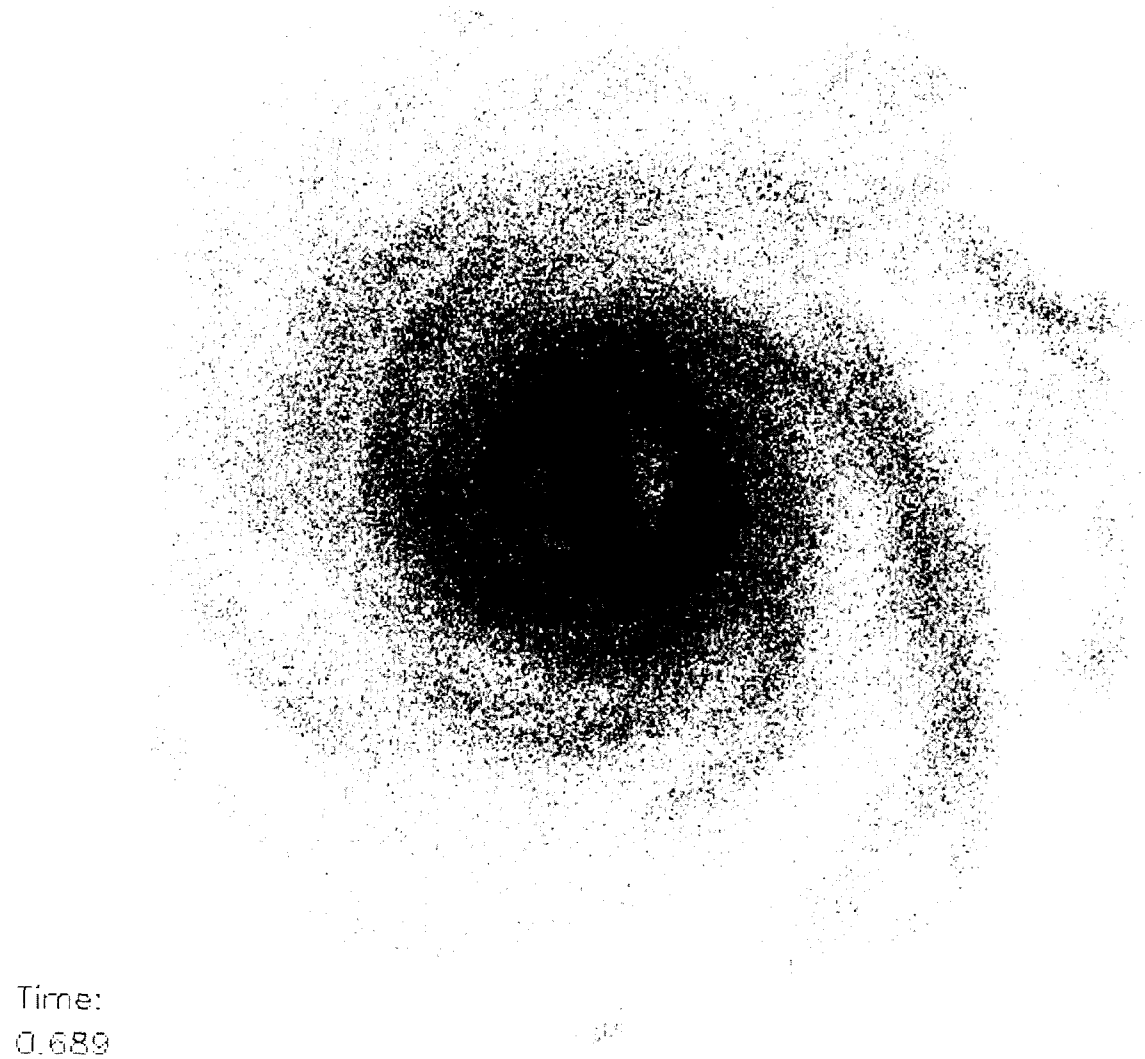

Figure 2.7: A snapshot of an MPEG movie. The grayscale colors in this snapshot indicate star particle density. Darker regions are regions with a high star density, The time index in the lower left corner refers to numbers of revolutions performed since the start of the simulation.

4. The individual *.YUV files are concatenated together back to back and encoded in the MPEG format.

Besides a number of shorter clips, a couple of large movies with up to one thousand individual frames have been created. These include a movie of a "base run" as described in Section 3.1, a movie of a simulation with 50% counter-rotating components as described in Section 3.2.4, a movie of a simulation with an intruder galaxy as described in Section 3.3, and a movie of a simulation with stellar evolution switched on, as described in Section 4.9, and listed as run # 51 in Appendix B. The latter movie also shows the locations of new star formation, in addition to the star density.

Examples of some of the movies created for this thesis can be downloaded from <http://butch.umephy.maine.edu/kickers/Research/Movies>.

The creation of movies with even more than one thousand frames is desirable to obtain a higher time resolution, but this is unfeasible at present due to disk space limitations (several gigabytes of temporary disk space are required to make a movie).

2.8.5 Data Output after every Integration Cycle

For testing new or modified portions of the GALAXY program, or to test the behavior of the program for a certain set of initial input parameters, it was desirable to have a monitoring feature that would allow observation of the evolution of the simulated

galaxy in real-time, i. e. while the simulation is running. For this purpose a new switch was introduced in Datinp.DAT that switches live output on or off. Live output here simply means that certain variables (e. g. star positions, gas pressure, or gas density) would be stored in temporary files after each and every integration cycle. While this could in principle have been accomplished by creating a data dump after each time step, the use of temporary files which are constantly rewritten has the advantage of saving disk space, and it makes the analysis of the files more efficient because the same files are read over and over again in an open loop. Using this method for the live analysis of the simulations requires the least amount of system resources. Live output slows down the overall performance of the simulation considerably. But in case the program starts to behave erroneously, the time to react is shorter than to wait till the end of the simulation and then to analyze it afterwards. As the total execution time of a single simulation can easily exceed several days, the reduction in time lost is invaluable. Live output is, therefore, particularly useful for testing new or modified portions of the code and should only be used for this purpose.

2.8.6 Fourier Analysis

The mass distribution of the galactic disk can be studied through a Fourier analysis. This results in a series of numbers a, (with $m \in \{0, 1, 2, 3, \ldots\}$) that quantitatively describe the azimuthal mass distribution. A large amplitude in the m = 1 mode indicates the presence of a one-armed feature in the galaxy. A strong m = 2 amplitude

hints at the presences of a bar shaped mass perturbation. A large m = 3 amplitude is due to the presence of a three-armed structure, and so forth. The Fourier amplitudes are normalized so that $a_0\ (t = 0) = 1.0$.

Plots of Fourier modes (for $m \in \{1, 2, 3, 4\}$) for stars and clouds of the simulations done for this dissertation are included in Chapter 3 and in Appendix C. The $m = 1$ and m = 2 modes are the most interesting ones for the simulations done for this dissertation, because they indicate the presence of a one-armed spiral, and of a central bar, respectively. These two perturbation types occur frequently in N-body simulations of disk galaxies (see for example Chapter 3). The m = 3 and m = 4 modes have also been included to monitor multi-arm development, which often occurs at the beginning of a simulation. Modes with m > 4 have generally smaller amplitudes, and the mass perturbations responsible for these modes are also short-lived, because they tend to merge and form perturbations with $m \leq 4$.

2.8.7 Resonances

In spiral galaxies, stars travel in nearly circular orbits. Due to gravitational perturbations, and due to radial velocity components they attained at the time of their formation, they also tend to "wobble" in their orbits. These wobbles are periodic, and the frequency of this oscillation around the circular orbit is called the epicyclic frequency κ. If Ω_p denotes the angular velocity of a density perturbation ("pattern")

in a disk galaxy, then a star particle experiences “Lindblad resonance”, if its own angular velocity, Ω, and its epicyclic frequency κ satisfy the following condition (Binney and Tremaine, 1987; Elmegreen, 1998):

$$\Omega - \Omega_p = \pm\frac{\kappa}{2} \tag{2.21}$$

In the “+” case the star experiences the inner Lindblad resonance and its orbit is at the inner Lindblad radius. In the “−” case we talk of the *outer* Lindblad resonance and the *outer* Lindblad radius, respectively. In these cases the star completes one epicycle, while the pattern − for example a bar − completes one half revolution. Thus, the star is at the same phase of its epicycle every time it has the same angular position relative to the bar. Gravity near a density perturbation is increased, and the star experiences this increased gravity always at he same position in its epicycle: resonance occurs (similar to pushing a swing).

Resonances other than the Lindblad resonance can occur, too. If $\Omega = \Omega_p$, we talk of the “corotation resonance”, because the star rotates in sync with the density perturbation. If a galaxy’s rotation curve and any one resonance are known, then the pattern speed and all other resonances can be determined (Elmegreen, 1998). The observation of density perturbations allows to find the locations of these resonances. For example, two bright outer arms generally end at the outer Lindblad resonance. A bar’s ends are usually located between the inner Lindblad resonance and the corotation resonance.

3 SIMULATIONS WITHOUT STELLAR EVOLUTION

This chapter discusses the results of simulations that include only stars and the halo, but no clouds or ISM, and consequently no stellar evolution. The first section of this chapter introduces the base run, against which all other runs in this chapter are compared. Section 3.2 presents the results of simulations in which a certain fraction of the stellar components has been sent into a counter-rotating orbit. These simulations have been done to study the influence of counter-rotating components on the formation of a one-armed spiral, and to study their ability to suppress the formation of a central bar in the galaxy. Section 3.3 shows that a high-speed interaction between two galaxies can produce lopsided galaxies. In Section 3.4, this lopsidedness is studied further, through simulations in which the center of mass of the stellar disk has been offset "artificially" by a certain amount from the halo center of mass, and with a varying (low or high) angular momentum.

All runs presented in this chapter used 10^5 star particles, a star mass fraction of 25%, a halo mass fraction of 75%, a softening factor of 0.25, a grid utilization of 0.75, and a simulation grid of 256 x 256 cells. They are also described in Comins et al. (1997) and in Zeltwanger et al. (2000).

3.1 The Base Run

This kind of run is the simplest simulation one can perform with the GALAXY program. It utilizes only stars and the halo. There are no clouds or gas present, and stellar evolution is entirely switched off. All stars are in co-rotating motion, except for a few which are sent into counter-rotating orbits, due to the random Monte Carlo loading procedure. These make up a fraction of at most 5 x 10^{-3} of the total number of stars and thus don't affect the overall dynamics of the stellar disk in any significant way. The centers of mass of the stars and of the halo are both located at the center of the simulation grid.

Despite the simplicity of this kind of simulation, one can learn a lot from its dynamics, and comparing any more complex simulation to this one can provide a great deal of insight into the effects triggered by the various parameters of the GALAXY program.

The base run quickly forms a set of trailing spiral arms (see Figure 3.1), and simultaneously a bar starts to form at the core of the stellar disk. While the multi-arm spirals have mostly faded away by revolution number five, the central bar grows stronger and stronger. In fact, Figure 3.2 reveals that during the first three revolutions of this simulation, the m = 3 and m = 4 modes are dominating the dynamics of the disk. But after about 3.5 revolutions, the m = 2 mode (which is responsible for the bar formation) begins to get larger than the m = 3 and m = 4 modes, and continues to grow

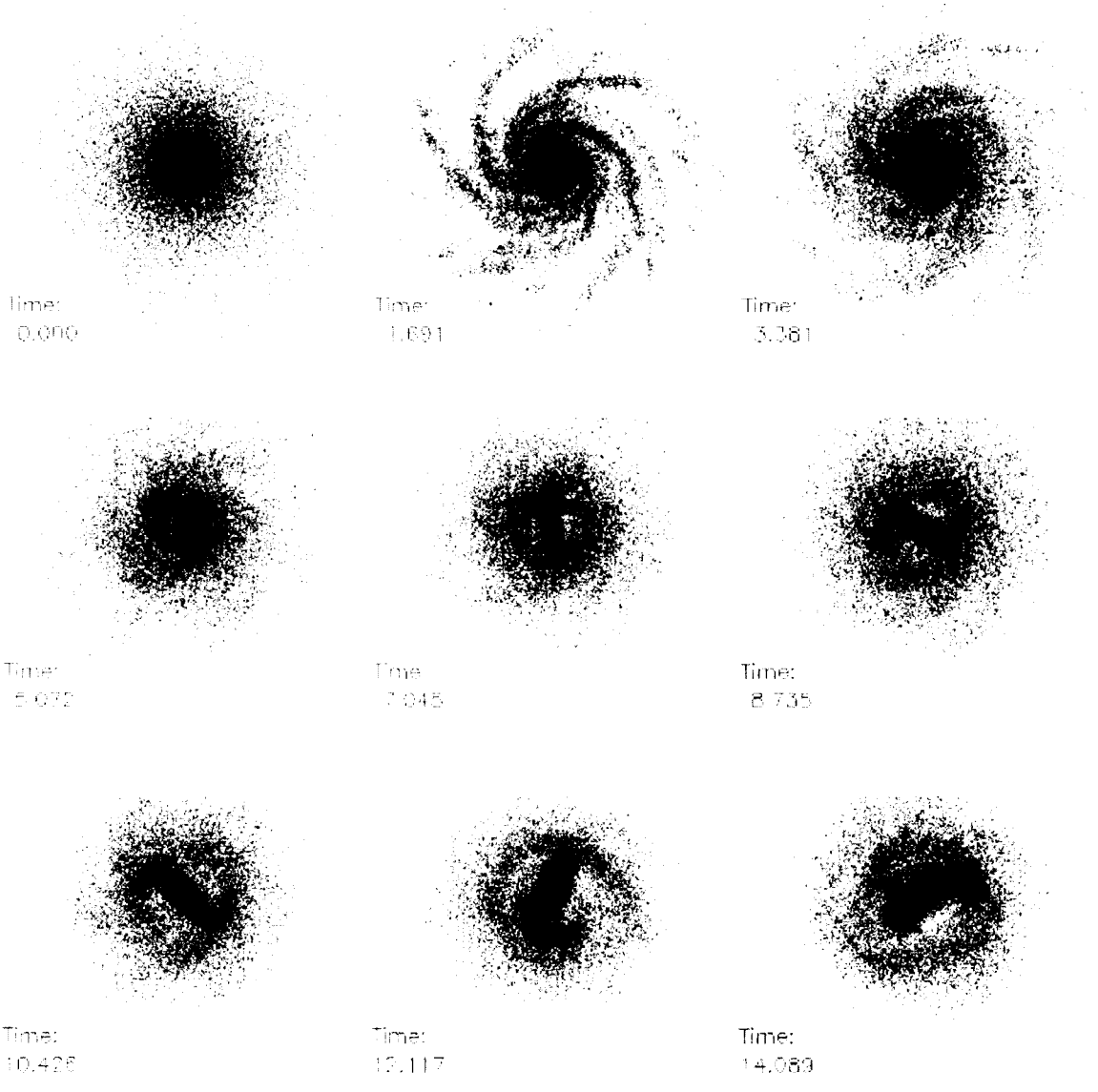

Figure 3.1: Base run – star mass distribution.

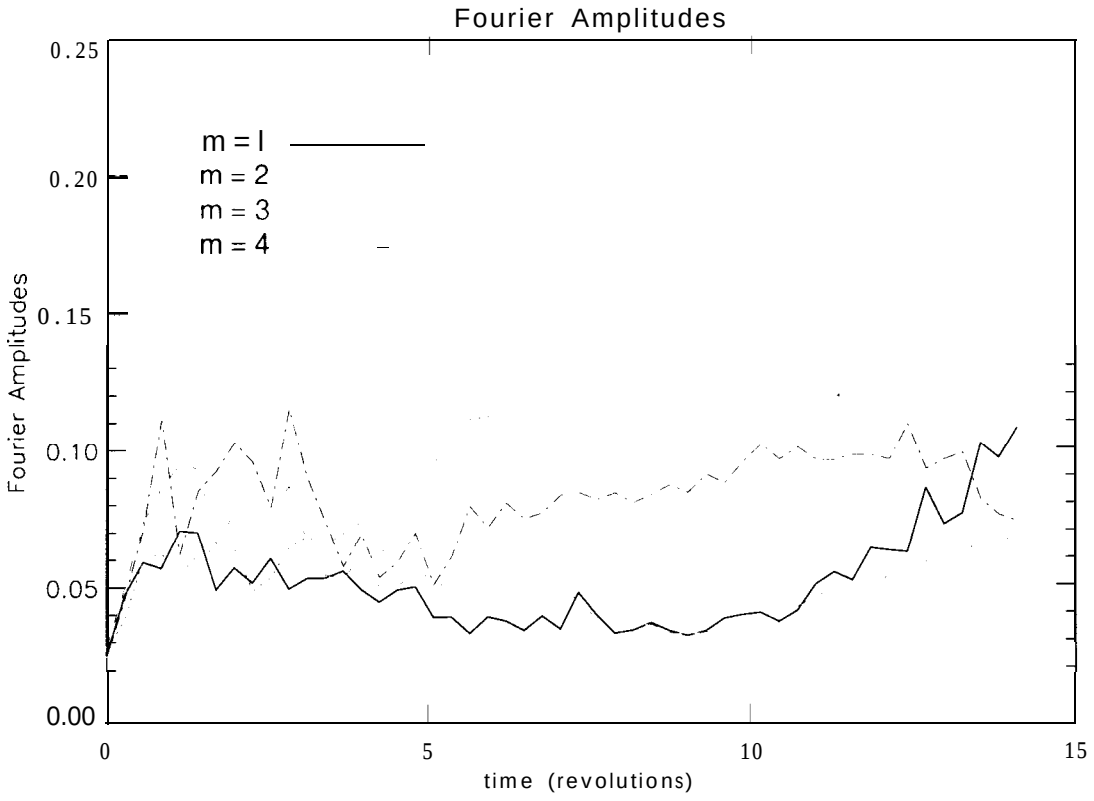

Figure 3.2: Base run – Fourier amplitudes. Fourier modes of the star mass distribution.

until t = 11.5 revolutions, when it flattens. At this point the ends of the central bar have reached the location of the corotation resonance, which limits further growth of the bar (Binney and Tremaine, 1987; Elmegreen, 1998). It is interesting to notice that the m = 4 mode prevails relatively strongly throughout the simulation, and that the m = 1 mode (which is responsible for the formation of a one-armed spiral) starts to grow at about the time when the m = 2 mode flattens. The last two frames in Figure 3.1 reveal that a corresponding one-armed feature starts indeed to develop.

Table 3.1 on page 58 lists the base run discussed in this section as run # 1.

3.2 Simulations with Counter-rotating Components

3.2.1 12.5% Counter-rotating Stars

A 12.5% fraction of counter-rotating components is still a rather small fraction, and, not surprisingly, this run shows little difference from the base run. Just like that reference simulation, the 12.5% case goes through an initial series of multi-armed spirals, which fade away after some five revolutions (see Figure 3.3).

Again during this part of the simulation, the dynamics of the disk are dominated by the higher modes, particularly by the m = 4 mode (the m = 3 mode is somewhat smaller in the 12.5% case, compared to the base run), see Figure 3.4.

The central bar develops later here than it did in the base run. In fact, up to 3.6 revolutions there is no indication that a bar is going to form at all. But by the fifth revolution the m = 2 (bar) mode takes off and grows similar to the previous run up to about t = 13 revolutions. The final bar is visibly weaker, though, in the 12.5% case compared to the base run, and this impression is supported by the fact that at its peak the m = 2 mode in the 12.5% case is below the peak level of the $m = 2$ mode for the base run. Again, the m = 4 mode prevails fairly strongly throughout the simulation, though well below the level of the m = 2 mode. And after 11 revolutions, the m = 1 mode starts to grow slowly, hinting at the birth of a weak one-armed feature, the presence of which is visible in the last two frames of Figure 3.3.

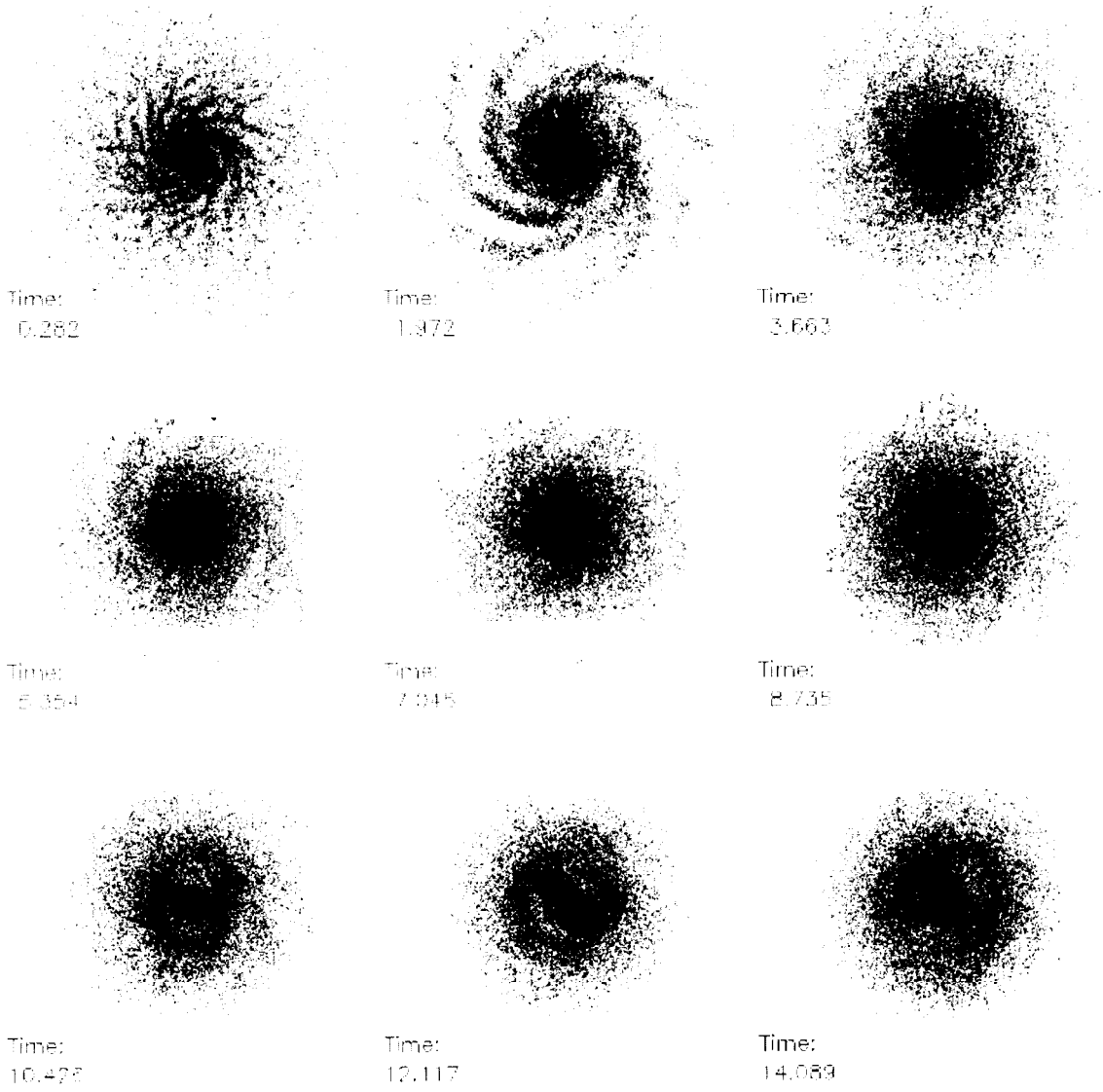

Figure 3.3: 12.5% counter-rotating stars – star mass distribution.

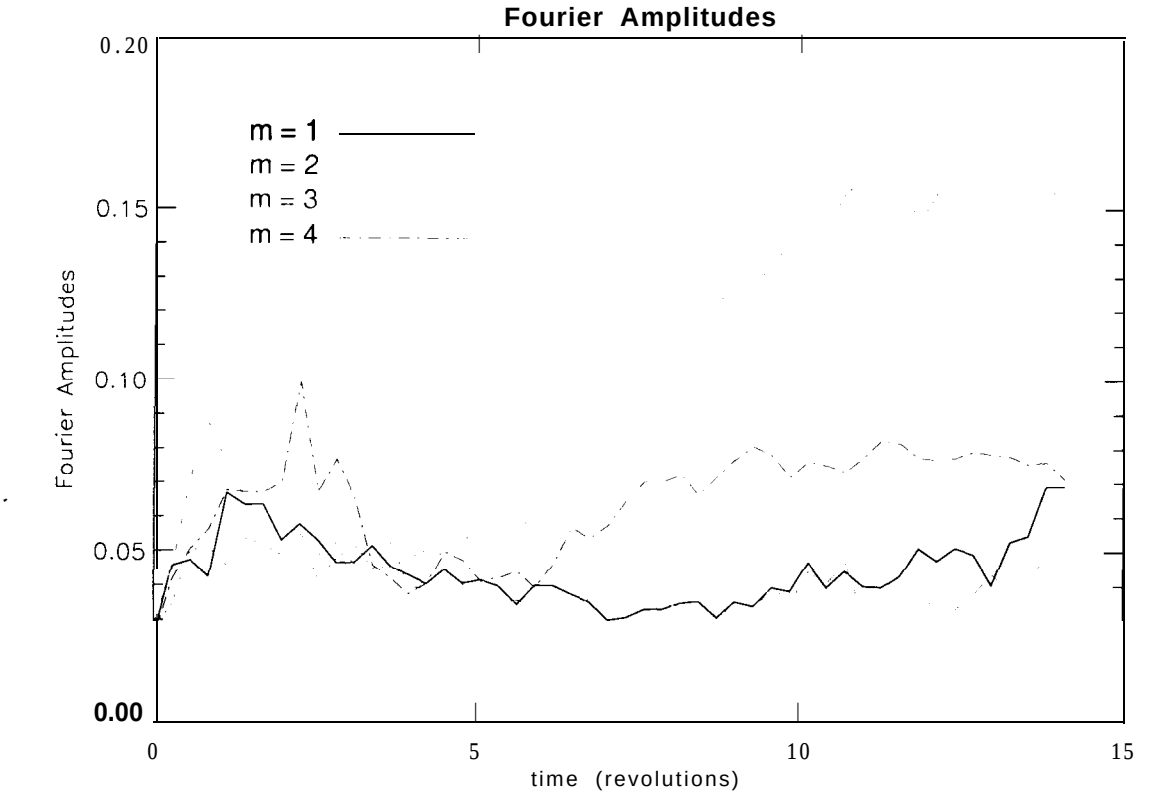

Figure 3.4: 12.5% counter-rotating stars – Fourier amplitudes. Fourier modes of the star mass distribution.

Overall, the presence of a small (12.5%) fraction of counter-rotating components has only little effect on the dynamics of the stellar disk, especially with respect to the formation of a one-armed spiral. But even this small amount of counter-rotating stars exhibits some resistance against the formation of a central bar: it starts to form later than in the base run, and it doesn't grow to the same strength as in the reference simulation.

Table 3.1 on page 58 lists the 12.5% case discussed in this section as run # 2.

3.2.2 25% Counter-rotating Stars

In the 25% case (run # 3 in Table 3.1), things are decisively different from the base run and the 12.5% case. In the initial phase of this simulation, the multi-arm modes m = 3 and m = 4 are significantly lower than in the previous two runs and the multi-armed spiral at the beginning of this run is less prominent (see Figures 3.5 and 3.6). In fact, during this initial multi-armed phase, one of the arms stands out as the visibly strongest arm, giving rise to the fact that up to t = 8 revolutions the m = 1 (one-armed) mode is the strongest one. A central bar does not appear until t = 7 revolutions, but from that point on the m = 2 mode dominates the remainder of the simulation and continues to rise at a nearly constant rate. At the end of the simulation the bar has reached almost the same strength as the bar in the 12.5% case and continues to climb. The m = 1 mode, however, after it reaches its peak level for this run at 3.5 revolutions, decreases slowly, and the corresponding one-armed spiral ceases to exist after 8 revolutions. Note that the m = 4 mode, unlike in the previous two runs, remains low up to t = 8 revolutions, but increases thereafter. In all runs so far, the m = 4 mode grows as soon as the bar reaches its maximum length (the corotation resonance prevents further growth). From this point on, the bar's ends grow small leading arcs, and typically two more arclets form at about the same radius. These may eventually combine to form a complete circle at the location of the Inner Lindblad Resonance, if the simulations were to run long enough. These four symmetric arc segments give rise to the increased m = 4 mode.

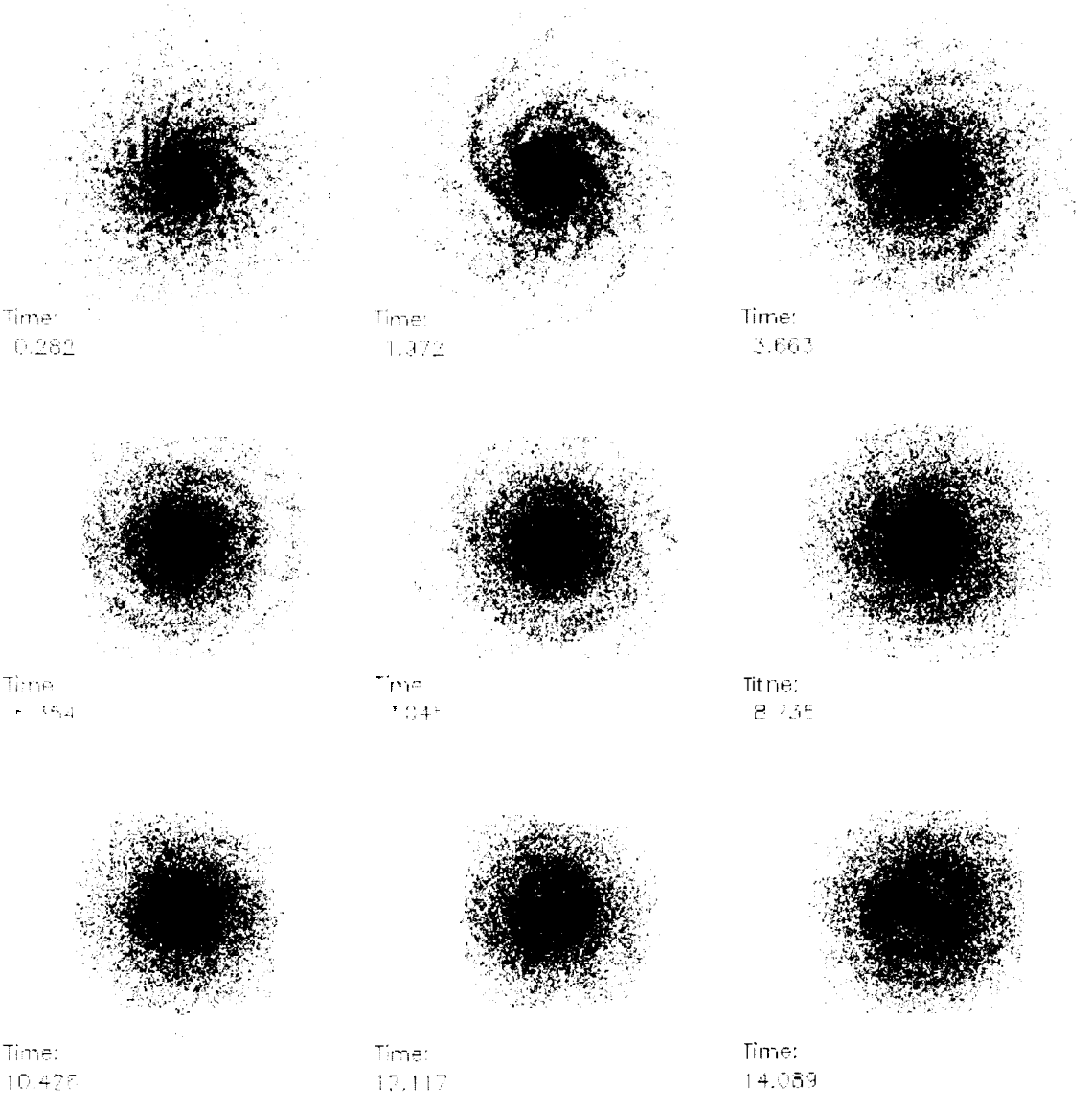

Figure 3.5: 25% counter-rotating stars – star mass distribution.

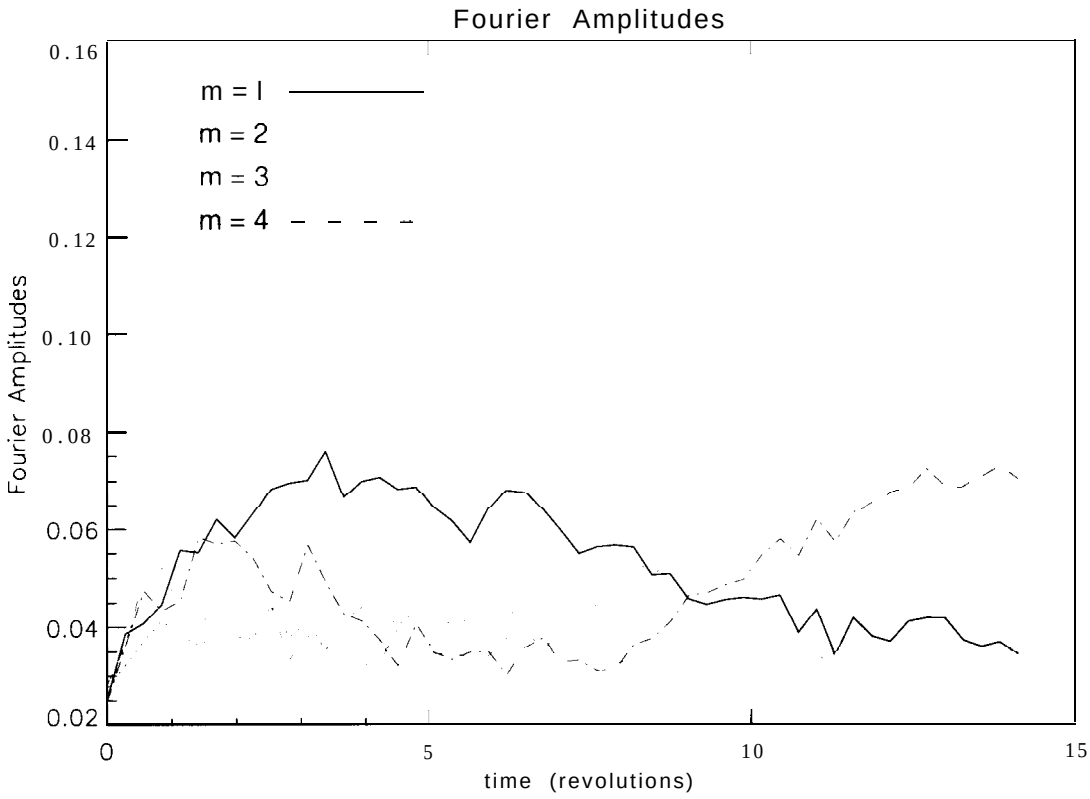

Figure 3.6: 25% counter-rotating stars – Fourier amplitudes. Fourier modes of the star mass distribution.

3.2.3 37.5% Counter-rotating Stars

The trend observed in the 25% case continues in the 37.5% case: a stationary, trailing, one-armed spiral forms very quickly in this simulation (Figure 3.7) and remains very strong through t = 8 revolutions. Although it then starts to fade away, the one-armed spiral remains visible until the very end of the simulation. Accordingly, the m = 1 (one-armed spiral) mode increases sharply at the very beginning of the simulation (Figure 3.8), reaches its highest level of this run between t = 3 and t = 6 revolutions, when the one-armed spiral is visibly most prominent. Though the m = 1 mode

decreases during the third quarter of the run (going hand in hand with the fading of the one-armed spiral), it remains the strongest mode for the entire simulation. Interestingly, the one-armed spiral changes directions at least once. While it is clearly trailing (the galaxy as a whole rotates counterclockwise) in the second frame of Figure 3.7 at t = 1.972 revolutions, the spiral arm goes through a transition in the following frame (t = 3.663 revolutions) during which its direction is not clearly determined. In all following frames and most clearly visible at t = 7.045 revolutions, the spiral arm is leading.

The multi-arm phase seen in the previous four simulations is barely visible in the first frame of Figure 3.7. The $\boldsymbol{m}$ = 2, $\boldsymbol{m}$ = 3, and m = 4 modes remain on a nearly constant (low) level throughout this simulation. The formation of a central bar doesn't start until about t = 10 revolutions, and the bar remains very weak (there is a slight increase in the m = 2 mode during this end phase of the simulation).

Clearly, a 37.5% fraction of counter-rotating stars is a strong trigger for the formation of a one-armed spiral, and also a strong inhibitor against the formation of a central bar.

Table 3.1 on page 58 lists the 37.5% case discussed in this section as run # 4.

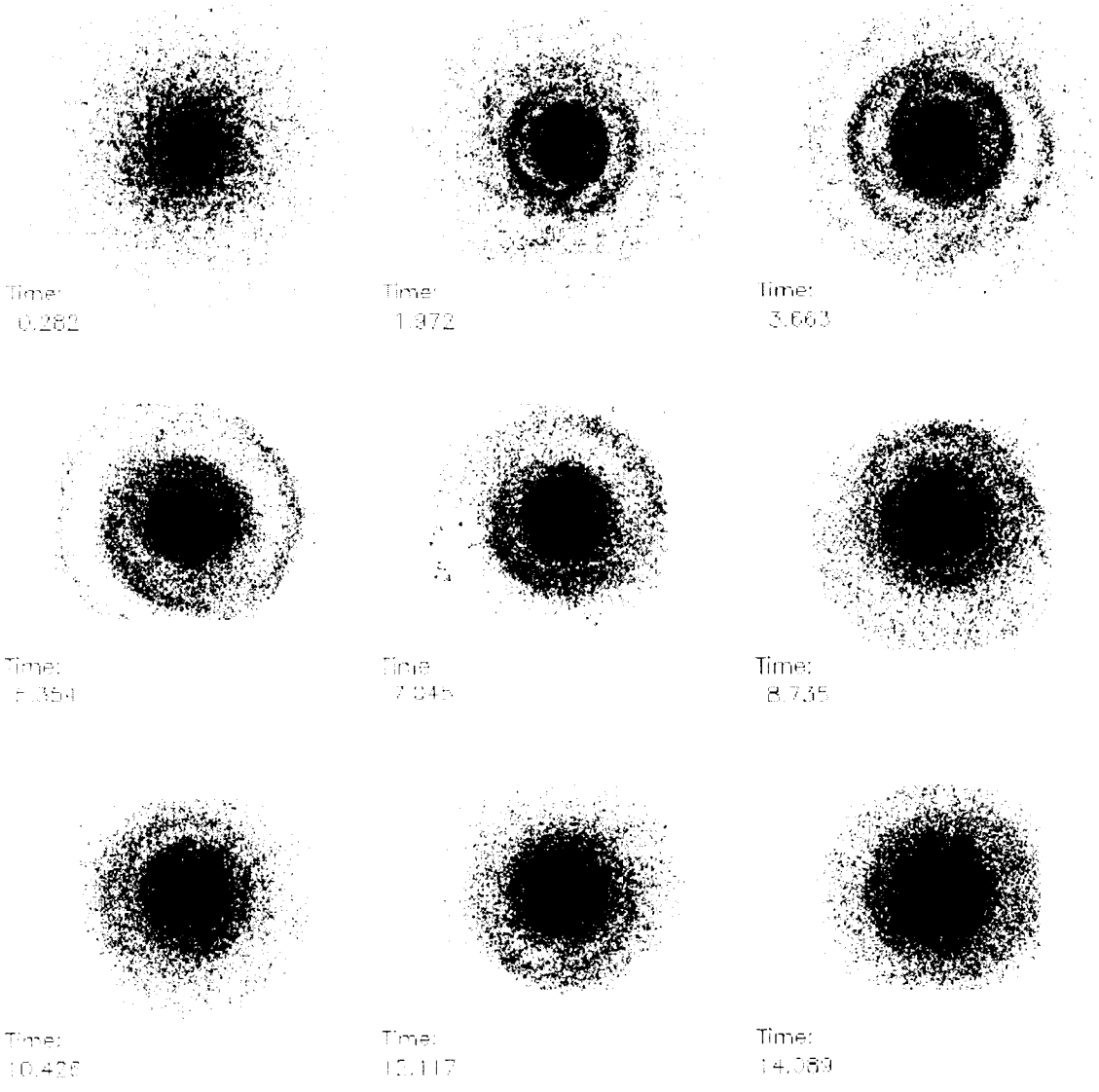

Figure 3.7: 37.5% counter-rotating stars – star mass distribution.

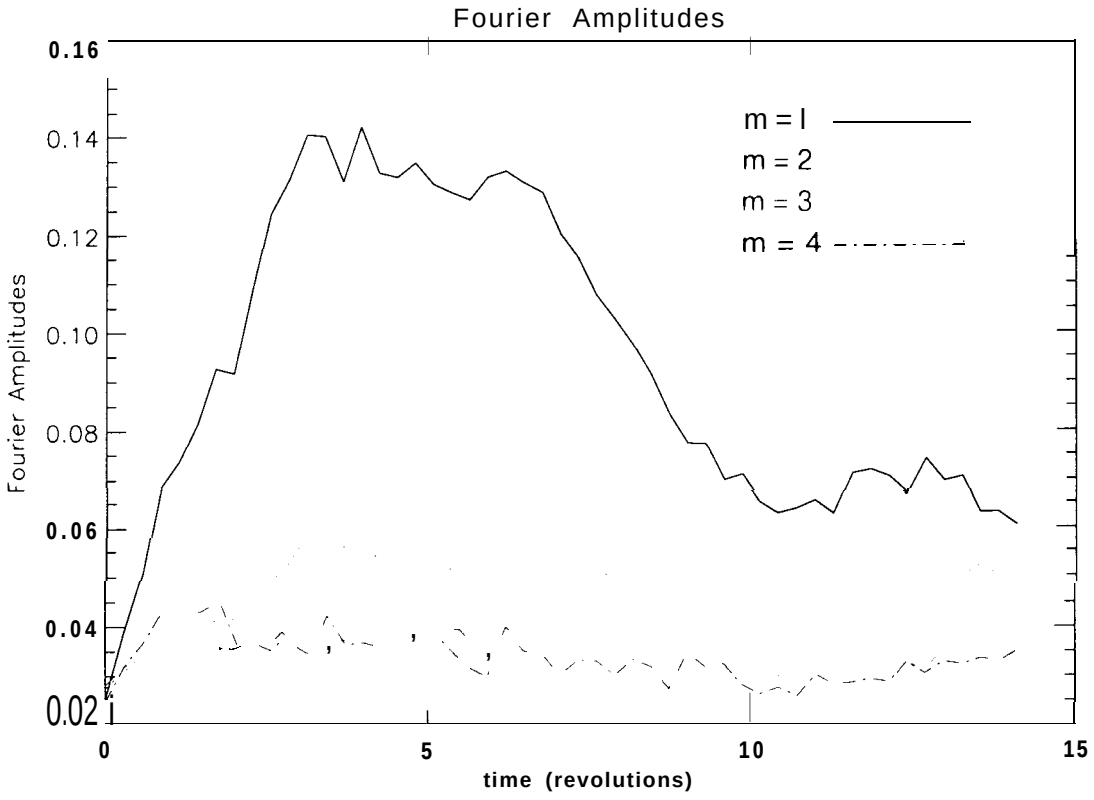

Figure 3.8: 37.5% counter-rotating stars − Fourier amplitudes. Fourier modes of the star mass distribution.

3.2.4 50% Counter-rotating Stars

Stepping up one more notch and increasing the fraction of counter-rotating components to 50% does not provide many new results. Most noticeably though is the total absence of a central bar throughout the entire simulation. The previous 37.5% case had at least a hint of a small bar forming towards the end of the run. The multi-arm phase seen at the beginning of the previous simulations is also skipped altogether. Instead, the disk leaps straight into the development of a strong, one-armed spiral (the distinction “leading” or “trailing” is meaningless in a case where half of the star

particles rotate one way, and the other half rotates the other way. The net angular momentum of this galaxy is zero). It is noted that similar to the previous 37.5% case, the spiral arm in this 50% case changes directions, and it does so at about the same time as the 37.5% case. This transition occurs roughly at the time of the third frame (at t = 3.663 revolutions) in Figure 3.9. The spiral arms before and after this frame have clearly different directions.

The dominance of the one-armed spiral is again indicated by the strength of the m = 1 mode (Figure 3.10). The m = 1 mode is by far the strongest mode throughout the simulation, and reaches its highest level when the one-armed spiral has its greatest dominance between t = 3 and t = 5 revolutions. The m = 2, m = 3, and m = 4 modes, in contrast, remain as one would expect on about the same low level as seen in the 37.5% case.

Again, a 50% fraction of counter-rotating stars is a strong trigger for the formation of a one-armed spiral, and also a strong inhibitor against the formation of a central bar.

Table 3.1 on page 58 lists the 50% case discussed in this section as run # 5.

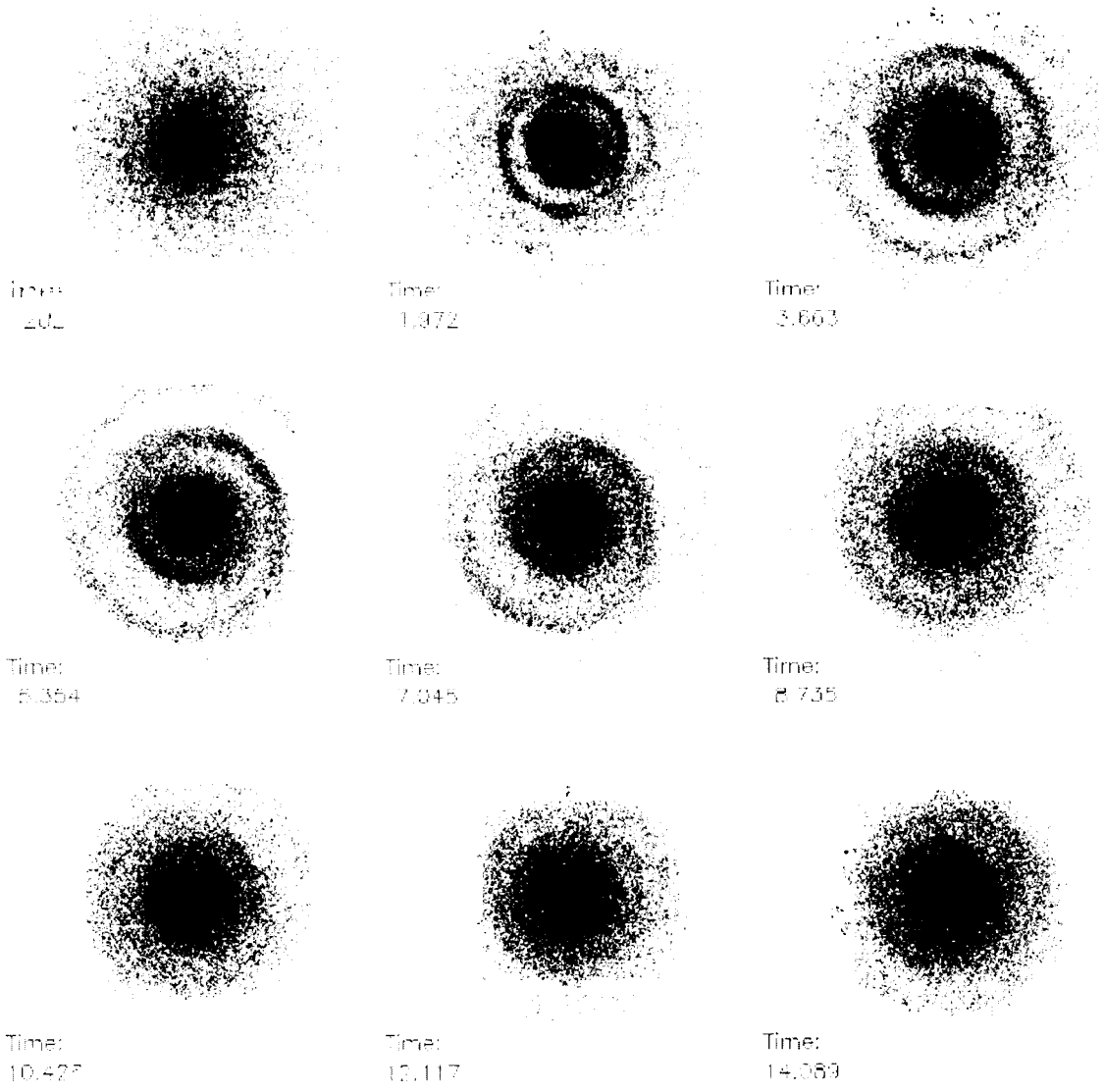

Figure 3.9: 50% counter-rotating stars − star mass distribution.

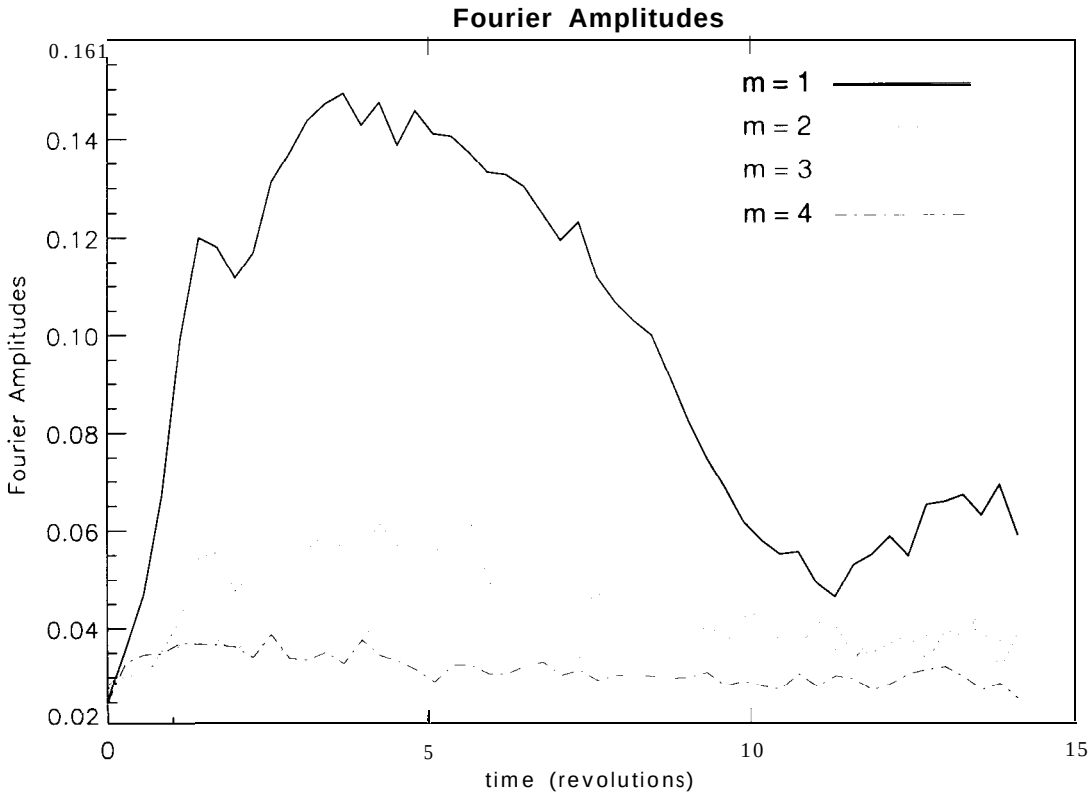

Figure 3.10: 50% counter-rotating stars – Fourier amplitudes. Fourier modes of the star mass distribution.

3.2.5 Summary of Runs with Counter-rotating Components

Table 3.1 gives a quick overview of the results involving counter-rotating components. They support many features of the two-stream instability theory in galactic disks with counter-rotating stars (Lovelace et al., 1997). The theory predicts that the m = 1 mode, responsible for the formation of a one-armed spiral, decreases in amplitude as Toomre's Q of the disk exceeds 1.8. A look at the Q values of all simulations (Figure 3.11) and the m = 1 modes (see Figures 3.2, 3.4, 3.6, 3.8, and 3.10) confirms this, particularly for the cases with a strong m = 1 mode development (cases with 25%,

37.5%, and 50% counter-rotating stars, respectively). The m = 1 amplitude starts to decrease at about the time when Q increases beyond 1.8.

Table 3.1: Summary of runs with counter-rotating components

Run #	Fraction of counter-rotating components	Final Spiral?	Final Bar?
1	0%	no	yes (strong)
2	12.5%	no	yes (strong)
3	25%	no	yes (strong)
4	37.5%	yes (weak)	yes (weak)
5	50%	yes	no

Further, the theory predicts that the strength of the one-armed spiral increases with higher fractions of counter-rotating components. The simulations found this also to be true: the m = 1 Fourier amplitudes are consistently higher in cases with a high fraction of counter-rotating components, compared to the cases with a lower fraction of counter-rotating components.

Also, it is expected from the two-stream instability theory, that the developing one-armed spiral is a leading spiral arm. While the direction of the one-armed spiral in the various simulations was found to flip over every once in a while, the “last” one-armed spiral formed (before this instability faded away) was a leading arm. The 50% case is inconclusive in this respect because a galaxy with 50% counter-rotating components has no preferred direction of rotation, and an angular momentum of zero (see also Figure 3.12).

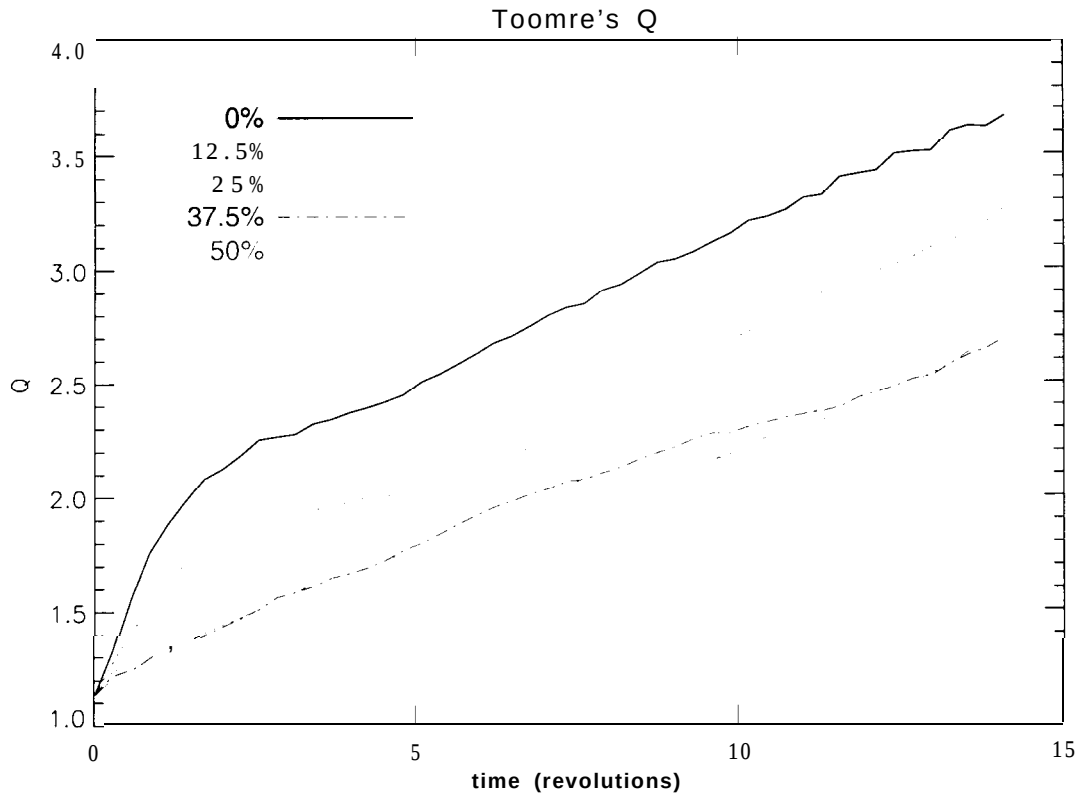

Figure 3.11: Toomre's Q for the runs with counter-rotating components.

It was found in this series of simulations that counter-rotating components in disk galaxies are a successful suppressor against the formation of a central bar, and that they are capable of triggering the formation of one-armed spiral features. Real galaxies with observed one-armed features may therefore have counter-rotating components in them (Comins et al., 1997). And, vice versa, galaxies with observed counter-rotating components are likely to show one-armed spirals (Comins et al., 1997). The simulations presented in the last few sections suggest that the fraction of counter-rotating components needs to be at least 25% to establish long-lived one-armed spirals, and to be able to significantly inhibit the formation of a central bar. There are,

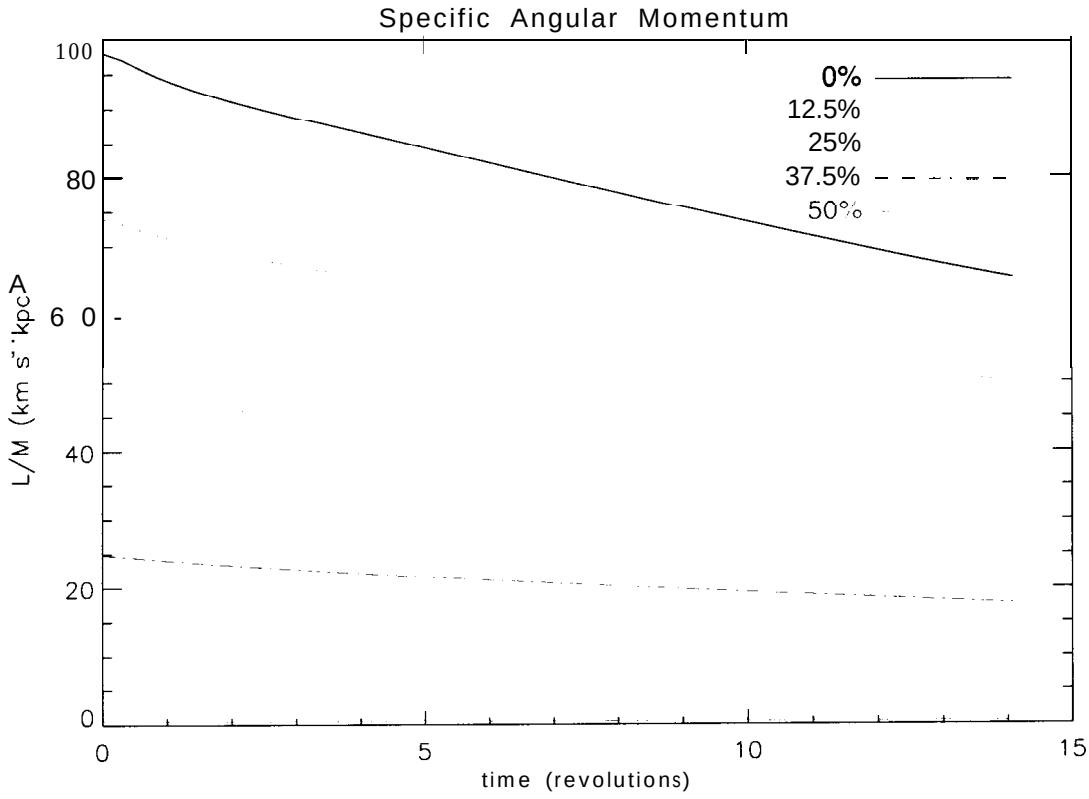

Figure 3.12: Specific angular momentum. The specific angular momentum decreases with an increase in the fraction of counter-rotating components.

however, other possible mechanisms that prevent bar formation, as we'll see in the next section.

3.3 High Speed Interactions between two Galaxies

To motivate the simulations with the "artificial" lopsidedness described in the next section, it was first desirable to find a mechanism which can produce this lopsidedness in a natural way. The scenario investigated for this purpose is the rapid passage of a massive companion galaxy. Lopsided structures in disk galaxies interacting with

neighboring galaxies can be seen for example in Karachentsev 64 (Figure 3.13) and in M101.

The intruder galaxy passes the target galaxy in a high speed coplanar orbit. In reality a coplanar orbit is unlikely to happen, however. The two interacting galaxies would instead have random orientations with respect to each other, and their gravitational pull would result in effects (for example warping of one or both galaxies) which can not be simulated with a two dimensional code. While the intruder is on the simulation grid, its distance varies between 64 grid cells initially, and about 25 grid cells at the time of the closest encounter. The intruder has 20% the mass of the target galaxy, and the interaction lasts for just under one revolution period. After that time, the intruder galaxy leaves the simulation and subsequently, its gravitational effect on the model galaxy is ignored.

The purpose of this series of simulations was to determine if such a scenario is capable of separating the centers of mass of the stellar disk and of the halo. The halo was modeled in several different ways to examine if the specific structure of the halo would influence the outcome of these simulations. It was modeled as either another N-body component, or as a hydro component. For both cases, it was distinguished between a hot halo and a cold halo ("hot" and "cold", in the case of the N-body halo, refers to an initially high and low value for Toomre's Q, respectively). These simulations are summarized in Table 3.2. The maximum offset listed in that table is in units of grid

Figure 3.13: Photo of Karachentsev 64. This pair of interacting spiral galaxies is number 64 in Igor Karachentsev's catalog of binary galaxies (Karachentsev, 1987), and it is also known as "Arp 273" in Halton Arp's "Atlas of Peculiar Galaxies" (Arp, 1966). The larger galaxy is strongly tidally distorted (lopsided), while the smaller edge-on companion galaxy (lower right) is relatively undisturbed. Photo credit: WIYN[1]/NOAO[2]/NSF[3].

[1]Consortium consisting of the University of Wisconsin, Indiana University, Yale University, and NOAO.
[2]National Optical Astronomy Observatories.
[3]National Science Foundation.

cell length. In the case of a hot hydrodynamic halo the separation between the halo and the stars still continued to increase at the end of the simulation.

Table 3.2: Summary of runs with an intruder

Run #	Halo Type	$Q_{0,halo}$	T_0	Maximum Offset
6	N-body, cold	0.3	n/a	0.75
7	N-body, hot	5.0	n/a	2.0
8	Hydro, cold	n/a	0.5 K	3.0
9	Hydro, hot	n/a	5×10^6 K	>18.0

In all cases a separation between the disk's center of mass and the halo's center of mass is observed (Figures 3.14 and 3.15). The amount of separation is greater in the cases of a hot halo. This is probably because the particles that make up the hot halo move more randomly (they have more kinetic energy) than in the cold halo case. Thus, a hot halo will be displaced less than a cold halo and the separation between the centers of mass of disk and halo will be greater for the hot halo case (Zeltwanger et al., 2000). That is what is observed in these runs. The motion of the hot halo's center of mass might have been underestimated, because due to the high-speed random motion of its constituents a hot halo loses mass that escapes beyond the simulation grid. For a cold halo this mass loss is less. The exact differences in the dynamics between hot and cold halos are subject to more detailed studies.

The case resulting in the largest separation between the centers of mass of halo and disk (hot gas halo) produces also the most asymmetric galaxy (Figures 3.16 and 3.17), a visible indication for its lopsidedness.

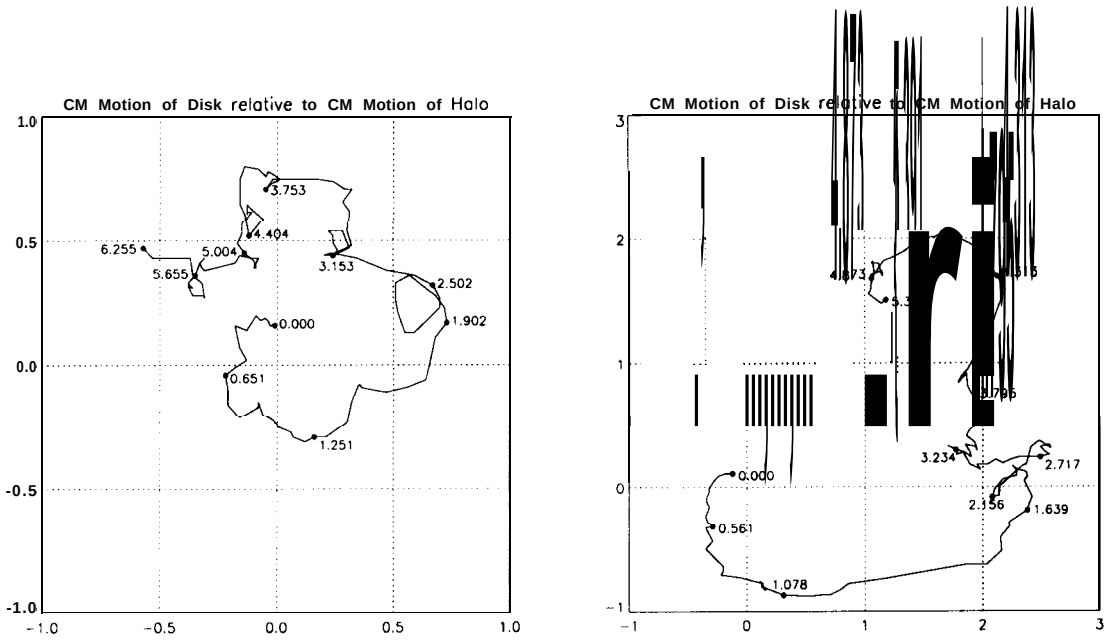

Figure 3.14: Relative center of mass motion for a cold halo. Shown is the motion of the stars' center of mass with respect to the center of mass of the halo. In the left case the halo is simulated by cold n-body particles. The right panel shows the results for a halo, simulated by a cold hydro component. The numbers along the trail are time indicators in revolutions.

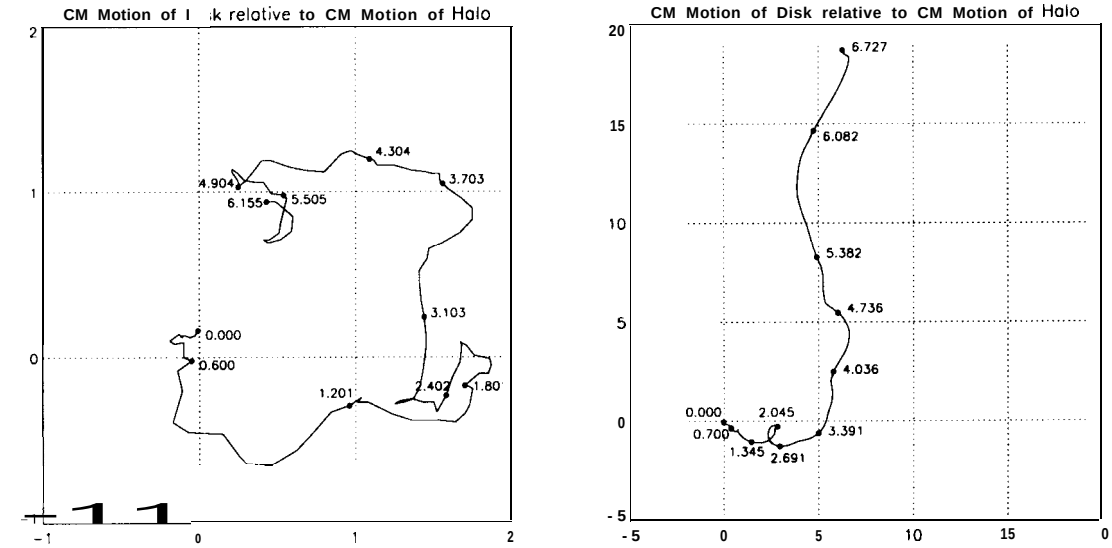

Figure 3.15: Relative center of mass motion for a hot halo. Shown is the motion of the stars' center of mass with respect to the center of mass of the halo. In the left case the halo is simulated by hot N-body particles. The right panel shows the results for a halo, simulated by a hot hydro component The numbers along the trail are time indicators in revolutions.

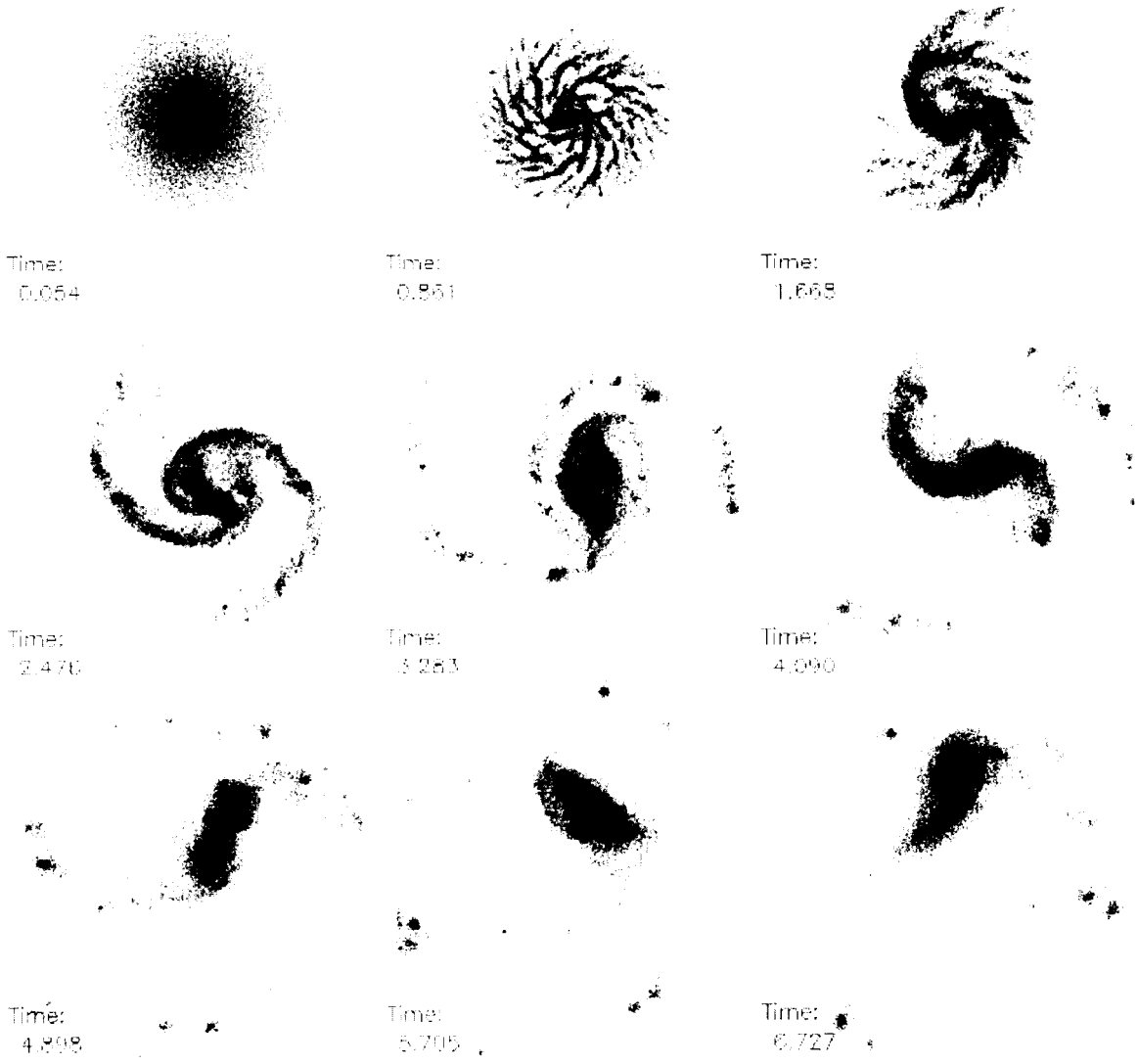

Figure 3.16: Star mass distribution for the hot gas halo. Clearly visible in the second and third frames is the elongation of the initially axisymmetric distributions, caused by the passage of the intruder along the right side of the galaxy. The intruder exits the simulation at just under t = 1.0 revolutions.

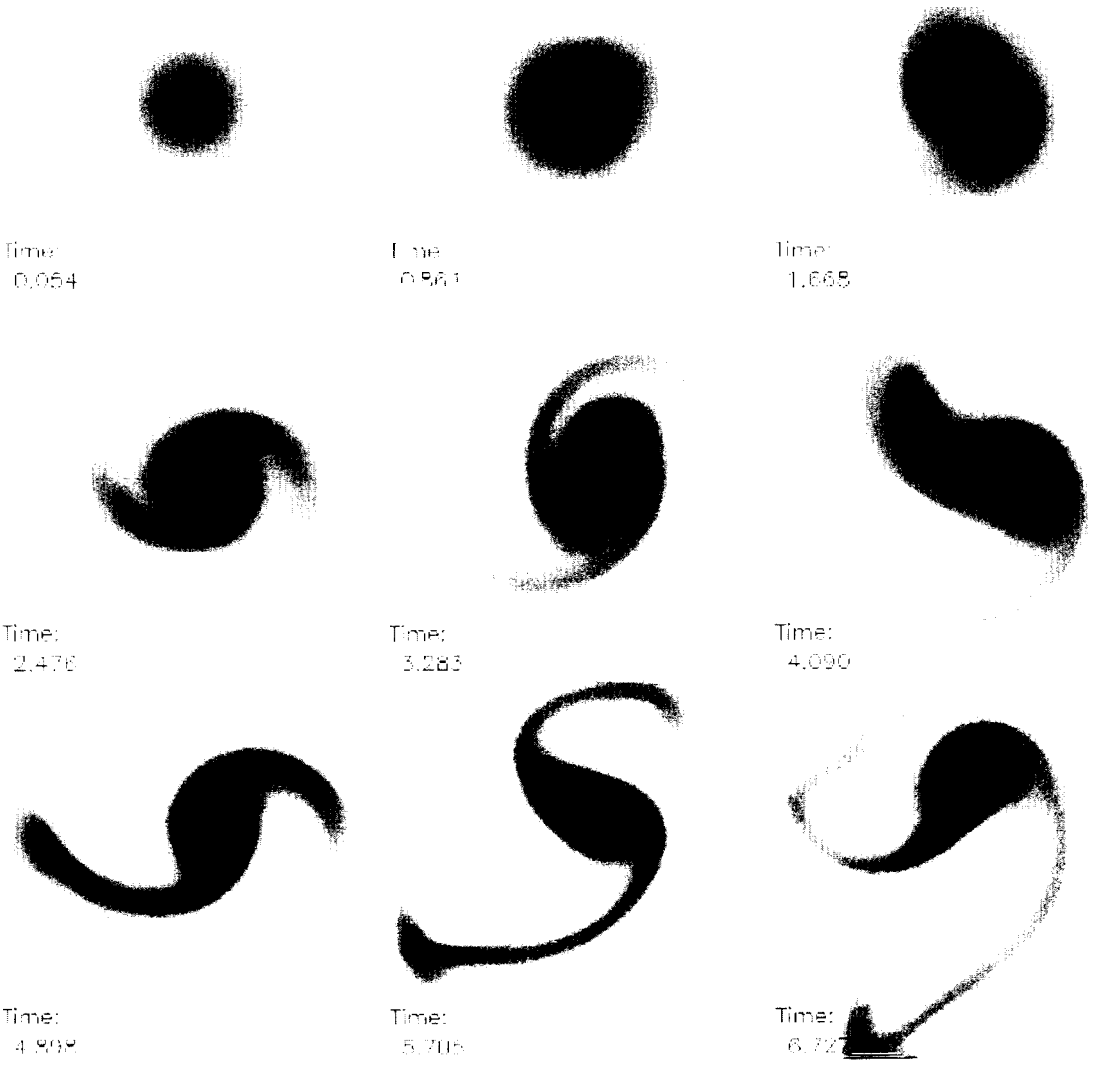

Figure 3.17: Gas mass distribution for the hot gas halo. Clearly visible in the second and third frames is the elongation of the initially axisymmetric distributions, caused by the passage of the intruder along the right side of the galaxy. The intruder exits the simulation at just under t = 1.0 revolutions.

We have found a mechanism that can produce lopsided galaxies. In Section 3.4, the properties of such galaxies will be studied and discussed in more detail.

3.4 Simulations of Lopsided Galaxies

Some lopsided galaxies may be explained as the result of interactions with close companions. A systematic study of the properties of such lopsided galaxies is now in order. The intruder runs presented in the previous section showed *qualitatively* the same behavior, regardless of their respective halo type. They showed only *quantitative* differences, in the amount of their center of mass separation between stars and halo. But regardless of the halo type, such a separation was observed to some degree, and the interaction between close neighbors provides, therefore, a possible scenario to produce such a separation.

In simulations with lopsided galaxies and a dynamic halo, the stars' center of mass moved generally at least three times as much as the halo's center of mass (Zeltwanger et al., 2000). This is conceptually understandable, given the fact that the halo mass fraction and the star mass fraction in those simulations were in a 3:1 ratio. In those simulations, the dynamic halo itself developed a spiral structure, for which there is no observational evidence yet. To avoid any potential non-axisymmetric influences from the halo, the offset runs described in this section used a static halo. Because of the above mentioned relatively small motion of the halo's center of mass, any limitations

that might arise from using a static halo are also relatively small. In fact, since halo mass fractions are believed to be even higher than the 75% used in our simulations, the effect of the halo motion will be even less than described above. For this reason, and to keep things simple, the runs in this section therefore employ exclusively a static halo model. This halo model is also the one that is generally used in most simulations with the GALAXY program. All runs with counter-rotating components and all runs described in Chapter 4 used the static SC halo. Additional simulations with lopsided galaxies, with other halo mass distributions, are described in Zeltwanger et al. (2000).

Two main characteristics of lopsidedness will be investigated: the amount of the offset of the stellar disk's center of mass from the halo's center of mass and the angular momentum of the stellar disk around the halo's center of mass. For the amount of the offset, two different values were chosen: $2\sqrt{2}$ cells ("small offset", representing about 300 pc) and $10\sqrt{2}$ cells ("large offset", corresponding to about $1500\,\mathrm{pc}$ in real units). The angular momentum could be either "low" or "high". "High" in this respect refers to the fact that in this case the stellar disk, in addition to being displaced, was given a slight "push" to force the disk's center of mass into a damped orbit around the halo's center of mass. The halo in these runs is a static SC distribution with a 75% mass fraction.

3.4.1 Small Offset, Low Angular Momentum

This simulation is a small offset, low angular momentum run. In this run (and in all other offset runs) the initial angular momentum of the disk's center of mass has the same direction as the individual star particles' initial angular momentum (no retrograde motion). The run starts with the development of an initial transient containing more spiral structure than our base run (run # 1 in Table 3.1). Following the transient is a phase of spiral structure with approximately eight arms that combine with each other and thus decrease in number as the simulation evolves. A noteworthy difference is the initial relatively strong one-armed spiral that is not seen in the base run. It is visible in the first frame of the left panel in Figure 3.19, and also evident through the m = 1 mode in Figure 3.18 (left), which is the strongest mode for the first 1.5 revolutions of the run. This one-armed spiral is due to the fact that the initially offset stellar disk sloshes towards the center of the gravitational well of the halo, leaving a string of stars in its trace which then becomes a one-armed spiral, as the disk turns counterclockwise. This one-armed spiral fades away then, and the disk is dominated by the above mentioned multi-armed spiral, until at about t = 3 revolutions a central bar forms, which remains the dominant feature of the simulation for the remainder of the run. The end stage of this run is very similar to the base run, both in visual appearance as well as in its Fourier amplitudes. The m = 2 (bar) mode of the base run is some 10% higher than in this small offset run though. This agrees with earlier findings that interactions of galaxies may inhibit or at least

weaken the formation of a central bar in an otherwise bar unstable disk (Athanassoula, 1996a; Athanassoula, 1996b). Runs with a higher initial offset (representing a stronger interaction with a neighboring galaxy), discussed in the following sections, will show that a higher offset is able to suppress the bar formation even more.

As a result of the offset, the stars' center of mass spirals unevenly inward ("sloshes") around the halo's center of mass (Figure 3.22, left). This kind of motion has also been observed by Levine and Sparke (1998). Once the stars' center of mass has reached the central grid cell at $(129,129)$, it essentially stays in that cell, displaying only small, apparently random, fluctuations. (129,129) is also the grid coordinate at which the halo's center of mass is located. The apparently random motion of the stars' center of mass during the second half of the simulation is at least in part due to star particles which escape from the simulation grid. These star particles are subsequently not taken into account any more for the calculation of the disk's center of mass (or for anything else in the simulation, for that matter). Generally, for a simple simulation like the base run, the mass loss, due to this escape, is 0.5% or less over the course of an entire simulation. For offset runs, this mass loss may be as high as several percent, depending on the amount of the offset, and whether it is a low angular momentum run or a high angular momentum run.

Table 3.3 on page 77 lists the run discussed in this section as run # 10.

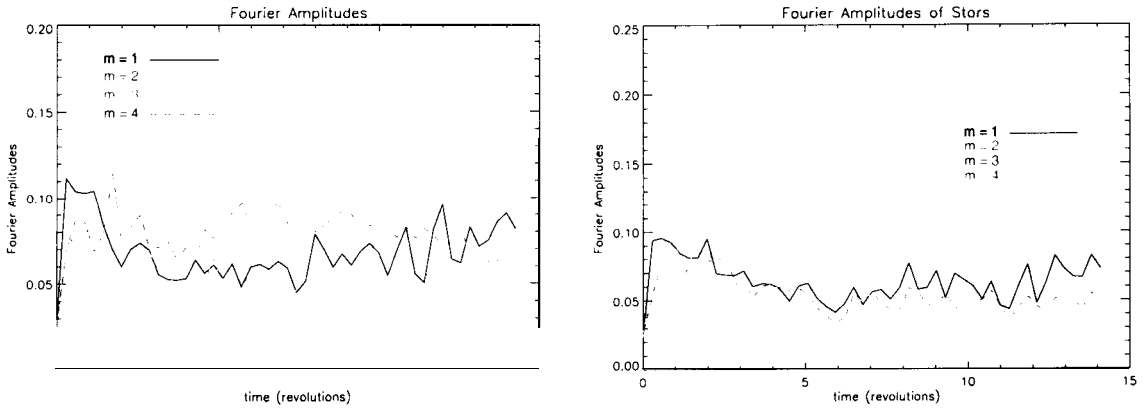

Figure 3.18: Small offset – Fourier amplitudes. Low angular momentum run is on the left, high angular momentum run is on the right.

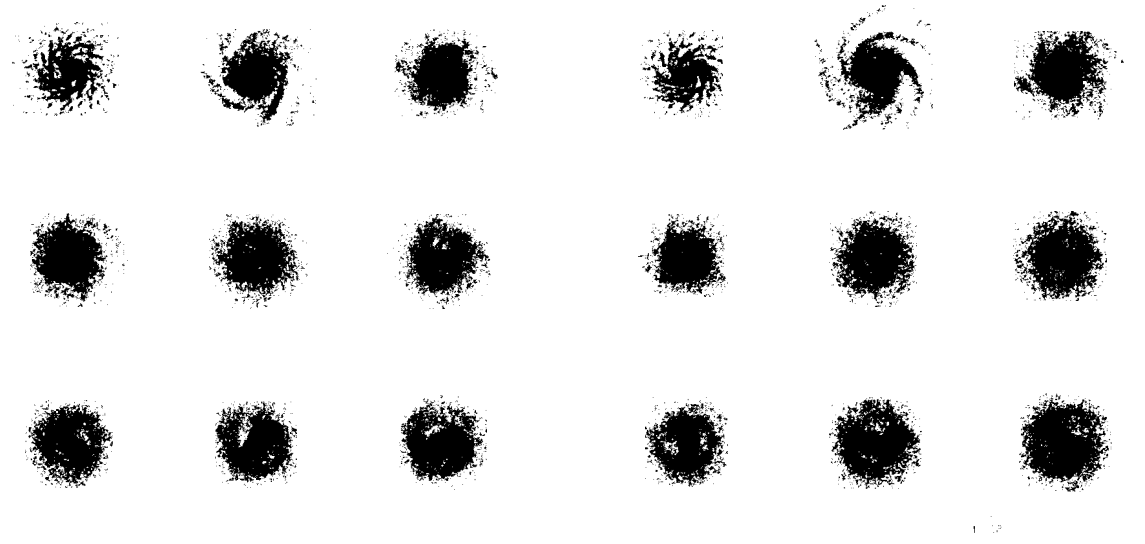

Figure 3.19: Small offset – star mass distribution. Low angular momentum run is on the left, high angular momentum run is on the right.

3.4.2 Small Offset, High Angular Momentum

Unlike the previous run, this simulation's stellar disk has been given an initial "push", forcing the disk's center of mass into a damped, counterclockwise orbit around the halo's center of mass. As a result of this push, this simulation develops no initial one-armed spiral, like the low angular momentum run did. The m = 1 mode of this simulation (see Figure 3.18, right panel) is consistently lower than the respective mode of the low angular momentum run (Figure 3.18, left panel). The stellar density distribution of this run does not show a comparably single-arm feature as the previous run (Figure 3.19, right panel). The multi-armed spiral seen in the previous simulation, however, develops in this run as well, and it goes through a very similar transient phase after which the eight or so individual spiral arms start to merge together and eventually fade away at around t = 5.3 revolutions. Consistent with the note at the end of the previous section is the fact that the development of the central bar is inhibited again. The overall development of the bar is comparable to the previous run. The disk's center of mass in this run displays similar behavior as its low angular momentum sibling (Figure 3.22, right). Due to the initial "push", responsible for the high angular momentum, the stars' center of mass requires more time before it reaches the central grid cell at $(129,129)$, where the halo's center of mass is located. The stars' center of mass then bounces around that central grid cell, just as observed in the low angular momentum case. Because the inward sloshing phase takes longer in this case, the motion following the inward spiral appears less random, but essentially

the random motion just sets in a little bit later than in the previous case. Table 3.3 on page 77 lists the run discussed in this section as run # 11.

3.4.3 Large Offset, Low Angular Momentum

The run described in this section has an initial offset five times larger than run # 10 (small offset, low angular momentum), but is otherwise the same. The larger offset causes the initial one-armed feature, already noticed in run # 10, to become much stronger. This is because the trail of stars, originating from the initial location of the disk's center of mass (= high star density), now sloshes through less densely populated areas of the disk and is thus less disturbed and can persist longer. In fact, the m = 1 mode of this run is consistently the highest mode, although it is decreasing in strength over time (see Figure 3.20). This mode, at its peak, is more than three times as strong as in the small offset run.

This run does not develop as many transient multi-armed spirals as its small offset sibling, but a set of four or five spiral arms can be seen in the star distribution through t = 5.3 revolutions (Figure 3.19, left panel). The one-armed feature is visible even longer, up to t = 8.7 revolutions. No bar develops in this simulation at all, supporting previous findings that galaxy interactions may prevent stellar disks from developing a bar. The center of mass motion of the disk behaves in the same manner as in the small offset runs: it spirals inward around the central grid cell. Due to the larger

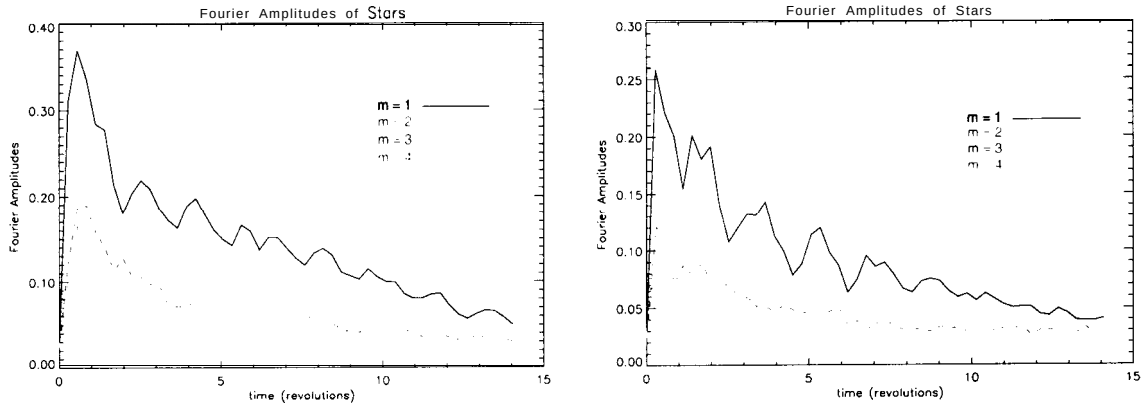

Figure 3.20: Large offset − Fourier amplitudes. Low angular momentum run is on the left, high angular momentum run is on the right.

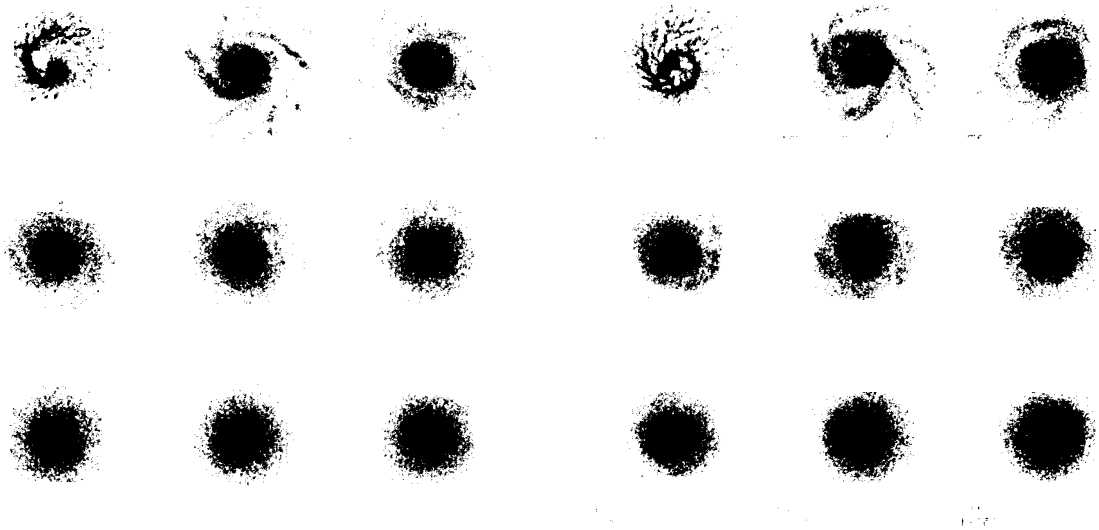

Figure 3.21: Large offset − star mass distribution. Low angular momentum run is on the left, high angular momentum run is on the right.

offset, this phase takes longer than in the small offset runs. In fact, at the end of the simulation, the stars' center of mass is still sloshing around the halo's center of mass (Figure 3.23, left). The random motion, observed in the small offset runs, has not yet set in. Had the simulation been run longer than 14 revolutions, then the stars' center of mass would eventually start to bounce around the central grid cell, as the distance of the two centers of mass decreases. Table 3.3 on page 77 lists the run discussed in this section as run # 12.

3.4.4 Large Offset, High Angular Momentum

The last run in this series of simulations confirms previous results and does not offer any surprises. As in the cases of the small offset runs, the initial one-armed feature is weaker in the high angular momentum case compared to the low angular momentum case. This is evident in the m = 1 Fourier amplitude (Figure 3.20), which is lower for the high angular momentum case and in the plot of the star density (Figure 3.21). The multi-armed spirals persist until about t = 3.6 revolutions and a one-armed spiral is visible through about t = 8.7 revolutions. As in the previous large offset run, no bar develops. The stars' center of mass spirals very nicely inward in this case, as can be seen in the right panel of Figure 3.23. The combination of a large offset with a high angular momentum produces the initially large spiral motion, which continues, though gradually damping, until the end of the simulation. Table 3.3 lists the run discussed in this section as run # 13.

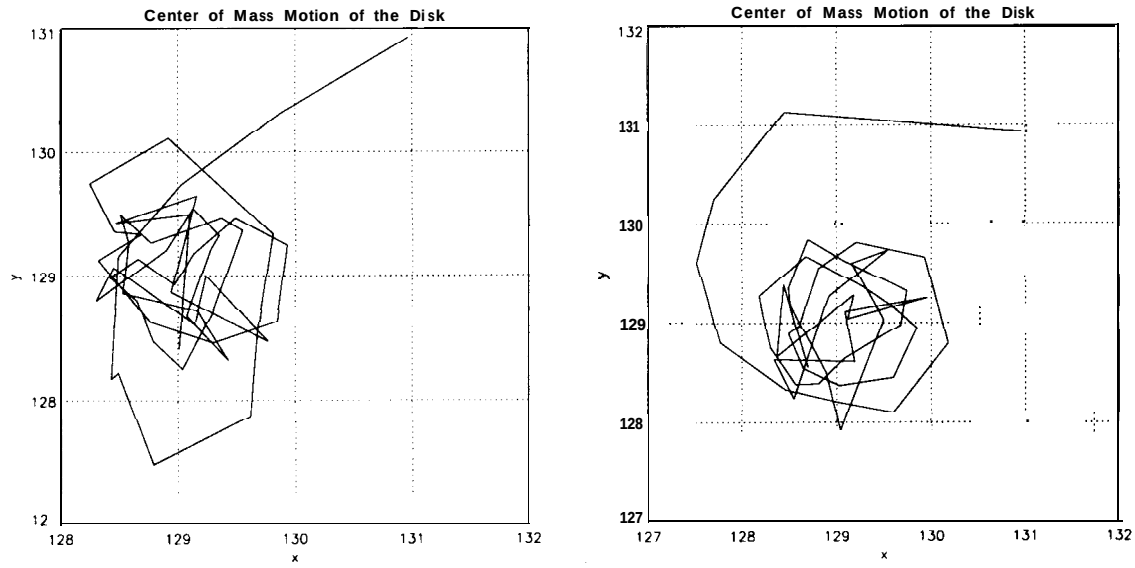

Figure 3.22: Center of mass motion of the stars, small offset. The halo is static, its center of mass is located at (129,129). Left: low angular momentum case. Right: high angular momentum case. The motion starts near (131,131), the simulations lasted for 14 revolutions.

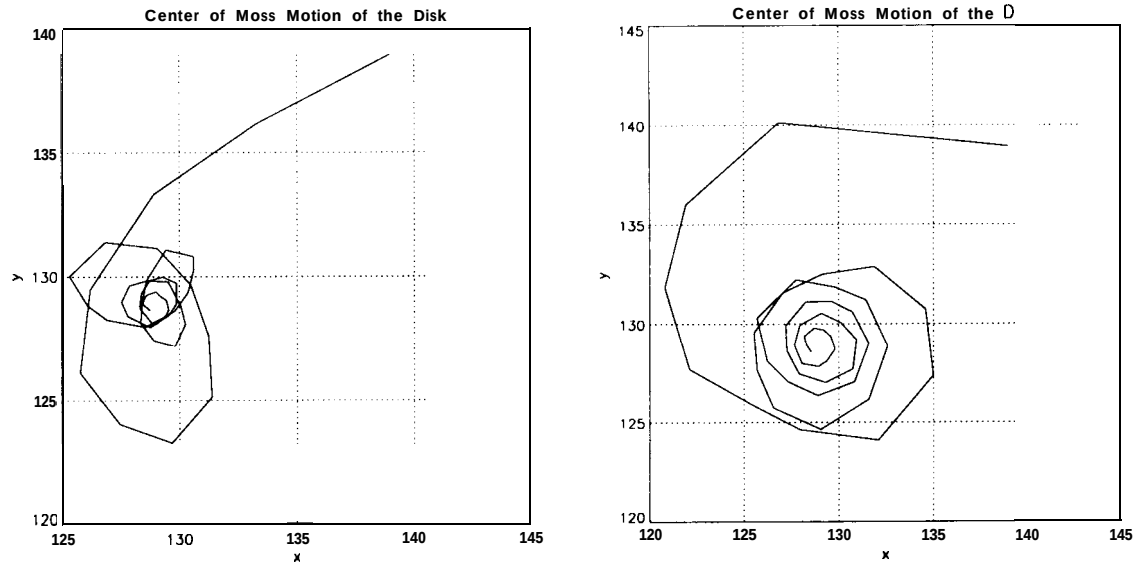

Figure 3.23: Center of mass motion of the stars, large offset. The halo is static, its center of mass is located at (129,129). Left: low angular momentum case. Right: high angular momentum case. The motion starts near (139,139), the simulations lasted for 14 revolutions.

3.4.5 Summary of Runs with Lopsided Galaxies

Table 3.3 summarizes the runs with lopsided galaxies. The prediction that interactions between galaxies can produce lopsidedness and subsequently prevent the formation of a central bar in an otherwise bar unstable disk was confirmed. The stronger the lopsidedness (simulated by a larger initial offset), the greater the suppression of bar formation.

Table 3.3: Summary of runs with lopsided galaxies

Run #	Offset	Angular Momentum	Final Bar?
10	$2\sqrt{2}$	low	yes
11	$2\sqrt{2}$	high	yes
12	$10\sqrt{2}$	low	no
13	$10\sqrt{2}$	high	no

Now that we explored the GALAXY code's ability to perform simulations without stellar evolution, it is time to test the code's performance in simulations with stellar evolution switched on.

4 SIMULATIONS WITH STELLAR EVOLUTION

Galaxies, whether they are spiral, elliptical, or irregular galaxies, are hosts to numerous dynamic processes. The GALAXY code is an attempt to realistically simulate some of these processes. I will start off this chapter by describing briefly each of these individual processes, and how they are implemented in the GALAXY code. More detailed descriptions have been given in previous publications (Schroeder, 1989; Shorey, 1996), and the reader may kindly refer to these for more in-depth elaborations of the evolutionary processes in the GALAXY program.

What complicates matters is that the evolutionary processes are not independent of each other. Instead, they influence and affect each other. In some regions of the parameter space governing these processes, the program behavior appears chaotic. Small changes in one or several of the parameters change the outcome of the simulation considerably. Other regions of the parameter space are more robust against minor parameter changes and produce stable spiral galaxies over several dozens of revolutions. And then there are regions in the parameter space, which, while not being chaotic, do not sustain long lasting spiral structures. It has been one of the main tasks for this thesis to map out this parameter space and find a set or sets of parameters which result in simulations of galaxies with long lived spiral structures that agree with observations of spiral galaxies. The presentation and description of the simulations performed to map out the parameter space of the GALAXY program make up the major part of this chapter.

All simulations discussed in this chapter are referred to by their "run #". Appendix B lists the input parameters of all simulations together with this run #. Shown in Appendix C are plots of Fourier Amplitudes of stars and clouds, Toomre's Q (also for stars and clouds), and the development of angular momentum and mass for the various components of the simulations (stars, clouds, gas, halo, and total). In most cases, pairs or groups of simulations are compared with each other, in which the sets of input parameters were identical except for one parameter. That way the influence of this particular parameter could be assessed. Some runs are mentioned and discussed on more than one occasion if their set of input parameters paired them more than once with other, similar simulations. This is particularly true for run # 14, which served as a reference run for runs # 15 through # 29. Due to this grouping by similar parameter sets, the simulation runs are not necessarily discussed in the order in which they have been performed.

4.1 Input Parameters of the GALAXY Code

There are two kinds of parameters used in the GALAXY program: parameters that directly influence an evolution process, and parameters that don't. Emphasis is on the evolution parameters, but some of the "other" parameters, at least those that have been studied as part of the parameter space mapping, shall also be listed in this section for completeness.

4.1.1 Evolution Parameters

4.1.1.1 Gas Infall

Infall from the halo onto the disk has been included in N-body simulations of disk galaxies to cool the disk (Sellwood and Carlberg, 1984; Schroeder, 1989; Shorey, 1996). Preventing the disk from getting too hot maintains favorable conditions for prolonged spiral structure in the disk. There is also observational evidence for such infall in our own galaxy, the Milky Way (Toth and Ostriker, 1992; van Woerden et al., 1985; Giovagnoli and Tosi, 1995; Wakker et al., 1999).

In practice, the infall is implemented by adding a fixed amount of halo mass, ΔM_{halo} (i, j), to cell (i, j) of the gas. The A M_{halo} (i, j) remain constant throughout the simulations and their value is proportional to the initial total mass in cell (i, j). This transformation of halo mass to gas mass is done at every time step. Thus, after t rotation periods into the simulation, the total amount of halo mass $\Delta M(i, j)$ that was added to cell (i, j) since the start of the simulation, can be computed from:

$$\Delta M(i,j) = 0.01\, \mathcal{P}_{in}\, t\, \Sigma(i, j, t = 0) \qquad (4.1)$$

$\Sigma(i, j, t = 0)$ is the total mass density of cell (i, j) at time $t = 0$. $\mathcal{P}_{in}$ is the user defined rate of infall (specified in the parameter input file). The factor 0.01 is used so that

$\mathcal{P}_{in}$ can be specified as a percentage value, rather than a fraction. Thus, for example, $\mathcal{P}_{in}$ = 1.0 means "During every rotation period, 1.0% of the initial total galaxy mass in cell (i, j) is taken away from halo cell (i, j) and added to gas cell (i, j)".

The infall material is assumed to have the same thermal and dynamic properties as the initial gas component. Thus, gas falling into cell (i, j) has the same velocity that the gas in this cell initially had at t = 0 revolutions. After some infall has accreted into a gas cell, the new speed of that cell is then calculated using the conservation of linear momentum.

To test the code's response to variation of the infall rate, simulations have been performed with $\mathcal{P}_{in} \in \{0, 0.25, 0.375, 0.5, 1.0, 1.5\}$.

4.1.1.2 Star Formation through Cloud Collisions

There is observational evidence for the existence of gravitationally bound gas clouds in the Milky Way (Chieze and Lazareff, 1980; Cowie, 1980; Casoli and Combes, 1982). To simulate such clouds, a cloud-particle N-body component is included in the GALAXY code. Unlike the star particles in the code, these cloud particles may collide with each other. Shorey (1996) has put in great effort to simulate these cloud-cloud interactions very realistically. While previous simulations modeled the clouds as inelastic billiard bails (Carlberg and Freedman, 1985; Shorey, 1990; Elmegreen et al., 1993), Shorey (1996) implemented a model based on the cloud fragmentation

model developed by Casoli and Combes (1982). The billiard ball model would cause significant changes in the cloud particles' trajectories when they collided, thus heating up the disk unnecessarily. In Shorey's (1996) approach, the cloud particles are treated as weakly bound spheres of gas that may exchange mass during a collision. They do not simply bounce off each other as they did in earlier billiard ball models. As a result, the trajectories of the cloud particles are not altered significantly by a collision.

Moreover, this fragmentation model has the potential to simulate star formation at the collision interface, as has been proposed in earlier works (Scoville et al., 1986; Shu et al., 1987; Elmegreen et al., 1993). The probability $\mathcal{P}_{sfcrc}$ for star formation through cloud collision is specified in the parameter input file. When clouds collide, a new star particle forms at the collision interface if a random number between 0 and 1 is less than $\mathcal{P}_{sfcrc}$.

As a result of the collision, the clouds involved may coalesce together to form one single cloud, or they continue as two clouds (mass exchange between the colliding clouds is possible though), or the collision interface may break off from both colliding clouds to form a new, third, cloud. For details on how the code decides which scenario applies, please see Shorey's thesis (1996).

To test the code's response to variation of the star formation rate through cloud collision, simulations have been performed with $\mathcal{P}_{sfcrc} \in \{0, 0.03, 0.1, 0.2\}$.

4.1.1.3 Cloud Formation by Jeans Collapse

The cloud formation by Jeans collapse has already been discussed in Section 2.3 and is here only quickly summarized for completeness: A localized portion of the ISM may undergo Jeans collapse, if this ISM portion's mass exceeds the critical Jeans mass, M_J, as defined by equation(2.11). The probability $\mathcal{P}'$ to form a new cloud is then given by equations (2.13) and (2.14) on page 20. The user has control over this cloud formation process through $\mathcal{P}_{cfrc}$ in equation (2.13). The value of $\mathcal{P}_{cfrc}$ is specified in the parameter input file.

To test the code's response to variation of the cloud formation rate, simulations have been performed with $\mathcal{P}_{cfrc} \in \{0, 0.1, 0.5, 1.0\}$.

4.1.1.4 Star Formation through Snowplow

When stars go supernova they produce shock waves that travel through the neighboring galaxy before they dissipate. These shockwaves increase the gas pressure of the ISM, and as a result of this increased gas pressure, nearby clouds may get dense enough to become Jeans unstable and collapse to form new star particles (Elmegreen, 1992; Shorey, 1996). This process, referred to as "snowplow", is included in the GALAXY code through the "Stochastic Self Propagating Star Formation" model, SSPSF (Gerola and Seiden, 1978; Seiden and Gerola, 1979; Shore, 1981; Statler et al., 1983).

In this model, a cloud may collapse and form new stars, if its mass, M_{cloud}, exceeds the critical Jeans mass, M_J (similar to the case of cloud formation from gas through Jeans collapse, see above). The star formation rate through this snowplow effect, P_{sfsp}, determines the probability that a cloud satisfying the Jeans condition actually produces a new star particle. If $M_{cloud} > M_J$ is satisfied, then a random number, s, is compared to P_{sfsp}. A new star forms, if $P_{sfsp} >$ s. P_{sfsp} is set in the parameter input file.

To test the code's response to variation of the star formation rate through the snowplow effect, simulations have been performed with $\mathcal{P}_{sfsp} \in \{0, 0.1\}$.

4.1.1.5 Supernovae

Supernovae are an empirically understood phenomenon. At the end of their life cycle, stars of sufficient mass will go out in a blaze of glory with a gigantic explosion. Much of their mass is ejected into the ISM in this process. Since each star particle actually represents a whole cluster of stars containing stars of different masses, which therefore evolve at different rates, the supernova activity in a given cluster will vary over time. The program keeps track of the age of each star and decides, based on each star's mass, when its time has come to blow up. The mass and energy released by a supernova is added to the hydro cell in which the supernova took place. Other than switching supernovae "on" or "off', there is no further control parameter for the supernovae defined in the parameter input file.

4.1.2 Non-Evolution Parameters

- Cloud mass fraction. The fraction of the total galaxy mass that is assigned to the clouds. Values tested: 0.0%, 0.5%, 2%, and 4%.
- Gas mass fraction. The fraction of the total galaxy mass that is assigned to the gas. Values tested: 0.0%, 0.5%, and 2%.
- Halo mass fraction. The fraction of the total galaxy mass that is assigned to the halo. Value has been kept fixed at 80%.
- Star mass fraction. The fraction of the total galaxy mass that is assigned to the stars. Values tested: 14%, 16%, 17.5%, and 20%.
- Initial gas temperature. Only used for isothermal start. Values tested: 0.5 K, 2 K, 5 K, 10 K, and 100 K.
- Initial energy density of gas. Only used for non-isothermal start. Values tested: 10, 150, and 1500.
- Initial number of star particles. Values tested: 1.0 x 10^5 and 2.5 x 10^5.
- Initial Toomre's Q of stars. Values tested: 1.1 and 2.0.
- Initial number of cloud particles. Values tested: 1.0 x 10^4 and 5.0 x 10^4.
- Initial Toomre's Q of clouds. Values tested: 1.1 and 2.0.

4.2 Number of Star Particles

Earlier simulations of spiral galaxies have already shown that the lifetime of a spiral structure increases with the particle number N (Shalit, 1995). Needless to say, to simulate a galaxy containing 2 x 10” stars as realistically as possible, one would want to run a computer model containing as many N-body particles. Current computer technology is not (yet) capable of mastering such a feat, although Moore’s Law, predicting that computer performance doubles every 18 months, provides us modelers with constantly improving equipment and thus new opportunities for more accurate simulations. But considering that the execution time of the GALAXY code is proportional to N log N, one frequently has to trade in accuracy of the simulation for faster execution to produce results sufficiently fast. On the fastest computer currently at my disposal, a typical GALAXY run with 2.5 x 10^5 star particles and full stellar evolution switched on requires a minimum of three days to execute and analyze.

This section will compare runs with different initial numbers of star particles. The runs discussed in this section will otherwise be identical to rule out any other influences for differences in the simulations’ outcome.

The runs to be compared here are listed in Table B.2 on page 156 as run # 14 and run # 20, respectively. Run # 14 will generally serve as a reference run for about the first half of the runs listed in Appendix B. It uses 10^5 star particles, while run # 20 simulates 2.5 x 10^5 star particles.

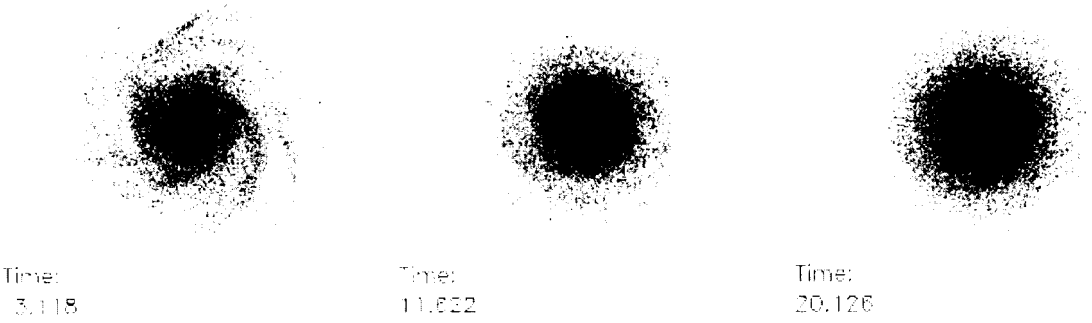

Figure 4.1: Star mass distribution of run # 14.

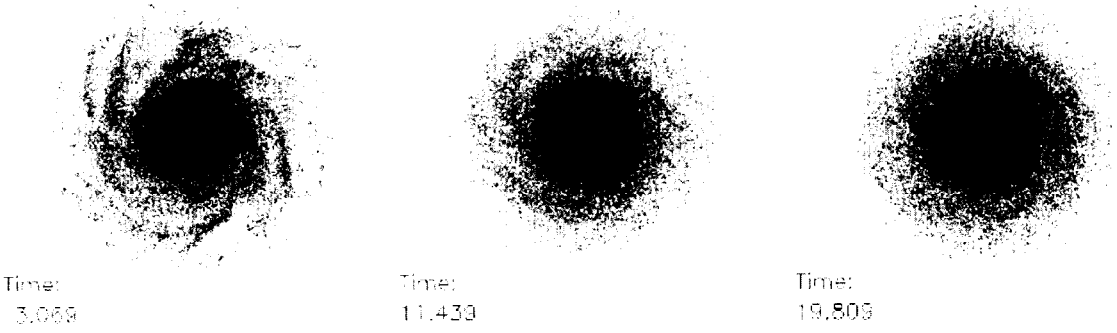

Figure 4.2: Star mass distribution of run # 20.

Figures 4.1 (run # 14) and 4.2 (run # 20) show the star density distributions for the two runs at three different time steps. Note that the time indices for the two runs differ slightly, although the GALAXY program performed the same number of iterations in each case. This slight difference is due to the dynamic calculation of the time step At between iterations. And because At depends in part on N, the slight difference in the time indices results.

Early into the simulation, the two runs show little difference. But already by time $t \approx 11.5$ revolutions run # 14 shows less structure and is more diffuse around the truncation radius than run # 20. This trend continues throughout the remainder of the simulations. These subjective indications are supported by a look at the Toomre's Q for the two runs (Figures C.l and C.7). At the end of the simulations, run # 14 is about 15% "hotter" than run # 20. Also note how the stellar disk in run # 14 "shrinks" with time. At $t \approx 20$ revolutions the disk in run # 14 is noticeably smaller than the disk in run # 20.

up to $t \approx 15$ revolutions, the rotation curves of the two simulations are very similar (see Figures 4.3 and 4.4). But after $t \approx 15$ revolutions, run # 14's rotation curve drops significantly at higher radii, which is generally not observed in real galaxies. Instead, a mostly flat rotation curve is measured. Run # 20 maintains such a flat rotation curve at ≈ 215 km s^{-1} until the end of the simulation. The reduced circular speed at higher radii causes the stellar disk in run # 14 to shrink, as mentioned above.

For comparison, the flat part of the Milky Way's rotation curve has been observed to be at $\approx 230\ \mathrm{km\,s^{-1}}$ (Tayler, 1993).

Not surprisingly, the obvious "winner" of this comparison is the run that employs a greater number of star particles. Thus, from run # 31 on, all simulations have been performed with N = 2.5 x 10^5.

4.3 Mass Fractions

The mass fractions of halo, stars, gas, and clouds of spiral galaxies have been determined by several groups, see for example Elmegreen (1998), Binney and Tremaine (1987), and references therein. In these reports, the halo's mass is estimated to contain from 75% to 95% of the total galaxy mass. The stars make up about 10% to 20%, and the clouds and gas "several percent". In this section, the effects of variations in the mass fractions of the galaxy components will be investigated.

Table 4.1: Runs differing by their mass fractions (with stellar evolution)

Run #	Halo	Stars	Clouds	Gas
14	0.8	0.16	0.02	0.02
26	0.8	0.14	0.04	0.02
27	0.8	0.175	0.02	0.005
28	0.8	0.175	0.005	0.02

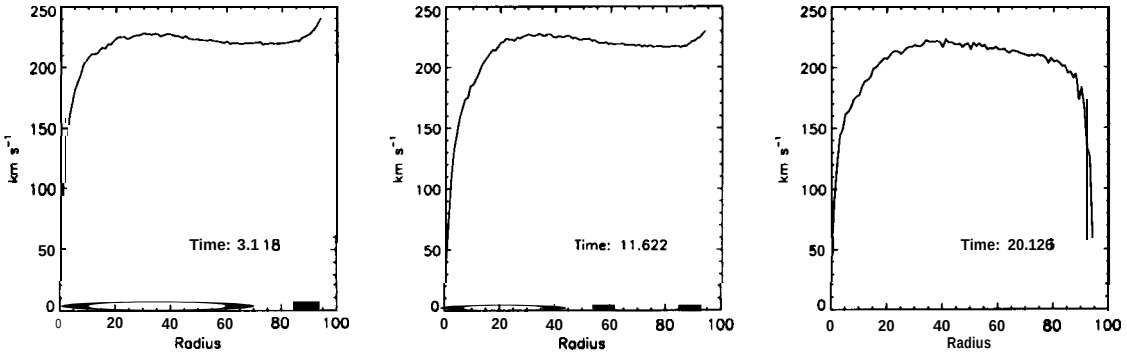

Figure 4.3: Rotation curve of run # 14.

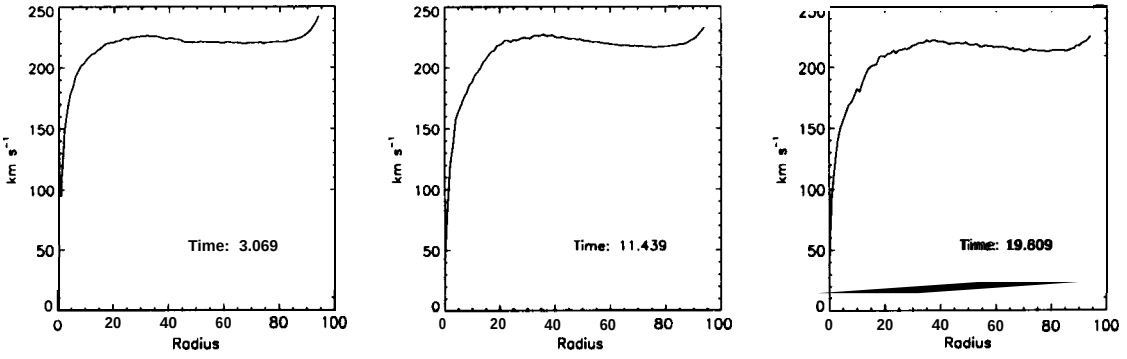

Figure 4.4: Rotation curve of run # 20.

Runs 14, 26, 27, and 28 differ by their mass fractions only, but are otherwise identical. Table 4.1 lists the sets of mass fraction values for these runs. The complete sets of parameters of all runs are listed in Appendix B. The halo has been kept at a mass fraction of 0.8, consistent with current belief that a substantial mass fraction in galaxies consists of “dark matter” surrounding the galaxy. This dark halo mass fraction may be as high as 0.95, and the chosen value of 0.8 represents a value well in the range of the reported halo mass fractions. The remaining 0.2 have been divided between stars, gas, and clouds, so that the stars have a roughly 5 to 10 times higher mass fraction than the gas and the clouds.

Runs # 14, 26, and 27 develop in virtually the same way. A noteworthy difference occurs in run # 28, which develops a central bar in the stellar disk, see Figures 4.5 and 4.6.

The red dots in the star density plots mark the locations where new stars formed at the respective time steps. There is no obvious difference in the star formation process of the two runs, neither in the rate of star formation, nor in the locations where they form. It should be noted that the runs reported here were done before the changes in the cloud formation routine (see Section 2.3) were incorporated into the code. The “starburst rings” of star formation that are visible in Figures 4.5 and 4.6 are a direct consequence of the high cloud formation activity in the galaxy center: The large cloud population due to the high cloud formation probability increases the frequency

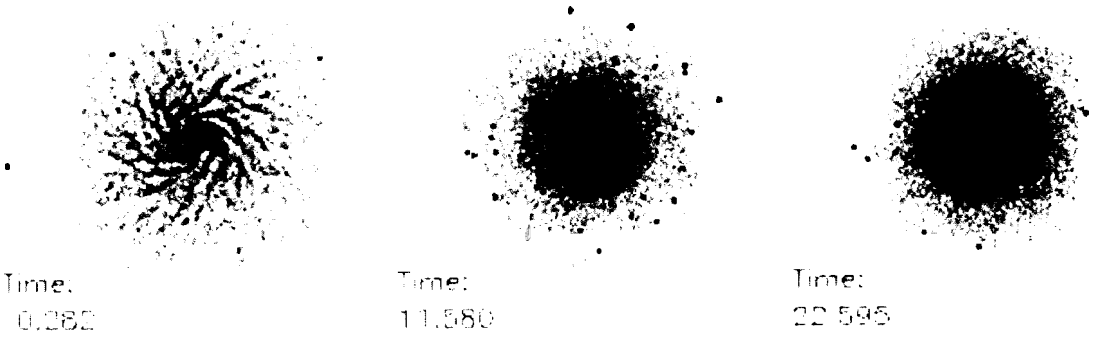

Figure 4.5: Star mass distribution of run # 27. No bar develops. Red dots mark the locations of newly formed stars. Runs # 14 and # 26 look very similar to this one.

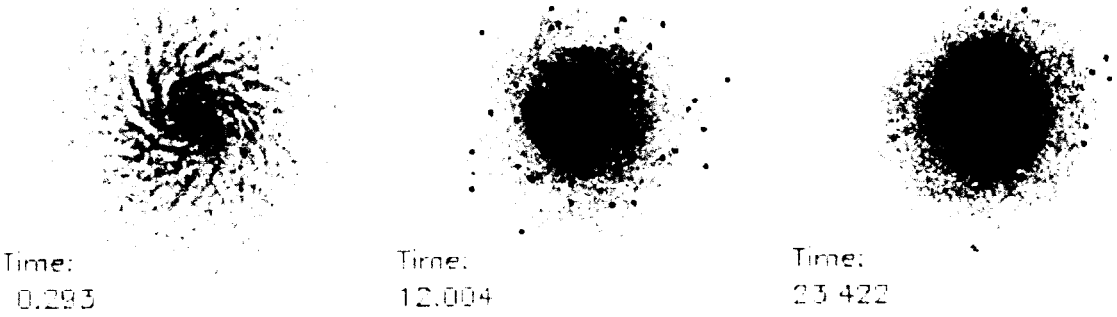

Figure 4.6: Star mass distribution of run # 28. A central bar develops. The red dots mark the locations of newly formed stars.

of cloud collisions. This, in turn, brings up the star formation rate through cloud collisions. The modified cloud formation routine does not confine star formation to such a starburst ring as observed in the runs described in this section. Star formation does still happen, for the most part, at or near the galaxy center, but is generally more spread out.

The development of the bar is also evident from a comparison of the Fourier modes of these two runs (Figures C.14 and C.15). Run # 28 quickly develops a strong $m = 2$ mode, consistent with the evolving central bar in this simulation. In run # 27 the m = 2 mode does not grow nearly as high – no bar develops here.

A preliminary series of simulations done for this thesis, involving runs with only halo and star components, showed that a sufficiently massive halo is capable of suppressing the formation of a central bar in the galaxy. This finding is well-known from the work of Ostriker and Peebles (1973) and it has also been reported by other authors (Binney and Tremaine, 1987; Sellwood, 1983). Since both the halo mass fraction and the star mass fraction remain unchanged from run # 27 to # 28, there must be other mechanisms affecting the bar formation here.

A look at Toomre's Q for these runs (Figures C.14 and C.15) shows that run # 27's Q is consistently about 20% to 25% higher compared to run # 28. Run # 27 is thus hotter and therefore more bar stable than run # 28. The disk in run # 28 may have been kept cooler due to the initially smaller cloud mass fraction in this run. The

cloud-cloud collision rate is therefore low, and it is well known that collisions are a major contributor to heating in disk simulations (Whitworth et al., 1998; Schroeder, 1989).

It should also be noted that these runs were done with "only" 10^5 star particles, and we observe the earlier reported "shrinking" of the stellar disk (see Section 4.2, page 88). While other factors may contribute to this shrinking, a low number of star particles is certainly a major influence for this observation. The shrinking is generally observed to a lesser degree for runs # 31 and later, when the number of star particles has been increased to 2.5 x 10^5.

In the category of runs which differ only in their initial mass fractions belong also runs # 39 and # 42. Those were originally not intended to be direct comparisons, but they fit into this section and are therefore included here. They are both runs with stellar evolution switched off, and were designed to be compared to corresponding runs with stellar evolution switched on. These runs were needed to assess the influence of the stellar evolution processes to the simulations. In fact, run # 39 is merely a modified version of the base run described in Section 3.1. Table 4.2 lists the mass fractions of these three simulations.

The first thing noticed, when comparing the base run from Section 3.1 with run # 39 is, that the bar develops to a lesser degree in run # 39. This can be seen in Figures 3.1 and 4.7, and it is even more obvious in the comparison of the $m = 2$ Fourier modes

Table 4.2: Runs differing by their mass fractions (no stellar evolution)

Run #	Halo	Stars	Clouds	Gas	# of stars
1	0.75	0.25	0.0	0.0	10^5
39	0.8	0.2	0.0	0.0	2.5 x 10^5
42	0.8	0.16	0.02	0.02	2.5 x 10^5

of the two runs (Figures 3.2 and C.26): the base run's m = 2 mode grows some 50% higher than run # 39's m = 2 mode. This is consistent with the previous remark that a high halo mass fraction may suppress the formation of a central bar in disk galaxies. Note that the halo mass fraction in run # 39 is 0.8 compared to 0.75 for the base run, a rather small difference. The apparent difference in size of the stellar disks in Figures 3.1 and 4.7 is merely due to a different scaling of the images. The simulated galaxies have the same "physical" size, and they occupy the same space on the simulation grid. This is true for all simulations described in this dissertation.

Taking away some mass from the stars and assigning it in equal parts to the clouds and the gas (run # 42) changes things considerably. There is no bar development in this run. The comparison of the Fourier modes of runs # 39 and # 42 (Figures C.26 and C.29) shows that there is no particularly strong mode dominating run # 42. Especially, no m = 2 development is observed here. In fact, the stellar distribution shown in Figure 4.8 reveals hardly any structure after $t \approx 10$ revolutions.

One contributing factor to this fact may be that, although the halo mass fractions of runs # 39 and # 42 are the same, the ratios of halo mass to star mass are different. In run # 39 it is 4: 1, and in run # 42 it is 5:1. As we saw in the comparison of the base run with run # 39, a relatively small increase in the halo mass to star mass ratio can already have significant impact on the bar development.

This variation in halo mass to star mass ratio is however only part of the explanation. The presence of the gas and clouds in run # 42 will undoubtedly affect the shape of the stellar disk. Particularly, as outlined above, the cloud-cloud collisions will heat up the disk. It is not surprisingly therefore, that the disk in run # 39 is cooler than the disk in run # 42 (see the stars' Q in Figures C.26 and C.29), and is therefore more bar unstable.

Within reasonable values for the mass fractions the simulations discussed in this section behaved similarly. The development of a bar in runs # 1, # 28, and # 39 is no distinguishing criteria between more realistic simulations and less realistic simulations, because barred spiral galaxies as well as unbarred spiral galaxies are observed in the universe. Other than the bar development there was little, if any, difference in the qualitative outcome of the simulations that would justify favoring one set of mass fractions over another.

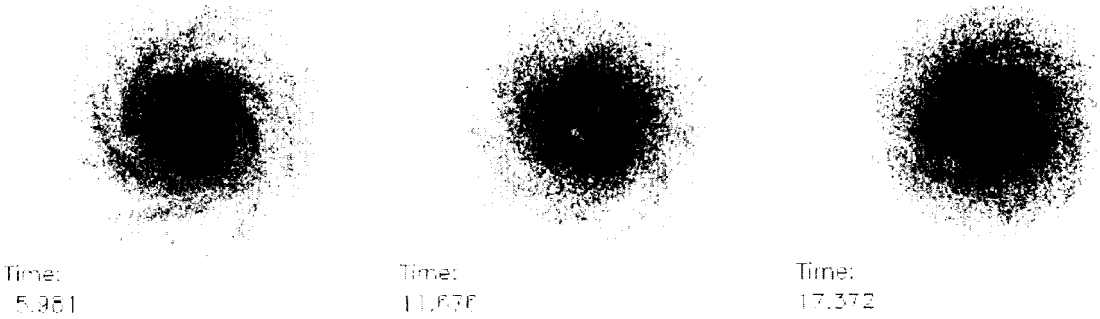

Figure 4.7: Star mass distribution of run # 39. A central bar develops.

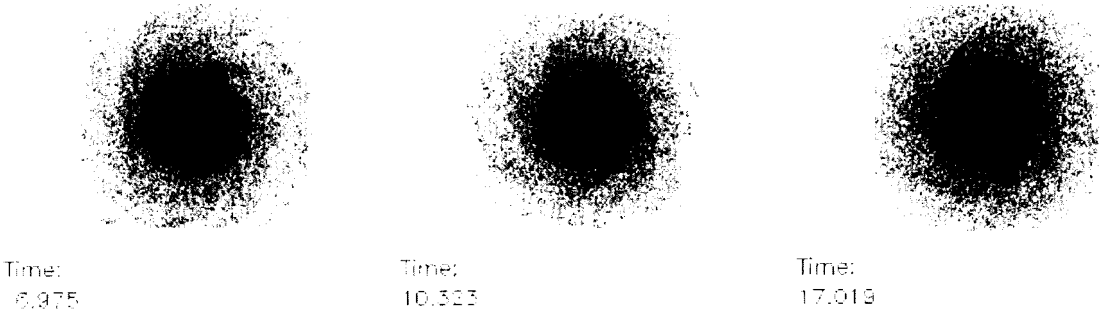

Figure 4.8: Star mass distribution of run # 42. No bar develops.

4.4 Toomre's Q for Stars

For all but one simulation described in this chapter, the initial value for the stars' Toomre's Q, Q_0, was set to a marginally stable value of 1 .1. One simulation, run # 15, was done with Q_0 = 2.0 and compared with run # 14. Aside from the value for Q_0, the two runs are identical.

Figures 4.1 and 4.3 show results from run # 14. Corresponding figures for run # 15 are not shown here, because they are virtually identical in almost every respect. The one noteworthy exception is the evolution of the one parameter in which the two runs differed initially: Toomre's Q.

Figures C.l and C.2 show the surprising result, that Q in run # 14 $(Q_0 = 1.1)$ not only quickly catches up with run # 15's Q value $(Q_0 = 2.0)$, it even ends up higher.

All simulations performed for this thesis show a rise in Q. This has also been reported by other authors (Shorey, 1996). Why the originally cooler disk would heat up faster than the originally warmer disk is unclear at this time and requires further testing.

4.5 Number of Clouds

Interstellar gas clouds have been observed in the Milky Way in a wide range of sizes and masses. They can be anywhere from 8 pc to 80 pc in size (Casoli and Combes,

1982) and from $10^{2.7}$ $M_\odot$ to $10^{5.7}$ $M_\odot$ in mass (Chieze and Lazareff, 1980; Cowie, 1980; Casoli and Combes, 1982). The GALAXY code models clouds as colliding N-bodies. The implementation of the collision process and the subsequent star formation as a result from such collisions have been mentioned earlier in this thesis, and they are described in more detail elsewhere (Schroeder, 1989; Shorey, 1996). The number of clouds is not as critical to the accuracy of the simulations as is the number of stars, and their number in galaxies is also considerably smaller. 10^4 cloud particles have been used for the simulations here. One simulation (run # 54) has been started with 5 x 10^4 cloud particles, and is compared to the otherwise identical run # 53.

With the exception that run # 54 (5 x 10^4 cloud particles) naturally shows a higher cloud number density across the galaxy, the two compared runs are remarkably similar. So similar, almost to the last detail in fact, that it can quickly be concluded that the number of employed cloud particles of 10^4 is sufficient to run simulations with the GALAXY code within the studied parameter range. Nothing further noteworthy has been observed in these runs.

4.6 Toomre's Q for Clouds

Having concluded that the number of clouds has little effect on the results of the simulations, let's now see how the initial value of Toomre's Q for the clouds affects the simulations. Most runs were done with an initial value of $Q_{0,cloud}$ = 1.1. One

simulation, run # 23, has been started with $Q_{0,cloud}$ = 2.0 and this run is compared to run # 14.

One observation from this comparison is that the run with the higher $Q_{0,cloud}$ sees an increase in angular momentum for the clouds after t = 3 revolutions (see Figure C.10). This increase is also seen in run # 14 (Figure C.l), but the clouds' angular momentum decreases again after t = 12 revolutions in that run, while in run # 23 it continues to climb.

The initial drop in the clouds' angular momentum is observed across all simulations to a varying extent, and is due to an initially high cloud-cloud collision rate. In many cases – like in run # 14 – the clouds' angular momentum starts to decrease again about half way through the simulation. This increased angular momentum of the clouds may trigger an overall increased star formation rate. Figures 4.9 and 4.10 show the star density of the two compared runs, together with the locations of newly formed stars.

It is noted that run # 23 indeed seems to have a slightly higher star formation rate, particularly noticeable at t = 22.677 revolutions, but also visible at t = 11.622 revolutions. Plus, run # 23 produces more stars in the outer regions of the galaxy, which is more obvious at t = 11.662 revolutions than at t = 22.677. The increased angular momentum of the clouds results in a higher cloud-cloud collision activity in those outer regions, which produces the higher star formation there.

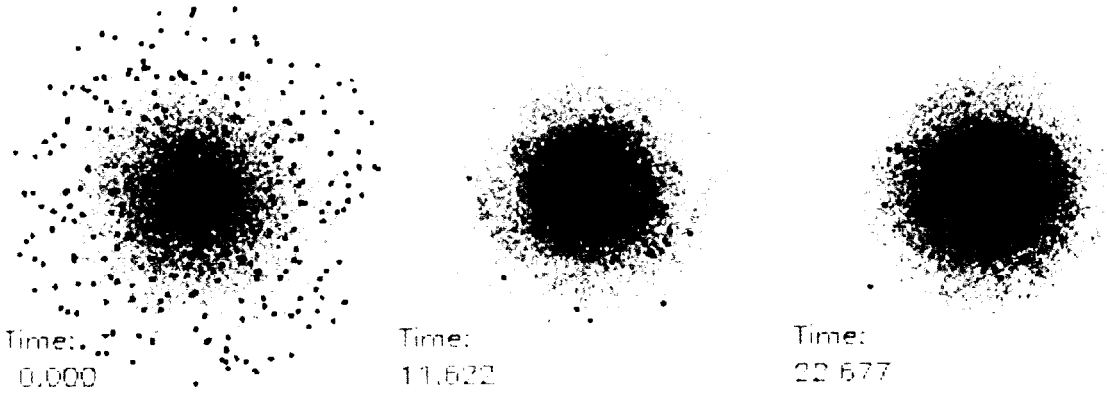

Figure 4.9: Star mass distribution of run # 14. The red dots mark the locations of newly formed stars.

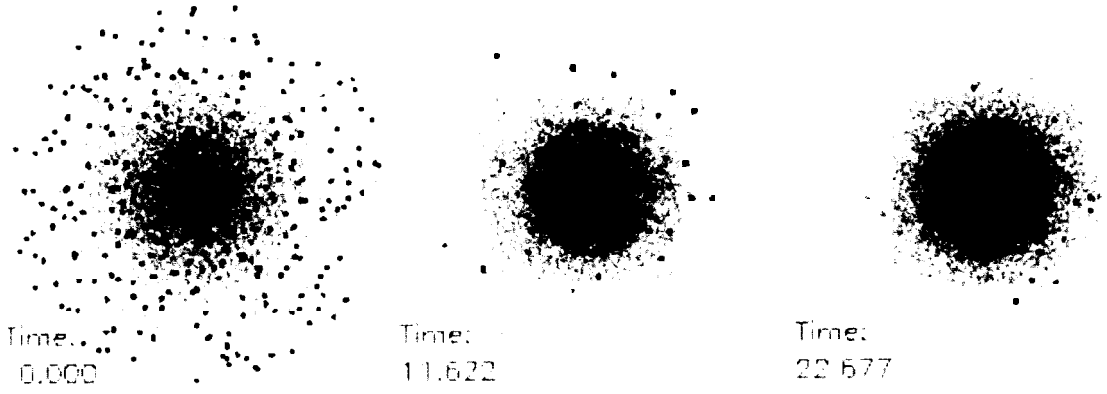

Figure 4.10: Star mass distribution of run # 23. The red dots mark the locations of newly formed stars.

Also visible in those plots is the aforementioned very high cloud-cloud collision rate at the very beginning of the simulations. The strong star formation activity at t = 0 manifests this. This high collision rate (and the corresponding star formation rate) decreases quickly after just a few time steps, going hand in hand with the observed initial drop of the clouds' angular momentum.

Toomre's Q for stars behaves nearly identically in the two compared runs, reaching a maximum value of 6 at the end of the simulations. For run # 14, this is shown in Figure C.1. For run # 23 this plot (Figure C.10) looks very similar. The clouds' Q, however, does not develop identically. Generally, Q_{cloud} reaches considerably higher values than the stars' Q. This is due to the collision processes that the clouds undergo. These collisions throw the clouds into much more random orbits than the stars' orbits, which causes an increase in the clouds' velocity dispersion, and thus in their Q. In run # 14, Q_{cloud} rises to about 175, while in run # 23 it reaches "only" about 110 (Figures C.l and C.10). It is interesting to notice that just as in the case of the stars' Q, the initially cooler model ends up hotter than the initially warmer model (at least in the cloud component). To determine whether this is a systematic behavior, or merely a coincidence, requires further testing.

4.7 Initial Internal Energy of the Gas

When a GALAXY simulation is initialized, one has the option to either set the initial temperature of the gas (for an isothermal gas), or to set the initial energy density of

the gas (for an isoergic gas). In this section, three runs will be compared which start with an isoergic gas with different initial energy densities ("initial energy density" is henceforth called "ceg"). The compared runs are # 14 with ceg = 150, run # 16 with ceg = 10, and run # 22 with ceg = 1500. Most simulations with an isoergic gas used ceg = 150, following a recommendation by Shorey (1996).

Giving the gas an initial uniform energy density (specified by the ceg value) is equivalent to giving the gas a temperature profile. Figure 4.11 shows such a temperature profile of the gas at t = 0 revolutions for ceg = 150, ceg = 800, and ceg = 1500. The plot with ceg = 800 is only included to further illustrate how initial energy density ceg and temperature T are related. No simulation with ceg = 800 has actually been done. ceg = 10 from run # 16 has been excluded from this plot, because for such a low energy density the temperature does not exceed 0.53 K anywhere on the grid. With the temperature scale given on top of Figure 4.11 the resulting plot is essentially black everywhere. Note that isoergic simulations assign higher temperatures to regions with smaller gas density. Equation (2.9) confirms that for an ideal gas with constant internal energy U, the mass M within a grid cell and its temperature T are inversely proportional. Each isoergic run eventually reversed the temperature map to a distribution in which the gas in the galaxy's center is hotter than the gas in the outer regions. Generally, this reversion occurred during the first half revolution of a simulation. Figure 4.11 also illustrates that the initial setup of the simulations is axisymmetric.

Gas with a higher ceg value is warmer than gas with a smaller ceg value. The gas with a high ceg value is thus less susceptible for Jeans collapse than gas with a low ceg value. This will affect the cloud formation rate and ultimately the star formation rate through cloud collisions. Therefore, it is expected that run # 16, which employs the lowest ceg value of the three compared runs, exhibits the highest star formation rate. This is what we observe in Figures 4.9, 4.12, and 4.13.

The higher susceptibility for Jeans collapse of the cold gas can also be seen in the individual components' mass development of these runs. In run # 16 (cold gas), the total cloud mass increases immediately after the start of the simulation, being at almost 3.5 times its starting value by the end of the run (see Figure C.3). The gas mass instead remains at a constant level for the first five revolutions. Only then does the gas mass start to increase slowly, and reaches about 1.5 times its starting value by the end of the simulation. At t = 5 revolutions, when the gas mass starts to increase, the growth rate of the cloud mass decreases visibly.

In the case of the hot gas (run # 22), the gas mass increases right away (it is constantly fed from the halo infall), and by the end of the simulation it reaches more than 3.1 times its starting level (Figure C.9). The cloud mass stays at a nearly constant level until t = 5 revolutions, before it starts to increase and reaches 2.5 times its starting value. By time t = 5 revolutions, portions of the gas have sufficiently cooled down (through cooling mechanisms like the halo infall) to invoke cloud formation through Jeans collapse.

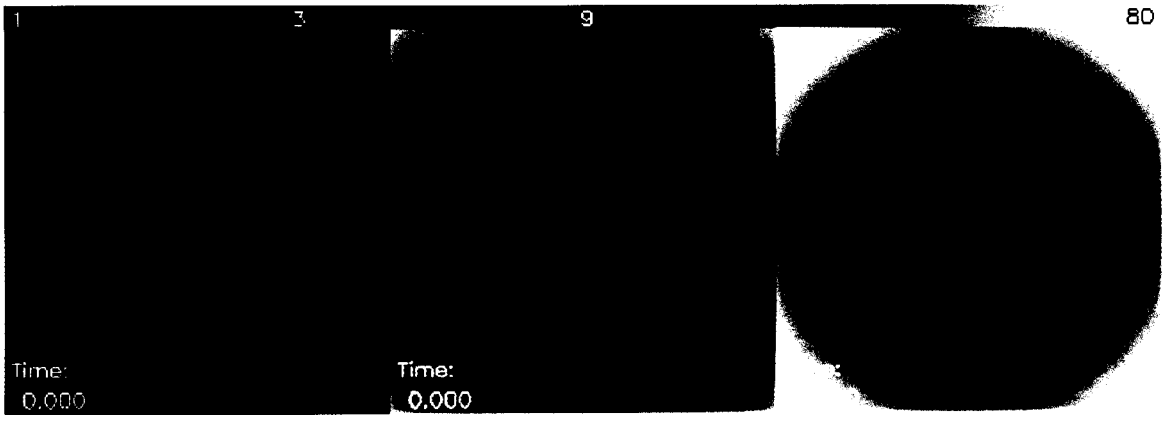

Figure 4.11: Temperature map for three different ceg values. ceg = 150 (left panel), ceg = 800 (middle panel), and ceg = 1500 (right panel).

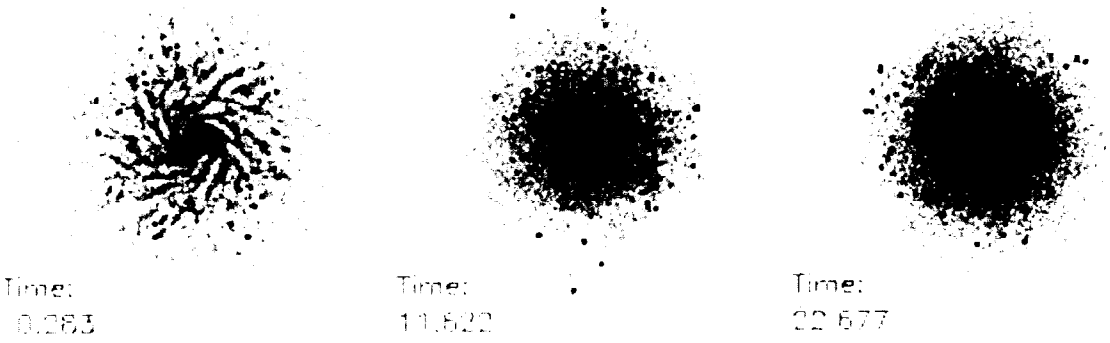

Figure 4.12: Star mass distribution of run # 16. The red dots mark the locations of newly formed stars.

Figure 4.13: Star mass distribution of run # 22. The red dots mark the locations of newly formed stars.

In run # 14 with the medium value of ceg = 150, both the gas component and the cloud component increase their respective total mass from the start of the simulation at moderate rates (Figure C.1). The chosen value of ceg = 150 therefore seems to be a good choice for an isoergic gas, because the gas is neither too hot to prevent Jeans collapse altogether, nor is it so cold that collapse occurs too fast.

4.8 Isoergic Gas vs. Isothermal Gas

A simulation with an isoergic gas (run # 33) is compared to three runs using an isothermal setup where the gas has a different initial temperature T_0 in every case. These are run # 37 with T_0 = 5 K, run# 35 with T_0 = 10 K, and run # 36 with T_0 = 100 K.

The isoergic run (with ceg = 150) develops rather uneventfully, but it does provide an excellent opportunity to demonstrate how the cloud formation and the star formation from cloud collisions are interrelated. At time t = 3.069 in Figure 4.14, the regions of new star formation are along a two-armed spiral. The underlying cloud density (left panel in Figure 4.15) shows high cloud concentrations along the very same spiral arms. The cloud density in those regions is sufficiently large to provide a high cloud-cloud collision rate, and subsequently a high star formation rate from these collisions. The gas density at the same time step (middle panel in Figure 4.15) shows a lower gas concentration along those arms, indicating that a substantial amount of gas in these

regions has collapsed to clouds. Since each cloud formation releases some energy to the gas, the gas temperature increases accordingly. This can be seen in the right panel of Figure 4.15, which shows higher temperatures along those spiral arms. Note that the temperature difference between the spiral arms and the surrounding regions is less than the image might suggest. The hottest (brightest) regions in this temperature map are not more than 12 K, and the coldest (darkest) regions are of the order of 1 K.

The spiral structure in run # 33 is not maintained very long though. By time t = 11 revolutions it starts to fade away, and by time t = 22 revolutions the galaxy exhibits no more spiral features.

Runs # 35, # 36, and # 37 were the first runs which employed an isothermal gas rather than an isoergic gas. It was not a small surprise to see the difference. Runs # 35 and # 37 (T_0 = 10 K and T_0 = 5 K, respectively) both still show strong spiral structures by the end of the simulation at t = 22 revolutions. In fact, run # 37 was reinitialized to go twice the simulation time (44.6 revolutions), and it still shows strong spiral features at that time. Thus, encouraged from run # 37's prolonged spiral arms, most simulations from that point on have been run for that long.

Run # 36 used T_0 = 100 K, which was obviously too hot to allow a sufficiently large cloud formation rate. As a result, the star formation comes also almost to a stop, see Figure 4.18. Plus, this run got terminated prematurely due to a power outage, unfortunately.

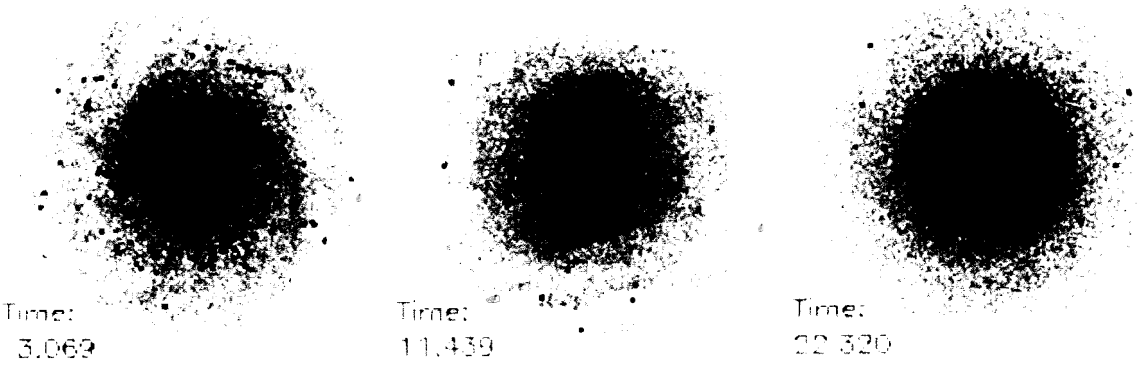

Figure 4.14: Star mass distribution of run # 33. The red dots mark the locations of newly formed stars.

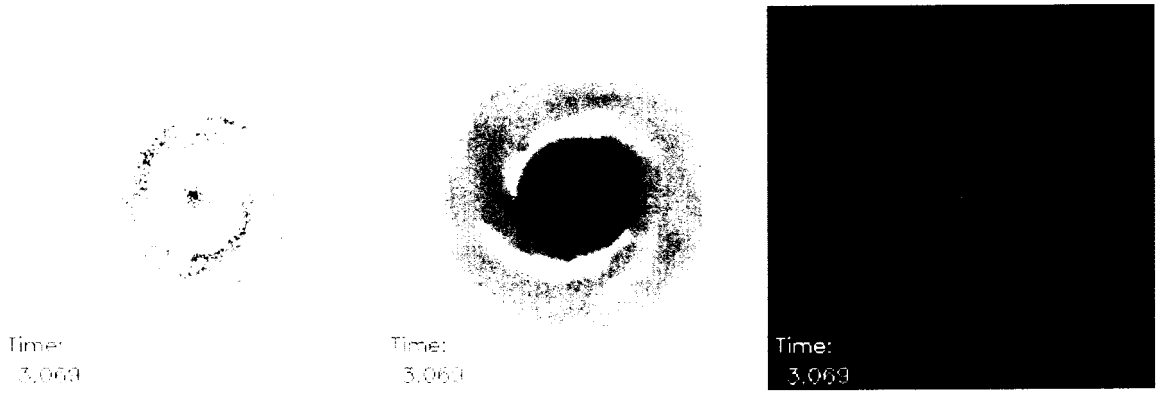

Figure 4.15: Clouds, gas, and temperature of run # 33. The clouds (left panel) show high density in the regions of star formation (compare with Figure 4.14, left panel). The gas density (middle) is thinner in those regions, because the cloud formation used up some of the gas, and because the higher temperature in those regions (right panel) drives the gas away.

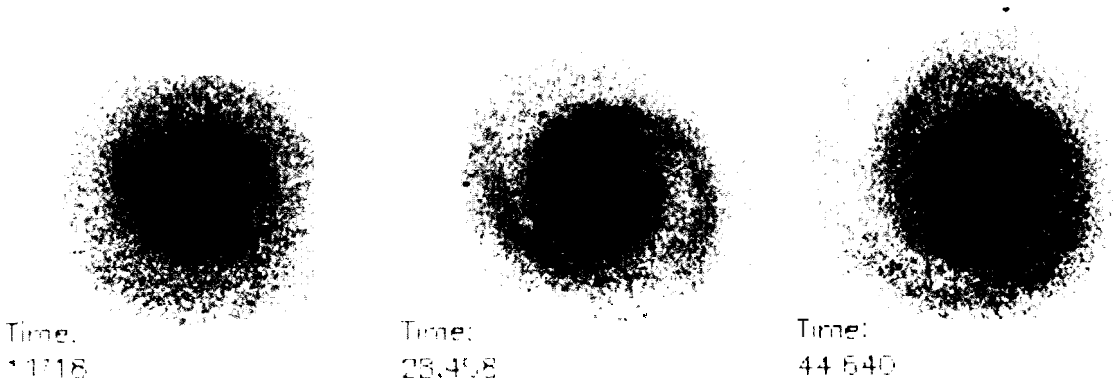

Figure 4.16: Star mass distribution of run # 37. The red dots mark the locations of newly formed stars.

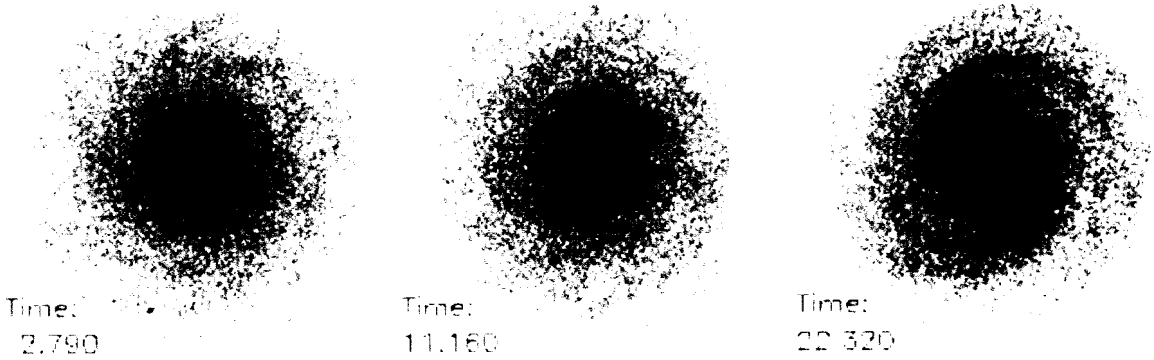

Figure 4.17: Star mass distribution of run # 35. The red dots mark the locations of newly formed stars.

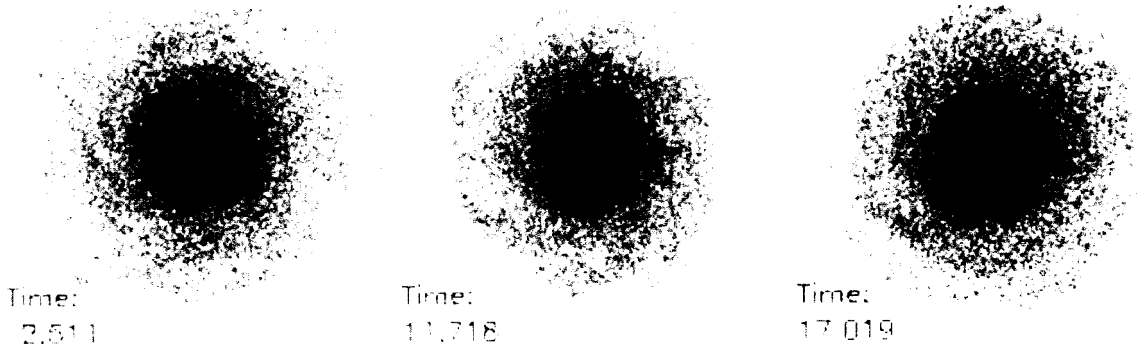

Figure 4.18: Star mass distribution of run # 36. The red dots mark the locations of newly formed stars.

Three more pairs of simulations are listed in Appendix B, in which runs differ only by the initial state of the gas (isoergic vs. isothermal), or by their initial temperature for an isothermal setup. The first of these pairs consists of run # 47 and # 48. Run # 47 uses an isothermal gas with T_0 = 2 K, and run # 48 starts with an isoergic gas and ceg = 1500. Just as before, the isothermal setup delivers the more promising result. That run starts off much cooler than the isoergic run, as a look at Figure 4.11 illustrates. The inherent differences in the development of these two runs can therefore in large part be attributed to the difference in initial temperature, rather than to the fact that one run starts isothermal, and the other isoergic. An initially cool gas will in most cases produce better results than a warm gas.

The isothermal run # 47 maintains a strong spiral structure through t = 28 revolutions (shown in Figure 4.19 is t = 22.878 revolutions). Run # 48's spiral structure is at t = 22.878 already mostly faded away (Figure 4.20). By the end of the run, both simulations evolved into a mostly featureless disk, although run # 47 has still a hint of a weak spiral arm. The fact that the locations of newly formed stars are suddenly represented by blue dots instead of red dots as before merely acknowledges that young stars are frequently very massive, very hot, and thus bluish stars. Hot and massive stars burn their fuel at a much faster rate than cooler and less massive stars, and they therefore have a much shorter life cycle. Thus, if one detects a young star, odds are good that it is also a hot (blue) and massive star. Other than that there is no reason for using blue dots instead of red dots to represent new stars.

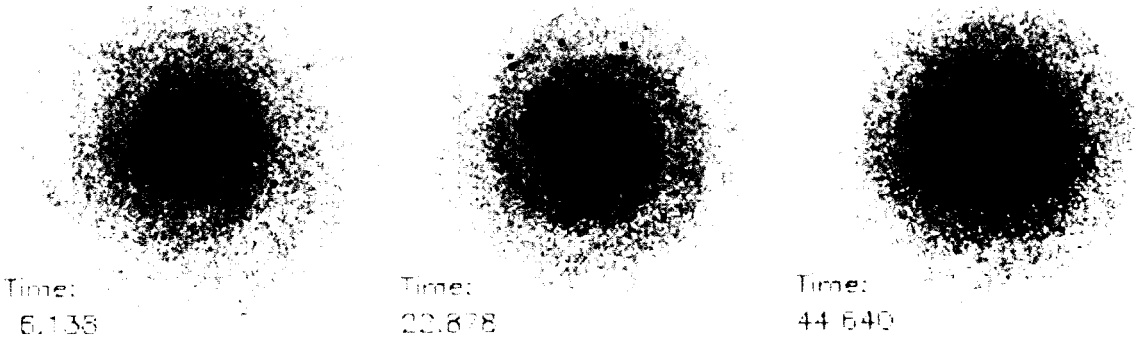

Figure 4.19: Star mass distribution of run # 47. The blue dots mark the locations of newly formed stars.

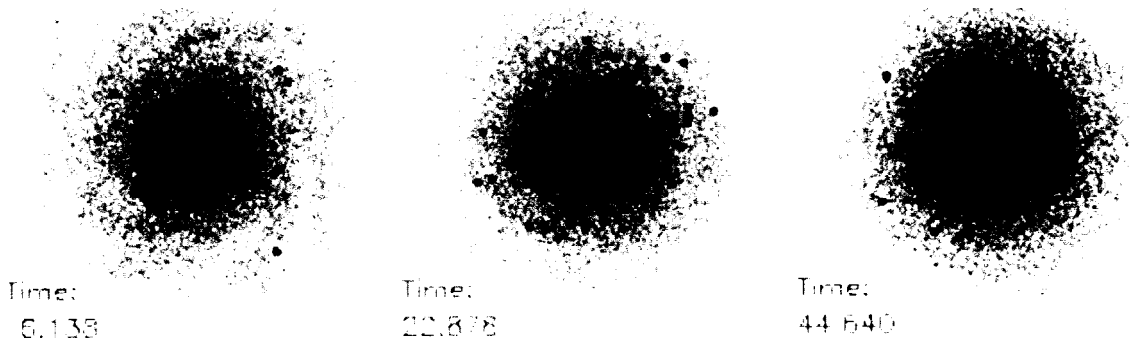

Figure 4.20: Star mass distribution of run # 48. The blue dots mark the locations of newly formed stars.

Another pair of simulations appropriate for comparison in this section are runs # 40 and # 41. Run # 40 is an isothermal run with T_0 = 10 K, and run # 41 is an isoergic run with ceg = 150. Both runs are otherwise identical, and they are listed here although they have most evolution processes switched off. The only evolution process switched on in these runs is the halo infall. What makes these two runs so exciting is that they both display among the strongest and longest lasting spiral structures seen in any simulation with the GALAXY program. At the end of the simulations at time t = 44.64 revolutions, both runs maintain very strong spiral arms (see Figures 4.21 and 4.22. The apparent different size of the stellar disk in Figure 4.22 is merely due to a different scaling factor for the images). What's more, the strength of those spiral arms continues to increase until the very end of the runs. The Fourier amplitudes for both runs show strong and increasing m = 1 and m = 2 modes (Figures C.27 and C.28). In the development of Toomre's Q, both runs rise to just over Q = 5 before flattening out. Because halo infall is the only evolutionary process, the gas mass fraction increases continuously throughout the runs, rising to 20 times its starting value of 0.02. The halo mass fraction is reduced accordingly, it falls to 0.42 by the end of the runs.

The two runs develop remarkably similarly. There is no particular difference detectable that could be attributed to the fact that one of the two runs starts isothermally (run # 40), and the other one isoergically (run # 41). The major contributor to the prolonged spiral structures observed in these runs is the rather high value of

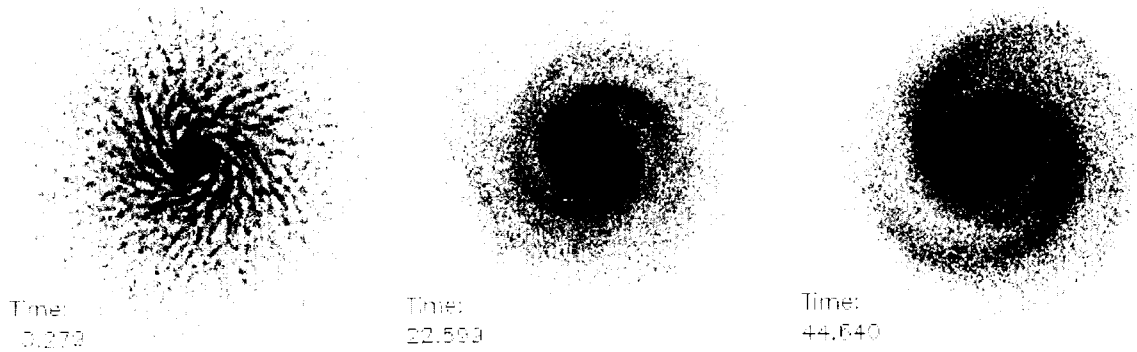

Figure 4.21: Star mass distribution of run # 40.

Figure 4.22: Star mass distribution of run # 41.

the infall rate ($\mathcal{P}_{in}$ = 1.0). In a section later in this chapter the influence of the infall rate will be investigated further.

As a last comparison in this section we'll look at two isothermal runs that differ only in their initial temperature. Run # 38 has T_0 = 10 K, and run # 49 has T_0 = 2 K. Run # 38, the warmer of the two runs, develops spiral arms and maintains them until the end of the simulation (Figure 4.23). Both the m = 1 and the m = 2 Fourier modes confirm with their strength the presence of these spiral arms (Figure C.25). The cooler run # 49 also develops spiral features, but they are much weaker than in run # 38 (Figure 4.24). The spiral arm in this run is strongest about half way through the simulation (the m = 1 Fourier mode peaks at around that time, see Figure C.36). At the end of the run the spiral arms are still visible, but they have clearly faded. This pair of simulations deviates from the general observation that initially cooler gas results in longer lasting spirals than initially warmer gas. It is the combination of warm gas with a large cloud formation probability $\mathcal{P}_{cfrc}$ = 1.0 that works well for run # 38. The decreased susceptibility for cloud formation through Jeans collapse of the warm gas is compensated by the high cloud formation probability.

Run # 38 displays interesting behavior in its clouds' Toomre's Q. It increases during the first quarter of the simulation, and decreases continuously thereafter. Being the warmer run of the two, its gas component is more resistant to Jeans collapse than run # 49, and run # 38's cloud mass therefore increases at a slower rate during the

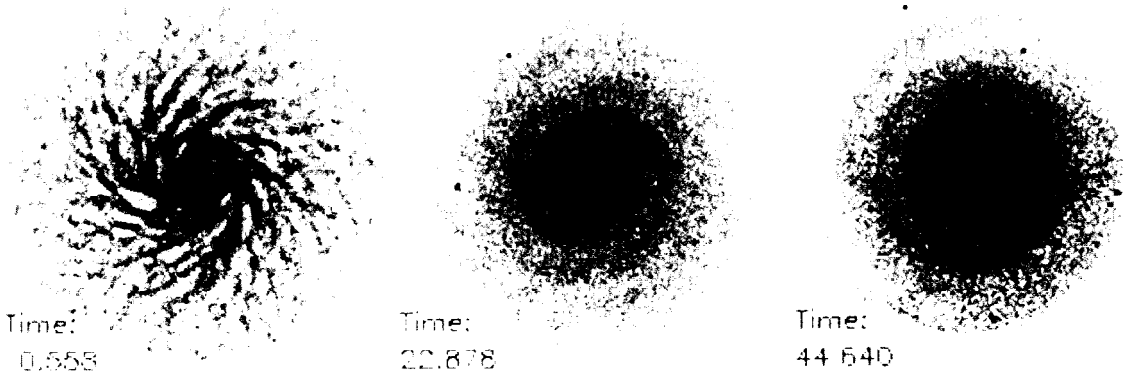

Figure 4.23: Star mass distribution of run # 38. The red dots mark the locations of newly formed stars.

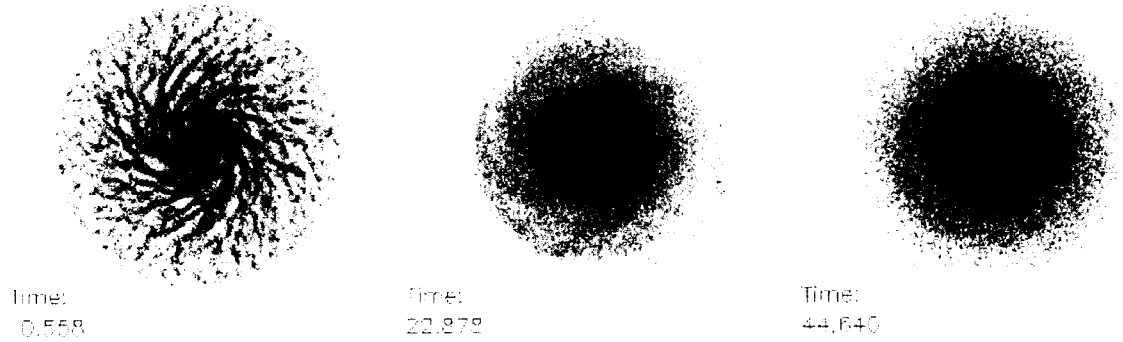

Figure 4.24: Star mass distribution of run # 49.

first half of the simulation. The gas mass, however, increases rather quickly to 14 times of its starting value. Runs # 40 and # 41, discussed above, showed a similar strong increase in the gas mass fraction, and produced exceptionally strong spiral features (Figures 4.21 and 4.22). Such high gas mass fractions do not hold up against observational evidence though (Ostriker and Peebles, 1973; Elmegreen, 1998).

The results with an initially isothermal gas were truly encouraging. So much so, that from that point on most simulations were done using an isothermal setup. The initial temperature of the gas, T_0, should probably be not more than 10 K.

4.9 Modified Cloud Formation

Section 2.3 discussed the modifications to the cloud formation through Jeans collapse routine that have been implemented into the GALAXY code. In this section I will present the results of tests performed with various versions of the cloud formation routine.

Run # 31 uses the original cloud formation routine as described by Shorey (1996). Run # 32 tried the following modification for the cloud formation probability:

$$\mathcal{P}^{\dagger} = \frac{\mathcal{P}}{(30 - r)^2} \tag{4.2}$$

Compare this with equation (2.14) in Section 2.3. Equation (4.2) is only applied for locations with $r \leq 29$. Thus, with this model the original cloud formation probability, $\mathcal{P}$, and the new cloud formation probability, $\mathcal{P}^{\dagger}$, are identical for $r > 29$. For $r \leq 29$, $\mathcal{P}^{\dagger}$ is decreased through a square law.

For run # 33 the cutoff radius was pushed out to $r = 39$, and we arrive at the cloud formation probability P' as given by equation (2.14), discussed in Section 2.3.

Figure 4.25 shows the cloud densities of the three runs at the end of the simulations. Runs # 31 and # 32 show a very dense cloud core, while run # 33's center region is not quite that populated. Run # 33 also reveals some weak spiral structure in its cloud distribution.

The effects of the modifications to the cloud formation can be seen in the star distribution, and in the formation of new stars (Figure 4.26). Most noticeable is that the "starburst ring" that develops in runs # 31 and # 32 is less sharply localized in run # 33. The central region of the disk is also not as densely populated by stars in that run. The total rate of star formation is about the same in each of the three runs compared here. All three runs ended up as a mostly featureless disk, but run # 33 developed a more detailed and slightly longer lasting spiral than runs # 31 and # 42. The $m = 1$ Fourier mode of run # 33 is consistently a little bit higher than the corresponding mode of the other two runs.

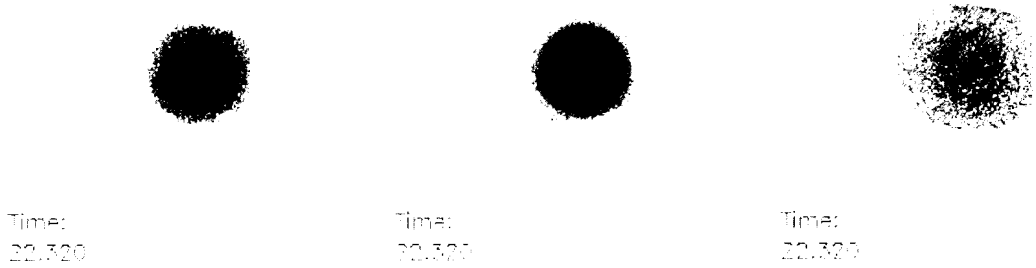

Figure 4.25: Cloud mass distribution of runs # 31, # 32, and # 33.

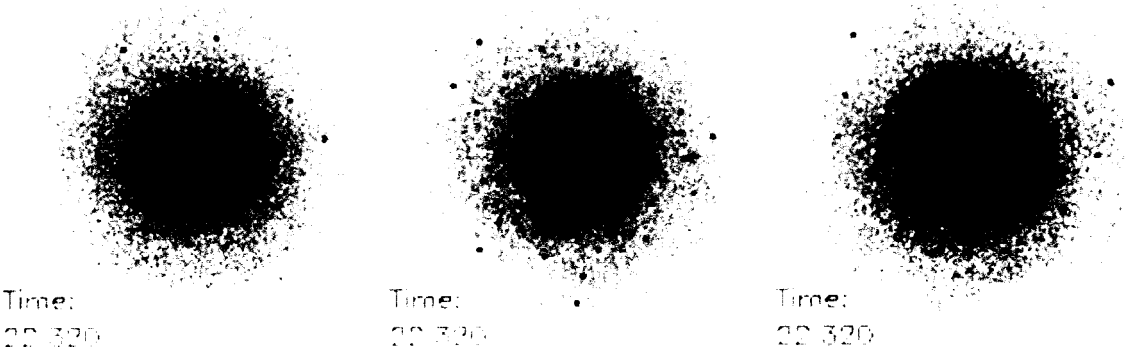

Figure 4.26: Star mass distribution of runs # 31, # 32, and # 33. The red dots mark the locations of newly formed stars.

After these tests, the cloud formation model given by equation (2.14) was adopted for most of the remaining runs. Unless otherwise noted, the runs up to # 31 utilize the original cloud formation routine, while from run # 33 on, the modified model was used. It should be stressed again that its usage is based merely on empirical findings. The original cloud formation routine produced a very dense cloud population in the galaxy center. The high cloud density in the center in turn resulted in very active star formation, leaving the overall shape of the resulting disks mostly featureless. The star formation with the old model was mostly concentrated around a thin circular region around the galaxy core, which gradually expanded outwards, as the dense region slowly increased in size.

4.10 Star and Cloud Formation Rates

The rates at which the GALAXY code produces new stars and clouds can be tweaked through the following parameters:

- $\mathcal{P}_{cfrc}$ for the probability of cloud formation by Jeans collapse
- $\mathcal{P}_{sfcrc}$ for the probability of star formation by cloud collision
- $\mathcal{P}_{sfsp}$ for the probability of star formation by the snowplow effect

These parameters have been explained in Section 4.1 and they have been discussed more thoroughly by Schroeder (1989) and Shorey (1996).

4.10.1 Cloud Formation Rate

$\mathcal{P}_{cfrc}$ has been given more attention than the other two parameters because the cloud formation rate also directly influences the star formation rate through cloud collisions. It is therefore expected that a higher cloud formation rate results in an increase in star formation, even with $\mathcal{P}_{sfcrc}$ kept constant.

Variations in the cloud formation probability have been tested with runs # 14 ($\mathcal{P}_{cfrc}$ = 0.5), # 18 ($\mathcal{P}_{cfrc}$ = 1.0), # 19 ($\mathcal{P}_{cfrc}$ = 0.1), and # 25 ($\mathcal{P}_{cfrc}$ = 0.0). None of these runs uses the cloud formation model given by equation (2.14). These simulations had been done before this modification was introduced into the code. They display therefore the now familiar dense core in both the stellar and cloud distributions, as seen for example in Figure 4.1 for run # 14, and also in Figure 2.2. An exception to this observation is run # 25, which has cloud formation suppressed altogether ($\mathcal{P}_{cfrc}$ = 0.0). This run is therefore instructive to study how the cloud population behaves when its supply has been cut off.

Figure 4.27 illustrates how the cloud population migrates towards the center of the galaxy during this simulation. The clouds' angular momentum decreases during this process (Figure C.12). Generally, when new clouds are formed, they are placed in nearly circular orbits, which keeps the angular momentum of the clouds up and also helps in the cooling of the cloud population. The lack of cloud formation in run # 25

causes the observed decrease in angular momentum, and also the extreme increase in the clouds' Toomre's Q.

The other three runs studied here develop remarkably similarly, despite the fact that the cloud formation probability $\mathcal{P}_{cfrc}$ differs by a factor of 10 between run # 18 and run # 19. Particularly surprising in this context is the almost synchronous increase in the cloud mass in these simulations (Figures C.5, C.6, and C.12). The only conclusion – if any – that can be drawn from this is that at least for this set of input parameters a cloud formation probability $\mathcal{P}_{cfrc} < 0.1$ should be chosen. Between two time steps, the properties of the gas in a cell will not change significantly. If a gas portion satisfies the conditions for Jeans collapse at time step t_n, and the cloud formation doesn't occur at that time step because of failure of the probability test, then chances are good that the same gas portion will still satisfy the Jeans condition at time step t_{n+1}. Another probability test will then determine if the gas portion is ripe for collapse this time around. For $\mathcal{P}_{cfrc} = 0.1$, there is a more than 50% chance that cloud

Figure 4.27: Cloud mass distribution of run # 25.

formation occurs within the first seven time steps after the Jeans condition has been met: $1 - (1 - \mathcal{P}_{cfrc})^7 \approx 0.52$. Therefore, with $\mathcal{P}_{cfrc} \geq 0.1$, a gas portion that satisfies the Jeans criteria will most likely eventually collapse.

It should be stressed again that the runs discussed here use the old cloud formation model, and they use an initially isoergic gas. Tests described in previous sections have indicated that both properties have more satisfying alternatives: the modified cloud formation given by equation (2.14), and an isothermal gas rather than an isoergic gas.

There is one more pair of simulations that differs only by their cloud formation rate. The two simulations in question are run # 35 (with $\mathcal{P}_{cfrc}$ = 0.5) and run # 38 (with $\mathcal{P}_{cfrc}$ = 1.0). They make use of the new cloud formation model, and they start with an isothermal gas. Both runs have already been discussed in a different context in Section 4.8, where they have been compared to an isoergic simulation (run # 35), or to a simulation with another initial temperature of the isothermal gas (run # 38), respectively. Figures 4.17 and 4.23 show their stellar density distributions. Figures C.22 and C.25 display some of their other properties. The two runs resemble each other in many ways:

- They develop strong spiral structures and maintain them until the end of the simulations (note that # 35 runs only half as long as run # 38).

- The spiral structure corresponds to a strong m = 2 Fourier mode. Additionally, run # 38 maintains also a strong m = 1 mode, which is not the case for run # 35.

- Their clouds' Q increases for the first 10 or 12 revolutions, and decreases thereafter. At about the same time the cloud mass starts to increase, supporting the earlier made point that cloud formation cools the cloud population.

The fact that it takes both runs about 12 to 15 revolutions before cloud formation kicks in can be attributed to the fact that the isothermal gas is relatively warm at 10 K in both runs. Compare this with the runs presented earlier in this section, which used a cooler isoergic gas at ceg = 150 (see Figure 4.11 for the corresponding temperature map). For this warmer gas, the Jeans condition for collapse is not as easily met as for the cooler isoergic runs mentioned above. Obviously, it requires those 12 to 15 revolutions until portions of the gas have sufficiently cooled down to succumb to the Jeans collapse. For that reason, and in combination with a relatively high infall rate of $\mathcal{P}_{in}$ = 1.0, the gas mass increases continuously in runs # 35 and # 38. For the set of input parameters employed in these runs, a cloud formation probability of up to $\mathcal{P}_{cfrc} \leq 0.5$ seems justified, because the cloud mass of run # 35 has increased by only about 25% at the end of the simulation.

4.10.2 Star Formation Rate (i): From Cloud Collisions

The influence of the star formation from cloud-cloud collisions is studied in two different pairs of simulations. Each pair uses a different set of input parameters, but the two runs in each pair are identical except for their star formation by cloud collision probability, $\mathcal{P}_{sfcrc}$. The first pair we'll look at are runs # 14 with $\mathcal{P}_{sfcrc}$ = 0.1, and # 21 with $\mathcal{P}_{sfcrc}$ = 0.2.

Due to the higher value for $\mathcal{P}_{sfcrc}$, run # 21 has an overall higher star formation rate than run # 14 (see Figures C.1 and C.8). By the end of the run, its star mass has increased by some 12% since the start of the simulation, compared to a roughly 4% increase in run # 14's stellar mass. Consequently, the stars' Q climbs at a smaller rate than in run # 14. It arrives at just over Q = 5 in run # 21, and at just over Q = 6 in run # 14. This is because newly formed stars are placed in nearly circular orbits, and they have therefore a small velocity dispersion and help cool the disk.

The higher star formation of run # 21 can be seen in Figure 4.28 (compare with Figure 4.9 for run # 14). No qualitative difference in the development of spiral arms is detectable. Either visually from the star density plots, or from the Fourier amplitudes.

Another pair of simulations differing only by their star formation through cloud collision probability, are run # 50 with $\mathcal{P}_{sfcrc}$ = 0.1, and run # 51 with $\mathcal{P}_{sfcrc}$ = 0.03.

The rather low values for $\mathcal{P}_{sfcrc}$ in these runs have been chosen because for the low temperature gas (isothermal at 2 K) combined with the high cloud formation probability ($\mathcal{P}_{cfrc}$ = 1.0) we expect to observe a high cloud formation rate through Jeans collapse, and subsequently a high cloud-cloud collision rate. Figures C.37 and C.38 confirm the high cloud formation rate through the increase in cloud mass (7-fold, and 8-fold, respectively). This high cloud formation rate helps keep the cloud population cool, by placing newly formed clouds in nearly circular orbits with a low velocity dispersion. Q_{cloud}, therefore, increases only to a rather moderate extent in both runs.

The clouds' Fourier amplitudes show an increase in the m = 2 mode towards the ends of both runs. The m = 2 mode is an indicator for bar formation, and a look at the cloud distribution in both cases (Figures 4.29 and 4.30) confirms the presence of a small elongated bar-like feature in the galaxy center.

The small values for the star formation by cloud collision probability chosen for these runs takes its toll on the star population. In run # 50 the star mass increases by not more than about 5% at the end of the simulation. For run # 51, with the small value of $\mathcal{P}_{sfcrc}$ = 0.03, the star mass even drops by about 12%. Star mass is lost in two ways during a GALAXY run: through a supernova (mass is given off to the ISM), and when a star particle with a large radial velocity component manages to reach the edge of the simulation grid and escapes. In the latter case the total galaxy mass is reduced accordingly.

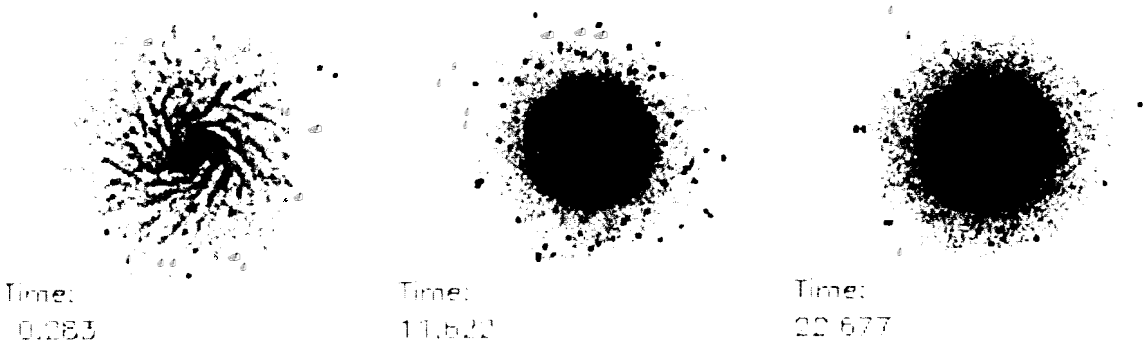

Figure 4.28: Star mass distribution of run # 21. The red dots mark the locations of newly formed stars.

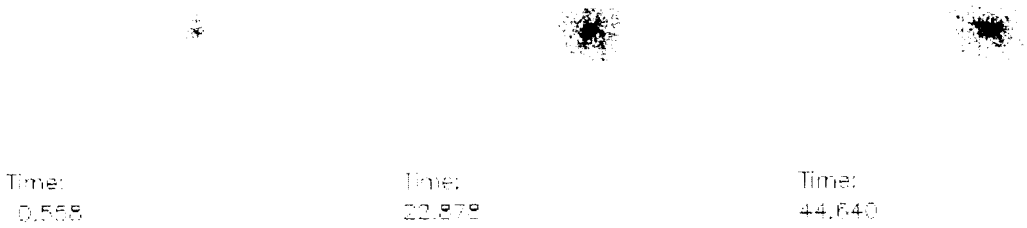

Figure 4.29: Cloud mass distribution of run # 50.

In contrast to the clouds, which are kept relatively cool by a high formation rate, the low star formation rate cannot aid in cooling the star population. For these two runs, we witness among the largest increases in the stars' Q seen in any run done for this dissertation. This is particularly true for run # 51 with its very low star formation through cloud collision probability of $\mathcal{P}_{sfcrc}$ = 0.03, where Q climbs to above 15. The stellar distribution in both runs goes through an intermediate phase with pronounced spiral structures and accompanying strong m = 1 and m = 2 Fourier modes. This spiral structure fades slowly away after t = 35 revolutions, and is mostly gone by the end of the simulations. The stellar distribution for run # 51 is shown in Figure 4.31. For run # 50 it looks very similar.

4.10.3 Star Formation Rate (ii): From Snowplow

The star formation through the snowplow effect was probed with two different values of its formation probability $\mathcal{P}_{sfsp}$. Run # 14 used $\mathcal{P}_{sfsp}$ = 0.1, and run # 30 disabled the star formation through snowplow altogether: $\mathcal{P}_{sfsp}$ = 0.0. Using $\mathcal{P}_{sfsp}$ = 0.0 and $\mathcal{P}_{sfsp}$ = 0.1 seemed appropriate for initial tests with the star formation through snowplow, because in earlier tests with this parameter its useful range was determined to be between 0.005 and 0.04 (Shorey, 1996). With $\mathcal{P}_{sfsp}$ = 0.0 and $\mathcal{P}_{sfsp}$ = 0.1 the upper and lower limits of this range got pushed a little bit further.

Cutting off the star formation through the snowplow effect in run # 30 foremost results in a slightly higher cloud mass. This is understandable, because when the

Figure 4.30: Cloud mass distribution of run # 51.

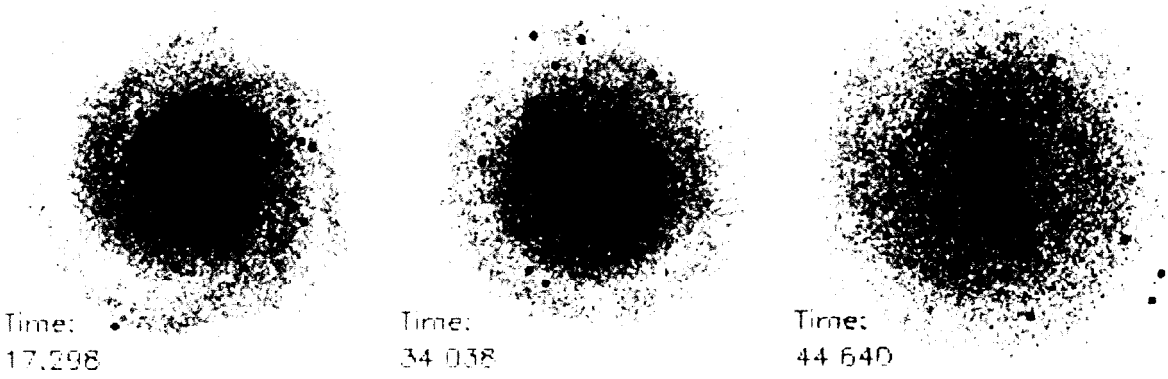

Figure 4.31: Star mass distribution of run # 51. The blue dots mark the locations of newly formed stars.

snowplow effect is enabled, then cloud mass is converted to star mass every time a star is created through this effect. The difference in cloud mass at the end of run # 14 compared to run # 30 is rather low, however (see Figures C.l and C.17). This indicates that the snowplow effect produced only a small number of stars in run # 14. Each star formation through snowplow also blows some mass into the ISM. The gas mass in run # 30, therefore, increases only slightly. Mass gain from the infall and mass loss from the cloud formation are nearly balanced in the second half of the run. In run # 14 the gas mass increases by 60% at the end of the simulation, due to the additional mass the ISM receives from the snowplow. Apart from this there are no noteworthy differences. Within the probed range, a variation of $\mathcal{P}_{sfsp}$ has no significant impact on the simulations. Schroeder used the Kuz'min disk for most of his simulations, rather than the SC disk (Schroeder, 1989), and he reported a stronger influence of the star formation through snowplow probability than what was observed here. Compared to the star formation through cloud collisions, the star formation through the snowplow effect was found to have a relatively minor effect.

4.11 Energy Deposit to the ISM

Some of the evolutionary processes in the GALAXY code – namely cloud formation from gas through Jeans collapse, star formation through cloud collision or through snowplow, and supernovae – have the potential to deposit energy into the ISM and increase the energy density in the grid cell in which the respective process takes

place. The momentum of the gas is updated separately. Therefore, the added energy increases the *internal* energy of the gas. Energy, mass, and momentum are carefully conserved during cloud formation, star formation, and supernovae. Because each of these processes generally also changes the mass density in that cell (a supernova always adds mass to the ISM, cloud formation always takes away mass from it, and cloud collision may add mass to ISM), its temperature may also be affected. The parameters which specify these energy outputs are:

- *ecform* for the energy added to the ISM by cloud formation.
- *esform* for the energy added to the ISM by star formation.
- *enova* for the energy given off by a supernova, and added to the ISM.

The tests with the energy deposits served two purposes. First, the sensitivity of the simulations to these energy outputs was investigated. Second, the robustness of the hydro code itself was put to the test. In the past, the hydro code would occasionally cause problems when gradients in the hydro variables became too steep (see Section 2.6). Specifically to address the latter issue, runs were performed where *ecform*, *esform*, and *enova* were first set to zero, and then deliberately to an unrealistically high value. Shorey (1996) performed similar tests for the Kuz'min disk, depositing not more than 100 energy units to the ISM.

Run # 14 has *ecform*, esform, and *enova* set to zero. For each of the energy deposit parameters, one simulation was performed in which one of them was set to a non-zero

value. Run # 24 uses esform = 150, run # 29 uses *enova* = 15, and run # 56 uses *ecform* = 100. The first two (runs # 24 and # 29) differ only by their energy deposit parameter from run # 14 and are therefore compared to this run. The latter (run # 56) uses a completely different set of input parameters from run # 14 and can therefore not readily be compared with it. Instead, run # 56 is compared to run # 46, which has *ecform* = 0 and is otherwise identical to run # 56.

The first two simulations to be studied in this section, run # 14 with esform = 0 and run # 24 with esform = 150, develop very similarly to each other. The stellar distribution and the star formation, shown in Figure 4.9 for run # 14, looks qualitatively the same for run # 24. A noteworthy difference is the mass development of the gas (Figures C.l and C.11). Due to the energy deposit to the ISM in run # 24, the pressure of the gas increases, pushing portions of the gas off the simulation grid. Therefore the gas mass of run # 24 stays nearly constant for most of the simulation. The fact that the gas mass increases in the first place is due to the continuous halo infall to the ISM. The higher energy content of the gas in run # 24 causes the produced clouds to be hotter (see Toomre's Q for clouds) and to carry more angular momentum than in run # 14.

The next comparison showcases once again run # 14 (*enova* = 0) and teams it up with run # 29 (*enova* = 15). The conclusions drawn from this comparison are mostly the same as from the previous one. The resulting stellar disk develops qualitatively

the same for the two runs. They differ essentially in the gas mass development, with the subsequent consequences for the clouds' Q, and the clouds' angular momentum, as explained above (Figures C.1 and C.16).

The test of $ecform$ with run # 46 ($ecform$ = 0) and run # 56 ($ecform$ = 100) paints a slightly different picture, though. The gas mass in the run with energy deposit is a few percent higher than in the run without energy deposit (Figures C.33 and C.43). These two runs use a rather high value for the star formation through cloud collision probability, $\mathcal{P}_{sfcrc}$ = 1.0. Since every star formation through cloud collision also releases some mass to the ISM, the gas mass increase in these two runs is higher than in the runs previously discussed in this section. Run # 56 may be more effective in the cloud-cloud collision process, because the clouds are produced from gas with higher energy, due to the energy deposit from star formation. Therefore the produced clouds attain higher velocities, making collisions between clouds happen more frequently.

Fortunately, the GALAXY code proved to be stable even when the gradients in the hydro variables got artificially increased through the ISM energy deposits discussed in this section. Furthermore, the outcome of the simulations indicated little sensitivity to variations in these energy deposit parameters. A value of zero compared to a value of 150 energy units made little difference. Note that the value of 150 energy units was chosen because in most isoergic runs discussed in this chapter, the initial energy density of the gas, ceg, was also set to 150. With that observation, most simulations

were done with all three energy deposit parameters set to zero. Doing so saves a little bit of execution time because the respective routines of the GALAXY program are bypassed.

4.12 Infall Rate

The infall from the halo onto the gas helps cooling the disk, and may therefore play a significant role in maintaining prolonged spiral structures in galaxies. How significant its importance is shall be studied in this section.

Run # 47 uses an infall rate of $\mathcal{P}_{in}$ = 0.5, run # 49 uses $\mathcal{P}_{in}$ = 1.0, run # 50 uses $\mathcal{P}_{in}$ = 1.5, and run # 53 uses $\mathcal{P}_{in}$ = 0.375.

Obviously, the higher the infall rate, the more mass is eventually accumulated onto the gas. Figures C.34, C.36, C.37, and C.40 confirm this. We can also see from the "Normalized Mass" plot, that the higher the infall rate, the earlier the cloud mass starts to increase. This is no surprise, because the higher the mass of a gas portion, the more likely is it for this gas portion to undergo Jeans collapse and form a cloud. Plus, due to the infall's ability to cool the disk, a high infall rate will keep the gas cooler than a low infall rate. This also helps to kick off cloud formation earlier. In fact, the two runs with the highest infall rates (# 49 with $\mathcal{P}_{in}$ = 1.0 and # 50 with $\mathcal{P}_{in}$ = 1.5) cool down the gas to such an extent that the gas mass loss due to cloud formation surpasses the gas mass gain from the infall. The gas mass therefore

decreases again after t = 15, respectively t = 20, revolutions. In the two runs with the lower infall rates, the gas mass increases at a slower rate up to about t = 30 revolutions. Thereafter, the gas mass remains roughly constant for the remainder of the simulations. The gas mass loss from cloud formation and the gas mass gain from the infall are in balance here.

The more active cloud formation for higher infall rates is directly influencing Q_{cloud}. It has been pointed out earlier that newly formed clouds have a small velocity dispersion and that they therefore prevent the clouds' Q from increasing very fast.

Stellar distributions for runs # 47 and # 49 have already been shown in Figures 4.19 and 4.24. Figures 4.32 and 4.33 show it for run # 50 and for run # 53, respectively. Ail four runs discussed here develop spiral structures, but they are stronger and longer-lasting for higher infall rates. A look at their Fourier amplitudes supports this observation.

4.13 The Effects of Stellar Evolution

The ultimate test of the stellar evolution model, as implemented in the GALAXY code, is to assess how the whole system of stellar evolution processes affects the formation of spiral structures in a model galaxy. For this test we first looked at simulations which do not use any stellar evolution. The only evolutionary process enabled in these runs is the halo infall, but this process is not directly related to the

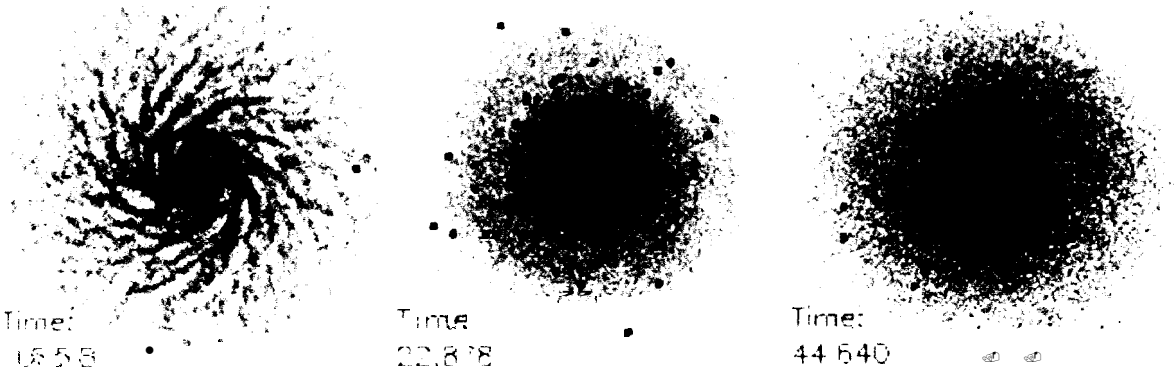

Figure 4.32: Star mass distribution of run # 50. The blue dots mark the locations of newly formed stars.

Figure 4.33: Star mass distribution of run # 53. The blue dots mark the locations of newly formed stars.

formation or destruction of either clouds or stars. These runs are then compared to simulations, which start with the same initial conditions, but use the full body of evolutionary processes.

Two evolution vs. non-evolution pairs will be studied. In one of these pairs the halo infall is set to the rather low value of $\mathcal{P}_{in}$ = 0.25, and in the other pair this infall is considerably higher: $\mathcal{P}_{in}$ = 1.0. This was done because it was determined in previous runs that a rather high infall rate favors the maintenance of prolonged spiral structures, while runs with low infall rates generally develop less distinct spiral structures, if any. The objective was to determine whether the stellar evolution strengthens, or maybe obstructs, the formation of spiral features.

The non-evolution simulations studied here are run # 40 (with $\mathcal{P}_{in}$ = 1.0) and run # 44 ($\mathcal{P}_{in}$ = 0.25). Run # 40 is compared to run # 38 which uses the same infall rate, but has stellar evolution enabled. Similarly, run # 44 is compared to its stellar evolution enabled version, run # 45.

Run # 38 and run # 40 have both been already discussed in different contexts: run # 38 in Sections 4.8 and 4.9, and run # 40 also in Section 4.8. Run # 40 produced extraordinary strong spiral features, which continued to grow until the very end of the simulation (see Figure 4.21). Run # 38, which has stellar evolution enabled, does also maintain spiral structures, but they are not as strong as in the non-evolution run # 40 (Figure 4.23). Particularly the m = 2 Fourier mode of run # 40 is considerably

stronger than in run # 38, especially in the second half of the simulation. In the m = 1 mode the difference is less pronounced, yet still visible, although run # 38's m = 1 mode picks up in the final quarter of the simulation and ends up higher than in run # 40.

Run # 40's Q for stars climbs to just over 5 at $t \approx 32$ revolutions, and oscillates then around that value, without further increasing. In run # 38 the stars' Q increases continuously, reaching $\approx$ 6.4 at the end of the simulation (see Figures C.25 and C.27). Both runs increase their gas mass considerably, due to the fairly high infall rate. Naturally, in the run with evolution enabled the gas mass does not increase as much as in the non-evolution run, because gas is converted to clouds through Jeans collapse. As previously pointed out, this cloud formation helps keep the cloud population cool, and Q_{cloud} decreases as soon as the cloud mass fraction increases at around t = 10 revolutions.

As a result of this comparison it is noted that in the case of a simulation which produces strong spiral features without stellar evolution switched on, enabling stellar evolution may apparently inhibit, or at least weaken, the formation of a spiral structure.

For the final comparison of this dissertation, we'll look at runs # 44 and # 45. Both runs have the low infall rate of $\mathcal{P}_{in}$ = 0.25, and run # 44 is the non-evolution version of run # 45. Run # 44 develops very little structure during the simulation,

a consequence of the low infall rate (see Figure 4.34). The m = 1 and m = 2 Fourier modes increase during the final third of the simulation (Figure C.31), suggesting the development of weak one-armed and two-armed structures. These features, if present, are too weak to show in Figure 4.34. Switching stellar evolution on in run # 45 results in the development of a spiral structure (see Figure 4.35). Though weak in nature, with everything else being equal, its development is exclusively due to the evolutionary processes. From about t = 20 revolutions on the m = 1 and m = 2 Fourier modes in run # 45 are slightly higher than in run # 44, except for the phase from about t = 35 to t = 40 revolutions (Figure C.32). The new stars form generally in the weak spiral arms, thus enforcing them. Also noticeable is the fact that the evolution run's disk edge is more diffuse than in the non-evolution run.

While the spiral arm developed through stellar evolution in run # 45 may be apparently weak compared to other spiral structures observed throughout this dissertation, one has to keep in mind that the newly formed stars are frequently hot and massive stars with a very high luminosity. Therefore, they have the potential to boost the brightness of their immediate neighborhood considerably, although they increase the number density of the star population in that region by only a small amount. The star mass distribution figures show surface mass density and not luminosity. They do, therefore, not take into account the brightness boost that the young and bright stars impose on their neighborhood. Figure 4.35 therefore under-represents the real surface brightness, particularly in the regions of new star formation.

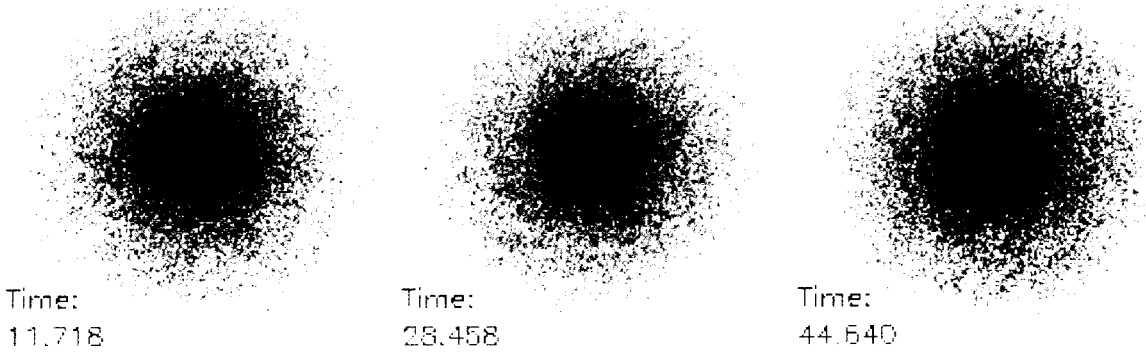

Figure 4.34: Star mass distribution of run # 44.

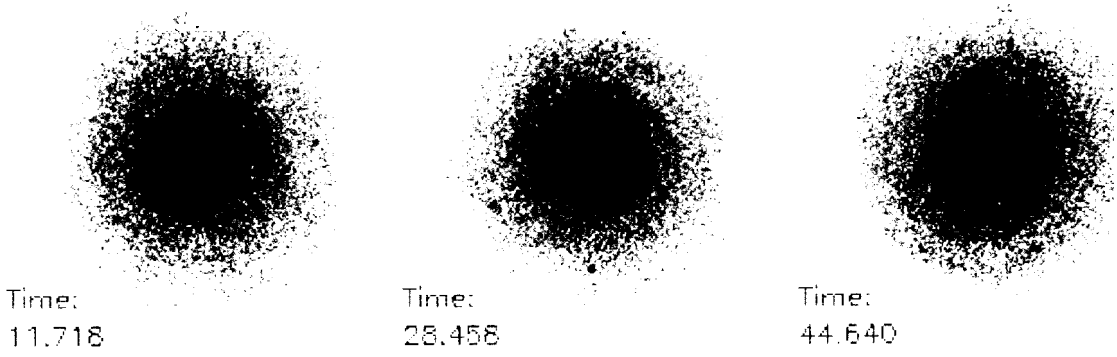

Figure 4.35: Star mass distribution of run # 45. The blue dots mark the locations of newly formed stars.

Runs # 44 and # 45 showed that the stellar evolution model of the GALAXY code may be able to trigger the formation of spiral structures in disk systems which otherwise would not develop them. This fact stands out as one of the key results of this dissertation.

5 CONCLUSIONS AND OUTLOOK

In the final chapter of this thesis, I will sum up the presented results and I will discuss the conclusions that can be drawn from them. Further, I will take a look at what's lying ahead for the GALAXY code, in terms of potential research projects, and also in terms of further code improvements.

5.1 Summary and Conclusions

The GALAXY code has proved its versatility for simulations of spiral galaxies. It is capable of producing spiral structures for well over 40 rotation periods, We used it successfully to confirm analytically derived predictions with the runs involving counter-rotating components. With stellar evolution switched on, new stars are found to be produced primarily in regions of high cloud concentration, where the formation of new stars is triggered by cloud-cloud collisions. The cloud distribution is therefore critical for realistic modeling of stellar evolution. Spiral galaxies owe their shape in part to the presence of bright massive stars in the spiral arms. The variation in the underlying star number density is generally less than the brightness of the spiral arms would suggest. Such massive stars burn their fuel at an accelerated rate compared to less massive stars. They therefore also have a shorter life cycle, and young stars are thus primarily to be found in the spiral arms, giving rise to their brightness.

The stellar evolution model of the GALAXY code can trigger the formation of spiral structures. Some simulations, which had the stellar evolution modules disabled, evolved into a mostly featureless, axisymmetric disk (these were typically runs with a small halo infall rate of $\mathcal{P}_{in} < 0.5$). When the simulations were re-initialized under the same initial conditions, and with the evolution modules enabled, then spiral features would eventually be observed. New stars form preferentially in those spiral arms, thus strengthening them further. This process is to some extent self-sustaining, because clouds are more likely to collide in the potential troughs of the spiral arms, thus providing more new stars through cloud collisions. The fact that the stellar evolution models in the GALAXY code can trigger spiral arm formation is strong evidence for the program's realistic behavior.

In non-evolution simulations which produce strong spiral features, however, the effect of the stellar evolution model can lead to a weakening of the spiral structure. The observed spiral structure in these cases is mostly the result of a quasi-stationary density wave, initiated by random density fluctuations in the disk or other external forces (Lin and Shu, 1964). In these runs, generally, there is also a lesser degree of correlation between the locations of new star formation, and the underlying spiral structure. The locations of new star formation are more uniformly distributed across the disk in these cases, and they may therefore contribute to the observed weakening of spiral structures (run # 38 vs. run # 40 in Section 4.13). In runs where the spiral arm formation is triggered by the evolution processes, this correlation is much

stronger. The halo infall rate, $\mathcal{P}_{in}$, played a critical role for the spiral arm formation in these simulations. Without stellar evolution, a high value of the halo infall rate ($\mathcal{P}_{in} \geq 1.0$) is more likely to produce spiral structures. Enabling stellar evolution in these runs weakened the spiral structure. The fact that in simulations with a low infall rate ($\mathcal{P}_{in} < 0.5$) the stellar evolution triggers the formation of spiral structures, and that new stars primarily form in those spiral arms, suggests that the halo infall in spiral galaxies is rather low. This can be tested against observations, and studies of Wakker et al. (1999), and Giovagnoli and Tosi (1995), confirm a low infall rate for our Milky Way.

Without any doubt, N-body simulations like the GALAXY code should be run with as many individual star particles as one can afford, in terms of time per simulation one is willing to invest. As the execution time T_{exec} increases with the number N of simulated particles ($T_{exec} \propto$ N log N), one has to compromise between higher accuracy and quick result output. This issue has been particularly critical when the parameter space of the GALAXY code was scoured in Chapter 4 of this thesis. With no less than 17 parameters to consider, and some 72 hours per single simulation (execution plus analysis), some of the parameters may not have received the attention that they deserved. Parameters which quickly proved to have critical impact for the simulations' outcome (like the halo infall rate $\mathcal{P}_{in}$, or the initial state of the gas), have been studied more extensively with more simulations. Other parameters, with presumably less critical influence, have been tried with only two different values.

To arrive at a quasi steady state model, the mass fractions of the individual galaxy components – stars, gas, clouds, and halo – should remain nearly constant over at least a couple of revolutions. Note that a true steady state model will not be achieved with the current version of the GALAXY program, because halo mass is continuously converted to gas through the infall process. There is no process that would return mass back to the halo. Plus, the stars, clouds, and the gas components spill some of their mass over the edge of the simulation grid. The resulting total mass loss of a simulation through spilling is typically of the order of one to a few percent. Only for an infall rate $\mathcal{P}_{in}$ = 0 could the mass fractions of all four components in theory be kept at a nearly constant level for a very long time. In practice, however, realistic infall rates in compliance with observations will limit the duration for which a substantial halo mass can be sustained, to a few tens of revolutions. The infall from the halo to the gas proved also to be an effective coolant to the model and supports the formation of prolonged spiral structures.

5.2 Suggested future Work

While the GALAXY code itself has certainly plenty of room for improvement, the present version is certainly good enough for serious research. As with any model, a major aspect of any use of the GALAXY code must always be the connection to observations. With that in mind, the code can be used to make predictions about real galaxies' behavior under certain conditions, as well as to aid in understanding of

some observational findings. Chapter 3 of this thesis gives some examples of where the code has been successfully used to model some real galaxies' behavior, and two scientific publications (Comins et al., 1997; Zeltwanger et al., 2000) are evidence for the code's potential. In this last section of my dissertation I will outline some possible future research projects with the GALAXY code, and I will suggest some further code improvements.

Two independent research groups have already expressed their interest for future collaborations involving the GALAXY code: Gregory D. Bothun (University of Oregon) would like to use the code to find the range of mass ratios between luminous and non-luminous material inside a certain radius which is consistent with some Fabry-Perot data on the velocity field of late type spiral galaxies. Dr. Bothun presents evidence that the best fitting rotation curves, for some cases, are obtained by allowing the center of the fit to vary (Beauvais and Bothun, 1999). He found a kinematic sloshing motion of the velocity field, similar to the center of mass sloshing motion presented in Sections 3.3 and 3.4 of this thesis, and in our second publication (Zeltwanger et al., 2000).

Another group (Steve Gottesman, University of Florida) is studying one-armed spirals in galaxies, and has expressed interest in using the GALAXY code to model some of the intriguing peculiarities found in NGC 772, NGC 5291, and NGC 7479 (Malphrus et al., 1997; Laine and Gottesman, 1998).

Other future projects might take the simulations discussed in Chapter 3 of this thesis, and try them with stellar evolution switched on. It will be particularly exciting to see if the one-armed spiral waves in the stellar distribution, which we observed in the simulations with counter-rotating components, will also occur in the gas and cloud distributions. If so, then new stars are expected to form primarily along the very same one-armed spiral.

As far as code improvements are concerned, it is my belief that the addition of a third dimension is essential for some kinds of simulations, especially for a more realistic modeling of galaxy interactions. For the latter, it would also be desirable to be able to model an intruder galaxy as an extended object rather than a point mass. At present, a "low-tech" version of interactions between two extended galaxy models can be realized by using a certain fraction of counter-rotating components, and offsetting the co-rotating components separately from the counter-rotating components. That way, two interacting galaxies with opposite angular momentum would be simulated.

The gas in real galaxies has a minimum temperature of 2.7 K, due to the microwave background radiation. The GALAXY program currently does not take this into account, and the gas temperature is allowed to drop below 2.7 K. A future version of GALAXY should include such a minimum gas temperature.

A more realistic representation of the appearance of a galactic disk can be achieved by taking into account the ages and masses of the individual star particles. That

way, the young, hot, and massive stars in the spiral arms will visibly enhance spiral structures. The necessary information is already available for every GALAXY run, but it is presently not taken into account.

The halo infall is currently modeled in a way that maximizes its effect on the formation and maintenance of density perturbations (i. e. spiral structures). This is achieved by transferring cold gas from the halo to the disk. More specifically, the infalling gas is set to the same thermal properties that the gas had at the beginning of the simulations. A more realistic modelling of the infalling gas should be implemented.

The hydrodynamic portion of the code behaves satisfactory with the new smoothing algorithm. Unsatisfactory remains the fact that such an artificial smoothing scheme is necessary to control the gas. In future versions of GALAXY – particularly when it is extended to three dimensions – one might want to consider replacing the hydrodynamics portion of the code with a more modern algorithm, like "Smooth Particle Hydrodynamics" (SPH) .

To better understand how the various evolution processes of the GALAXY program interact with each other, a more thorough probing of its parameter space than is presented in this dissertation may be necessary. Due to the amount of time that this would require this may not be practical, however, because it would delay the production of research results. If there will ever be several equally powerful computers available, then it would be advisable to set one or two of those aside to continue the

mapping of GALAXY's parameter space in greater detail. The IDL scripts developed for this dissertation analyze most of the data automatically, and do not require any further supervision from the GALAXY user.

It has been pointed out on several occasions that the number of stars N is an essential parameter for realistic behavior of the simulations. Thus, to run simulations with a large N in a reasonable amount of time, the code should run on very fast computers with a lot of memory, preferably on a parallel computer. Porting the code to a parallel machine will, however, require a considerable amount of coding effort.

A large number of stars N would not only require a longer execution time of the code, it would also take its toll on the analysis of the produced data, particularly for the star particle plots, or for the grayscale images of the star mass density. This part of the analysis could be sped up significantly by including only a fraction of the stars in the analysis. Qualitatively there will be little, if any, difference in the appearance of the resulting images. The necessary changes in the IDL routines should be straightforward.

REFERENCES

Arp, H.: 1966, *"Atlas* of Peculiar Galaxies", Pasadena: California Inst. Technology, 1966

Athanassoula, E.: 1996a, in ***Barred Galaxies, IAU Colloquium 157,*** Vol. 91 of ***ASP Conference Series***

Athanassoula, E.: 1996b, in ***Barred Galaxies and*** Circumnuclear ***Activity,*** Vol. 474 of ***Lecture Notes in Physics***

Athanassoula, E. and Bureau, M.: 1999, ***The Astrophysical Journal 522, 699***

Baldwin, J. E., Lynden-Bell, D., and Sancisi, R.: 1980, ***Mon. Not. R. Astron.*** *Soc.* 193, 313

Batuski, D. J.: 2000, private communication

Beauvais, C. and Bothun, ***G.:*** 1999, ***The Astrophysical Journal Supplement*** 125, 99

Bertola, F., Cinzano, P., Corsini, E. M., and Pizzella, A.: 1998, ***The Astrophysical Journal Letters 458,*** L67

Binney, J. and Tremaine, S.: 1987, ***Galactic Dynamics,*** Princeton Series in Astrophysics, Princeton University Press, Princeton

Bosma, A.: 1981, ***The Astronomical Journal 86,*** 1825

Bosma, A.: 1999, in D. R. Merritt, M. Valluri, and J. A. Sellwood (eds.), Galaxy ***Dynamics, proceedings of a conference held at Rutgers University,*** Vol. 182 of ***ASP Conference Series***

Carlberg, R. G. and Freedman, W. L.: 1985, ***The Astrophysical Journal 298, 486***

Casoli, F. and Combes, F.: 1982, Astronomy *&* ***Astrophysics*** 110, 287

Chieze, J. P. and Lazareff, B.: 1980, ***Astronomy & Astrophysics*** 91, 290

Comins, N. F., Lovelace, R. V. E., Zeltwanger, T., and Shorey, P.: 1997, ***The Astrophysical Journal Letters 484,*** L33

Conselice, ***C.*** J.: 1997, *Publ.* ***Astron.*** *Soc.* ***Pac.*** 109, 1251

Cowie, L. L.: 1980, ***The Astrophysical*** Journal 236, 868

Davidge, T. J., Rigaut, F., Doyon, R., and Crampton, D.: 1997, *The* Astronomical ***Journal*** 113, 2094

de Vaucouleurs, G. and Pence, W. D.: 1978, ***The Astronomical Journal 83,*** 1163

Elmegreen, B. G.: 1992, in G. Tenorio-Tagle, M. Prieto, and F. Sanchez (eds.), *Star* ***Formation in Stellar Systems,*** p. 381, Cambridge University Press

Elmegreen, B. G., Kaufman, M., and Thomasson, M.: 1993, ***The Astrophysical Journal*** 412, 90

Elmegreen, B. G., Kimura, T., and Tosa, M.: 1995, ***The Astrophysical Journal*** 451, 675

Elmegreen, D. M.: 1998, Galaxies *&* ***Galactic Structure,*** Prentice-Hall, Inc.

Englmaier, P. and Shlosman, I.: ***2000, The Astrophysical Journal 528, 677***

Faber, S. M. and Gallagher, J. ***S.:*** 1979, ***Ann. Rev. of Astron. and Astroph.*** 17, 135

Ferrarese, L., Ford, H. C., and Jaffe, W.: 1998, in ***The Central Regions of the Galaxy and Galaxies,*** Vol. 184 of ***IA U Symposium,*** p. 445

Freeman, K. ***C.:*** 1970, ***The Astrophysical Journal*** 160, 811

Fukuda, H., Habe, A., and Wada, K.: 1999, in ***Numerical Astrophysics,*** p. 73

Fux, R.: 1999a, ***Astronomy & Astrophysics 345, 787***

Fux, R.: 1999b, in D. R. Merritt, M. Valluri, and J. A. Sellwood (eds.), Galaxy ***Dynamics, proceedings of a conference held at Rutgers University,*** Vol. 182 of ***ASP Conference Series***

Gates, E. I. and Gyuk, ***G.:*** 1999, in ***American Astronomical Society Meeting,*** Vol. 195, p. 2901

Gerola, H. and Seiden, P. E.: 1978, ***The Astrophysical Journal*** 223, 129

Giovagnoli, A. and Tosi, M.: ***1995, Mon. Not. R. Astron.*** *Soc.* ***273, 499***

Green, A. M.: ***2000, The Astrophysical*** Journal 537, 708

Hozumi, S. and Hernquist, L.: 1999, in D. R. Merritt, M. Valluri, and J. A. Sellwood (eds.), Galaxy ***Dynamics, proceedings*** *of* ***a conference held at Rutgers*** **University,** Vol. 182 of ***ASP Conference Series***

Jore, K. P., Broeils, A. H., and Haynes, M. P.: 1996, The ***Astronomical Journal*** **112, 438**

Jungman, G., Kamionkowski, M., and Griest, K.: 1996, Physics Reports 267, 195

Karachentsev, I.: 1987, ***Moscow*** *Izdatel Nauka*

Koopmans, L. V. E. and de Bruyn, A. G.: 2000, ***Astronomy & Astrophysics 358, 793***

Korchagin, V. and Theis, C.: 1999, ***Astronomy & Astrophysics 347, 442***

Kuchling, H.: 1988, ***Tuschenbuch der Physik,*** Verlag Harri Deutsch, Thun und Frankfurt/Main, 10th edition

Laine, S. and Gottesman, ***S.*** T.: 1998, ***Mon. Not. R. Astron.*** *Soc.* ***297,*** 1041

Lauer, T. R., Faber, S. M., Groth, E. J., Shaya, E. J., Campbell, B., Code, A., Currie, D. G., Baum, W. A., Ewald, S. P., Hester, J. J., Holtzman, J. A., Kristian, J., Light, R. M., Ligynds, C. R., O'Neil, Jr., E. J., and Westphal, J. A.: 1993, ***The Astronomical Journal*** **106, 1436**

Lauer, T. R., Tremaine, S., Ajhar, E. A., Bender, R., Dressler, A., Faber, S. M., Gebhardt, K., Grillmair, C. J., Kormendy, J., and Richstone, D.: 1996, ***The Astrophysical Journal Letters*** **471,** L79

Levine, S. E. and Sparke, L. ***S.:*** 1998, ***The Astrophysical Journal Letters 496,*** L13

Lin, C. C. and Shu, F. H.: 1964, ***The Astrophysical Journal*** **140, 646**

Lovelace, R. V. E., Jore, K. P., and Haynes, M. P.: 1997, ***The Astrophysical Journal*** **475**, 83

Malphrus, B. K., Simpson, C. E., Gottesman, S. T., and Hawarden, T. G.: 1997, ***The Astronomical Journal*** **114, 1427**

McCarthy, D. W., Probst, R. G., and Low, F. J.: 1985, ***The Astrophysical Journal Letters 290,*** L9

Merrifield, M. R. and Kuijken, K.: 1994, ***The Astrophysical Journal 432, 575***

Merritt, D.: ***2000, Galaxies and Black Holes,*** Accepted for publication in ***Comments on Astrophysics***

Ostriker, J. P. and Peebles, P. J. E.: 1973, ***The Astrophysical Journal*** **186, 467**

Persic, M. and Salucci, P.: 1990, ***Mon. Not.*** *R.* Astron. *Soc.* 245, 577

Prada, F., Gutierrez, C. M., Peletier, R. F., and McKeith, C. D.: 1996, The ***Astrophysical Journal Letters 463,*** L9

Press, W. H., Teukolsky, S. A., Vetterling, W. T., and Flannery, B. P.: 1994, Numerical Recipes in ***FORTRAN,*** Cambridge University Press, 2nd edition

Richstone, D.: 1998, in ***Second International LISA Symposium on the Detection and Observation*** of Gravitational Waves ***in Space,*** Vol. 456 of ***AIP*** Conference ***Proceedings***

Richstone, D., Ajhar, E. A., Bender, R., Bower, G., Dressler, A., Faber, S. M., a. V. Filippenko, Gebhardt, K., Green, R., Ho, L. C., Kormendy, J., Lauer, T., Magorrian, J., and Tremaine, S.: 1998, ***Nature 395,*** Al4

Richter, 0. G. and Sancisi, R.: 1994, ***Astronomy & Astrophysics 290,*** L9

Rix, H.-W., Franx, M., Fisher, D., and Illingworth, ***G.: 1992, The Astrophysical Journal Letters 400,*** L5

Rix, H.-W. and Zaritsky, D.: 1995, ***The Astrophysical Journal 447, 82***

Rubin, V. C., Burstein, D., Ford, W. K., and Thonnard, ***N.:*** 1985, ***The Astrophysical Journal 289, 81***

Rubin, V. C., Ford, W. K., and Thonnard, ***N.:*** 1980, ***The Astrophysical Journal 238,*** 471

Rubin, V. C., Ford, W. K., Thonnard, N., and Burstein, D.: 1982, ***The Astrophysical Journal*** 261, 439

Rubin, V. C., Graham, J. A., and Kenney, J. D. P.: 1992, ***The Astrophysical Journal Letters 394,*** L9

Salucci, P., Ratnam, C., Monaco, P., and Danese, L.: 2000, ***The Mass of Black Holes*** in ***the Nuclei*** of Spirals, accepted for publication in ***Mon. Not. R. Astron.*** *Soc.*

Schroeder, M. ***C.:*** 1989, ***Ph.D. thesis,*** University of Maine

Scoville, N. Z., Sanders, D. B., and Clemens, D. P.: 1986, ***The Astrophysical*** Journal ***Letters*** 310, L77

Seiden, P. E. and Gerola, H.: 1979, ***The Astrophysical Journal 233, 56***

Sellwood, J. A.: 1983, in E. Athanassoula (ed.), ***Internal Kinematics and Dynamics*** of Galaxies, Vol. 100 of ***IA U Symposium,*** p. 197

Sellwood, J. A. and Carlberg, R. G.: 1984, The ***Astrophysical Journal 282,*** 61

Shalit, D.: 1995, Ph.D. ***thesis,*** Boston University

Shore, ***S. N.:*** 1981, ***The Astrophysical Journal 249, 93***

Shorey, P. A.: 1990, ***Muster's thesis,*** University of Maine

Shorey, P. A.: 1996, ***Ph.D. thesis,*** University of Maine

Shu, F. H., Adams, F. C., and Lizano, ***S.:*** 1987, ***Ann. Rev. of Astron. and Astroph.*** 25, 23

Sridhar, S. and Touma, J.: 1999, ***Mon. Not. R. Astron.*** *Soc.* ***303, 483***

Statler, T., Smith, B. F., and Comins, ***N.:*** 1983, ***The Astrophysical Journal 270, 79***

Tayler, R. J.: 1993, *"Galaxies,* ***structure and evolution",*** Cambridge [England] ; New York, NY, USA : Cambridge University Press, 1993. Rev. ed.

Thakar, A. R., Ryden, B. S., Jore, K. P., and Broeils, A. H.: 1997, ***The Astrophysical Journal 479, 702***

Toomre, A.: 1964, ***The Astrophysical*** Journal 139, 1217

Toth, G. and Ostriker, J. P.: 1992, ***The Astrophysical Journal 389, 5***

van Woerden, H., Allen, R. J., and Burton, W. B. (eds.): 1985, ***"The Milky Way*** *Galaxy"*, Vol. 106 of ***IA U Symposium***

Wakker, B. P., Howk, J. C., Savage, B. D., Tufte, S. L., Reynolds, R. J., van Woerden, H., Schwarz, U. J., and Peletier, R. F.: 1999, in ***ASP Conf. Ser.*** *166: Stromlo* ***Workshop on High-Velocity Clouds,*** p. 26

White, R. L.: 1988, ***The Astrophysical Journal 330, 26***

Whitworth, A., Boffin, H., Watkins, S., and Francis, ***N.:*** 1998, ***Astronomy and Geophysics*** **39(6)**, 10

Zaritsky, D. and Rix, H.-W.: 1997, ***The Astrophysical Journal 477,*** 118

Zeltwanger, T.: ***2000, GALAXY User Manual,*** University of Maine

Zeltwanger, T., Comins, N. F., and Lovelace, R. V. E.: ***2000, Sloshing in high-speed*** *Galaxy* ***Interactions,*** accepted for publication in ***The Astrophysical Journal***

Appendix A

UNIT CONVERSION

To minimize floating point operations during execution of the GALAXY code some physical constants, like the gravitational constant $\mathcal{G}$, are set to unity. Similarly, the length unit $\mathcal{L}$ is chosen to be the length of one grid cell, and the time unit $\mathcal{T}$ corresponds to one revolution of the galaxy ($\mathcal{T} \approx$ 250 Myr). The length and time units, together with the constraint $\mathcal{G}$ = 1, determine the mass unit ***M:*** the total mass of the simulation galaxy equals the total mass of a typical disk galaxy, M_{gal} = 2 x 10^{11} $M_{\odot}$. Unless otherwise noted, the simulations for this thesis were run on a 256 x 256 grid with a grid utilization of 0.75 and either 10^5 or 2.5 x 10^5 star particles. With these parameters, the simulation units can be converted to SI units or other commonly used units as listed in table A.l.

Table A. 1: Unit conversions

unit name	in SI units	other units
grid cell length $\mathcal{L}$	***3.2*** x 10^{18} m	104.2 pc
time per revolution $\mathcal{T}$	7.9×10^{15} s	***2.5*** x 10^8 yr
mass $\boldsymbol{M}$	5.9 x 10^{34} kg	***3.0*** x 10^4 $M_{\odot}$
ang. mom. $\boldsymbol{M}\ \mathcal{L}^2\ \mathcal{T}^{-1}$	***7.8*** x 10^{55} kg m^2 s^{-1}	none
spec. ang. mom. $\mathcal{L}^2\ \mathcal{T}^{-1}$	1.3×10^{21} m^2 s^{-1}	***4.2*** x 10^{-2} kpc km s^{-1}
velocity $\mathcal{L}\ \mathcal{T}^{-1}$	406.9 m s^{-1}	none

Appendix B

OVERVIEW OF THE SIMULATIONS

For a quick reference, all runs with stellar evolution are listed in this appendix, together with a brief description of each parameter. For a more thorough discussion of each parameter refer to Chapter 4.

Table B.l: Explanation of parameters

Parameter	Description
cmf	Cloud mass fraction
gmf	Gas mass fraction
hmf	Halo mass fraction
smf	Star mass fraction
temp0	Initial temperature of the gas, if isothermal setup is used
ceg	Initial internal energy of the gas, if isothermal setup is not used
nstr	Initial number of stars
omgs	Initial Toomre's Q of stars
ncloud	Initial number of clouds
omgc	Initial Toomre's Q of clouds
cfrc	Probability of cloud formation by Jeans collapse
ecform	Energy deposited to gas through cloud formation
sfcrc	Probability of star formation by cloud collision
sfsrc	Probability of star formation by snowplow effect
esform	Energy deposited in gas through star formation
enova	Energy deposited in gas by each supernova
pinfal	Rate of mass infall from the halo onto the disk

Table B.2: Runs 14 through 20

Parameter	Run 14	Run 15	Run 16	Run 17	Run 18	Run 19	Run 20
cmf	0.02	0.02	0.02	0.02	0.02	0.02	0.02
gmf	0.02	0.02	0.02	0.02	0.02	0.02	0.02
hmf	0.8	0.8	0.8	0.8	0.8	0.8	0.8
smf	0.16	0.16	0.16	0.16	0.16	0.16	0.16
temp0	n/a	n/a	n/a	n/a	n/a	n/a	n/a
ceg	150	150	10	150	150	150	150
nstr	10^5	10^5	10^5	10^5	10^5	10^5	2.5×10^5
omgs	1.1	2.0	1.1	1.1	1.1	1.1	1.1
ncloud	10^4	10^4	10^4	10^4	10^4	10^4	10^4
omgc	1.1	1.1	1.1	1.1	1.1	1.1	1.1
cfrc	0.5	0.5	0.5	0.5	1.0	0.1	0.5
ecform	0.0	0.0	0.0	0.0	0.0	0.0	0.0
sfcrc	0.1	0.1	0.1	0.1	0.1	0.1	0.1
sfsrc	0.1	0.1	0.1	0.1	0.1	0.1	0.1
esform	0.0	0.0	0.0	0.0	0.0	0.0	0.0
enova	0.0	0.0	0.0	0.0	0.0	0.0	0.0
pinfal	0.5	0.5	0.5	1.5	0.5	0.5	0.5

Table B.3: Runs 21 through 27

Parameter	Run 21	Run 22	Run 23	Run 24	Run 25	Run 26	Run 27
cmf	0.02	0.02	0.02	0.02	0.02	0.04	0.02
gmf	0.02	0.02	0.02	0.02	0.02	0.02	0.005
hmf	0.8	0.8	0.8	0.8	0.8	0.8	0.8
smf	0.16	0.16	0.16	0.16	0.16	0.14	0.175
temp0	n/a	n/a	n/a	n/a	n/a	n/a	n/a
ceg	150	1500	150	150	150	150	150
nstr	10^5	10^5	10^5	10^5	10^5	10^5	10^5
omgs	1.1	1.1	1.1	1.1	1.1	1.1	1.1
ncloud	10^4	10^4	10^4	10^4	10^4	10^4	10^4
omgc	1.1	1.1	2.0	1.1	1.1	1.1	1.1
cfrc	0.5	0.5	0.5	0.5	0.0	0.5	0.5
ecform	0.0	0.0	0.0	0.0	n/a	0.0	0.0
sfcrc	0.2	0.1	0.1	0.1	0.1	0.1	0.1
sfsrc	0.1	0.1	0.1	0.1	0.1	0.1	0.1
esform	0.0	0.0	0.0	150	0.0	0.0	0.0
enova	0.0	0.0	0.0	0.0	0.0	0.0	0.0
pinfal	0.5	0.5	0.5	0.5	0.5	0.5	0.5

Table B.4: Runs 28 through 33

Parameter	Run 28	Run 29	Run 30	Run 31	Run 32	Run 33
cmf	0.005	0.02	0.02	0.02	0.02	0.02
gmf	0.02	0.02	0.02	0.02	0.02	0.02
hmf	0.8	0.8	0.8	0.8	0.8	0.8
smf	0.175	0.16	0.16	0.16	0.16	0.16
temp0	n/a	n/a	n/a	n/a	n/a	n/a
ceg	150	150	150	150	150	150
nstr	10^5	10^5	10^5	2.5×10^5	2.5×10^5	2.5×10^5
omgs	1.1	1.1	1.1	1.1	1.1	1.1
ncloud	10^4	10^4	10^4	10^4	10^4	10^4
omgc	1.1	1.1	1.1	1.1	1.1	1.1
cfrc	0.5	0.5	0.5	0.5	0.5	0.5
ecform	0.0	0.0	0.0	0.0	0.0	0.0
sfcrc	0.1	0.1	0.1	0.1	0.1	0.1
sfsrc	0.1	0.1	0.0	0.1	0.1	0.1
esform	0.0	0.0	0.0	0.0	0.0	0.0
enova	0.0	15.0	0.0	0.0	0.0	0.0
pinfal	0.5	0.5	0.5	1.0	1.0	1.0

Table B.5: Runs 34 through 39

Parameter	Run 34	Run 35	Run 36	Run 37	Run 38	Run 39
cmf	0.02	0.02	0.02	0.02	0.02	0.0
gmf	0.02	0.02	0.02	0.02	0.02	0.0
hmf	0.8	0.8	0.8	0.8	0.8	0.8
smf	0.16	0.16	0.16	0.16	0.16	0.2
temp0	n/a	10 K	100 K	5K	10 K	n/a
ceg	150	n/a	n/a	n/a	n/a	n/a
nstr	2.5×10^5	2.5×10^5	2.5×10^5	2.5×10^5	2.5×10^5	2.5×10^5
omgs	1.1	1.1	1.1	1.1	1.1	1.1
ncloud	10^4	10^4	10^4	10^4	10^4	10^4
omgc	1.1	1.1	1.1	1.1	1.1	1.1
cfrc	0.5	0.5	0.5	0.5	1.0	0.0
ecform	0.0	0.0	0.0	0.0	0.0	n/a
sfcrc	0.1	0.1	0.1	0.1	0.1	0.0
sfsrc	0.1	0.1	0.1	0.1	0.1	0.0
esform	0.0	0.0	0.0	0.0	0.0	n/a
enova	0.0	0.0	0.0	0.0	0.0	n/a
pinfal	0.0	1.0	1.0	1.0	1.0	0.0

Table B.6: Runs 40 through 45

Parameter	Run 40	Run 41	Run 42	Run 43	Run 44	Run 45
cmf	0.02	0.02	0.02	0.02	0.02	0.02
gmf	0.02	0.02	0.02	0.02	0.02	0.02
hmf	0.8	0.8	0.8	0.8	0.8	0.8
smf	0.16	0.16	0.16	0.16	0.16	0.16
temp0	10 K	n/a	10 K	10 K	10 K	10 K
ceg	n/a	150	n/a	n/a	n/a	n/a
nstr	2.5×10^5	2.5×10^5	2.5×10^5	2.5×10^5	2.5×10^5	2.5×10^5
omgs	1.1	1.1	1.1	1.1	1.1	1.1
ncloud	10^4	10^4	10^4	10^4	10^4	10^4
omgc	1.1	1.1	1.1	1.1	1.1	1.1
cfrc	0.0	0.0	0.0	0.0	0.0	1.0
ecform	n/a	n/a	n/a	n/a	n/a	0.0
sfcrc	0.0	0.0	0.0	0.0	0.0	1.0
sfsrc	0.0	0.0	0.0	0.0	0.0	0.1
esform	n/a	n/a	n/a	n/a	n/a	0.0
enova	n/a	n/a	n/a	n/a	n/a	0.0
pinfal	1.0	1.0	0.0	0.5	0.25	0.25

Table B.7: Runs 46 through 51

Parameter	Run 46	Run 47	Run 48	Run 49	Run 50	Run 51
cmf	0.02	0.02	0.02	0.02	0.02	0.02
gmf	0.02	0.02	0.02	0.02	0.02	0.02
hmf	0.8	0.8	0.8	0.8	0.8	0.8
smf	0.16	0.16	0.16	0.16	0.16	0.16
temp0	0.5 K	2 K	n/a	2 K	2 K	2 K
ceg	n/a	n/a	1500	n/a	n/a	n/a
nstr	2.5×10^5	2.5×10^5	2.5×10^5	2.5×10^5	2.5×10^5	2.5×10^5
omgs	1.1	1.1	1.1	1.1	1.1	1.1
ncloud	10^4	10^4	10^4	10^4	10^4	10^4
omgc	1.1	1.1	1.1	1.1	1.1	1.1
cfrc	1.0	1.0	1.0	1.0	1.0	1.0
ecform	0.0	0.0	0.0	0.0	0.0	0.0
sfcrc	1.0	0.1	0.1	0.1	0.1	0.03
sfsrc	0.1	0.1	0.1	0.1	0.1	0.1
esform	0.0	0.0	0.0	0.0	0.0	0.0
enova	0.0	0.0	0.0	0.0	0.0	0.0
pinfal	0.5	0.5	0.5	1.0	1.5	1.5

Table B.8: Runs 52 through 56

Parameter	Run 52	Run 53	Run 54	Run 55	Run 56
cmf	0.02	0.02	0.02	0.02	0.02
gmf	0.02	0.02	0.02	0.02	0.02
hmf	0.8	0.8	0.8	0.8	0.8
smf	0.16	0.16	0.16	0.16	0.16
temp0	10 K	2 K	2 K	n/a	0.5 K
ceg	n/a	n/a	n/a	150	n/a
nstr	2.5×10^5	2.5×10^5	2.5×10^5	2.5×10^5	2.5×10^5
omgs	1.1	1.1	1.1	1.1	1.1
ncloud	10^4	10^4	5×10^4	10^4	10^4
omgc	1.1	1.1	1.1	1.1	1.1
cfrc	1.0	1.0	1.0	0.5	1.0
ecform	0.0	0.0	0.0	0.0	100
sfcrc	1.0	0.1	0.1	0.1	1.0
sfsrc	0.1	0.1	0.1	0.1	0.1
esform	0.0	0.0	0.0	0.0	0.0
enova	0.0	0.0	0.0	0.0	0.0
pinfal	0.375	0.375	0.375	0.5	0.5

Appendix C

DATA ANALYSIS

For quick reference, plots of the quantities most commonly used in the data analysis are presented in this appendix. These are the Fourier Amplitudes of the stars and the clouds, Toomre's Q for stars and clouds, and the development of angular momentum and mass of the individual galaxy components.

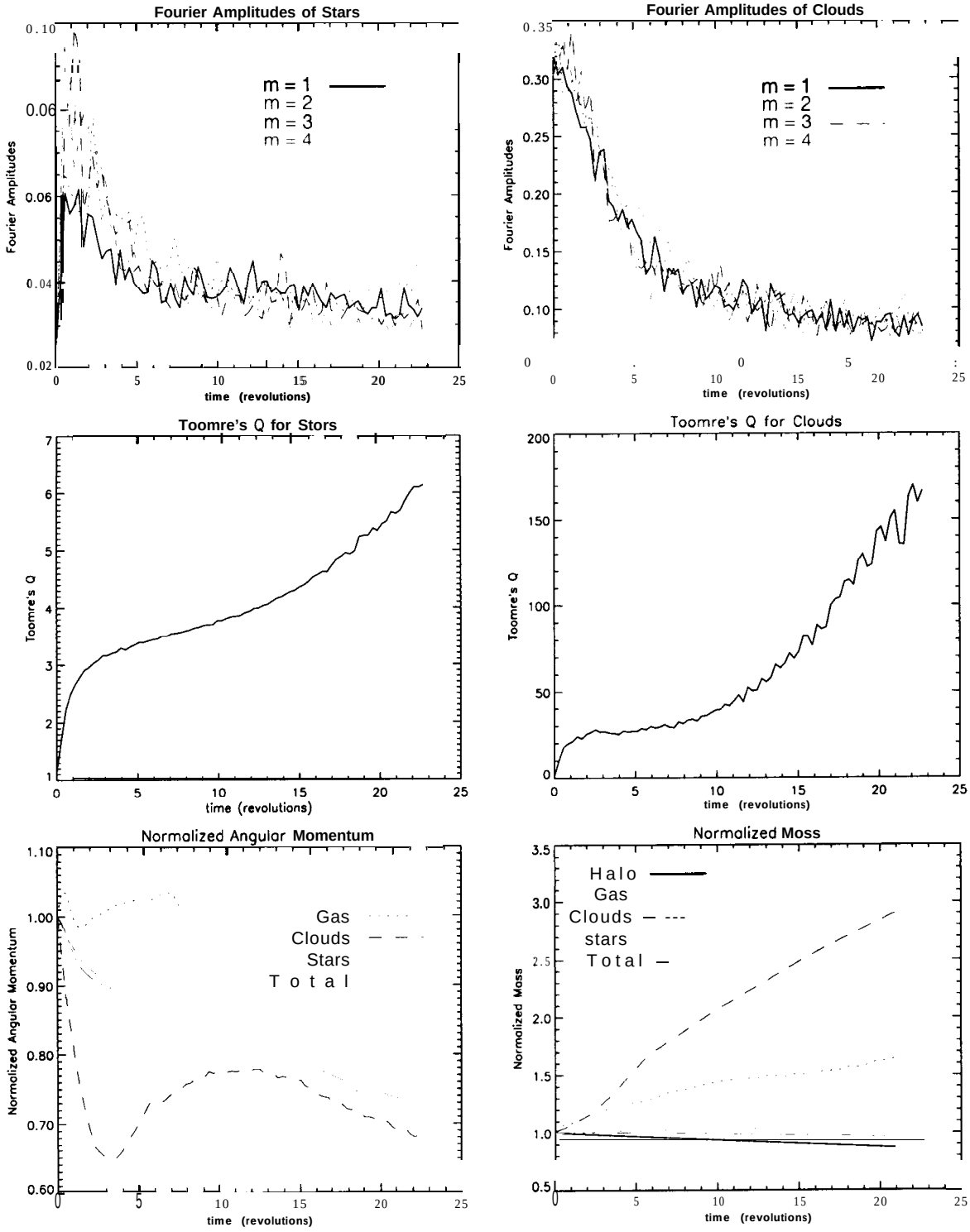

Figure C.l: Data Analysis of run # 14.

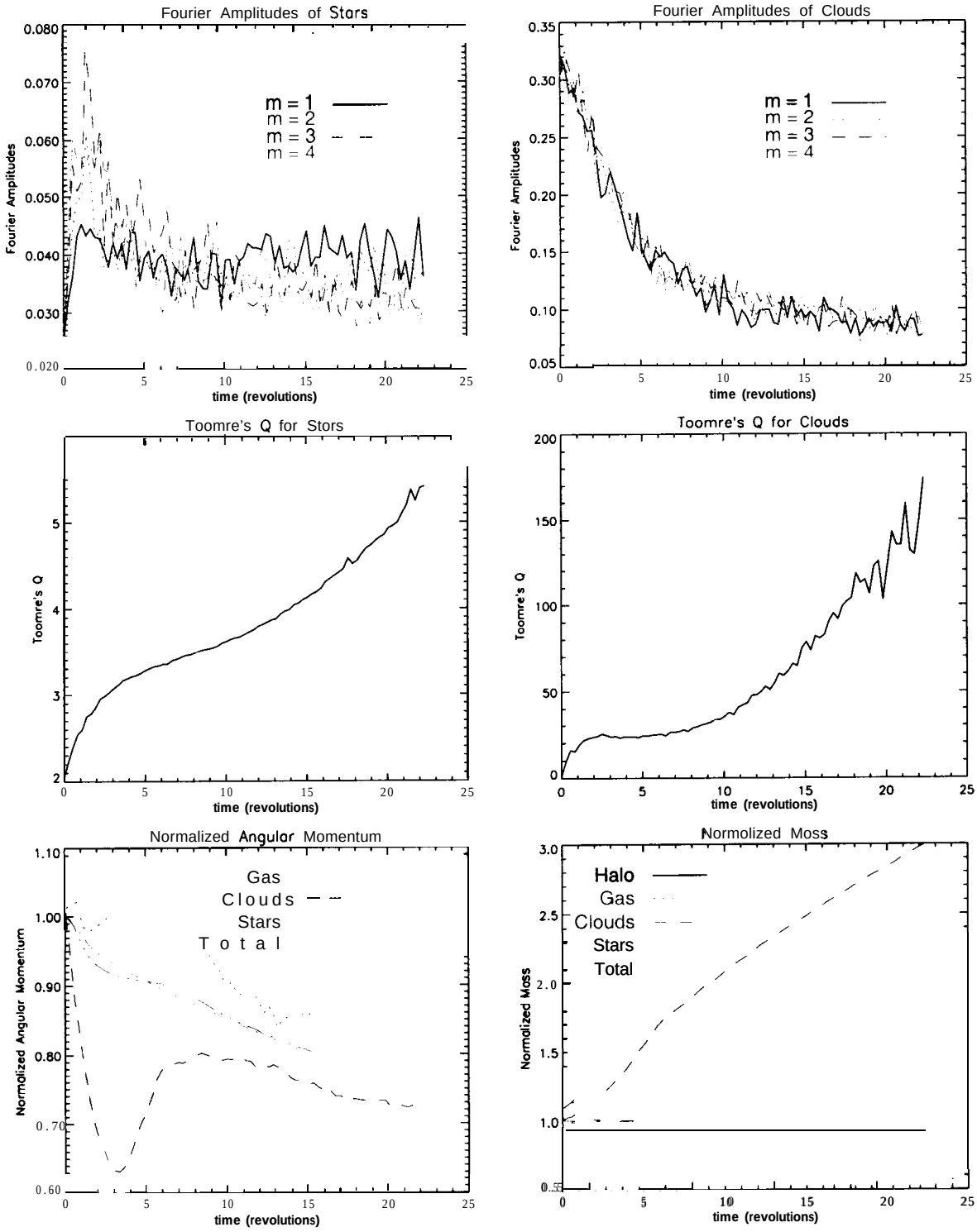

Figure C.2: Data Analysis of run # 15.

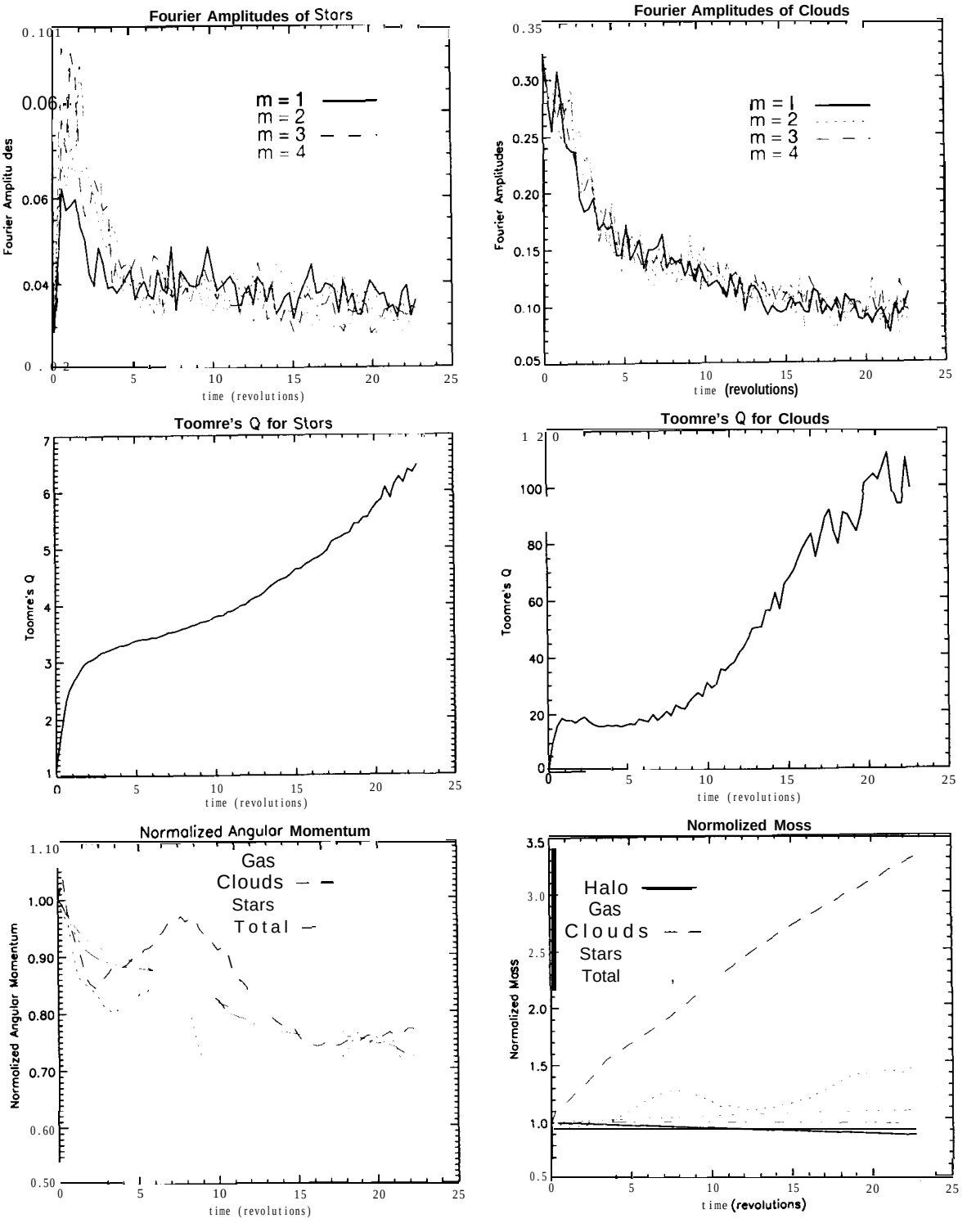

Figure C.3: Data Analysis of run # 16.

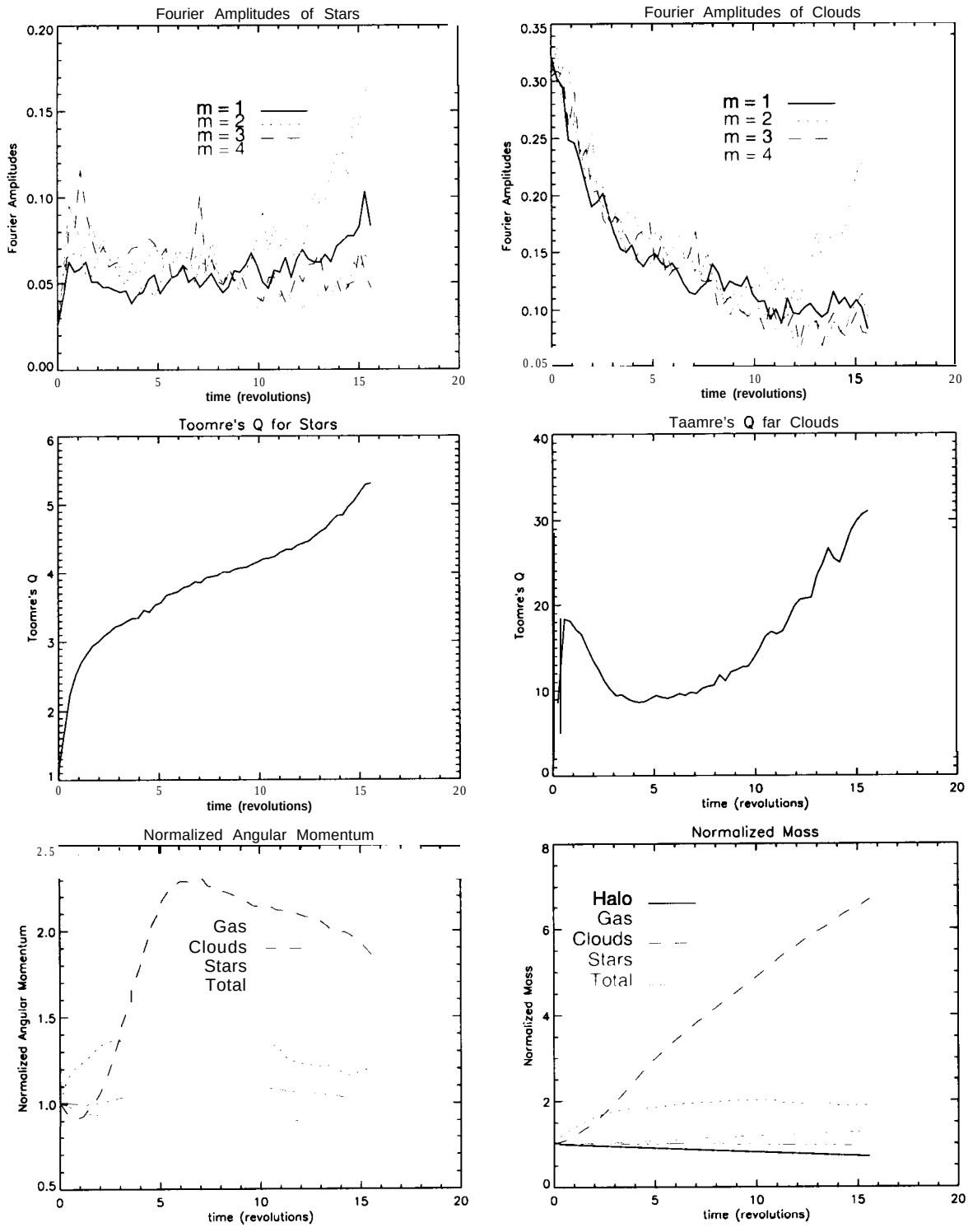

Figure C.4: Data Analysis of run # 17.

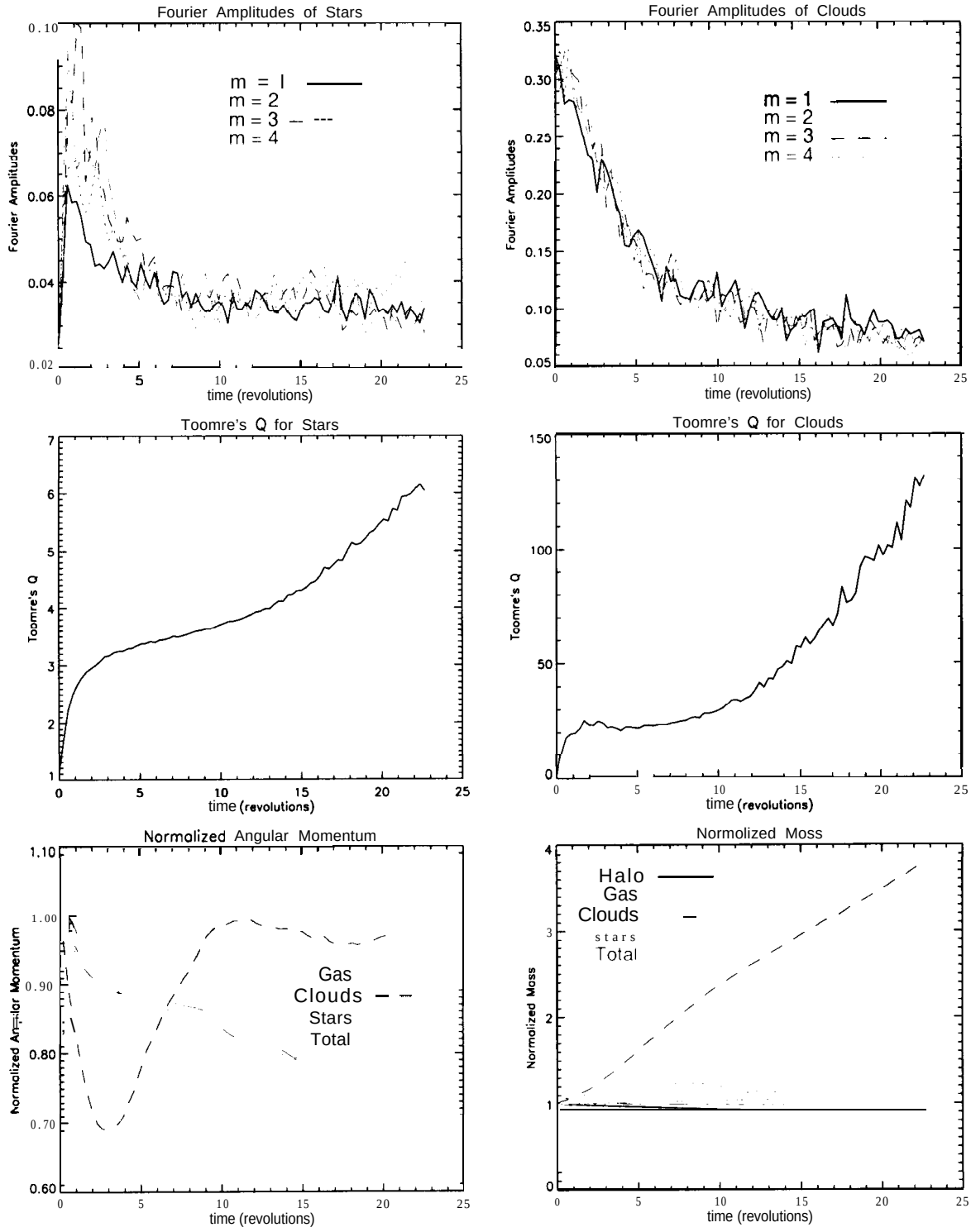

Figure C.5: Data Analysis of run # 18.

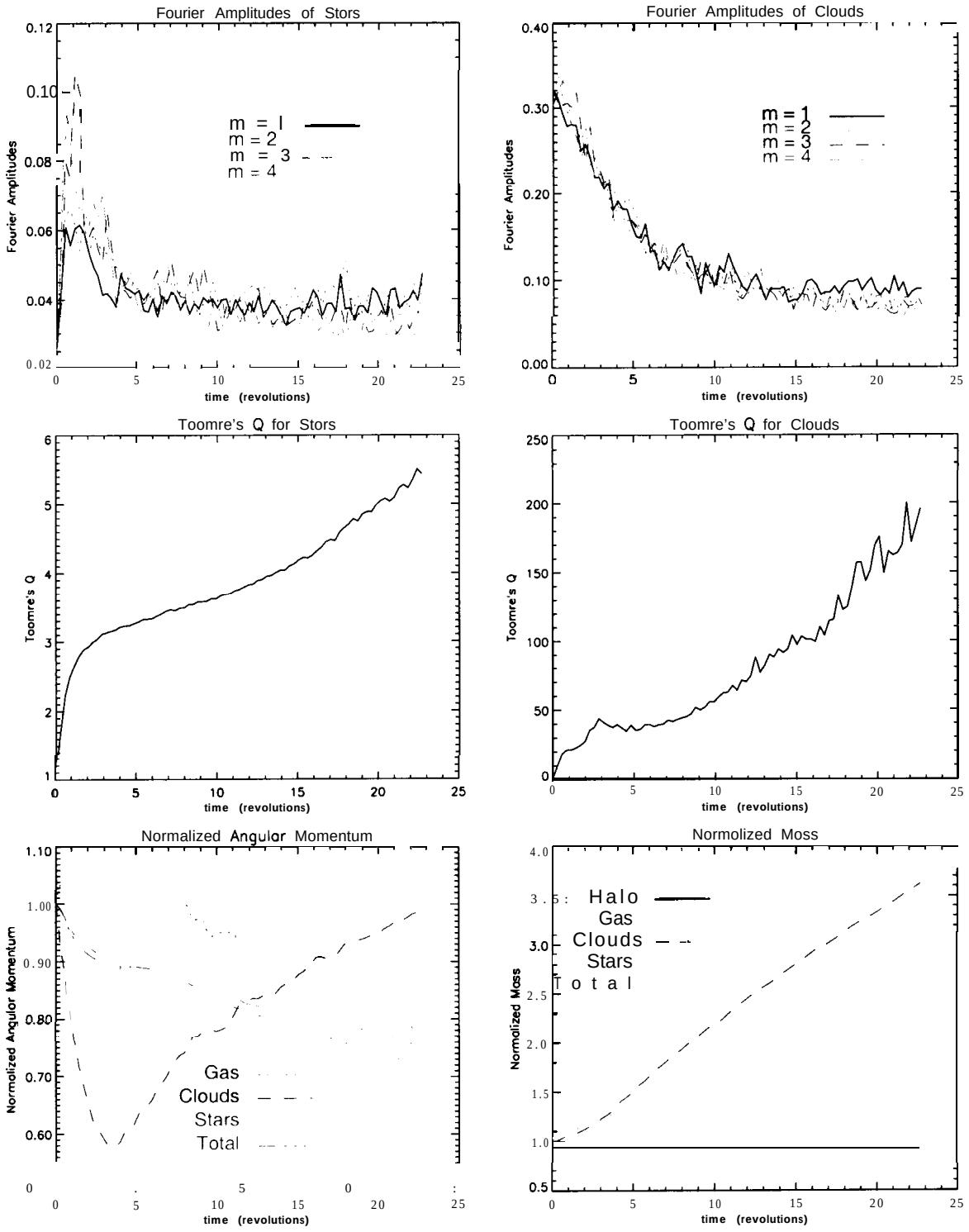

Figure C.6: Data Analysis of run # 19.

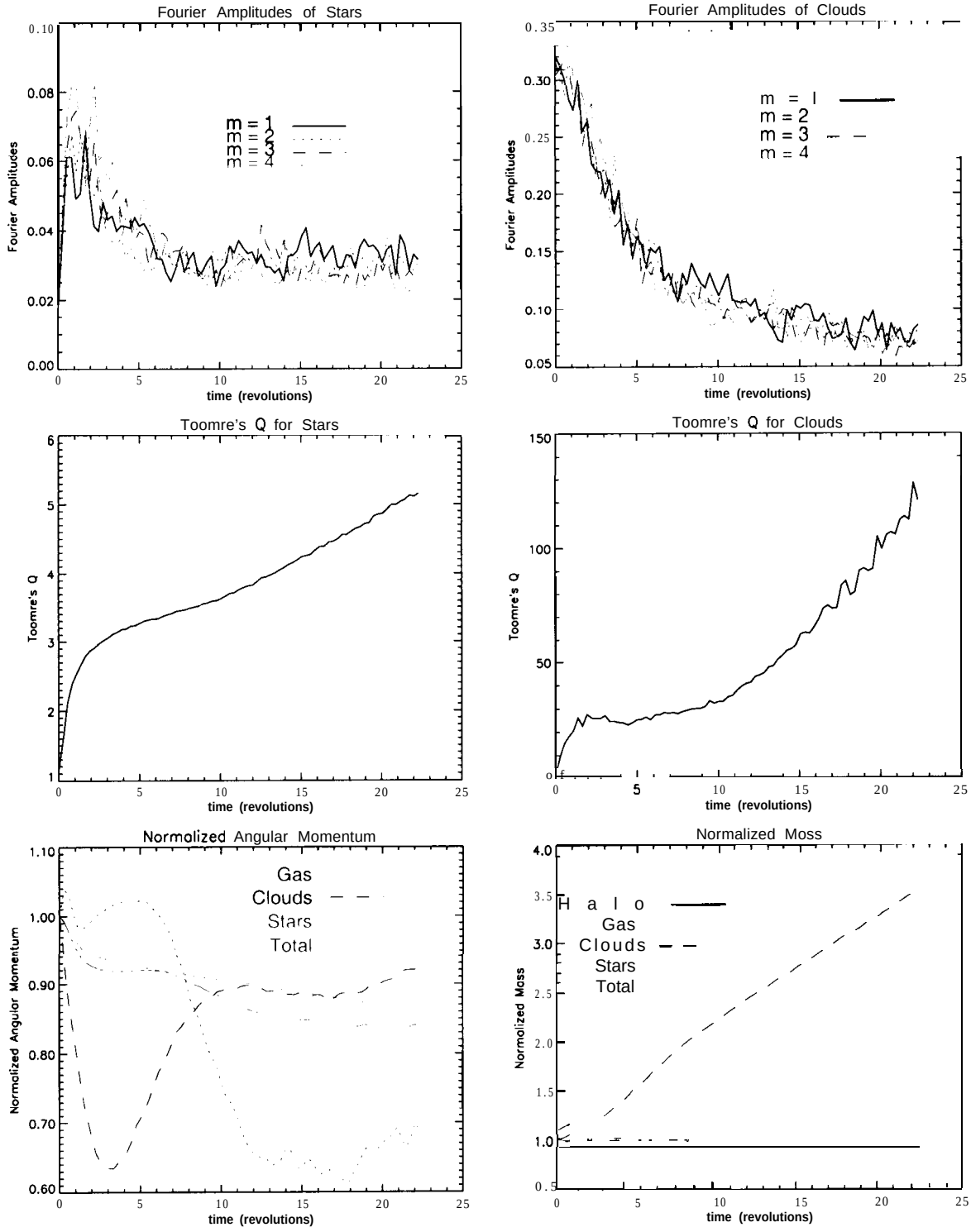

Figure C.7: Data Analysis of run # 20.

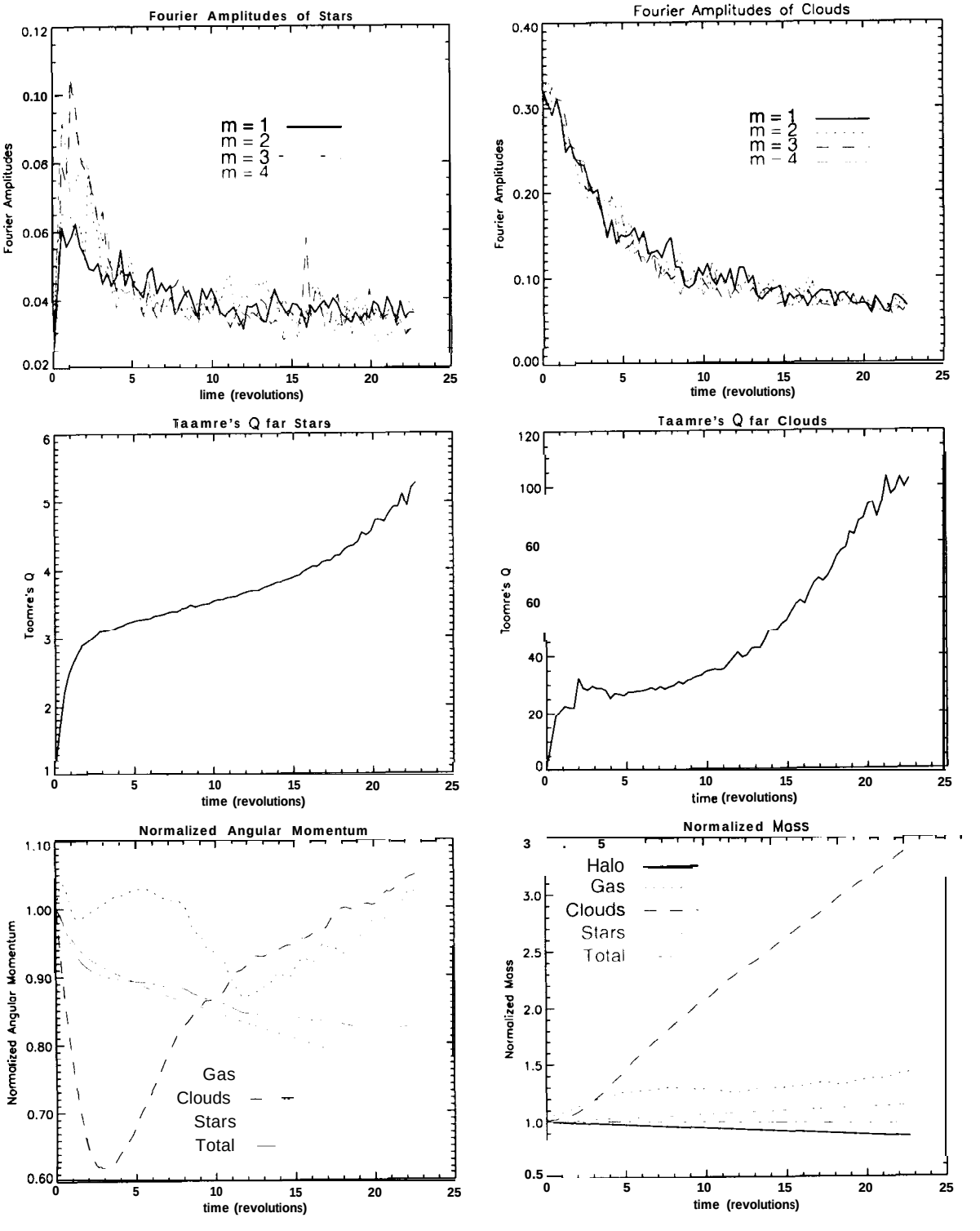

Figure C.8: Data Analysis of run # 21.

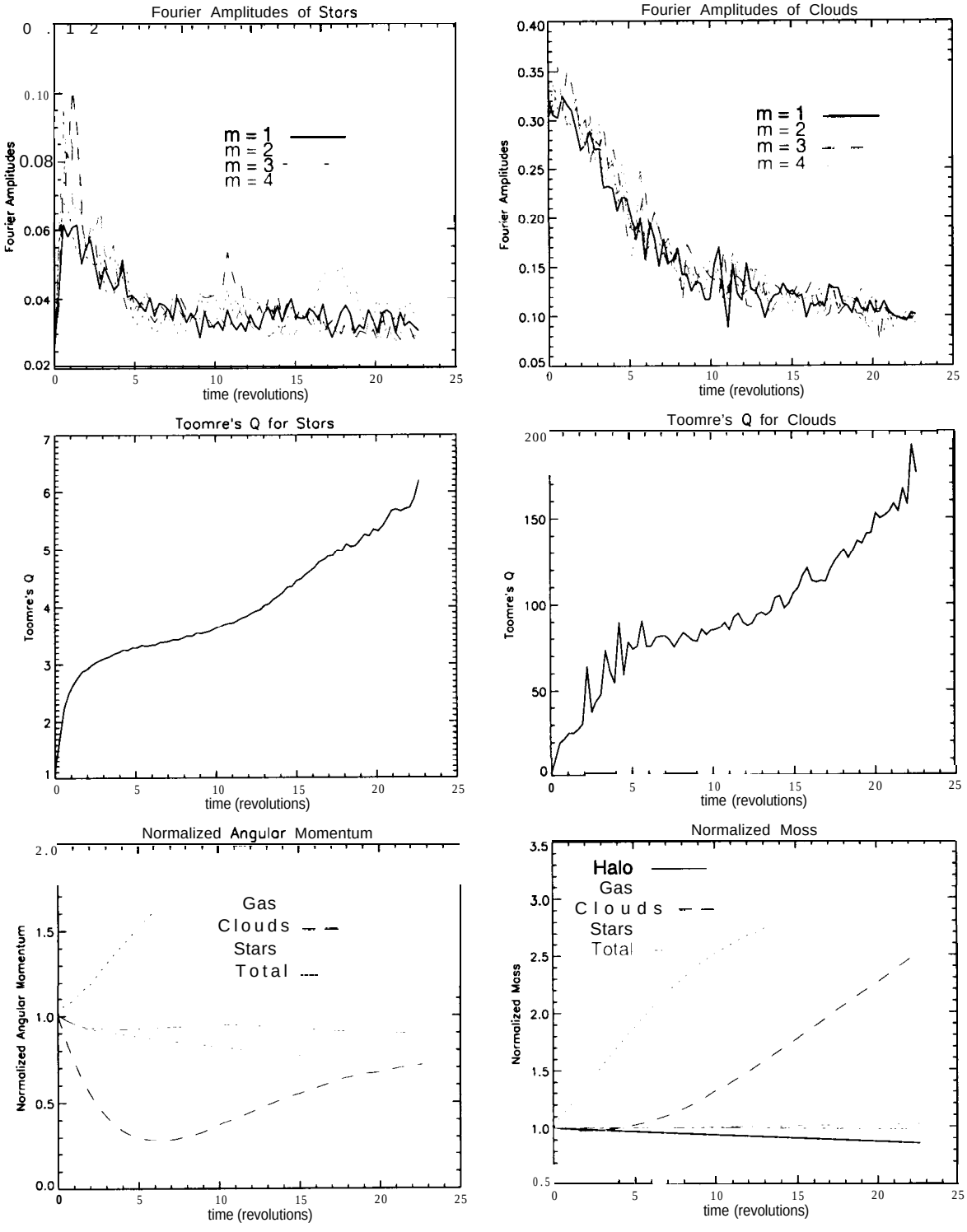

Figure C.9: Data Analysis of run # 22.

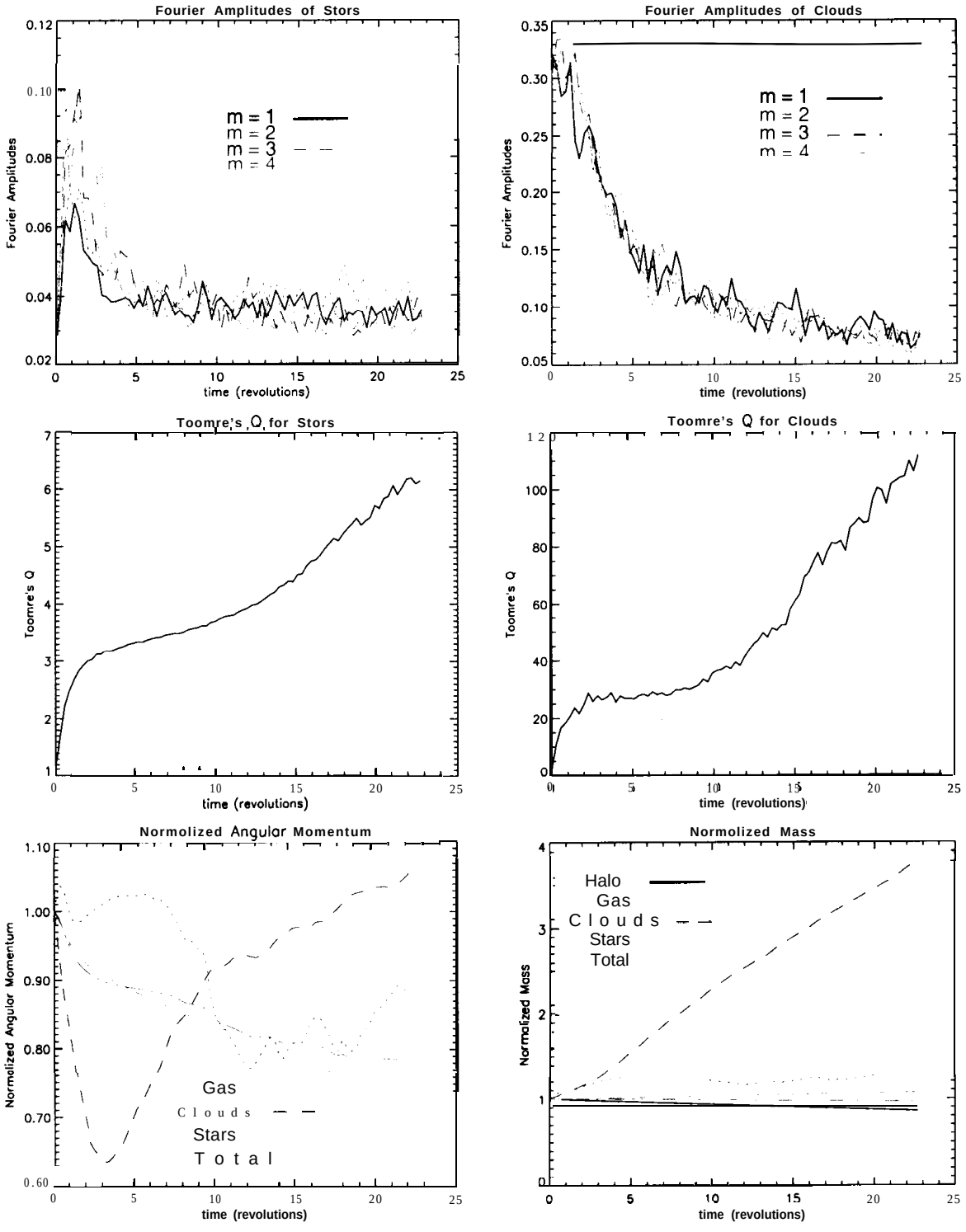

Figure C.10: Data Analysis of run # 23.

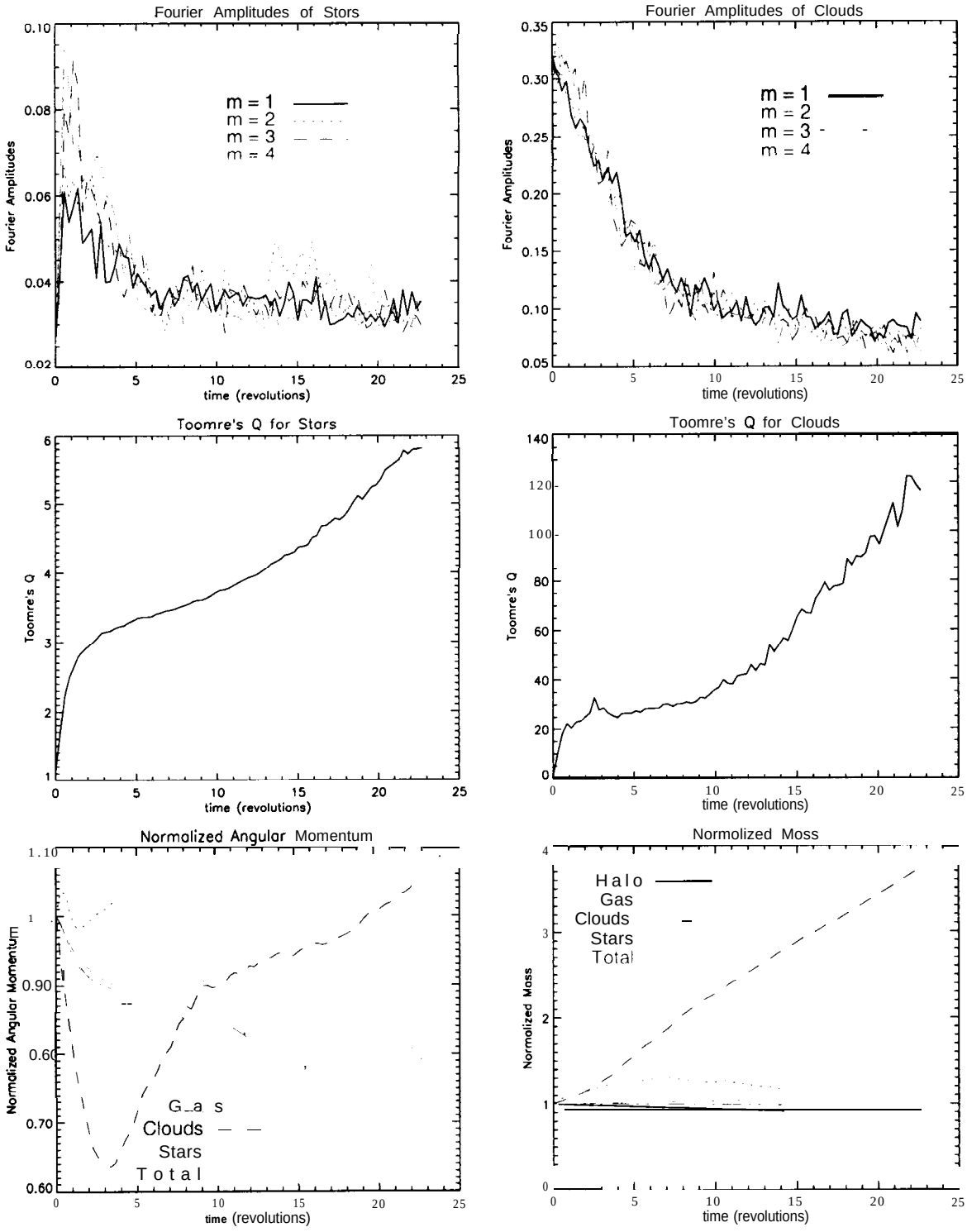

Figure C.ll: Data Analysis of run # 24.

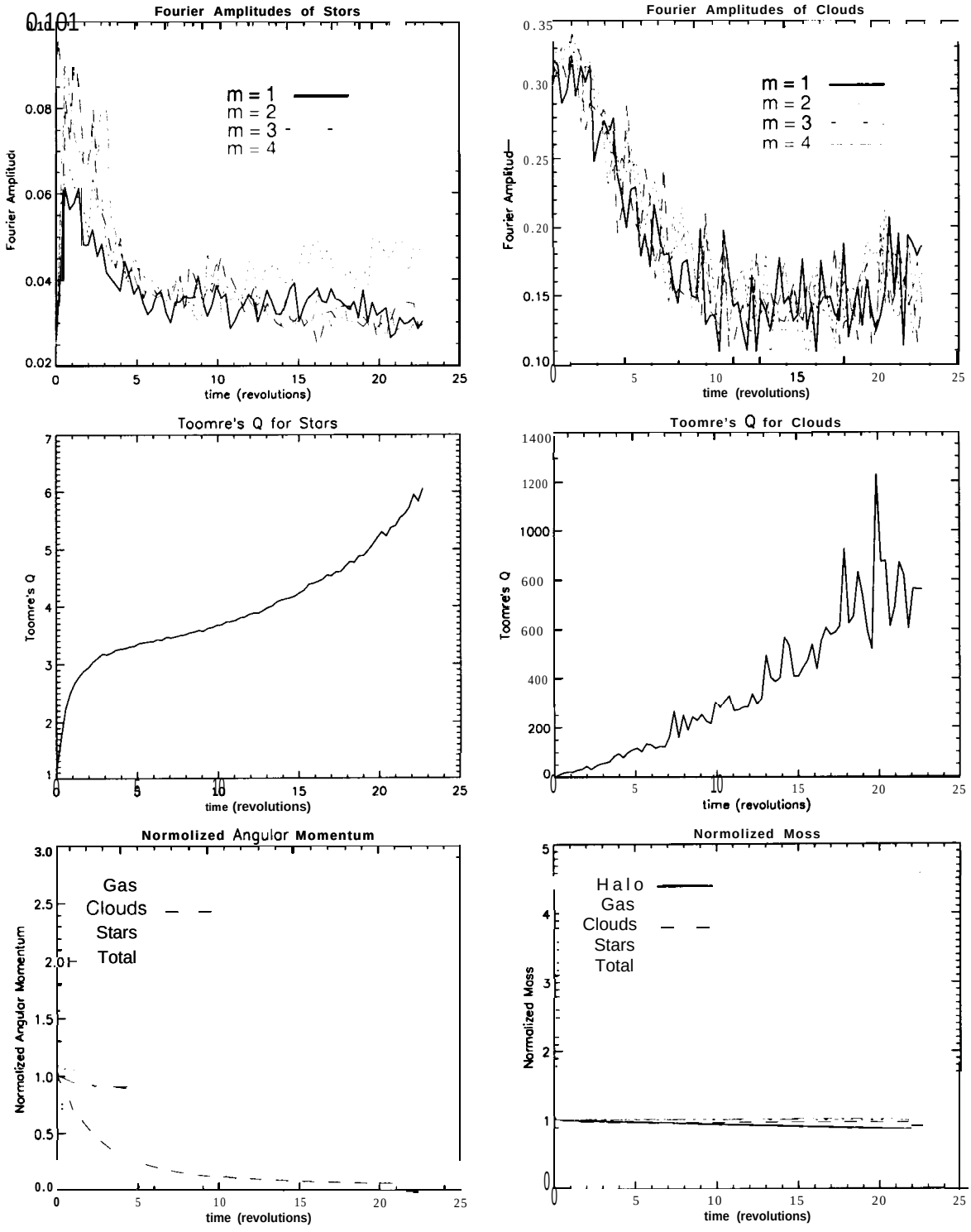

Figure C.12: Data Analysis of run # 25.

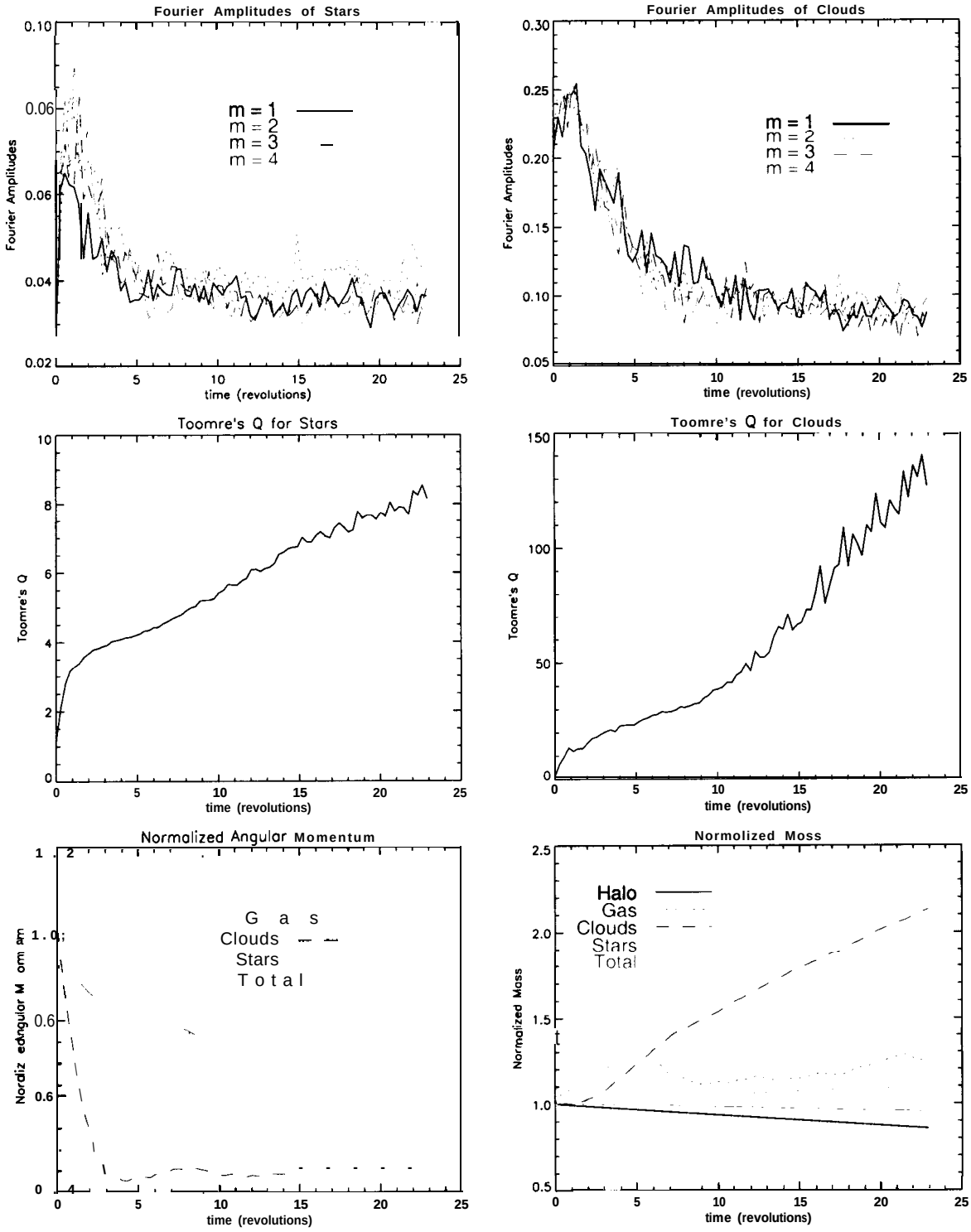

Figure C.13: Data Analysis of run # 26.

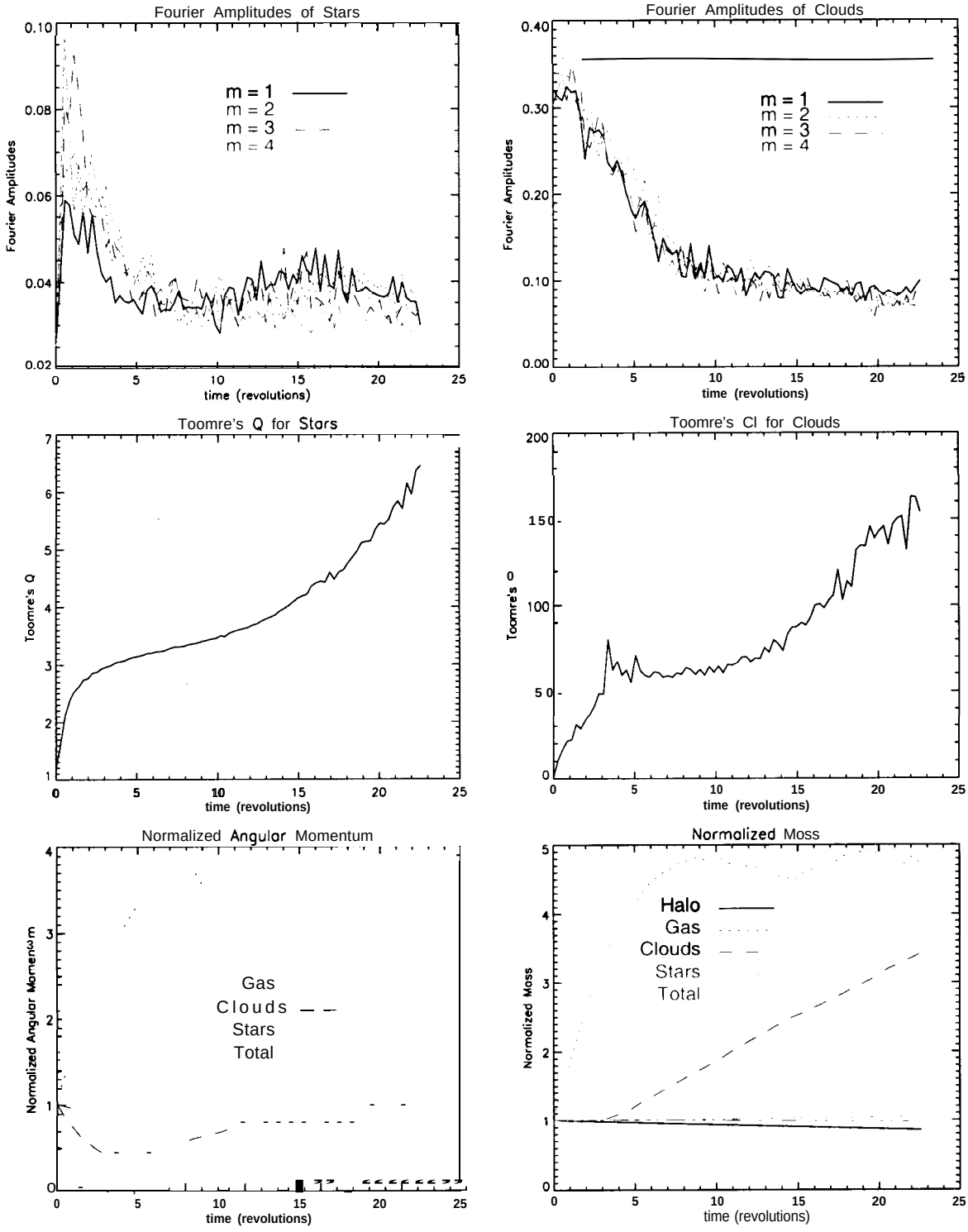

Figure C.14: Data Analysis of run # 27.

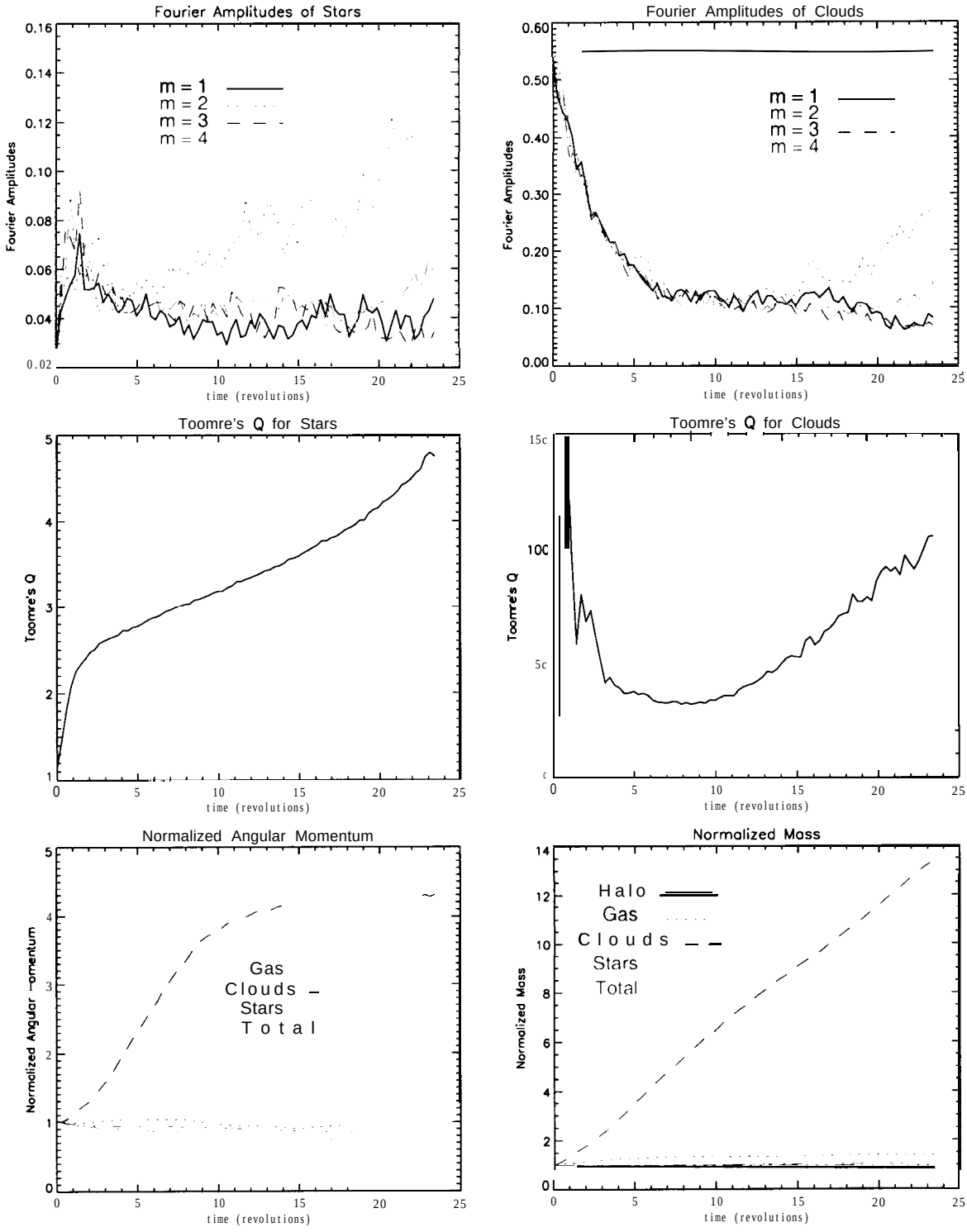

Figure C.15: Data Analysis of run # 28.

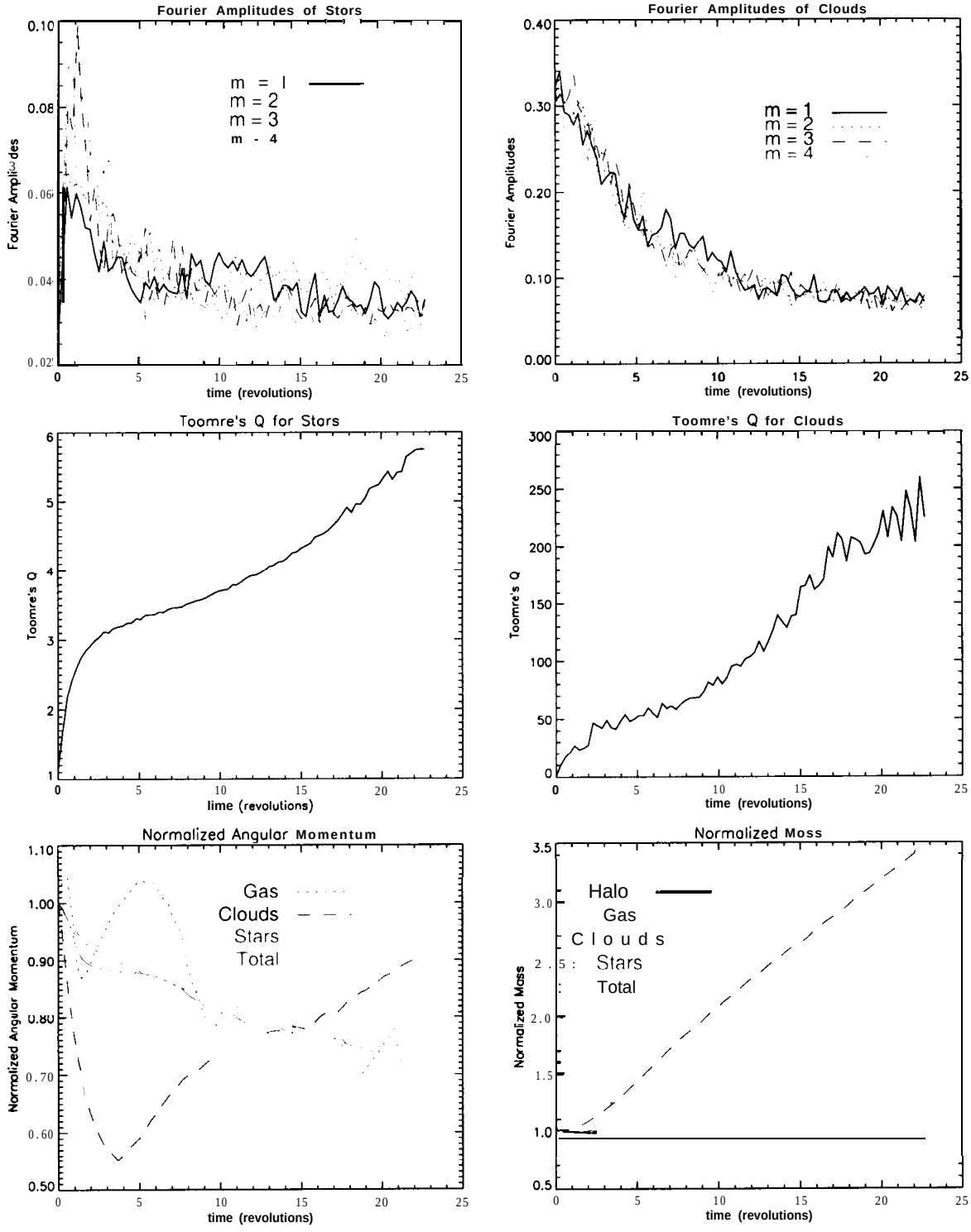

Figure C.16: Data Analysis of run # 29.

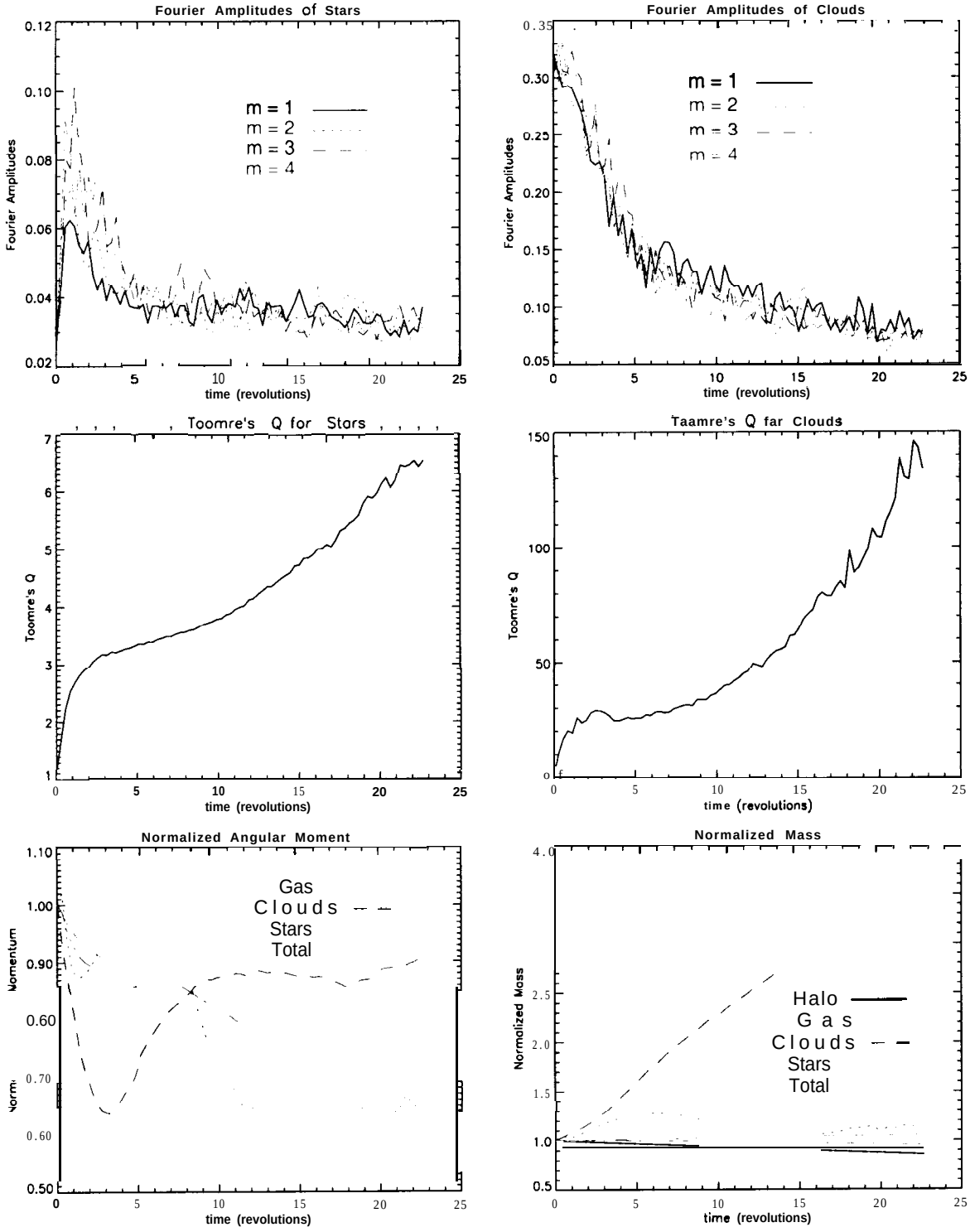

Figure C.17: Data Analysis of run # 30.

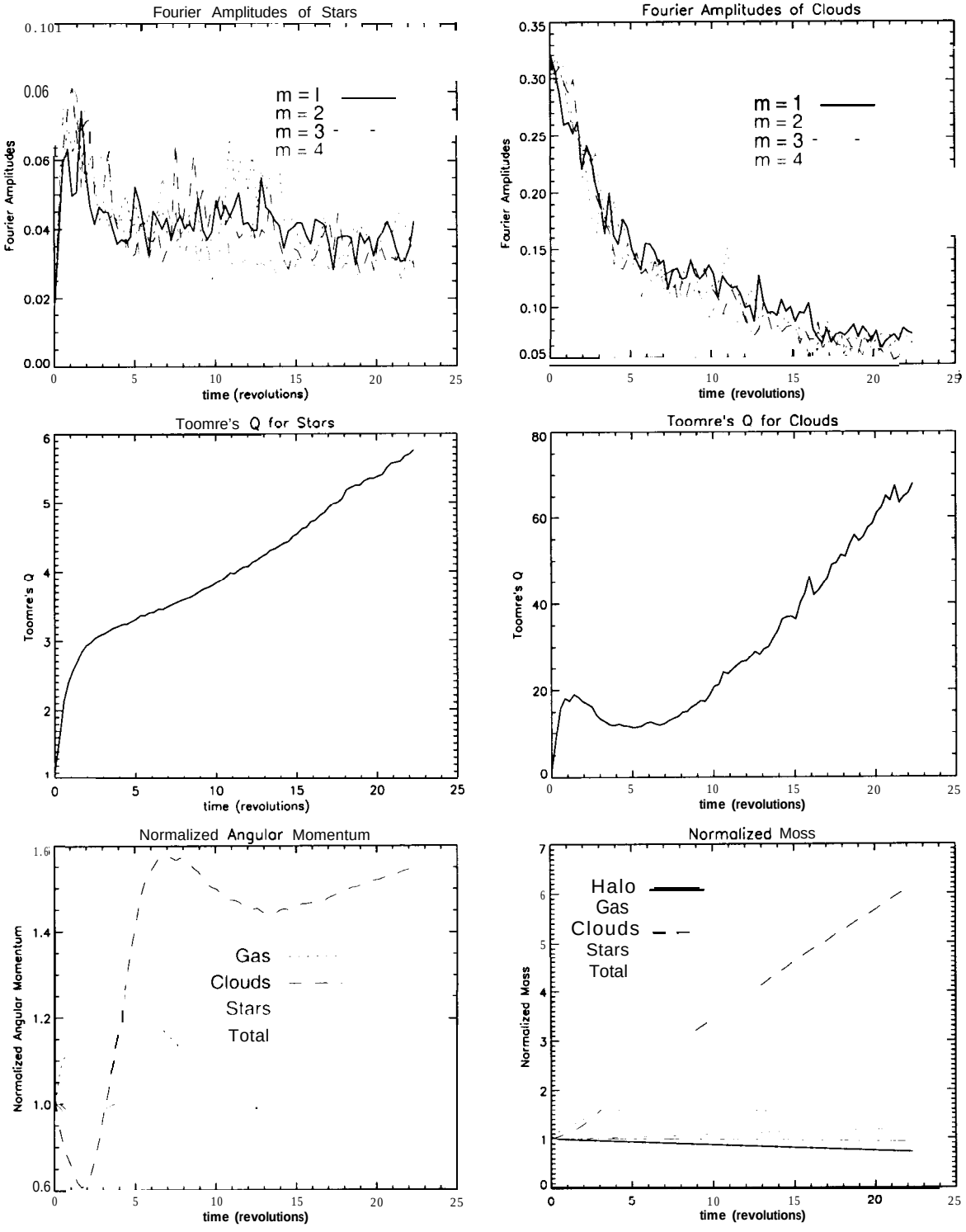

Figure C.18: Data Analysis of run # 31.

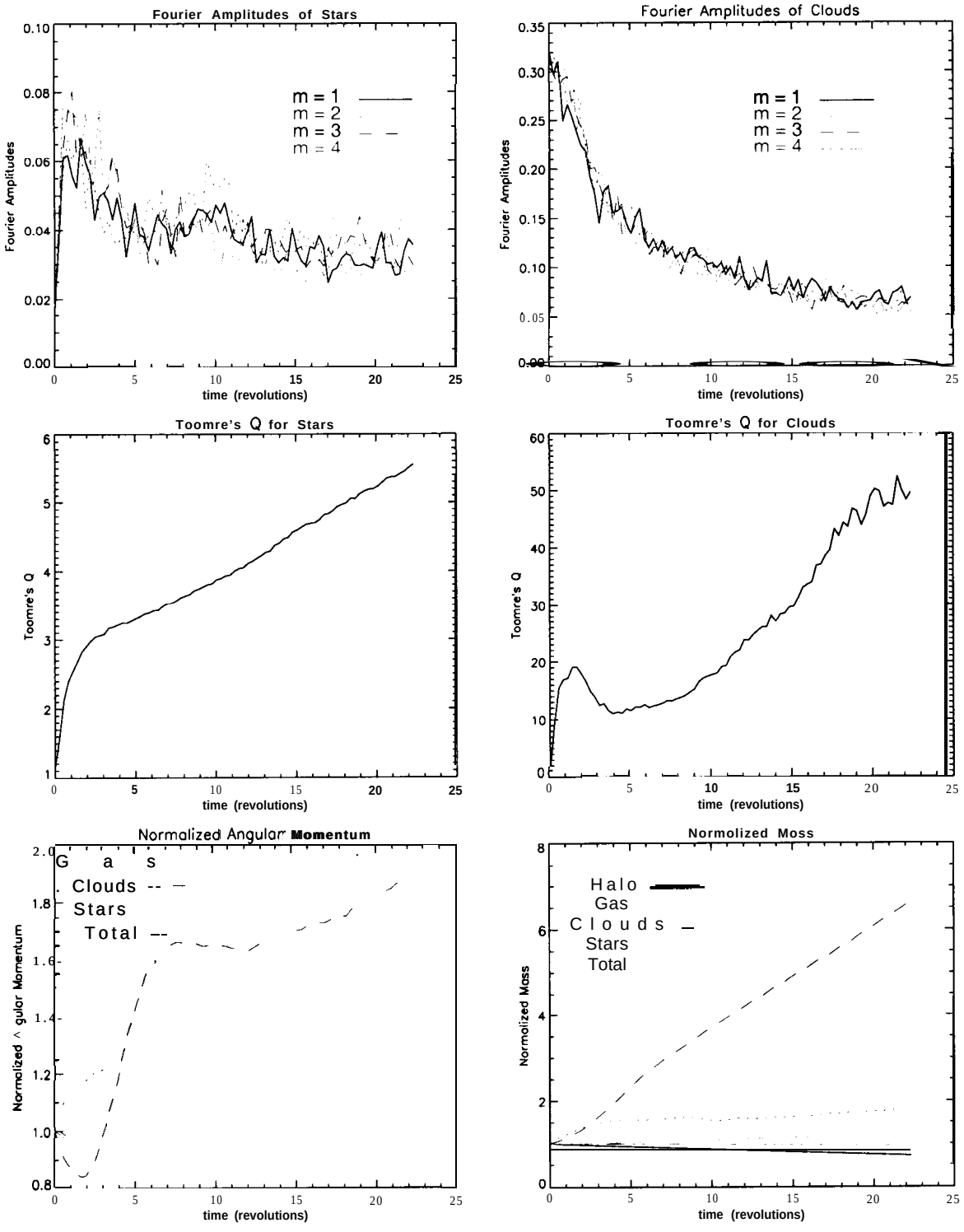

Figure C.19: Data Analysis of run # 32.

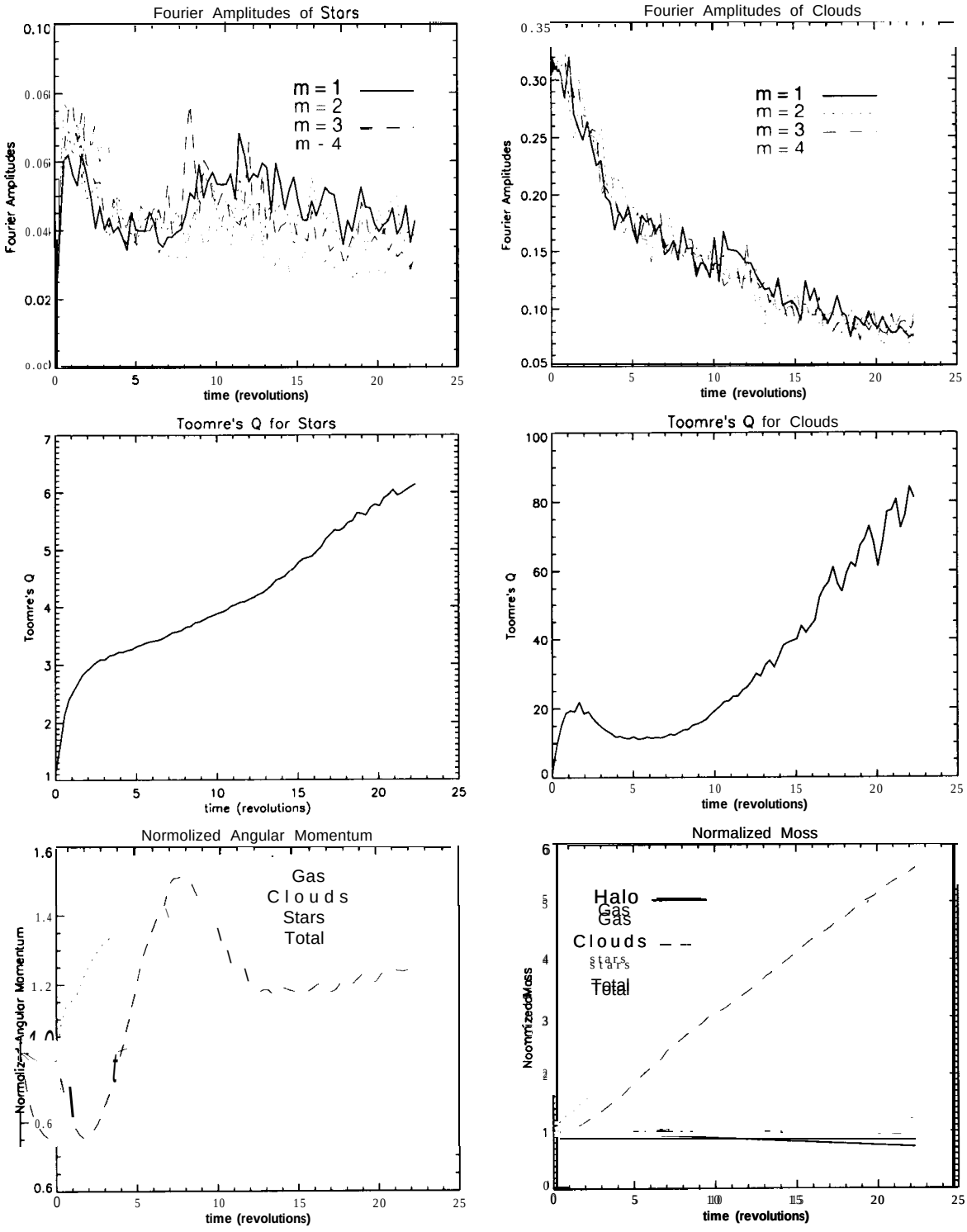

Figure C.20: Data Analysis of run # 33.

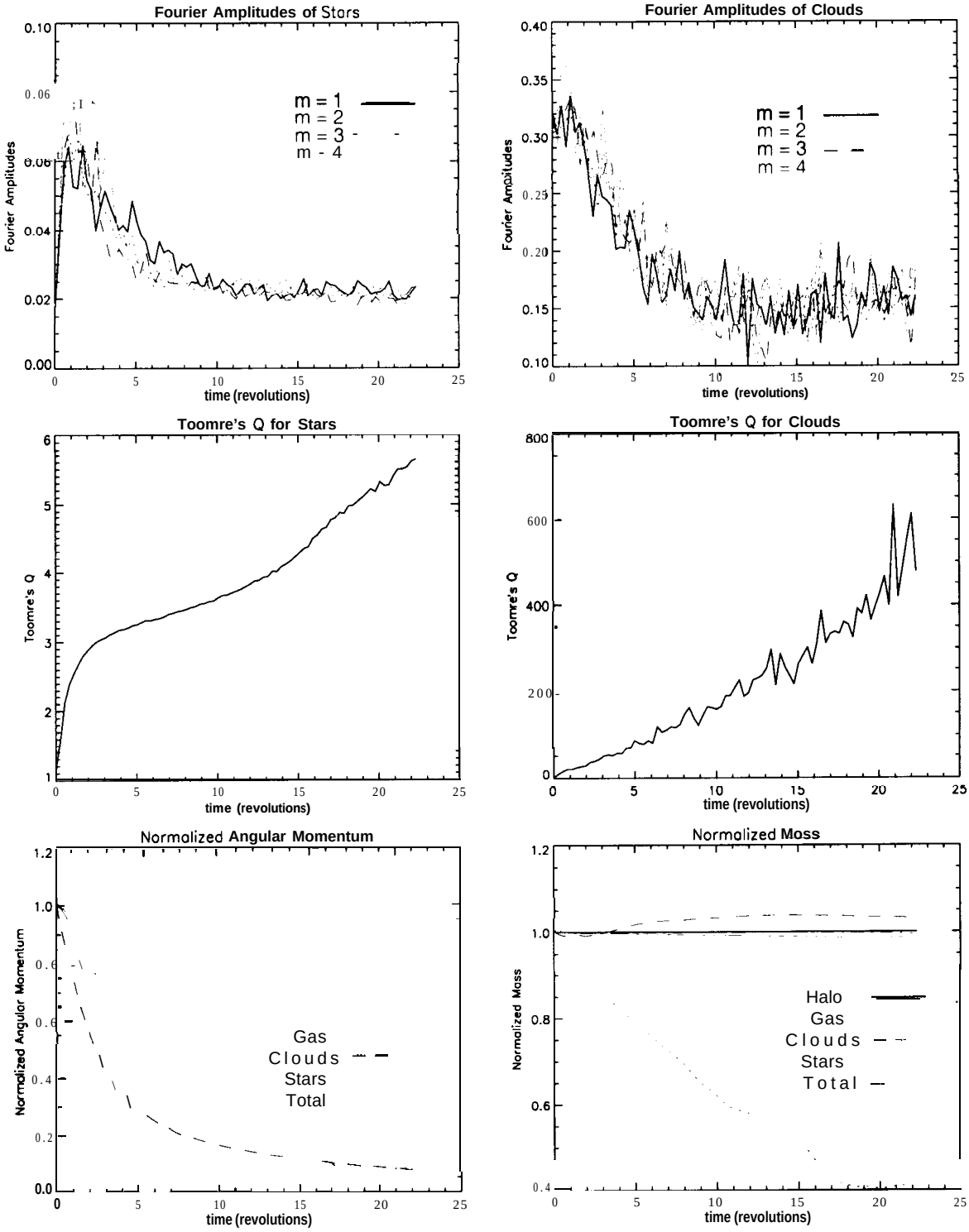

Figure C.21: Data Analysis of run # 34.

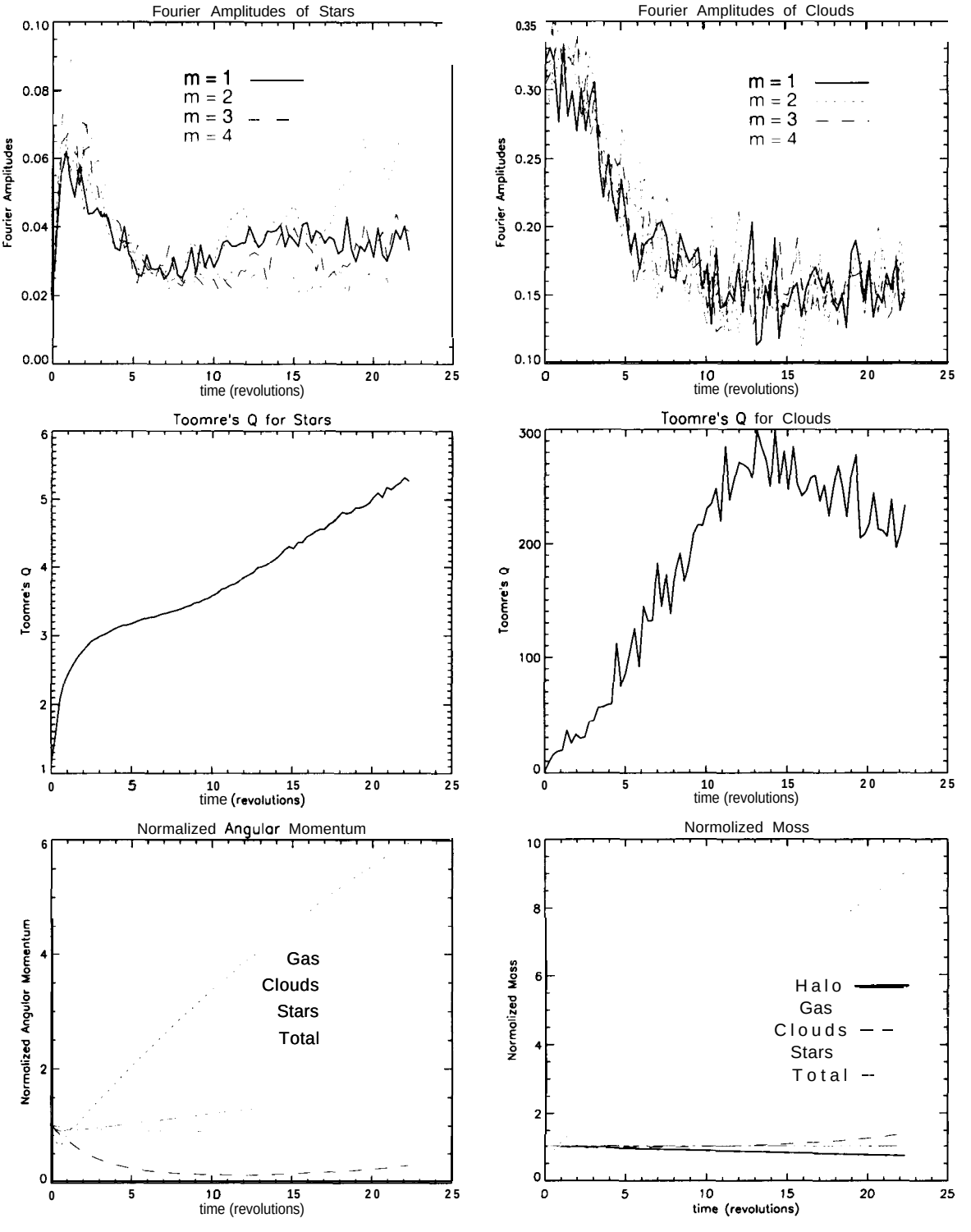

Figure C.22: Data Analysis of run # 35.

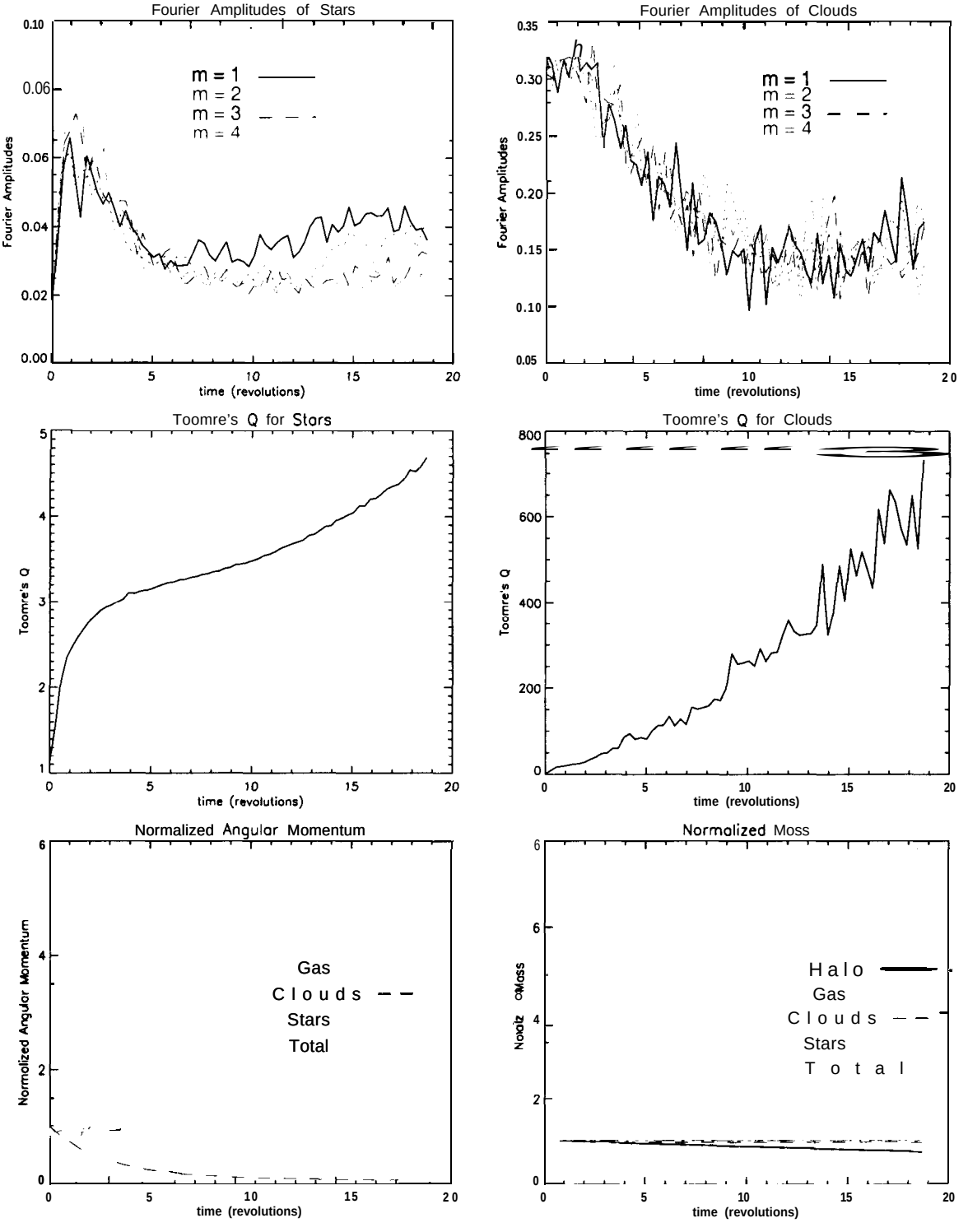

Figure C.23: Data Analysis of run # 36.

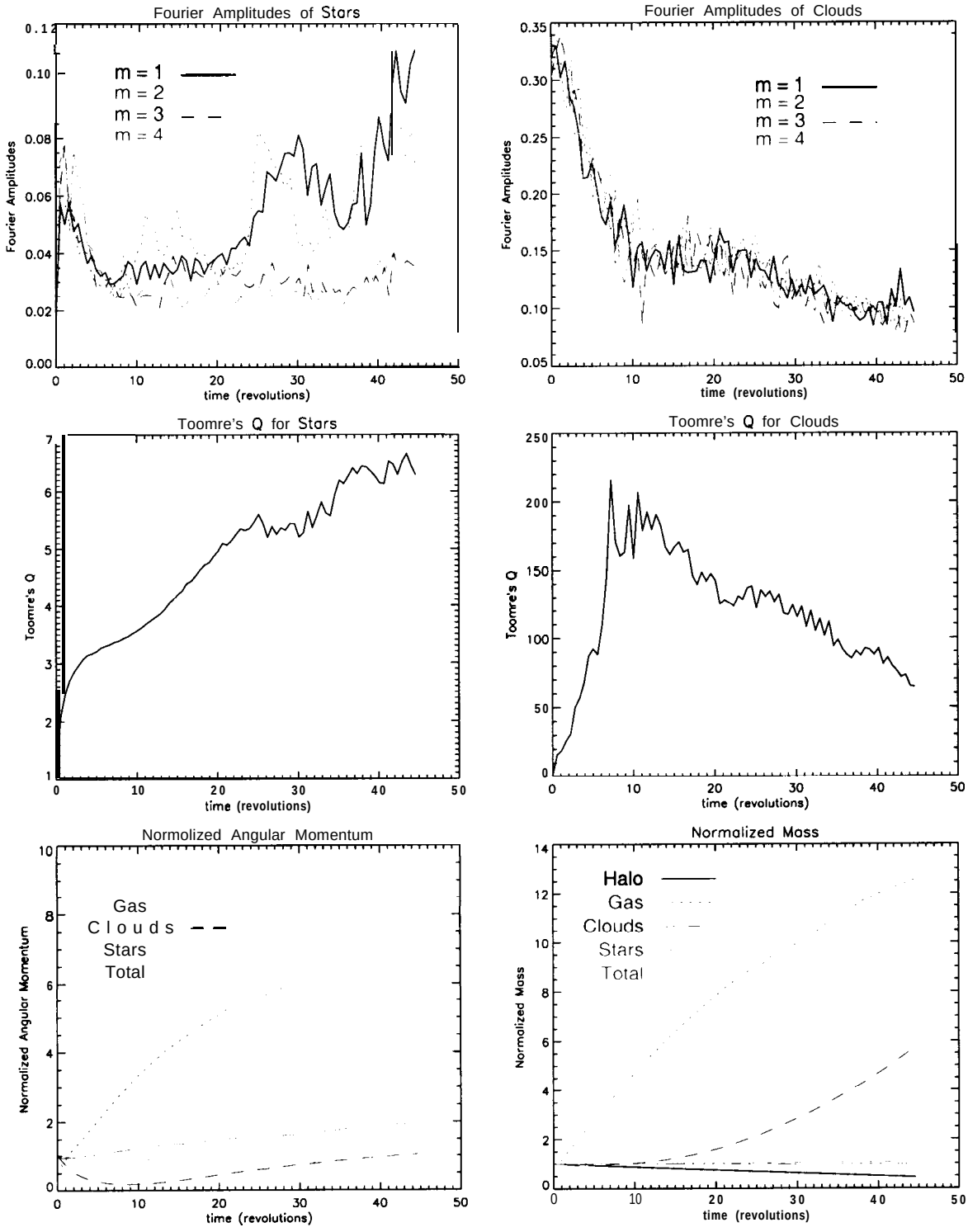

Figure C.24: Data Analysis of run # 37.

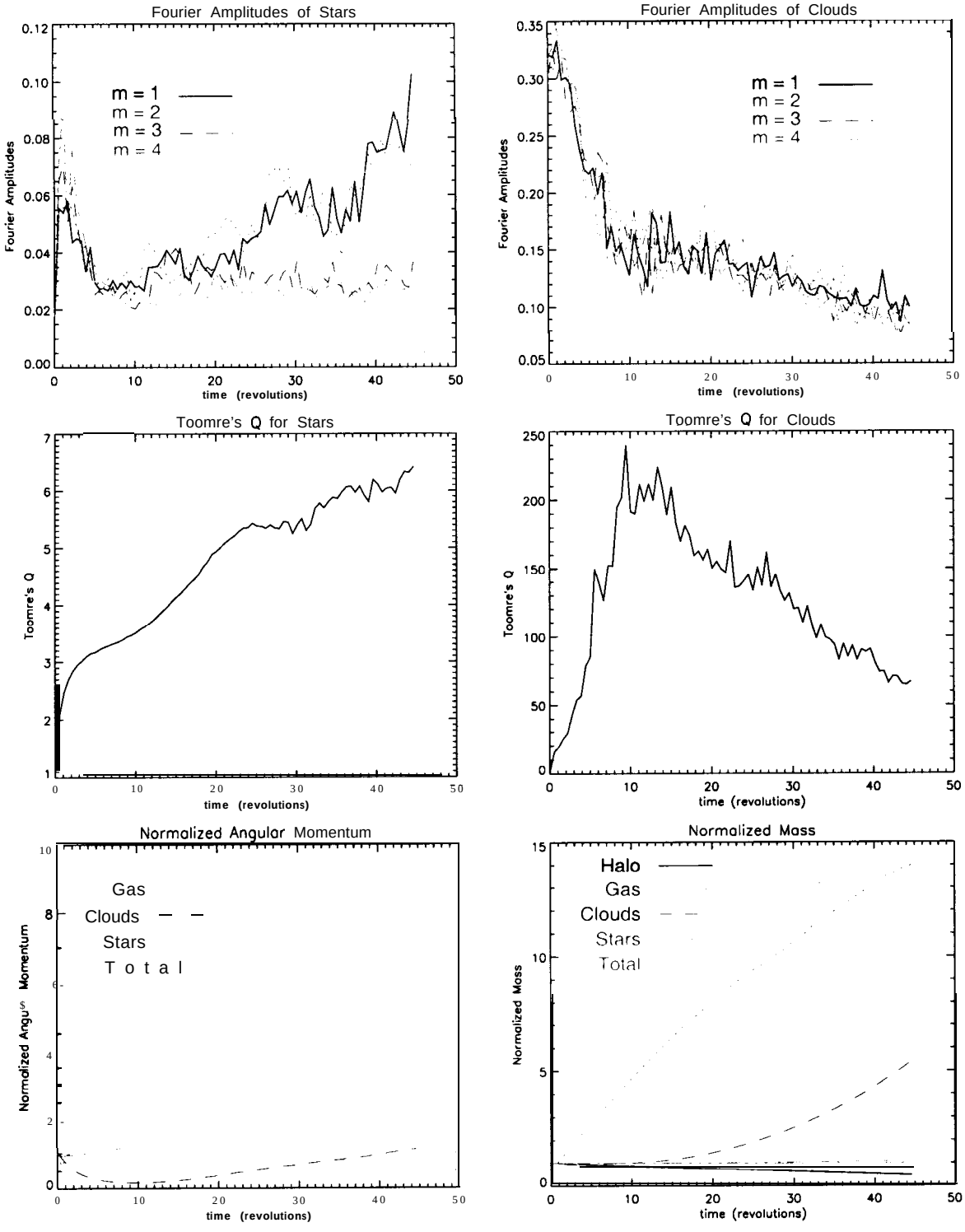

Figure C.25: Data Analysis of run # 38.

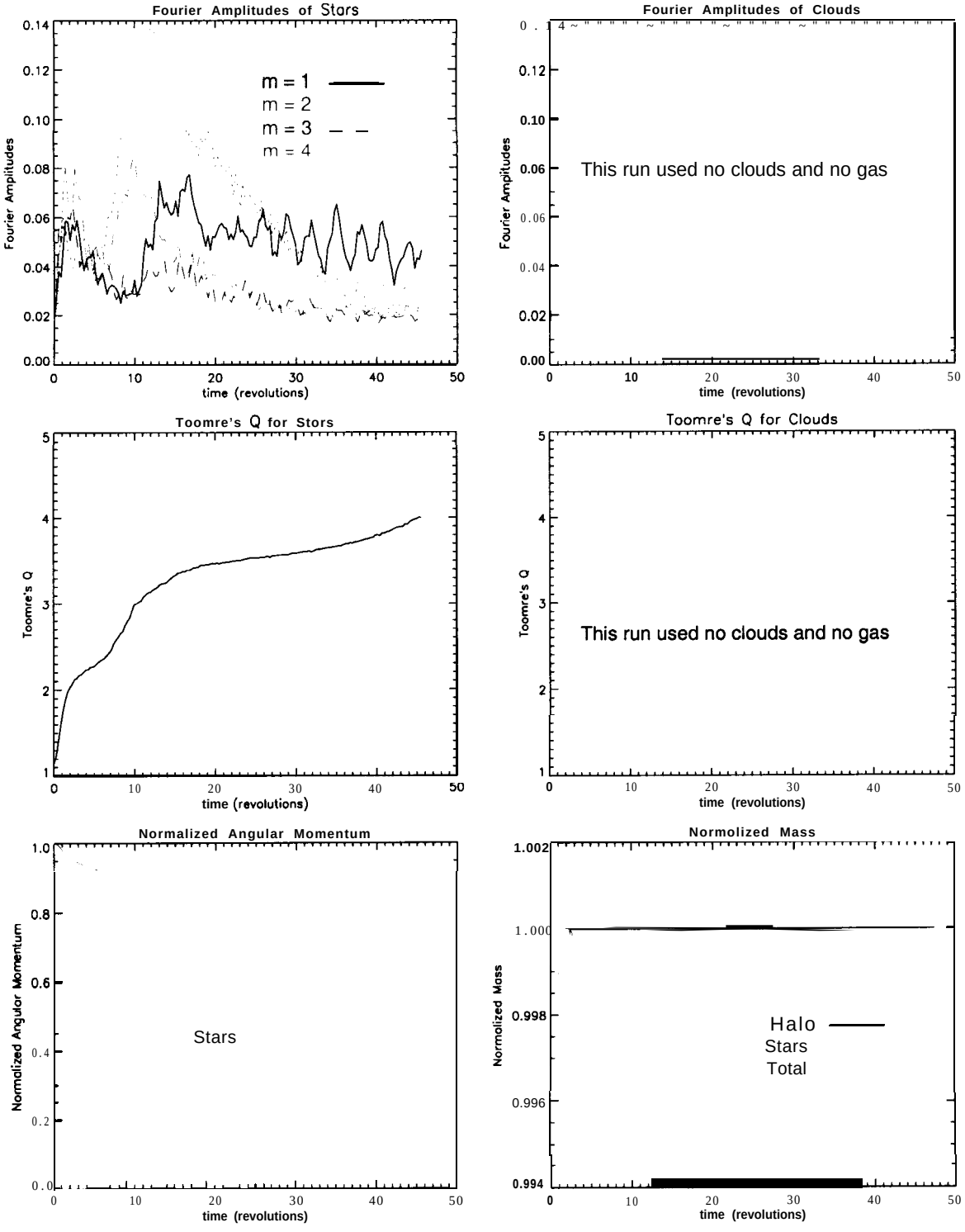

Figure C.26: Data Analysis of run # 39. This run used only halo and stars.

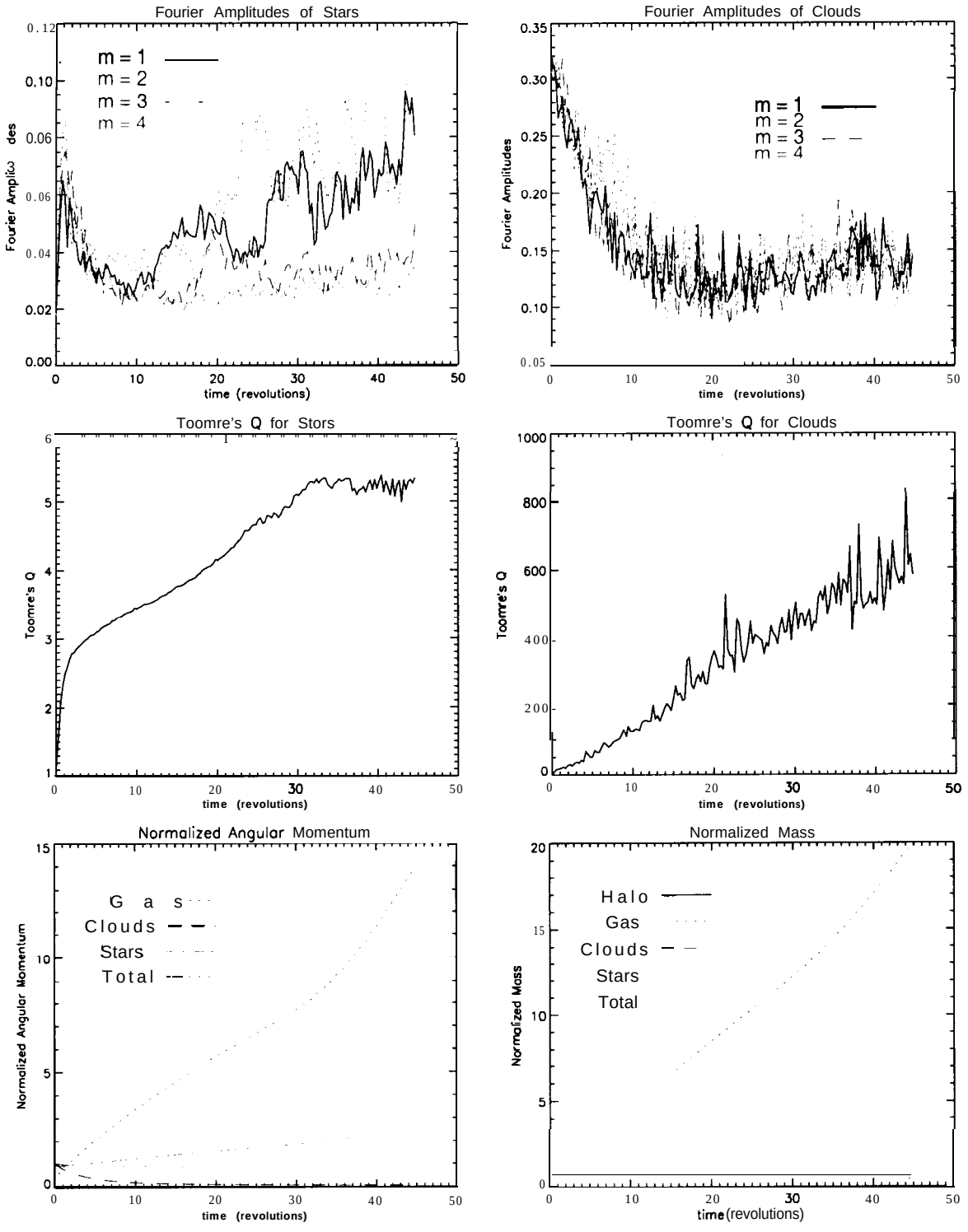

Figure C.27: Data Analysis of run # 40.

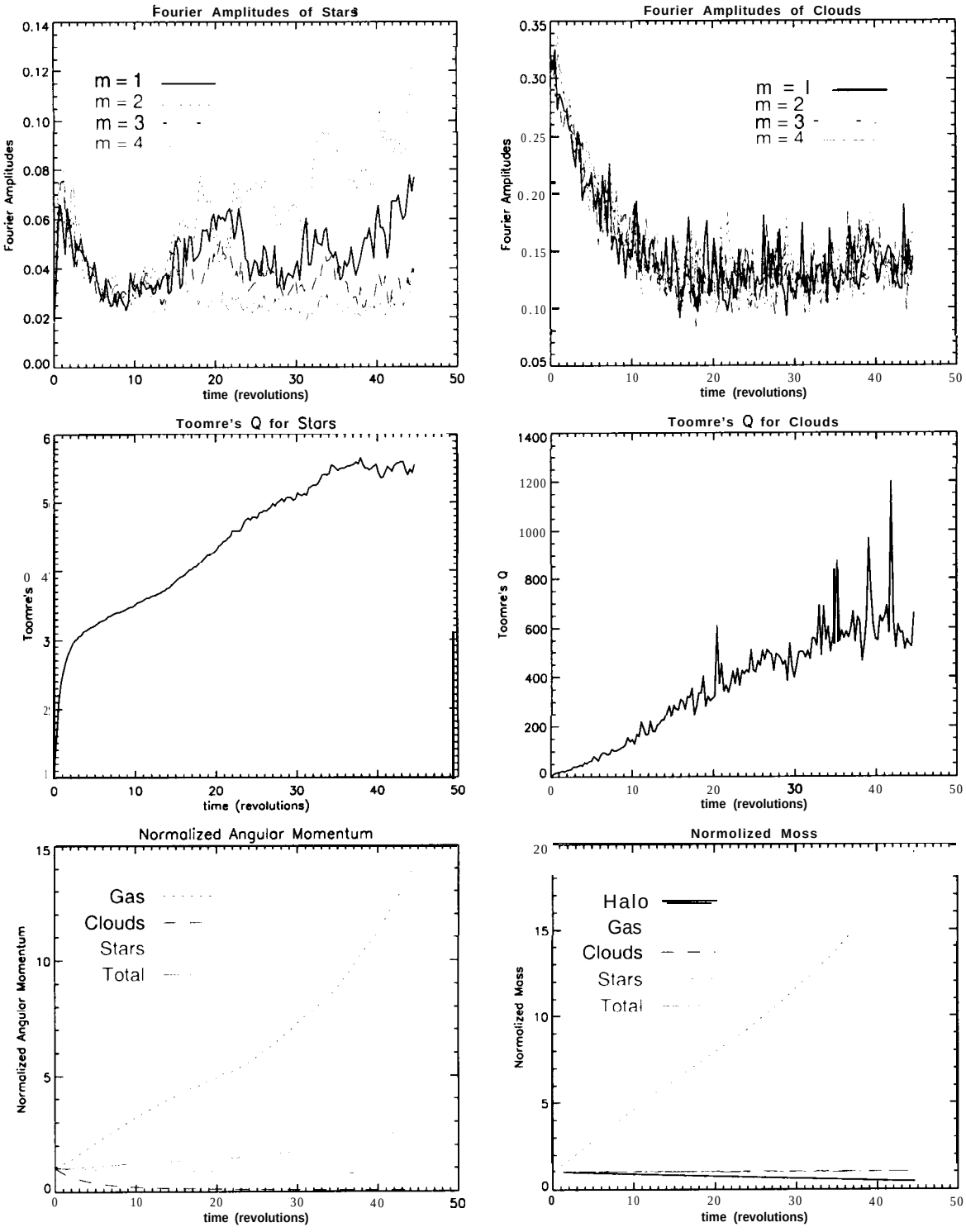

Figure C.28: Data Analysis of run # 41.

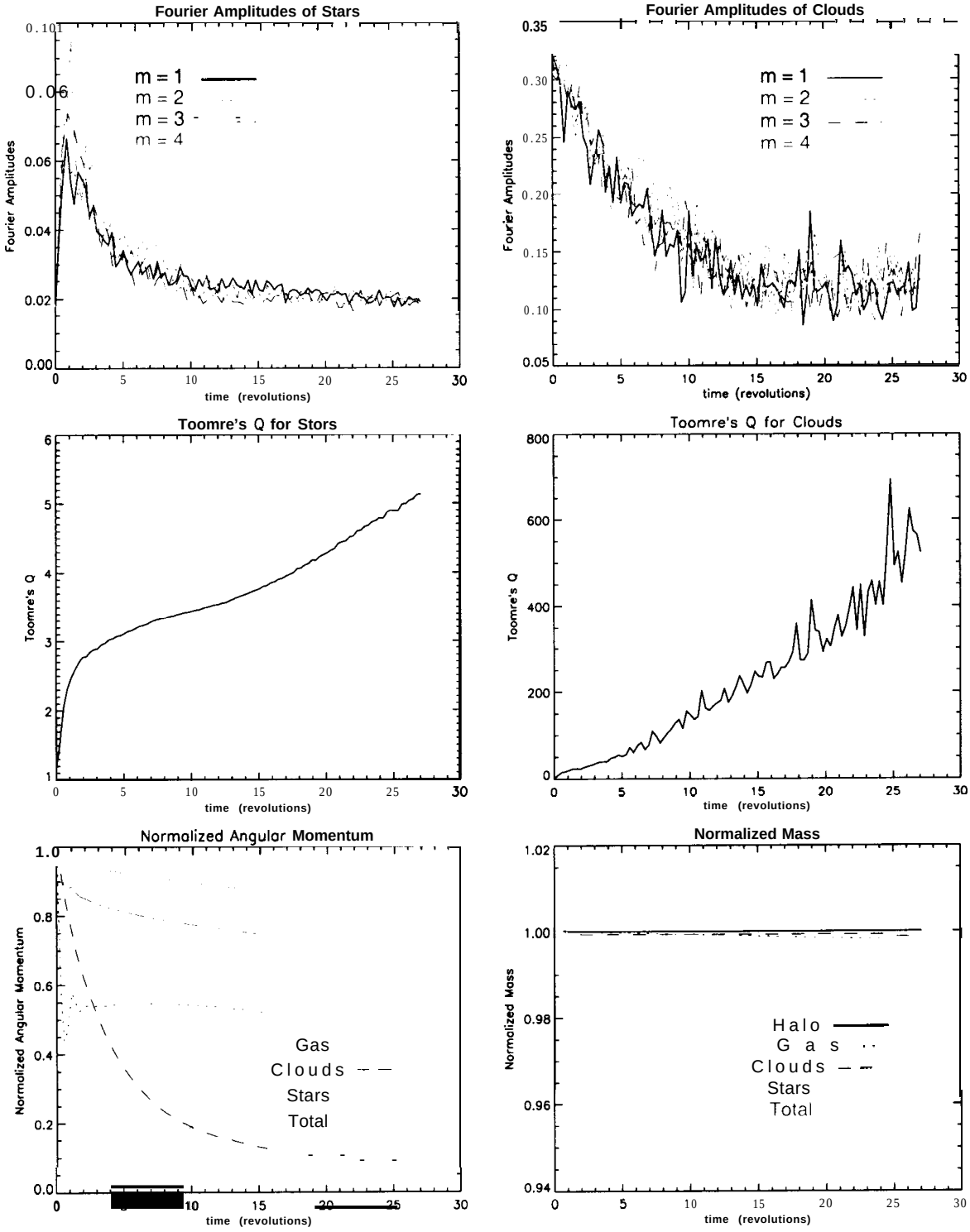

Figure C.29: Data Analysis of run # 42.

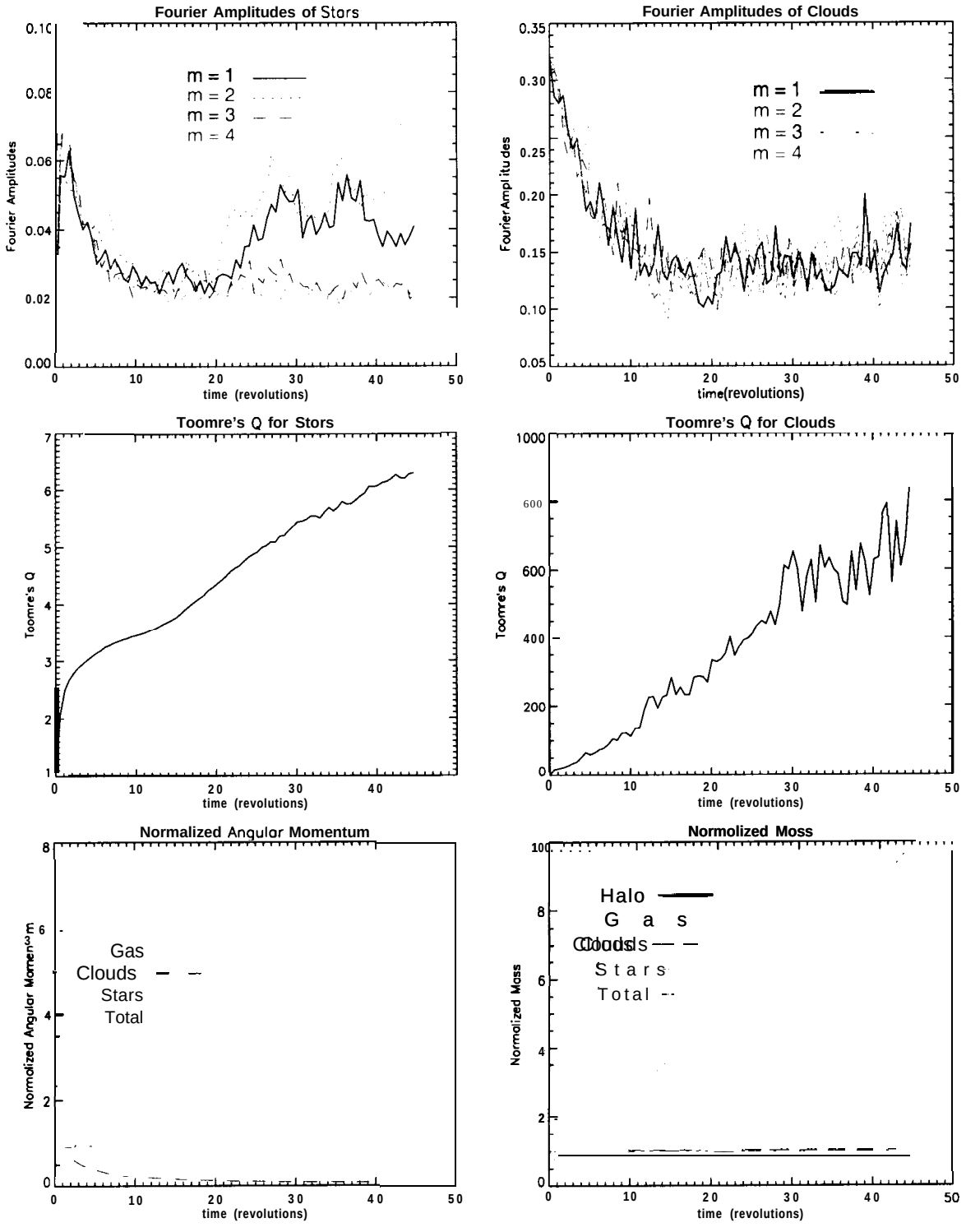

Figure C.30: Data Analysis of run # 43.

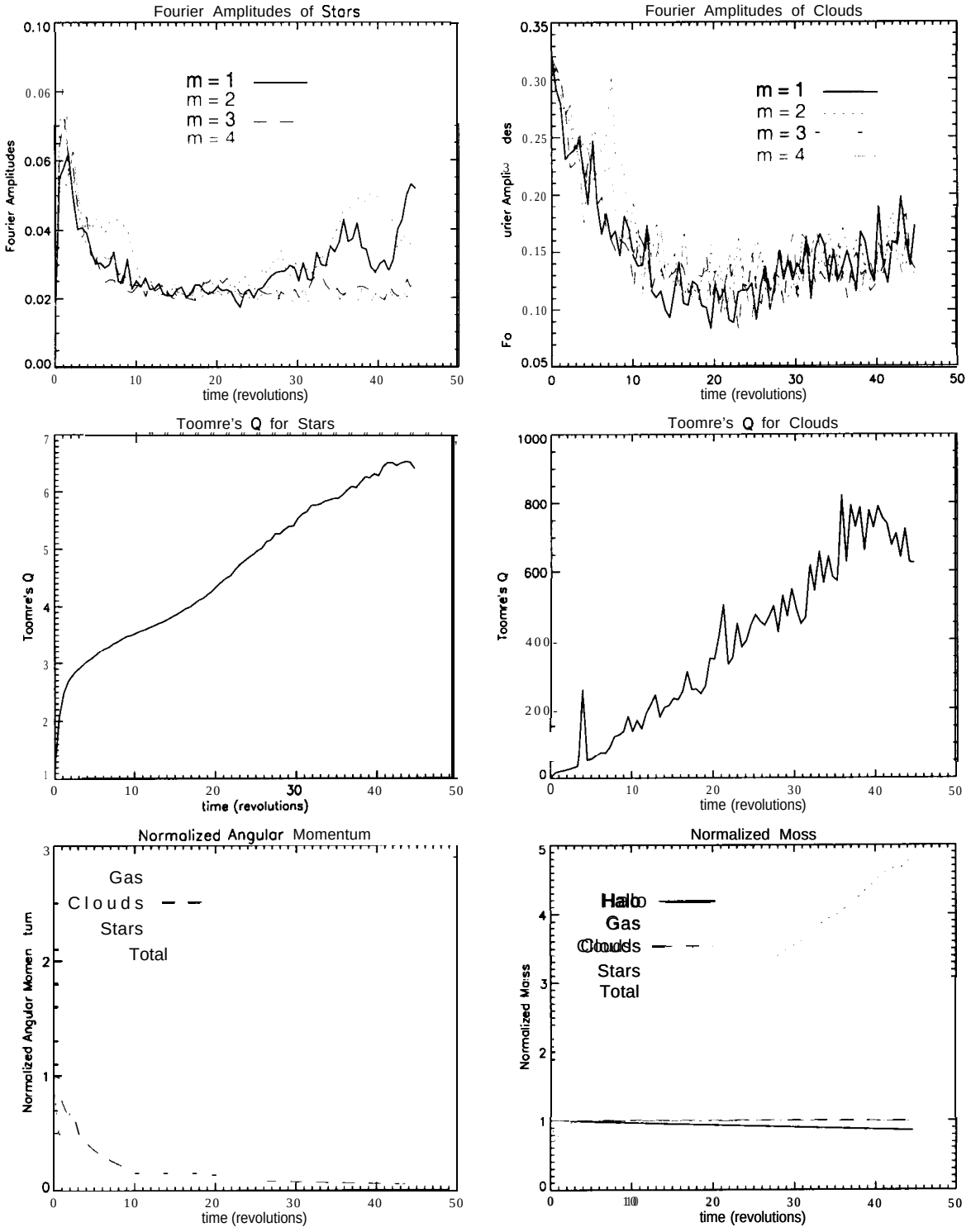

Figure C.31: Data Analysis of run # 44.

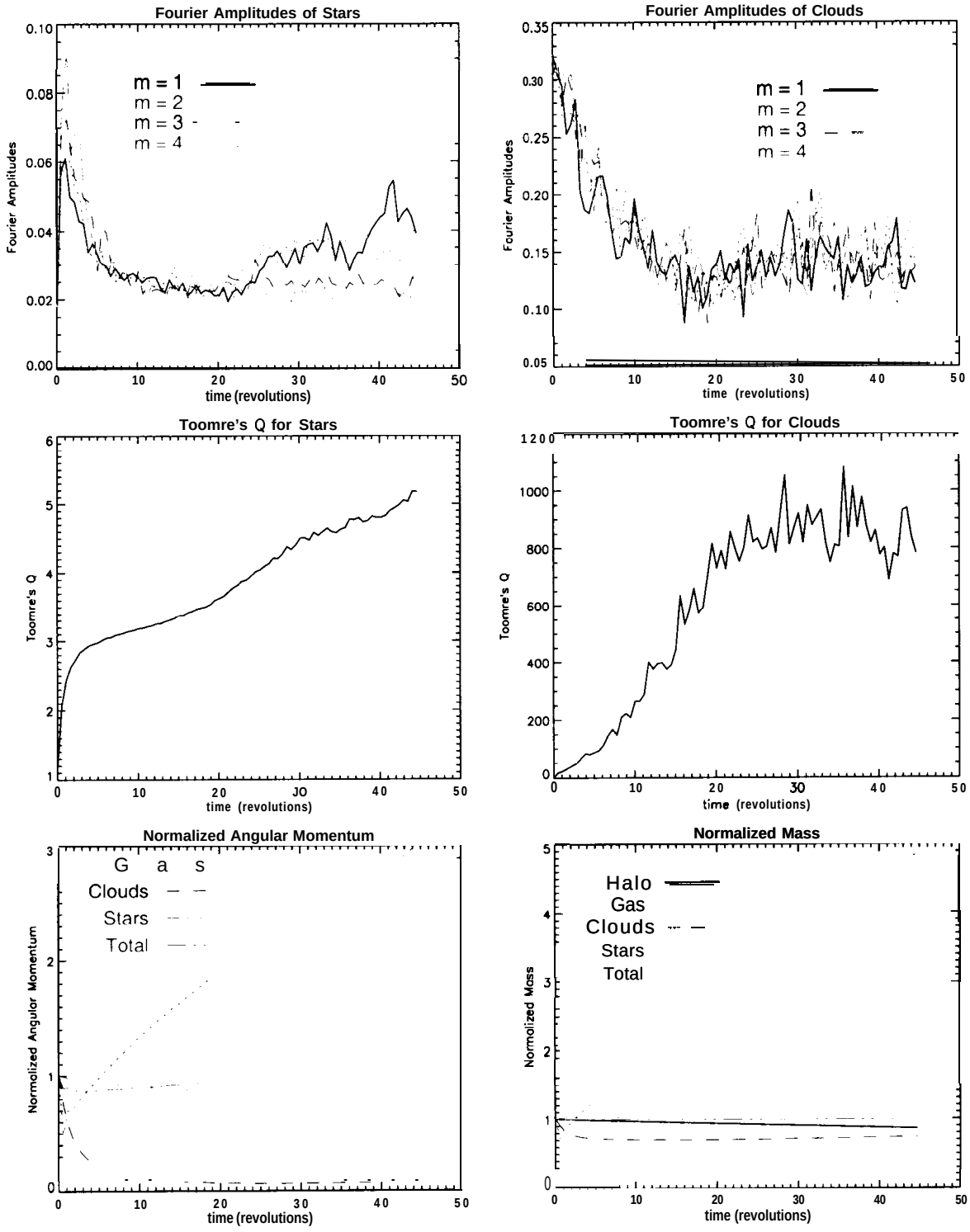

Figure C.32: Data Analysis of run # 45.

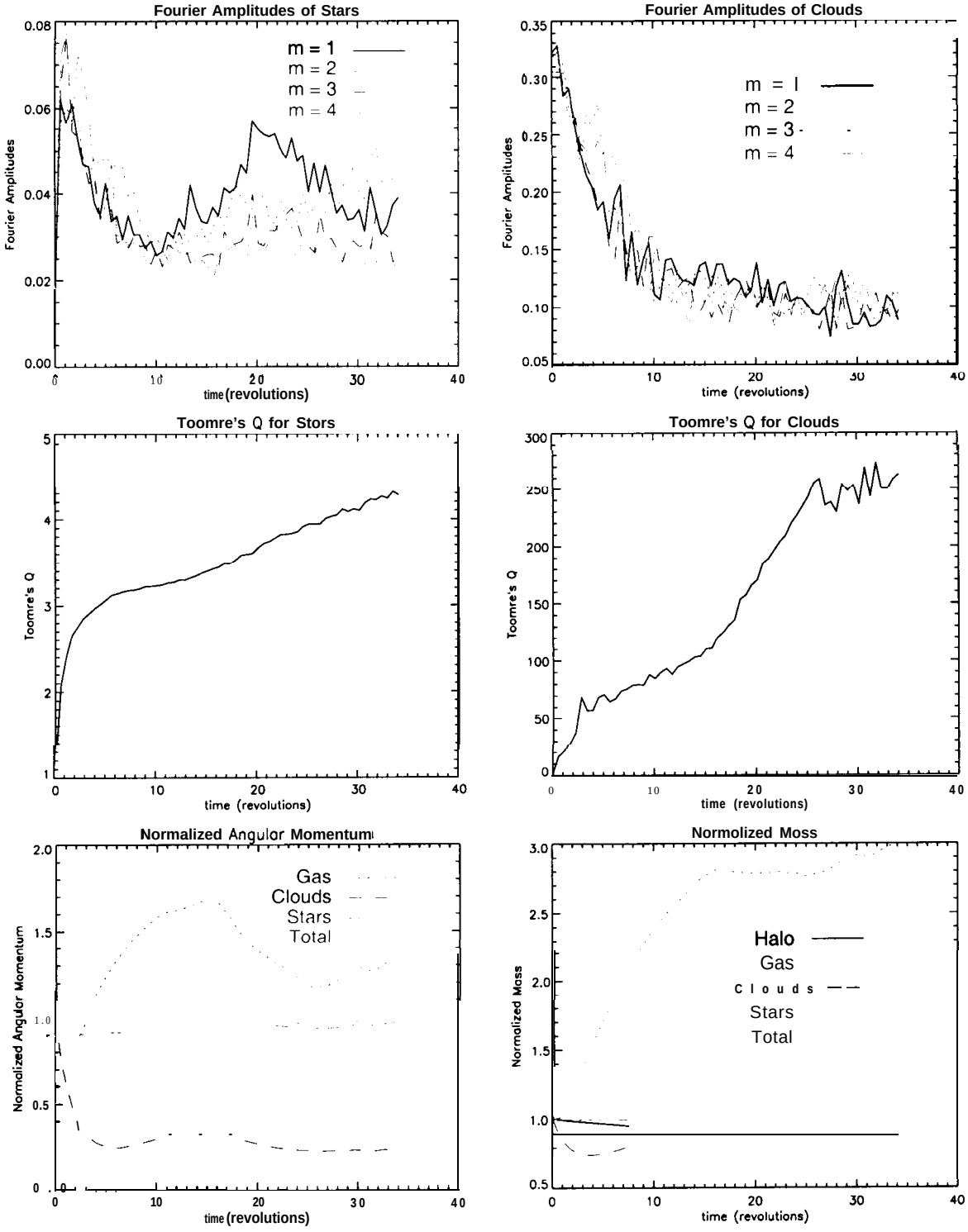

Figure C.33: Data Analysis of run # 46.

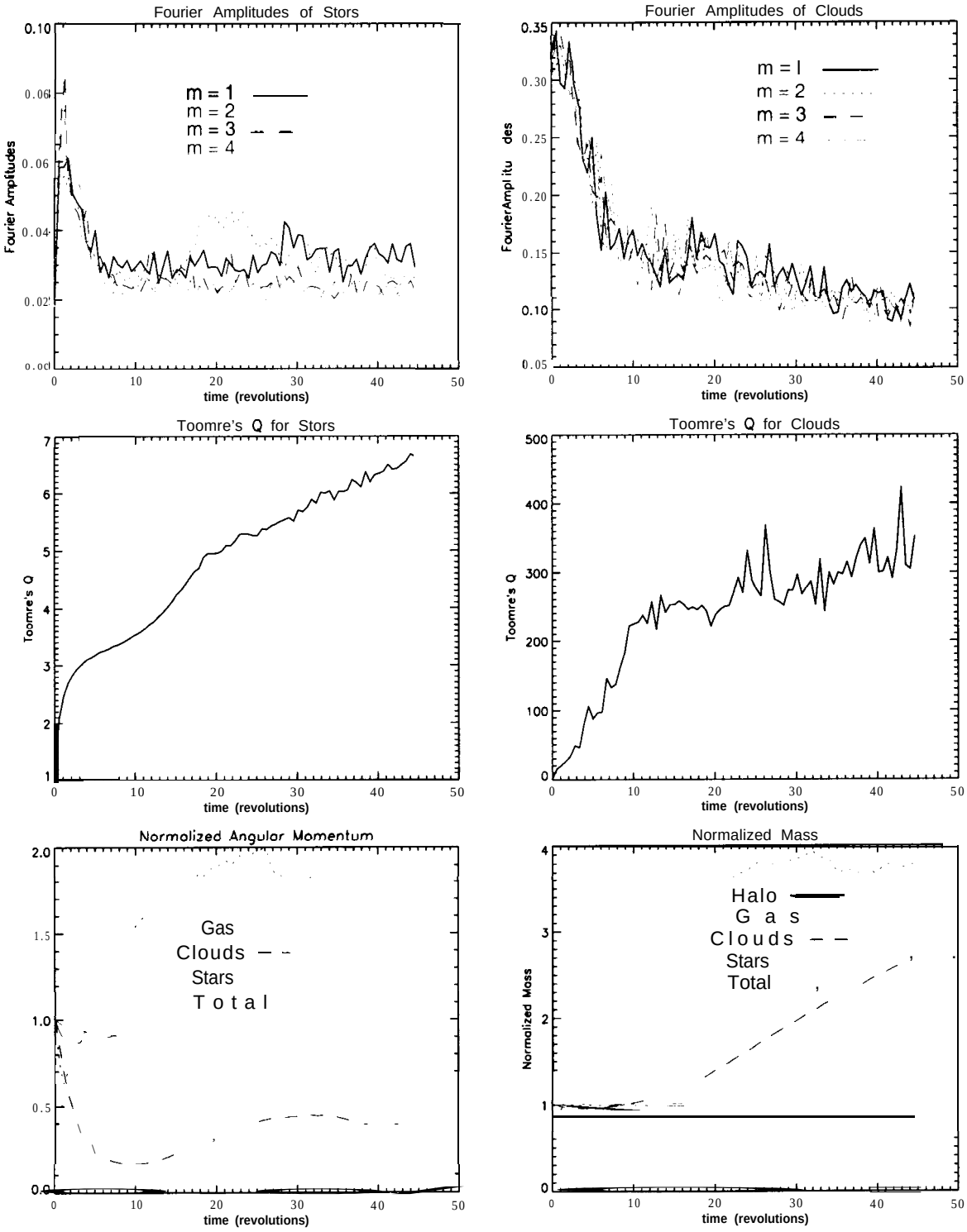

Figure C.34: Data Analysis of run # 47.

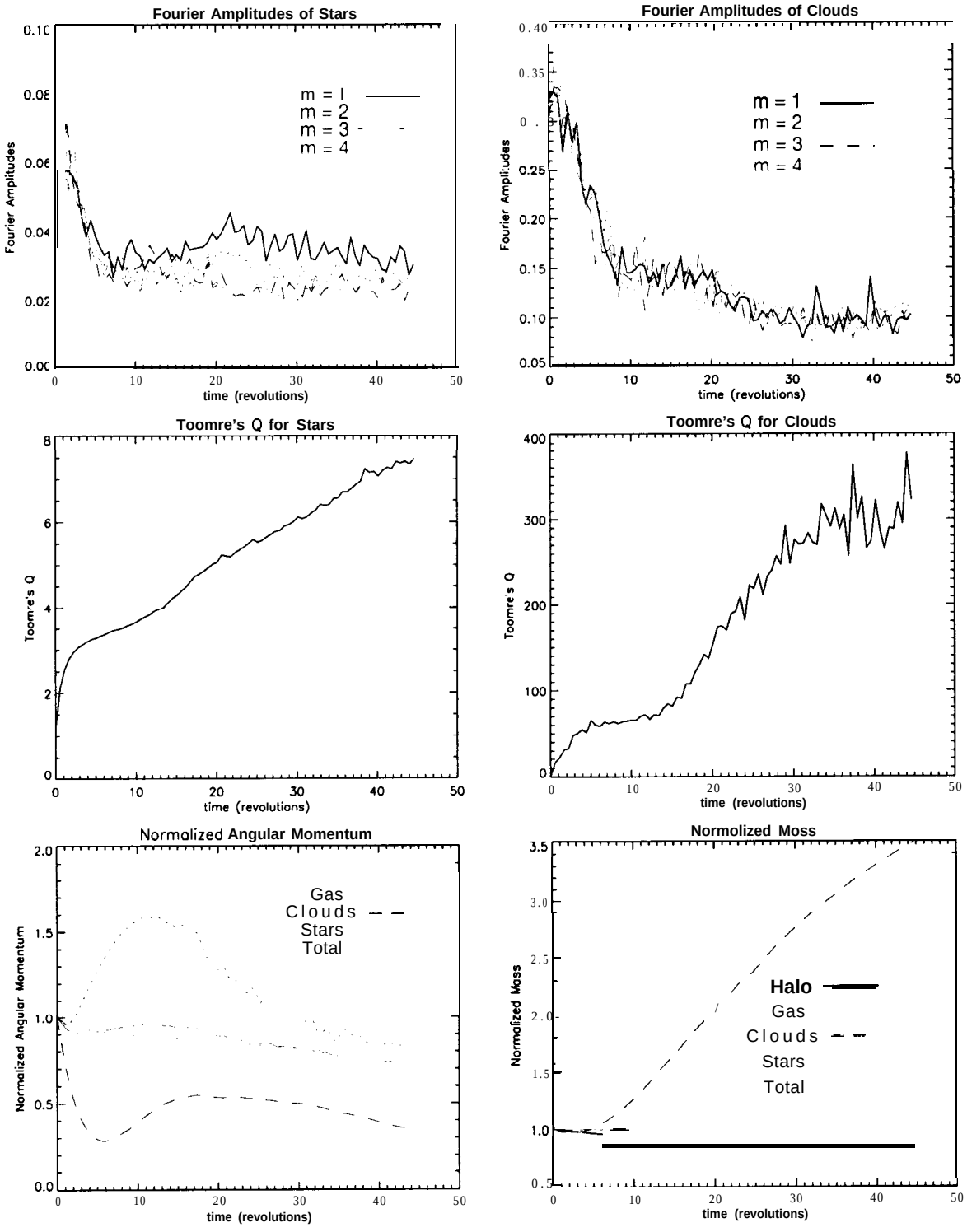

Figure C.35: Data Analysis of run # 48.

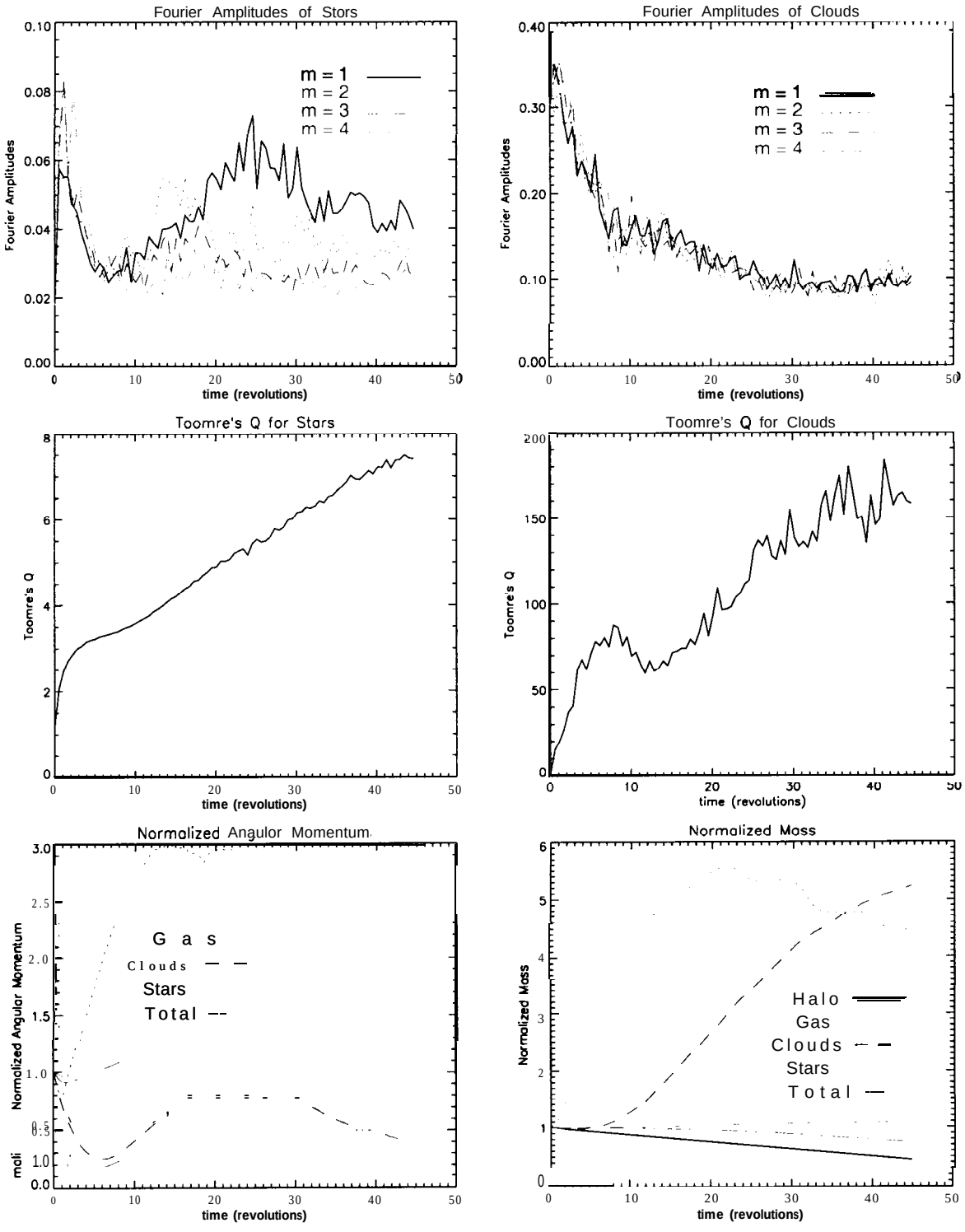

Figure C.36: Data Analysis of run # 49.

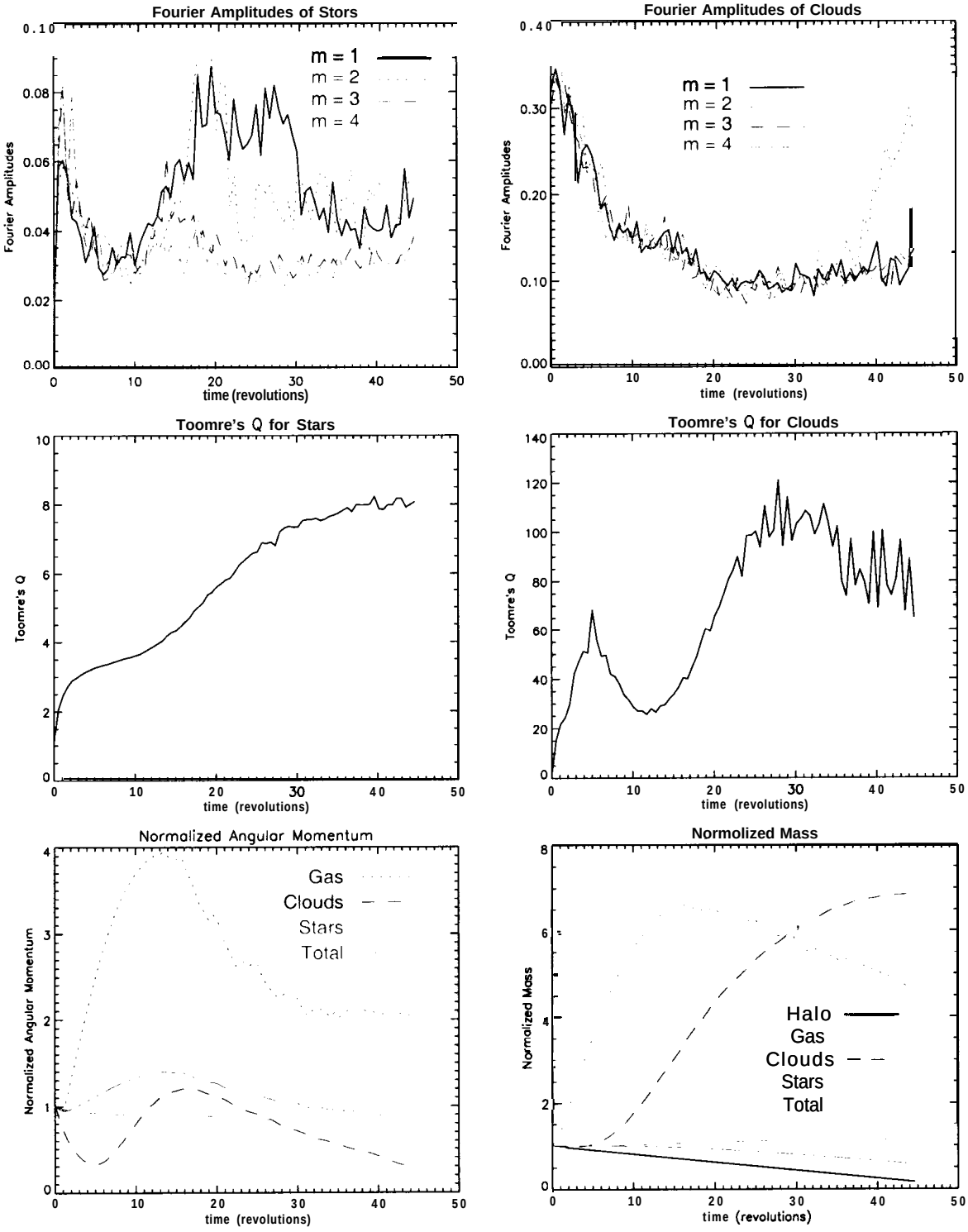

Figure C.37: Data Analysis of run # 50.

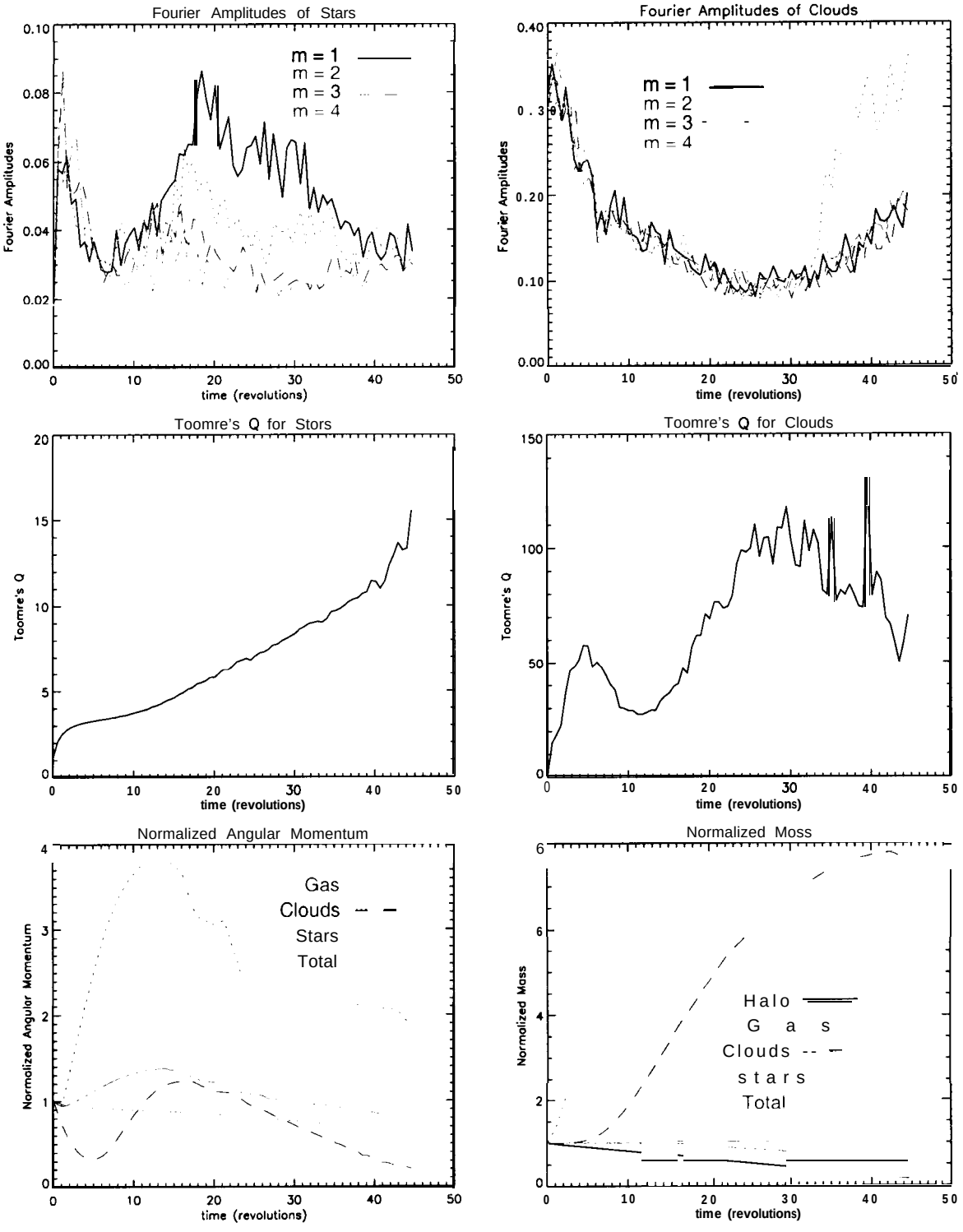

Figure C.38: Data Analysis of run # 51.

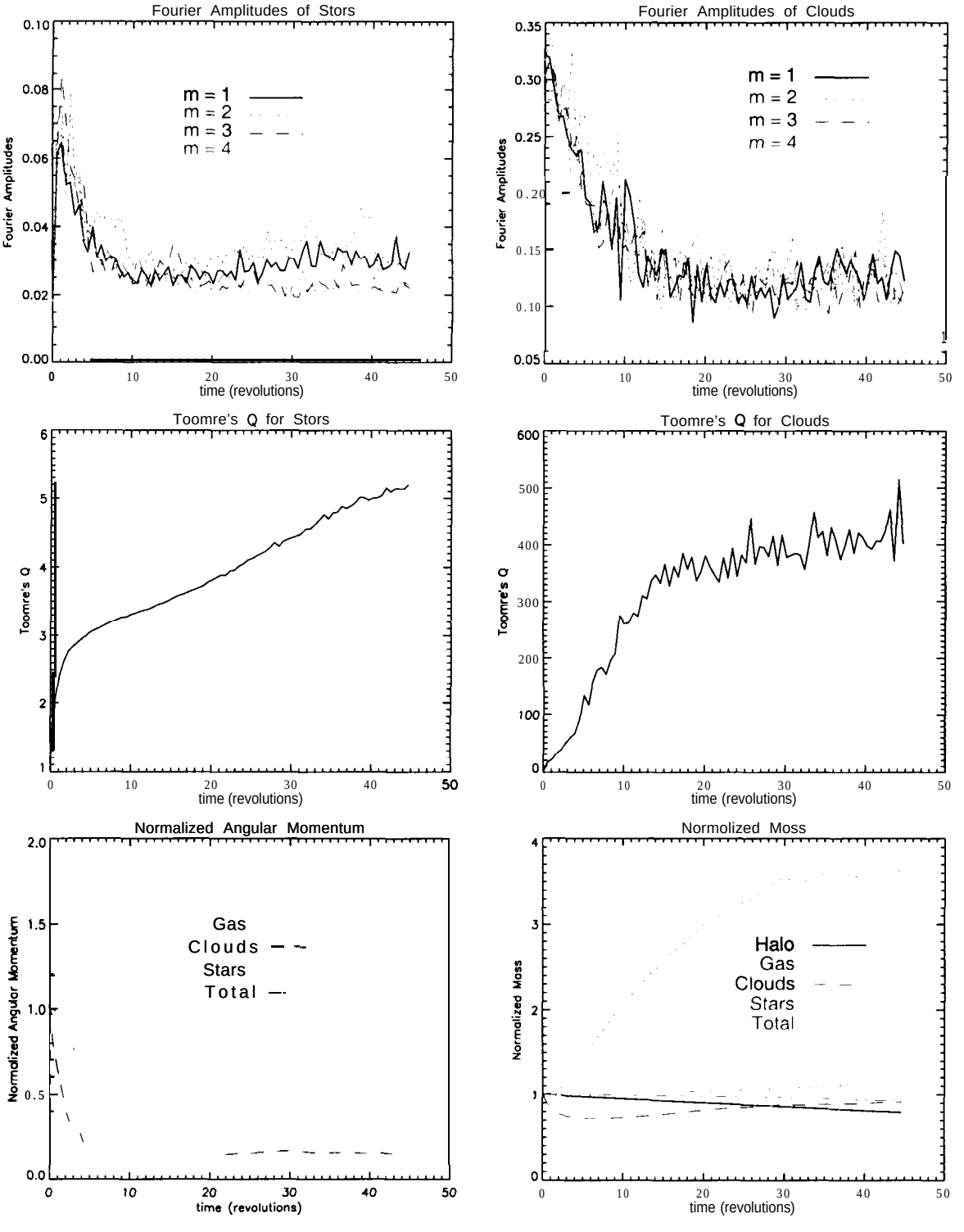

Figure C.39: Data Analysis of run # 52.

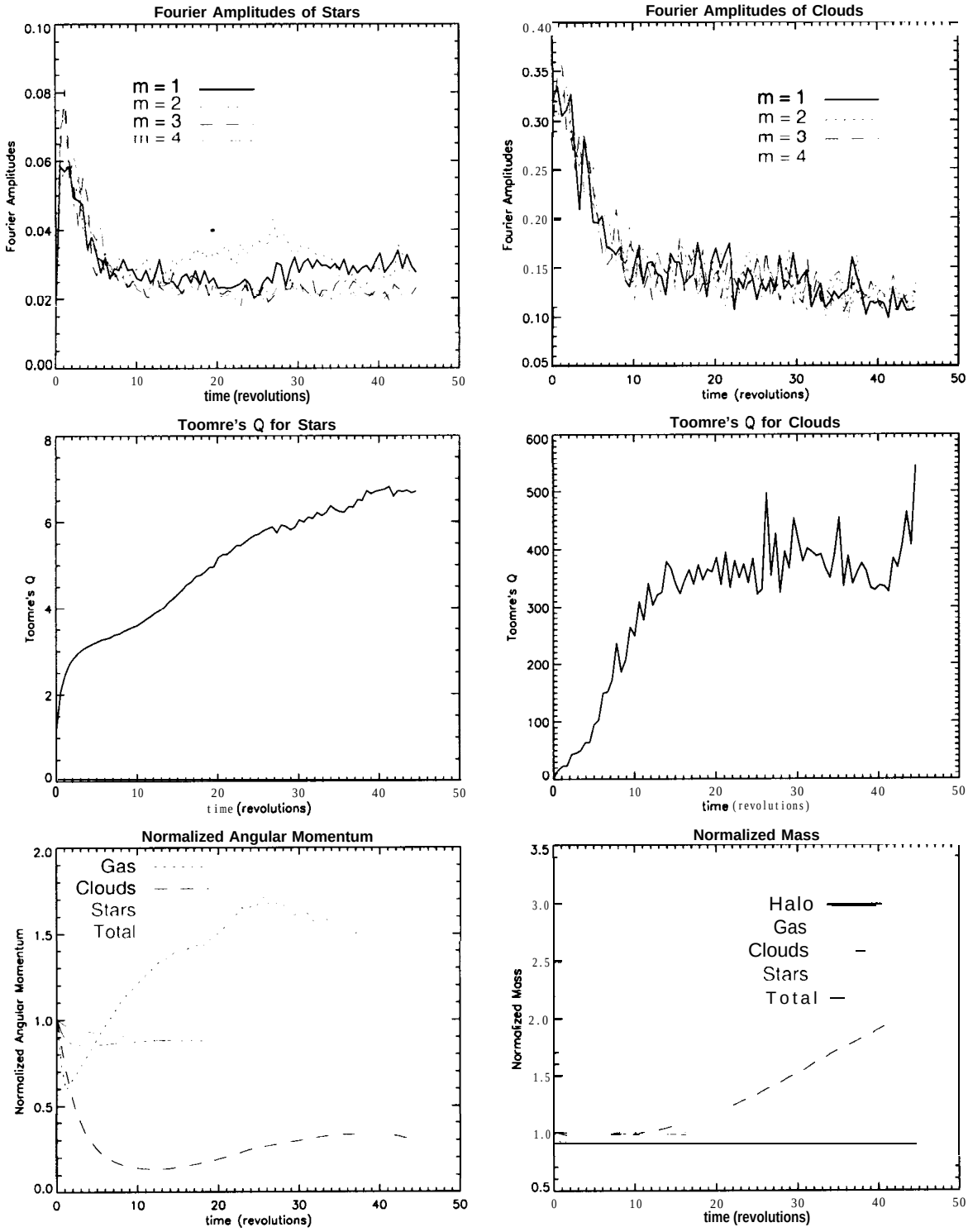

Figure C.40: Data Analysis of run # 53.

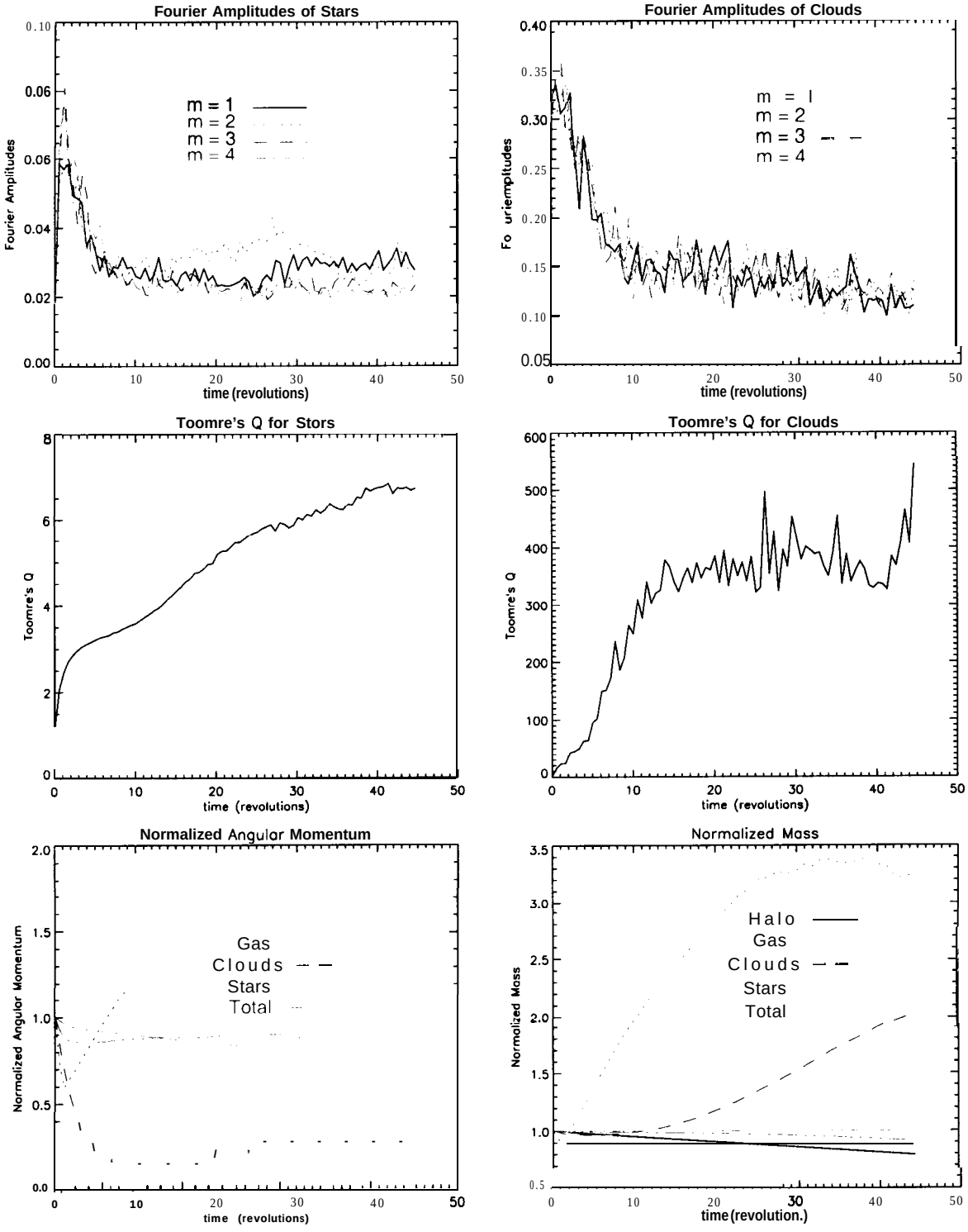

Figure C.41: Data Analysis of run # 54.

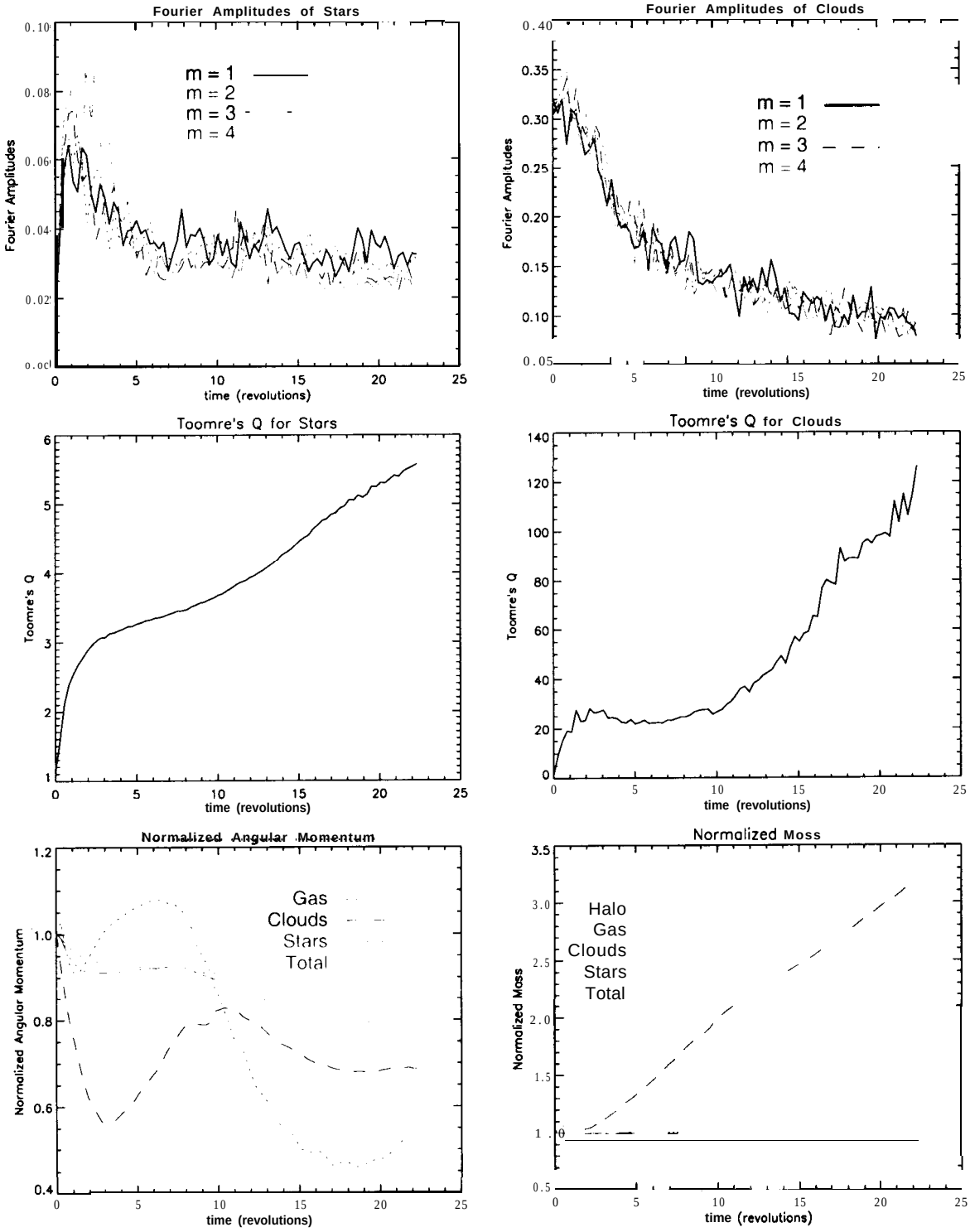

Figure C.42: Data Analysis of run # 55.

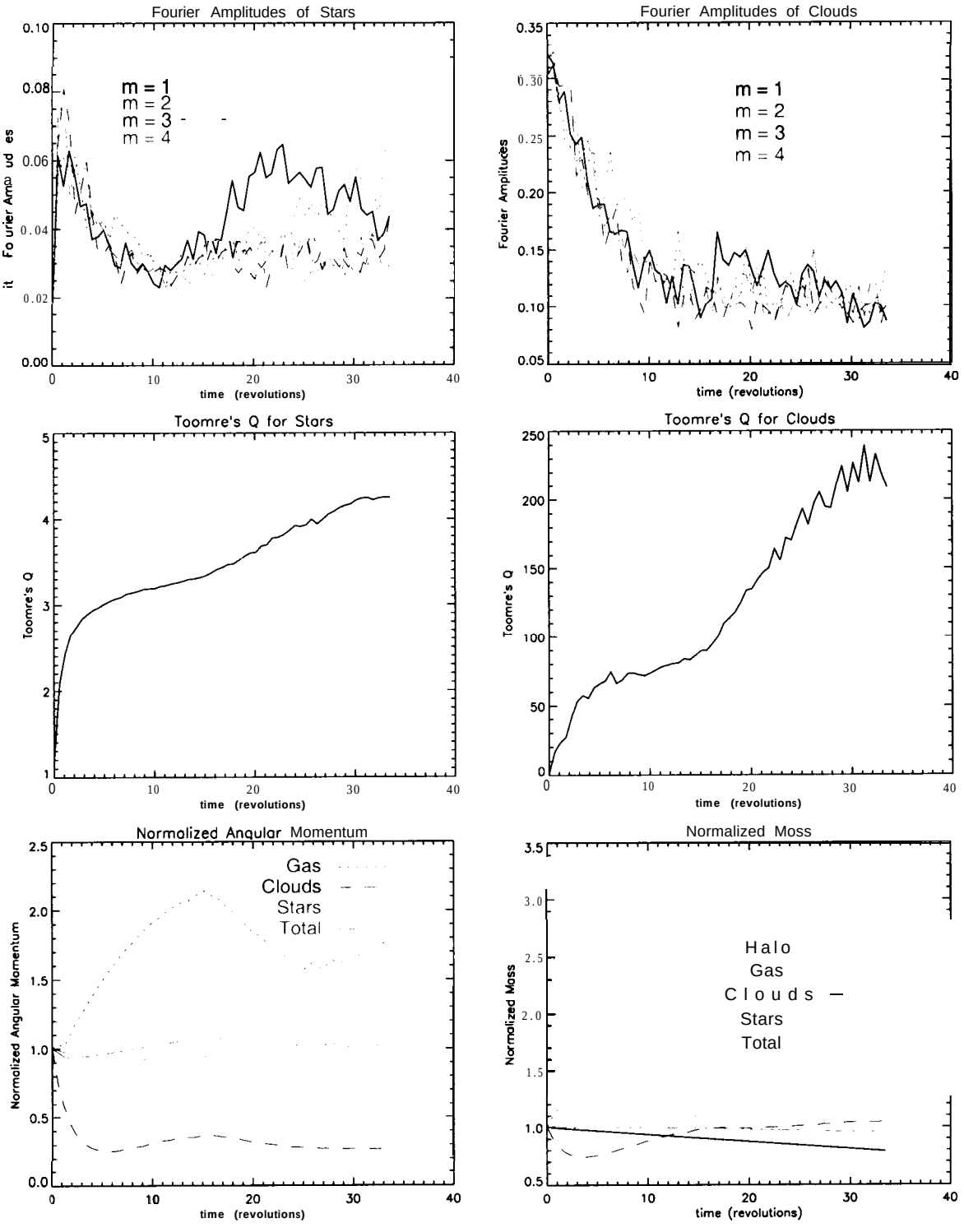

Figure C.43: Data Analysis of run # 56.

BIOGRAPHY OF THE AUTHOR

Thomas Zeltwanger was born in Bietigheim-Bissingen (Baden-Württemberg, Germany) on January 17 1967, and attended the Ellental-Gymnasium High School in his birth town. Following his high school graduation in June 1986, he completed the mandatory fifteen months service in the German armed forces.

In October 1987 he began studying physics at the Ludwig-Maximilians-University in Munich, Germany, and soon focused on astronomy and astrophysics as his major subjects. During his studies he gained valuable experience as an intern at the Institute for Astrophysics in Munich, and he also logged many observation hours at the Wendelstein Observatory in southern Bavaria. In December 1994 he graduated from the Ludwig-Maximilians-University and received the degree of a Diplom-Physiker (Univ.), a degree equivalent to a Master of Science in Physics. The topic of his master's dissertation was "Using Thermoluminescence to determine the Age of Volcanic Rocks".

In January 1995 Thomas started his graduate studies at the University of Maine. While a graduate student, he worked as a teaching assistant in astronomy and physics courses, and supervised undergraduate students during their observational projects at the Maynard F. Jordan Observatory and at the Maynard F. Jordan Planetarium.

Thomas was selected as the Outstanding Teaching Assistant of the Department of Physics and Astronomy for 1996/97. In the summer of 1997, he successfully applied to and attended the NASA Summer School for High Performance Computational Physics at the NASA/Goddard Space Flight Center in Greenbelt, Maryland. He is a member of AAPT (American Association of Physics Teachers), APS (American Physical Society), and AAS (American Astronomical Society). For the 1998-99 academic year he was awarded a University Graduate Research Assistantship. In 1998, 1999, and 2000 he received a Frank H. Todd Scholarship.

He co-authored "One-armed Spiral Waves in Galaxy Simulations with Counter-rotating Stars" and "Sloshing in High Speed Galaxy Interactions". The two refereed articles were published in *The Astrophysical Journal Letters* (Comins et al., 1997), and in *The Astrophysical Journal* (Zeltwanger et al., 2000), respectively.

Thomas Zeltwanger is a candidate for the Doctor of Philosophy degree in Physics from The University of Maine in December 2000.